OAK RIDGE NATIONAL LABORATORY LIBRARIES
3 4456 0548437 5

CENTRAL RESEARCH LIBRARY
DOCUMENT COLLECTION

ORNL-3652
UC-20 – Controlled Thermonuclear Processes
TID-4500 (31st ed.)

THERMONUCLEAR DIVISION

SEMIANNUAL PROGRESS REPORT

FOR PERIOD ENDING APRIL 30, 1964

CENTRAL RESEARCH LIBRARY
DOCUMENT COLLECTION
LIBRARY LOAN COPY
DO NOT TRANSFER TO ANOTHER PERSON
If you wish someone else to see this document, send in name with document and the library will arrange a loan.

OAK RIDGE NATIONAL LABORATORY
operated by
UNION CARBIDE CORPORATION
for the
U.S. ATOMIC ENERGY COMMISSION

Printed in USA. Price: $2.75 Available from the
Office of Technical Services
U. S. Department of Commerce
Washington 25, D. C.

LEGAL NOTICE

This report was prepared as an account of Government sponsored work. Neither the United States, nor the Commission, nor any person acting on behalf of the Commission:

A. Makes any warranty or representation, expressed or implied, with respect to the accuracy, completeness, or usefulness of the information contained in this report, or that the use of any information, apparatus, method, or process disclosed in this report may not infringe privately owned rights; or

B. Assumes any liabilities with respect to the use of, or for damages resulting from the use of any information, apparatus, method, or process disclosed in this report.

As used in the above, "person acting on behalf of the Commission" includes any employee or contractor of the Commission, or employee of such contractor, to the extent that such employee or contractor of the Commission, or employee of such contractor prepares, disseminates, or provides access to, any information pursuant to his employment or contract with the Commission, or his employment with such contractor.

ORNL-3652

Contract No. W-7405-eng-26

THERMONUCLEAR DIVISION

SEMIANNUAL PROGRESS REPORT

For Period Ending April 30, 1964

JULY 1964

OAK RIDGE NATIONAL LABORATORY
Oak Ridge, Tennessee
operated by
UNION CARBIDE CORPORATION
for the
U. S. ATOMIC ENERGY COMMISSION

OAK RIDGE NATIONAL LABORATORY LIBRARIES

3 4456 0548437 5

Contents

INTRODUCTION vii

ABSTRACTING SUMMARY xi

1. DCX-1 PLASMA EXPERIMENTS 1
   - 1.1 Introduction 1
   - 1.2 Investigations of Proton Losses from Plasmas Formed by Lorentz-Force Trapping 1
   - 1.3 Experiments with Movable End-Wall Configurations 8
   - 1.4 Additional Radio-Frequency Measurements 14
   - 1.5 Low-Frequency Phenomena 14
   - 1.6 Calculated Radial Density Distributions of Trapped Protons 22
   - 1.7 Theory of Longitudinal Oscillations 23
     - 1.7.1 Introduction: Experimental Observations 23
     - 1.7.2 Current-Ring Model 23
     - 1.7.3 Extension to a Nonconcentric Orbit Distribution, that is, to "Interlaced Orbits" 25
     - 1.7.4 Discussion of Observations in Terms of the Model 26

2. DCX-2 28
   - 2.1 Introduction 28
   - 2.2 Density Measurements 28
     - 2.2.1 Integral Method 28
     - 2.2.2 Density Measurements Based on $I_x \overline{\tau}_x$ 29
     - 2.2.3 Diamagnetic Measurements 31
   - 2.3 Plasma Distribution 31
   - 2.4 Secondary Plasma Measurements 34
   - 2.5 Particle Losses 35
   - 2.6 Radio-Frequency Emissions 36

3. ELECTRON-CYCLOTRON HEATING 39
   - 3.1 Electron-Cyclotron Heating Experiments in the EPA Facility 39
     - 3.1.1 Introduction 39
     - 3.1.2 Pinhole-Camera X-Ray Photographs 39
     - 3.1.3 EPA Cavity – Neutral Injection Entry 41
   - 3.2 Electron-Cyclotron Heating Experiments in the Physics Test Facility (PTF) 43
     - 3.2.1 Introduction 43
     - 3.2.2 Microwave Interferometer 43
     - 3.2.3 X-Ray Pinhole Photographs 44
     - 3.2.4 Pinhole Photographs of Atomic Hydrogen Emission 44

4. PLASMA PHYSICS 46
4.1 Observation of Burnout in a Steady-State Plasma 46
4.1.1 Identification of the Burnout Phenomena 46
4.2 Stabilized Plasma 49
4.2.1 Hot-Electron Plasmas 49
4.3 Measurement of Plasma Density in Hot-Electron Plasmas by X-Ray Flux – Impurity Considerations 52
4.4 Beam-Plasma Studies 53
4.5 Ion Beam Stabilization 55
4.6 Velocity of Moving Striations in Discharge Tubes as a Function of Gas Pressure 56
4.6.1 Introduction 56
4.6.2 Theoretical Properties of Ionic Sound Waves 57
4.6.3 Experimental Apparatus and Procedures 61
4.6.4 Data and Interpretation 62
4.6.5 Appendix: Calculation of σ 69

5. VACUUM ARC RESEARCH 71
5.1 Deuterium Arc Studies 71
5.1.1 Introduction 71
5.1.2 Flute Velocity and Plasma Transport 71
5.1.3 Ioffe Field Experiments 72
5.1.4 Laser Scattering Experiment 73
5.2 Operation of Long Solenoid 73
5.3 On a Vigorous Energy Pumping Cycle in the Energetic Carbon Arcs 74

6. CROSS-SECTION MEASUREMENTS 78
6.1 Cross-Beam Experiments 78
6.2 Excited States 79
6.3 Cross-Section Measurements 80
6.4 Proportional Counter for Particles of Low Energy 81

7. PRODUCTION, ACCELERATION, AND INJECTION OF IONIC AND ATOMIC BEAMS 84
7.1 High-Current Ion-Beam Production and Injection 84
7.2 Negative Ion Source 87
7.3 AC Ion Source 87
7.4 PIG Source for Ions and Plasma 87
7.4.1 Ion Source Development 87
7.4.2 Plasma from PIG-Type Ion Source 90
7.5 Neutral Beam Source 94

8. PLASMA THEORY AND COMPUTATION 96
8.1 Anomalous Diffusion 96
8.2 Effect of Finite Ion and Electron Temperatures on the Ion-Cyclotron Resonance Instability 97
8.3 Stability of Finite Plasmas 98
8.4 Some Qualitative Observations on the Stability of the Calutron Ion Beam 99
8.5 Impedance Properties of a One-Dimensional Beam-Plasma System 100

8.6 Scattering Losses in Minimum-B Experiments 102

8.7 Microwave Index of Refraction in a Mirror Field 103

8.8 Electron Streams and Arcs in Finite Plasmas 104

9. MAGNETICS AND SUPERCONDUCTIVITY 105

9.1 Field Homogeneity and Power Optimization of Magnet Coil Systems 105

9.1.1 Introduction 105

9.1.2 Magnetic Field of a Symmetrical Solenoid 105

9.1.3 Power Optimization of a Solenoid of the Second Order 106

9.1.4 Power Optimization of a Solenoid of the $2n^{th}$ Order, $n \geqq 2$ 107

9.1.5 Special Forms of $J(r,z)$ 108

9.1.6 Optimized Solenoids of Second, Fourth, Sixth, and Eighth Order, $v = 40$, $\beta = 2.0$ 109

9.1.7 Power-Optimized Solenoids of Second Order with Rectangular Cross Section and $v = 40$ 111

9.1.8 Power-Optimized Solenoids of $2n^{th}$ Order, $n \geqq 2$, with Rectangular Cross Section and $v = 40$ 112

9.2 Field Study on DCX-1 with Superimposed Quadrupole System 113

9.3 A Note on the Magnetic Field of a Straight Filament Segment 118

9.4 A Study of Quadrupole Current Sheet Arrangements 119

9.5 Minimum-B Configuration with Iron Quadrupole 125

9.6 Special Magnetometer Probes 127

9.7 Microsize Hall Probes for Superconductivity Measurements 129

10. VACUUM SYSTEMS, TECHNIQUES, AND MATERIALS STUDIES 132

10.1 Electron Bombardment Studies 132

10.2 Electronic Cleaning in DCX-1 136

10.3 Offgassing of Surfaces in High-Vacuum Systems 138

10.3.1 Programmed Temperature Desorption 138

10.3.2 A General Relation Between Molecular Flow Offgassing and Heat of Adsorption for Hydrocarbons 140

10.3.3 Some Methods of Estimating the Heats of Desorption of Organic Compounds 140

10.4 Electron Bombardment of Oil-Covered Vacuum System Surfaces in the Ultrahigh Vacuum Test Facility 143

10.5 Use of Ion Gage Grid Degassing Effects to Assess Surface Cleanliness 144

10.6 Lithium Ion Emission from β-Eucryptite 144

11. DESIGN AND ENGINEERING: NOTES 146

11.1 Friction Factors for Curved Hollow Copper Conductors 146

11.2 Considerations of Engineering Implications of Proposed Thermonuclear Reactors 149

11.3 A New, Versatile Vacuum Quick-Seal and Vacuum Lock 151

12. DESIGN AND ENGINEERING: SERVICE REPORT 153

PUBLICATIONS, PAPERS, AND TRAVELING LECTURE PROGRAM 154

Introduction

A. H. Snell

The DCX-1 experiments for the past six months have been concentrated upon the difficult region of long containment times (10 sec or more). In this they have been aided by a timely contribution from the Vacuum Group, in which wall cleaning by electron bombardment has been found to be helpful in lengthening the containment times; the technique is described in Sects. 10.1 to 10.4 in the pages that follow.

The results of the DCX-1 experiments as described in Sect. 1.2 are (1) a confirmation that for decay times greater than about 5 sec, the efflux of charge-exchanged fast neutrals from the trapped proton population fails to account for the rate of trapping, with the implication that when the total stored proton population reaches 10^{12} (maximum density 1 or 2×10^8 cm^{-3}), some of the particles begin to be lost *as protons*; (2) a finding that the loss is *not* due to radial spatial spread of a gradual nature; (3) a finding that the loss is *not* due to spatial spread into the mirror throats. There remain two possibilities: that the radial losses might exist as very rapid transport of protons to larger radius, and that the missing protons might be lost to the shouldered end walls of the liner. If neither of these is found to be true, then a more subtle effect must be entering the picture. Clearly, we have a central puzzle here; particle accountability must be reestablished before we can obtain meaning from many of the secondary experiments in DCX-1.

DCX-1 yields radio-frequency signals of three kinds (at least): (1) the proton cyclotron frequency and its harmonics; (2) a set of nonharmonic frequencies corresponding to longitudinal currents; and (3) a low-frequency signal, less than 100 kc and variable with injected beam current and τ (Fig. 1.26). The longitudinal oscillations have now been accounted for (Sects. 1.4 and 1.7) in terms of electrostatic coupling of trapped electrons and proton axial betatron oscillations. This coupling now becomes our prime candidate in explaining the spatial spread of the stored proton population; but note that it is not the Harris instability because azimuthal clustering of trapped protons is not necessarily involved. The low-frequency signals do not show a clear azimuthal phasing correlation and are thought not to be associated with a flute; they appear as a modulation on the longitudinal currents associated with the cold plasma (Sect. 1.5). When electron cyclotron heating is applied, they split into two frequencies (Figs. 1.27 to 1.29).

Thus the phenomena of DCX-1 appear to be a mixture of the orbit phenomena of storage rings and plasma phenomena. Finally, as there is a common misconception that the stored protons in DCX-1 occupy an ordered ring, we show calculations in Figs. 1.37 and 1.38 that indicate that the central part of the DCX-1 is quite filled with particles under normal circumstances with distributed trapping; only when the radial extent is deliberately limited does the population assume a configuration more like a hollow shell.

The steadily lengthening productive operating periods of DCX-2 have led to substantial further accumulation of information on the complicated performance of the plasma it generates. Operating with the lithium arc and about 50 ma of injected H_2^+ ions, it accumulates fast-ion densities of more than 10^{10} cm^{-3}, as indicated by the most believeable of four different methods of measurement. The mean density shows great sensitivity to small changes in the magnetic field distribution. The

stored ions have an astonishing energy spread: although trapped at 300 kev, they may have maximum energies close to 2 Mev and a mean energy of 1 Mev! The spatial distribution of the ions is less well known, because the density distribution of charge-exchange centers is uncertain, and both of these factors affect the rate of emission of the fast neutrals from various parts of the plasma. Under magnetic field conditions optimized for the ion density, most of the ion motion is found to be sharply in $v_\perp$. On the other hand, there is evidence that nearly all the injected beam is dissociated when the lithium arc is used, but nevertheless more than half of the H_2^+ beam power is being returned to the injector. At the moment, this tangle of observations can be resolved by the speculation that most of the beam power is going into atomic ions, most of which under plasma spreading run into the injector; the charge-exchanged neutrals with the strong $v_\perp$ would come from a subsidiary population produced by collective interactions which are then trapped in the peripheral field ripples. More diagnosis may change this picture. Frequency shifts of the ion cyclotron emission lines suggest a steady-state beta of 1.6%, but nevertheless there is no evidence for slow rotation or major plasma loss by hydromagnetic instability.

A large part of the effort on electron cyclotron heating has been devoted to the construction of a beam apparatus to enable us by fast-neutral-particle injection to probe the opacity of the fast-electron plasma against incoming neutrals. The objective is to see how large the hot-electron plasma would have to be to yield a burned-out central region. Not only had the injection system to be engineered (Sect. 7.5), but a rather knotty special technological problem had also to be solved (Sect. 3.1.3). Meanwhile, two variants of the pinhole technique have been applied to the electron cyclotron plasmas to give improved information about size and shape: one method uses x rays (Sects. 3.1.2 and 3.2.3), and the other uses charge-exchanged H^0 on a screen of MoO_3 (Sect. 3.2.4).

Although we have known for years that the "mode II" arc heats ions, the observations of simultaneous burnout described in Sect. 4.1 have sparked a sharp new interest. The experiments show that the electron-beam–plasma interaction has been made to yield simultaneously burnout, and ion heating; so the question immediately arises: To what extent can this fortunate combination be capitalized upon for injection purposes or to yield a steady-state fusion plasma, at least in a small experimental size? For injection purposes, we describe in Sect. 7.4 an open-ended version of this arc (without burnout) which can be used either as an ion source (0.25 amp) or as a plasma source. Further corroborative diagnostic work on the present plasma is being undertaken.

The accumulating observations of induced ion $v_\perp$ are worth noting. Figure 2.8(c) shows it appearing sharply in DCX-2. It has appeared in other experiments, manifesting itself, for example, by erosion patterns on metal surfaces, and the Russians see it too. All of this has made us recall an ion beam instability that was observed some time ago, and during the last few months we have tried without success to recapture it (see Sect. 7.1 for a speculation that it might be the cause for a mysterious difficulty that is being encountered in sending an ion beam through a tube). The underlying idea, of course, is that if by beam-plasma interaction an ion beam can be induced to generate a transfer of $v_{||}$ into $v_\perp$, then we might have a powerful means of endwise, efficient, snoutless injection into a magnetic mirror configuration. Note that the longitudinal spread in DCX-1, as treated in Sect. 1.7, is an inverse of the process: here $v_\perp$ is transformed into $v_{||}$ by the interaction with oscillating electrons.

In all the talk about instabilities that appears in fusion circles, it is perhaps refreshing to point to one case of stabilization that is simple and spectacularly successful, even if still somewhat occult. This is the stabilization of calutron beams, as described in Sect. 4.5 and discussed in Sect. 8.4. Attempts to adapt the technique to DCX-1, however, have not yet produced encouraging results; the experiments are described in Sect. 1.3.

The "flutes" on the deuterium arc have been closely examined, and they do not look like the classical hydromagnetic flutes; they appear to spit radially out of the core of the arc at velocities comparable with the longitudinal ion drift

velocity ($\sim 10^6$ cm/sec) (Sect. 5.1). Extra-long hydrogen arcs (20 ft) can now be run in the enlarged Long Solenoid, where the techniques of low-pressure operation will be worked out for possible application in the DCX's and for further arc research (Sect. 5.2). Collisions between metastable C^{2+} ions are suggested as a mechanism for ion heating in the carbon arc (Sect. 5.3); that is, energy is taken from electrons to create the metastables, and then is released into ionic kinetic energy when the metastables collide.

The cross-section group, whose activities are reported in Sect. 6, has been largely occupied in the preparation of apparatus: the cross-beam vacuum system, equipment for the production and excitation of H^0 produced by passing H_2^+ along a carbon arc, and a detector for ions or neutrals down to about 2 kev in energy. In addition to these activities, some measurements have been made on the attenuation of H_2^+ and H_3^+ beams (40–220 kev) in gases; the angular spread of the products suggests that for H_3^+ the details of the dissociation process are independent of the nature of the target gas (H_2, H_2O, Xe).

Power optimization of magnet coils for given degrees of field homogeneity (up to the "eighth order") is discussed in Sect. 9.1 on a basis that is at once practical and rather general. The distribution of current density is the parameter that is allowed to vary in seeking the optimization, and in simple cylindrical coils excellent homogeneity can be realized by allowing the current density to vary along the length of the solenoid. Work on minimum-$|B|$ configurations has yielded a map of the acceptable constant-B surfaces that could be achieved by applying quadrupole bars to DCX-1 (Sect. 9.2). New codes and automatic plotting not only readily give B-constant plots of beautiful detail (Figs. 9.9 to 9.11) but also permit the extension of the plots into the regions of the conductors (Sect. 9.2). The realization of an inexpensive, weak-field model using iron poles to produce a quadrupole-mirror hybrid field is described in Sect. 9.5. Special Hall probes have been developed that promise great utility in exploring multidirectional fields (Sect. 9.6) and, as microprobes, in the demanding work of field measurements for tiny regions in superconductors (Sect. 9.7).

In assorted matters of technique that have not already been mentioned, we have the doubling of the output of a duoplasmatron ion source (now 0.5 amp of mixed hydrogen ions) with a simultaneous improvement in beam quality (Sect. 7.1), further studies and theoretical understanding of gas desorption from the walls of a vacuum system (Sects. 10.3 and 10.5), a new gadget for quickly inserting probes or other things through vacuum walls (Sect. 11.3), considerations of the power densities to be expected in the wall and blanket of a fusion reactor (Sect. 11.2), and a study of water flow through a bent hollow copper conductor having a channel of grooved-circular cross section (Sect. 11.1).

In the injection-accumulation experiments that have long been this Laboratory's specialty, we have not been troubled with hydromagnetic instabilities, such as have been the subject of so much discussion in the literature of controlled fusion. At our densities, it has always been the microinstabilities that we see, evidencing themselves, for example, in the energy spreads of DCX-1 and DCX-2. It is therefore of importance to point to Sect. 8.1, which is a theoretical contribution appearing as the abstract of a paper that has been submitted for publication in *Physics of Fluids*. That paper sets forth, on general grounds, the factors that control growth rates of microinstabilities. Present indications are that this work will be tremendously illuminating for us in choosing future courses of action under which the effects of microinstabilities may be minimized.

Abstracting Summary

1. DCX-1 PLASMA EXPERIMENTS

Investigations of plasmas established by Lorentz-force trapping at very low pressures continue to indicate that the measured charge-exchange loss is less than the proton input current. This discrepancy does not appear to be the result of instrumental effects, of axial expansion into the coil throats or out of the mirrors, or of radial losses due to slow radial diffusion. Rapid radial transport or a combination of radial and axial scattering to the side walls of the high-vacuum region are suspect and are now being examined, as well as the possibility that the trapping rate is not constant.

Experiments with movable end walls of both tuned and grounded configurations showed no stabilization against fast-proton scattering, but did show that under some conditions the unstable longitudinal mode could be made to completely dominate. Panoramic data of the radio-frequency signals from this mode led to a theory which indicates that this instability is the result of electrostatic coupling of proton axial oscillation waves with trapped electrons.

Studies of the low-frequency oscillations were made by using electrostatic probes. It was not possible to arrive at a consistent interpretation of this phenomenon as a simple azimuthally revolving disturbance. The data suggest that the signals may arise from a set of oscillators (possibly involving only slow plasma components) in azimuthal rotation at different frequencies.

Calculations of the radial distribution of initially trapped protons and studies of gas desorption by energetic electron bombardment are also described.

2. DCX-2

Experiments in DCX-2, using a lithium arc for dissociation, have produced plasmas with densities in excess of 10^{10} ions/cm^3 over a volume of 100 liters. The mean energy of the trapped plasma is as high as 1.0 Mev under some conditions. Improved diagnostics, especially a current integrator for the charge-exchange flux following beam turnoff, permit continuous monitoring of the plasma density as a function of parameter changes. The magnetic field adjustment has been found to be particularly critical.

Use of the lithium arc for dissociation has resulted in as much as 90% dissociation of the 600-kev molecular ion beam. Particle and power accountability studies lead to the conclusion that five-sixths of the injected protons are lost to the snout; only one-sixth are lost by charge exchange at the highest density. The angular distribution (relative to the plane perpendicular to the axis) of the emitted charge-exchange flux shows a peculiar peak at 0° (present only at high densities) and side lobes at the injected pitch angle. It appears that the long decay times ($\gtrsim 0.1$ sec) and high density are associated with these particles, trapped by small mirrors in the central field which prevents them from reaching the snout.

Continued monitoring of the radio frequency has shown a shift in time following beam turnoff of the proton cyclotron fundamental frequency, possibly associated with the decay of the diamagnetism of the plasma ($\beta \sim 0.016$). Ion cyclotron lines at the lithium ion cyclotron resonances appear when the beam is injected. The predominant proton cyclotron radiation seen is at the second, third, and

fourth harmonics. Continued searching still exhibits no evidence of low-frequency rotations of the plasma as a whole.

3. ELECTRON-CYCLOTRON HEATING

During the period of this report, further investigations have been made of the electron-cyclotron plasmas in both the EPA Facility and the Physics Test Facility (PTF). The electron-cyclotron plasma (ECP) volume and shape in the EPA Facility have been studied with an x-ray pinhole camera. The plasma density in the PTF has been studied with a new microwave interferometer in conjunction with other diagnostic aids.

However, both machines have been inoperative for long periods of time due to necessary modifications. The EPA Facility has been modified for an experiment involving the injection of a 15- to 22-kev neutral hydrogen beam of several milliamperes into the ECP. The PTF has been modified for experiments involving rf ion-cyclotron heating in connection with microwave electron-cyclotron heating.

4. PLASMA PHYSICS

"Burnout," or complete ionization of a plasma, has apparently been accomplished by means of intense heating via electron-beam–plasma interaction. The burnout phenomenon appears to explain the old mode I–mode II transition phenomena. Preliminary studies of a burned-out plasma have been made, and ion heating effects have been observed. Studies of the hot-electron plasma have been made at lower background pressures using a new pressure-reducing technique. At reduced pressures, the plasma can still be stable. A simple calculation shows that density measurements of the hot-electron plasma by means of the x-ray bremsstrahlung flux were not grossly inaccurate due to high-Z contaminants. An energetic high-intensity electron beam has been observed to heat the electrons in a beam-generated plasma to temperatures about equal to the beam velocity, 15 to 30 kv, while operating in a uniform magnetic field. Plasma electron density is measured to be in the range of 10^{10}–10^{11} electrons/cm^3. Evidence of some type of ion-accelerating mechanism has been obtained from the severe erosion of the walls of the interaction region. Extensive studies of moving striations in the rare gases in gas discharge tubes have been made using a home-made image-converter stroboscope. These studies strongly suggest that the striation velocity corresponds to the ionic sound wave velocity as modified by ion-neutral collisions.

5. VACUUM ARC RESEARCH

The deuterium arc flute velocity and cross-field plasma transport measurements have been extended to a wider range of parameters. Flute velocities near the arc core are as high as several times 10^6 cm/sec. The weak radial density gradient dependence on the magnetic field strength has been verified out to the maximum available field strength.

Some effects of a very weak quadrupole Ioffe field have been measured, but a relatively weak Ioffe field distorts the mirror field lines sufficiently to extinguish the arc.

An experiment to measure the electron temperature by Thomson scattering of photons from a ruby laser was set up on the facility but was interrupted by the Ioffe field experiment.

The Long Solenoid has been doubled in length. Development of a hydrogen arc for DCX-2 has been started.

The magnetically confined carbon and gas-fed carbon arc plasmas are characterized by an unusual dynamic equilibrium – the ions appear to be as much as 100 times "hotter" than the electrons. This remarkable situation suggests the presence of a vigorous energy pumping mechanism whereby electrons pump energy in quantized amounts into ions which then, via exothermic ionic collisions, convert the internal potential energy into increased kinetic energy of the ions. These latter reactions correspond to fusion on an atomic scale with the result that the ions escalate to an energy well above that of the electrons.

6. CROSS-SECTION MEASUREMENTS

Pressures less than 10^{-10} torr have been obtained with the cross-beam cross-section apparatus. Preliminary measurements of the H^0 formation from H_2^+ dissociation in an arc discharge

has indicated 2% of the total incident H_2^+ being converted to neutrals. Total attenuation cross sections for H_2^+ and H_3^+ in hydrogen gas have been completed. The cross section decreases monotonically for both H_2^+ and H_3^+ in the energy range of 40 to 220 kev. Angular distribution measurements of H_2^+ and H^+ resulting from gaseous dissociation of H_3^+ indicate that these fragments arise from the same H_3^+ repulsive state independently of the target mass. Evaluation of a proportional counter to be used for detection of low-energy neutral particles has been completed. The resolution changed from 76% for 2.5-kev H^+ to 10% at 30 kev. The counter was nonlinear for proton energies less than 17 kev.

7. PRODUCTION, ACCELERATION, AND INJECTION OF IONIC AND ATOMIC BEAMS

Although 100 ma of H_2^+ beam at 600 kev has been passed through a cone roughly approximating the DCX-2 injection geometry on the test stand, DCX-2 injection is still limited to 50 ma. This limitation has been found to be the result of the slight difference in geometry. Variations in the design of the duoplasmatron ion source have resulted in hydrogen ion beams that are larger (500 ma) and less divergent.

8. PLASMA THEORY AND COMPUTATION

Thermodynamic upper bounds on anomalous diffusion across magnetic fields are found to agree with experiments. In particular, in quiet afterglows an observed rapid decrease of anomalous diffusion at large plasma radii is explained. The bound predicts adequate thermonuclear confinement in a torus stabilized against interchange and other "macroinstabilities" (minor radius <100 cm).

The thresholds in density and magnetic field for electrostatic (Harris) instabilities in plasmas created by high-energy injection are displayed graphically. Effects of ion and electron temperature and ion temperature anisotropy are surveyed. Also, the ion distribution is allowed to rotate at the ion cyclotron frequency, approximating the diamagnetic currents in plasmas one or two ion orbits across (DCX-1, DCX-2, OGRA). Finally, stability boundaries are determined from a new dispersion relation treating plasmas of finite radius, including both the above extreme case and also plasmas several orbits across (ALICE, PHOENIX).

Qualitative understanding of calutron instabilities is discussed, as well as plasma impedance calculations motivated by an attempt to understand the observed stabilization thereof by external circuits.

Ambipolar scattering losses in mirrors are calculated to provide an estimate of losses at high density in minimum-*B* experiments, such as that of Ioffe. Typical ambipolar enhancement of losses is a factor of about 3 to 4.

A further investigation of a possible anomaly in microwave interferometric density measurements in hot-electron plasmas has led to the conclusion that mirror curvature, like high-temperature relativistic effects investigated previously, makes a negligible correction to the appropriate refractive index.

Progress on calculations of electron-stream–plasma interaction is reported.

9. MAGNETICS AND SUPERCONDUCTIVITY

Two different problems in magnetics have been discussed by many authors in great detail: to minimize the power requirement of magnet coils and to find solenoid arrangements which produce very homogeneous fields. However, no systematic approach has been made to optimize the power requirement considering, simultaneously, a specified field homogeneity. Since this problem has appreciable practical importance, we made a rather extensive investigation on this subject. The guiding idea is to power-optimize solenoids to fourth, sixth, and higher order, that is, to add to the power minimum condition auxiliary conditions, namely to make terms in a zonal harmonic field development equal to zero. We obtained results which can be directly applied to the design of magnet coils. These calculations show how much field strength must be sacrificed in order to achieve a desired field homogeneity.

Furthermore, we studied several aspects of the problem to produce absolute *B*-minimum configurations. Based on a simple vector analytical expression we wrote a code which allows the calculation of the fields arising from Ioffe bars of complicated shape and which considers the effect

of end connections. Since the plotting of B-constant lines by hand is rather cumbersome, we developed two versions of a new CDC-1604 code for printing B-constant points by means of the ORNL Calcomp plotter.

With these devices at hand it was easy to study a hypothetical application of Ioffe bars to DCX-1. A quadrupole arrangement has been assumed with 600,000 amp total current per bar and 300,000 amp for each end connection. The radial distance of the bar centers from the axis is 12.5 in. in the midplane and 6 in. inside the mirror coil bores. With this arrangement the Ioffe bars could be mounted outside the vacuum liner. Field plots have been made for two different θ planes. One intersects the centers of two opposite Ioffe bars (each replaced by two filaments in order to consider a finite conductor cross section); the other is a symmetry plane between Ioffe bars. At the center of DCX-1 the field strength is 10 kilogauss. The B-constant lines in the first-mentioned plane are closed around the center for field strengths up to 16.4 kilogauss. This critical B-constant line intersects the axis at approximately ±9 in. and the midplane at about ±9.5 in. In the second plane the critical B-constant line corresponds to 12.7 kilogauss with intersections of about 7.5 and 5.5 in. on the z axis and midplane respectively.

In the paper described above, Ioffe bars of finite cross section were replaced by two current filaments each. A better approximation of such cross sections consists in thin annular sectors; that is, each bar is replaced by a current sheet. A field calculation of a system using such current sheets has been previously published by others. Truncated series developments have been used. We were able to calculate exactly the field distribution of current sheet multipoles by means of a very simple analytical solution using a field presentation by complex numbers. For a special case of a quadrupole system, numerical values for the current and power requirements have been calculated. The minimum power for this quadrupole system occurs with a sector angle of 61°, which is in agreement with the results of the mentioned publication. Around the circumference of the liner between each pair of current sheets, an access angle of 29° is available for plasma diagnostics. This might, however, be considered as insufficient. For other angles the necessary current and power can be easily found by means of graphs.

Another aspect of our recent research into the production of minimum-B fields has been the construction of a model coil system consisting of a mirror pair and a perpendicular quadrupole electromagnet set with iron pole pieces (Fe-Quad). Since the model was fashioned from an existing pair of mirror coils and a very simply constructed quadrupole set, the central field was limited to about 500 gauss and the general field shape was not as symmetrical as expected. Nevertheless, even with the relatively unsophisticated measuring equipment used thus far, it has been possible to show that a real minimum-B field exists. Results have been encouraging enough that we are now designing a similar system of usable dimensions, which will have a central field rising to about 2 kilogauss.

In connection with the problem of measuring the truly three-dimensional fields of minimum-B configurations, we have designed two magnetometer probes using commercial Hall elements. The first of these contains three mutually orthogonal elements with only about $\frac{1}{8}$ in. separation between active areas. Although it is now possible to read the three field components and add them vectorially, no suitable electronics system has yet been devised to do this addition automatically. The second type probe overcomes this electronic difficulty by using only one Hall element, which is provided motion in the five degrees of freedom necessary to translate the element to the desired location and to rotate it so that its face will be normal to the field vector.

Also, during this reporting period, we have continued the development of microprobes for measuring fields in the low temperatures encountered in superconductivity research. In order to obtain greater sensitivity and increased resolution in space, recent emphasis has been on bismuth deposited microprobes using the Hall effect (rather than the magnetoresistive effect employed earlier). Two types in an advanced state of development have been made and tested: the first consists of a tiny bismuth cross deposited on a suitably thin substrate of glass or plastic; the second also has a bismuth active element, but this time deposited on the polished ends of a bundle of four small insulated copper wires cast in an epoxy cylinder.

Probes of both types have been repeatedly cycled from room temperature to that of liquid helium and checked in fields from a few tenths of a gauss to several tens of kiloguass. Currently about half of those so tested survive and prove to be reliable magnetometers with linear output vs field curves, whose slope changes less than 10% with cycling.

10. VACUUM SYSTEMS, TECHNIQUES, AND MATERIALS STUDIES

The results of work on the chemical reactions and physical behavior of organic compounds in vacuum systems are described. The sequential desorptions of compounds from surfaces were experimentally studied during a temperature increase from 80 to 300°K. Of the ten desorption peaks observed, six were identified: methane, carbon dioxide, ethane, propane, water, and butane.

A derived relation between offgassing rates and the heat of adsorption of organic compounds is presented. Two methods of estimating heats of adsorption are discussed. The effect of electron bombardment is described for the special case of an octyl phthalate ester contaminant.

The products of hot-filament reactions are contrasted with those from electron bombardment. Bombardment was used to assess the progress of a baking cycle and was found to substantiate earlier conclusions on the effects of ionization gage grid heating. Platinum was found to be superior to tungsten or tantalum when used with β-eucryptite as a lithium ion source.

1. DCX-1 Plasma Experiments

J. L. Dunlap
R. S. Edwards
G. R. Haste
L. A. Massengill
C. E. Nielsen[1]
H. Postma[2]
L. H. Reber
R. G. Reinhardt
W. J. Schill
E. R. Wells

1.1 INTRODUCTION

The basic mechanical configuration of the DCX-1 facility was not altered during this report period.

Some data previously reported[3] had suggested that the molecular ion beam was being injected off the median plane. A careful check of the beam trajectory confirmed that this was indeed the case, and the injector system was completely realigned. At the same time a set of electrostatic deflector plates was added near the base of the accelerator tube to provide partial cancellation of the effects of the fringing magnetic field on the molecular ion trajectory.

The following material describes most of the experiments performed by the group during this report period. Some work on gas desorption in DCX-1 by energetic electron bombardment is given elsewhere.[4]

1.2 INVESTIGATIONS OF PROTON LOSSES FROM PLASMAS FORMED BY LORENTZ-FORCE TRAPPING

At low pressures, plasmas can be formed in DCX-1 by the Lorentz-force dissociation of an H_2^+ beam prepared by injecting H_3^+ into a water vapor cell. (This specially prepared H_2^+ beam is designated H_2^{+*}.) When such a beam is injected into DCX-1, trapping by Lorentz-force dissociation begins to dominate over trapping by gas dissociation at pressures which yield a containment time of about 0.1 sec. At lower pressures the proton input current to the plasma and the proton loss current are believed to be constant.

The previous report[5] described some experiments with Lorentz-force trapping in which the charge-exchange loss current was measured as a function of charge-exchange decay time (pressure) in the τ range from about 0.1 sec to beyond 10 sec. This loss current was essentially constant for τ values up to a few seconds, but it then decreased with increasing τ. The total number of stored protons and the central (maximum) proton density, both of which were calculated from the charge-exchange signals, were observed to saturate at long containment times. Changes in the Z distribution of the charge-exchange signals indicated that the operating regime characterized by deficient charge-exchange current was also characterized by significant axial expansion of the plasma.

Three factors were recognized as possible contributors to differences between the measured charge-exchange loss rate and the proton trapping rate.

1. Instrumental effect. – The neutral particle detectors (NPD) were the usual array of 12 foil-covered Faraday cups. The 10-μin. nickel foils

[1]Consultant from Ohio State University.

[2]Presently on leave at FOM Institute voor Plasma-Fysica, Rijnhuizen, Jutphaas, Netherlands.

[3]*Thermonuclear Div. Semiann. Progr. Rept. Oct. 31, 1963*, ORNL-3564, Sect. 1.4, p. 10.

[4]Sect. 10.2, this report.

[5]*Thermonuclear Div. Semiann. Progr. Rept. Oct. 31, 1963*, ORNL-3564, Sect. 1.5, p. 10.

employed attenuate the transmission of beams of energies below about 150 kev and have zero transmission at about 50 kev.[6] Severe dispersion and/or degradation of the trapped proton energy coupled with the energy dependence of the charge-exchange cross section could, therefore, result in measurement of only a portion of the true charge-exchange losses.

2. Axial expansion of the plasma. – The NPD array extended across $Z = \pm 6$ in. Axial expansion could produce significant charge-exchange losses outside this range and would eventually introduce mirror losses. Severe mirror losses appeared unlikely (the mirrors are at $Z = \pm 15\frac{5}{16}$ in.). However, the distributions of the measured charge-exchange currents did indicate significant axial expansion. Also the fact that these currents fell off quite rapidly at the ends of the NPD array (Fig. 1.1) could be interpreted as a decrease in the effective solid angle of the end detectors due to plasma expansion into the coil throats (Fig. 1.2).

3. Radial expansion of the plasma. – Protons are initially trapped into distributions that extend to the nearest radial barrier. Radial expansion would result in additional proton losses to the barrier.

Investigations to determine the extent to which each of these three factors contributed to measurement of deficient charge-exchange currents were conducted during the present report period. The instrumental effect was investigated by using

[6] *Thermonuclear Proj. Semiann. Rept. Jan. 31, 1959,* ORNL-2693, Fig. 1.1.2, p. 4.

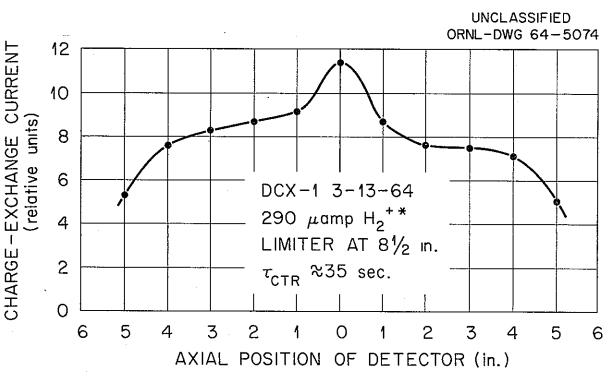

Fig. 1.1. Axial Distribution of Charge-Exchange Current.

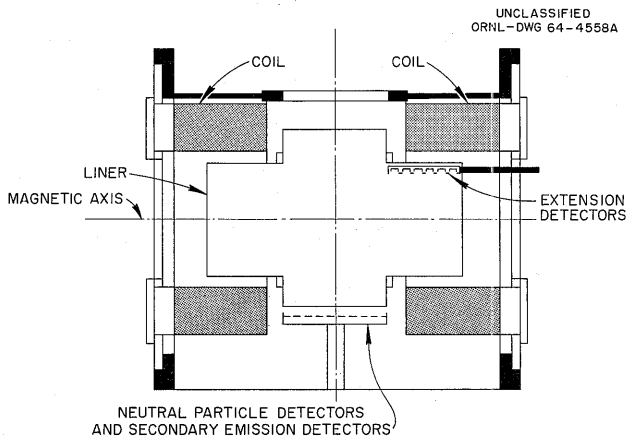

Fig. 1.2. Longitudinal Section of the Central Region of DCX-1.

foil-covered Faraday cups (NPD) and secondary emission detectors (SED) mounted at the same Z locations and side by side in azimuth. Eleven detectors of each type were incorporated in a complex detector array which was centered on the median plane and extended to $Z = \pm 6$ in. (Fig. 1.2). Measurements of the energy spectra of escaping charge-exchange neutrals have also been made. The possibility of axial expansion into the coil throats was investigated by supplementing these central detectors with a set of six NPD which extended to $Z = 13$ in. in one coil throat (Fig. 1.2). The effects of radial expansion were examined by using a movable radial limiter which extended across $Z = \pm 2\frac{5}{8}$ in. and several inches radially.

These investigations were conducted more or less simultaneously in order to provide a number of cross checks on the results.

The instrumental effect does not appear to be significant. In the τ regime of interest a number of comparisons were made of charge-exchange decay traces simultaneously recorded by adjacent SED and NPD. The NPD traces decayed gradually from the steady-state level without displaying a very rapid initial decay such as would be associated with a large steady-state signal component in the energy range of partial transmission. (The charge-exchange cross section for 100-kev protons in helium, which was usually employed as the gas leak, is about 30 times the cross section for 300-kev protons.) Upon beam cutoff, a significant portion of the SED signal decayed with the limiting time constant of the detecting circuit – about

30 msec. There was then a sharp transition to a much slower component which decayed with a time constant like that of the NPD signal. The amplitude of the fast component, but not the slow one, was sensitive to minor variations of the H_2^{+*} beam trajectory. The sharp transition from the fast component to the much slower one also supports an interpretation in terms of two definite signal components. The fast component is thought to be a response to low-energy particles produced by collisions of the H_2^{+*} beam with the walls surrounding the plasma, particularly in the vicinity of the entrance and exit apertures. The slow component is obviously a plasma signal. If the fast component is interpreted as the charge-exchange loss of a group of very low-energy protons, the failure to observe a gradual transition to the slow component would then suggest that the low-energy group is an isolated portion of the proton energy distribution. Such a distribution appears very unlikely. Energy spectra obtained from a silicon surface-barrier detector in the median plane showed proton distributions that were monotonically increasing functions of energy from 80 kev (excessive noise counts prevented obtaining data at lower energies) to nearly 300 kev.

Plasma expansion into the coil throats also does not appear to be significant. The supplementary array of NPD added in this region registered less than 1% of the charge-exchange current that was observed by the central detectors. The central detectors, however, continued to indicate that the regime characterized by deficient charge-exchange current was also characterized by appreciable axial expansion.

As noted earlier, the possibility of radial expansion was investigated by measuring the variation of charge-exchange loss with τ for different positions of a radial limiter. The location of the limiter influences the proton input current to the plasma (see Sect. 1.6), but the magnitude of this effect is determined by the dissociation mode employed, and for either gas dissociation or Lorentz-force trapping the effect is independent of pressure. For the pressure regime in which the charge-exchange loss current was invariant with τ, changes of current with limiter position would reflect the changes in proton input. If, however, radial expansion were important in the pressure regime of deficient charge-exchange current, the measurements might be influenced by this expansion as well as by the changes in proton input.

A few of the earlier measurements seemed to show effects of radial expansion at the longer τ values. Figure 1.3 is an example of these data. In the plateau region the reduction of the loss current is about that calculated for the effect of the limiter on the proton input current, but at the longer τ's the loss current decreases more rapidly with τ for the limiter at $7\frac{1}{2}$ in. than for the limiter at $8\frac{1}{2}$ in. A gradual radial diffusion could produce such observations.

This sort of response, however, did not prove to be consistent. In most of the investigations the effect of advancing the radial limiter was merely to reduce the charge-exchange current by a factor which was invariant with τ. Figures 1.4, 1.5, and 1.6 show the variation of charge-exchange current with τ and with limiter position for injected H_2^{+*} currents of 235, 125, and 30μa. Figures 1.7, 1.8, and 1.9 show the corresponding variations of the total number of trapped protons. For these last three figures, the calculations of the ordinate values involve time integrals of the charge-exchange current during plasma decay. The values shown are the result of treating the decays as exponential; so the integrals were simply the product of initial

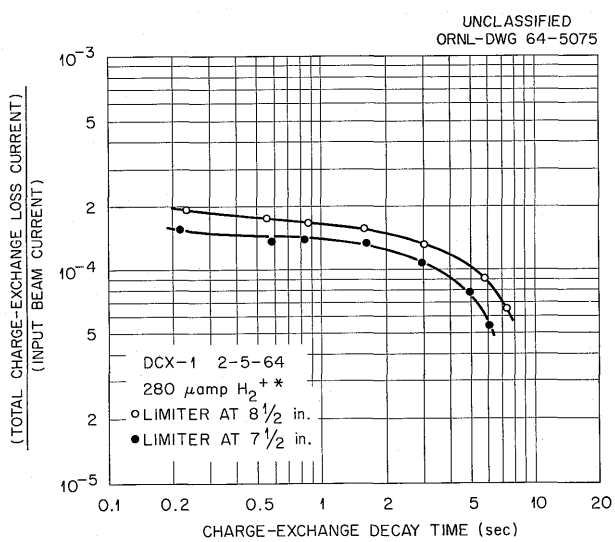

Fig. 1.3. The Ratio of Total Charge-Exchange Loss Current to Input Beam Current as a Function of Charge-Exchange Decay Time and Position of the Radial Limiter.

amplitude and decay time. At the longer decay times the decays progressively depart from exponential and the ordinate values are somewhat low. A number of points have been checked by numerical integration. At the maximum error encountered (at about 300 μa H_2^{+*} and 30 sec decay time) the value from numerical integration was only 40% larger than that resulting from the more simple procedure. The magnitude of the error decreased rapidly with decreasing beam current and/or decay time. With the largest H_2^{+*} currents available, the total number of stored protons saturates at about 1 or 2×10^{12}. The corresponding saturation value for the central (maximum) proton density is about 1 or 2×10^8 cm^{-3}.

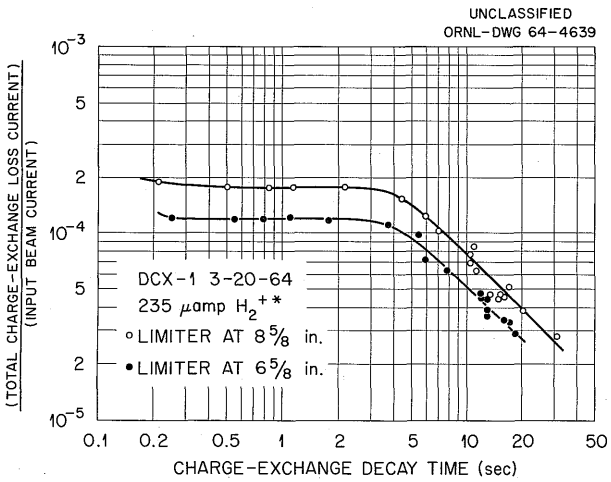

Fig. 1.4. The Ratio of Total Charge-Exchange Loss Current to Input Beam Current as a Function of Charge-Exchange Decay Time and Position of the Radial Limiter.

The bulk of the data obtained as functions of the position of the radial limiter did not show effects attributable to a gradual radial expansion. If radial losses existed by virtue of very rapid transport of protons to larger radius, they might not have been observed in these experiments. It is also conceivable that a combination of radial and axial scattering could drive protons onto the sides of the liner at $Z = \pm 6\frac{1}{2}$ in., for at these locations the liner radius is 6 in. (see Fig. 1.2). Experiments are planned to check these possibilities and also to verify that the trapping rate is indeed constant in the regime of deficient charge-exchange current.

That the center array of NPD indicated considerable axial expansion at the lower pressures has already been mentioned. Figures 1.10, 1.11, and 1.12 present data obtained during a single run. The expansion is typical of that observed during the present report period and is much less rapid than that reported earlier.[7] We do not have an explanation for this difference, but it may be connected with changes in the liner geometry that

[7] *Thermonuclear Div. Semiann. Progr. Rept. Oct. 31, 1963,* ORNL-3564, Fig. 1.25, p. 12.

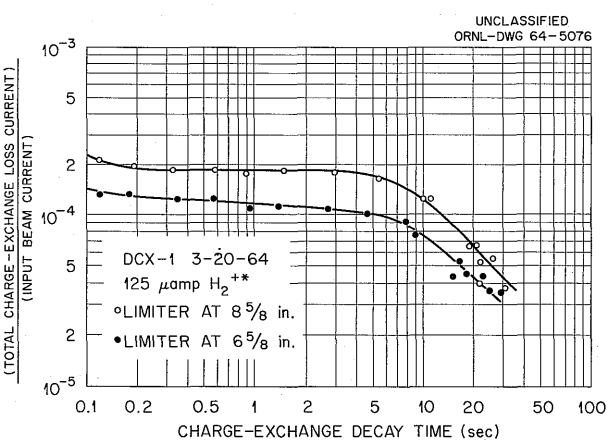

Fig. 1.5. The Ratio of Total Charge-Exchange Loss Current to Input Beam Current as a Function of Charge-Exchange Decay Time and Position of the Radial Limiter.

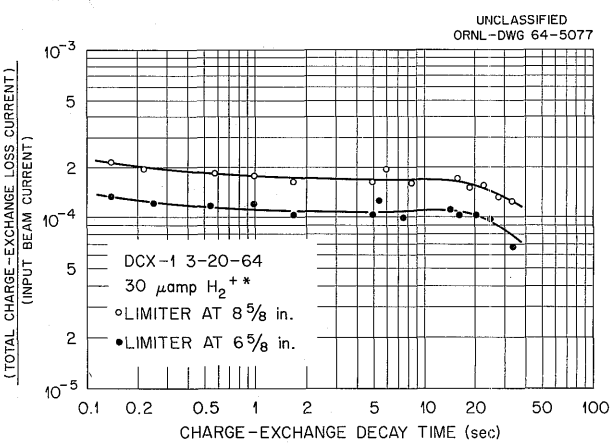

Fig. 1.6. The Ratio of Total Charge-Exchange Loss Current to Input Beam Current as a Function of Charge-Exchange Decay Time and Position of the Radial Limiter.

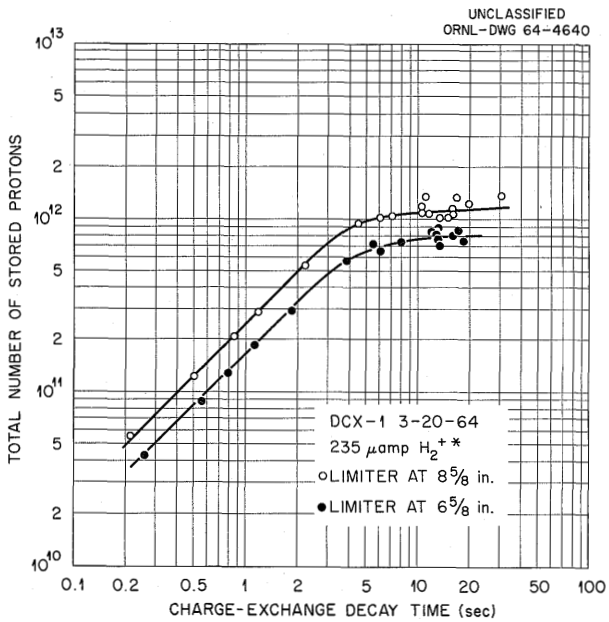

Fig. 1.7. Total Number of Stored Protons as a Function of Charge-Exchange Decay Time and Position of the Radial Limiter.

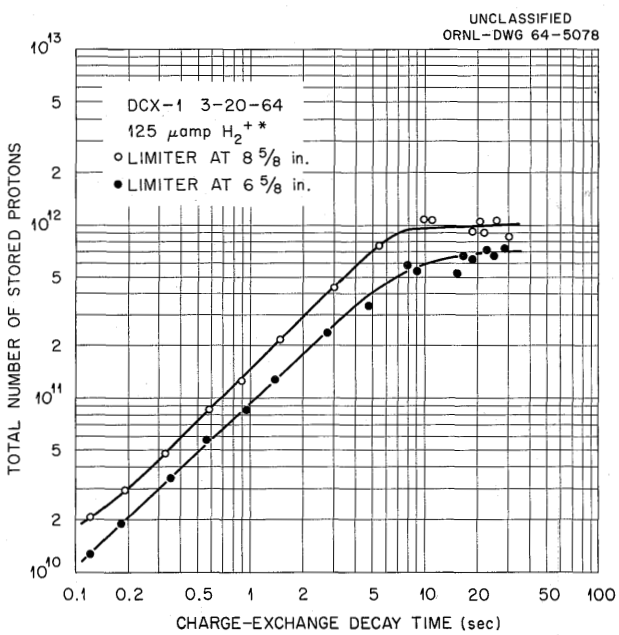

Fig. 1.8. Total Number of Stored Protons as a Function of Charge-Exchange Decay Time and Position of the Radial Limiter.

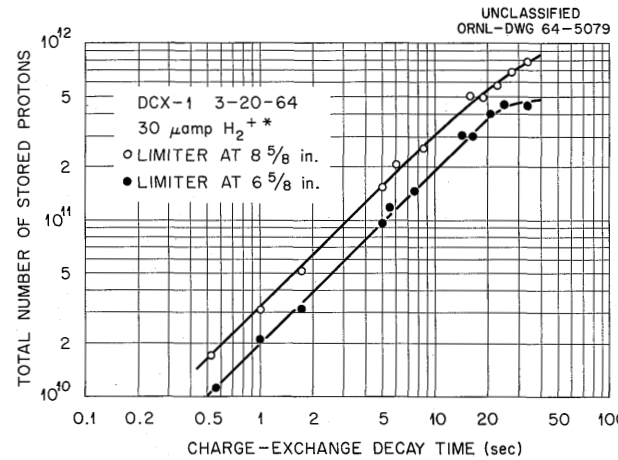

Fig. 1.9. Total Number of Stored Protons as a Function of Charge-Exchange Decay Time and Position of the Radial Limiter.

were made during the intervening time. The earlier data were obtained with a flattened portion of the liner wall which acted as a radial limiter at a radius of 7 in. Before the more recent measurements, the liner was changed to a circular cross section 11 in. in radius across $Z = \pm 6\frac{1}{2}$ in. Unfortunately, profile data in the later configuration with the radial limiter at approximately 7 in. are incomplete and do not allow a comparison with the earlier data.

These investigations of proton losses were also conducted during the application of several watts of microwave power at the frequency (26.6 kMc) appropriate for electron-cyclotron heating in the median plane. Studies of the instrumental effect and of axial expansion into the coil throats produced the same results as for operation without microwave power. However, the experiments that employed the movable radial limiter revealed some interesting differences for which we presently have no explanation. Figure 1.13 shows the effect of microwave power on loss current vs τ curves measured with the limiter at $6\frac{5}{8}$ in. Figures 1.14 and 1.15 present similar data for $7\frac{5}{8}$ in. and $8\frac{5}{8}$ in. positions of the limiter. In each case the application of microwave power had little effect on the loss currents in the plateau region, and decreased the loss currents at longer τ values. These data indicated that the microwaves were least effective in reducing the loss currents for the smallest plasma radius. This point was explored further with runs in which τ and the limiter

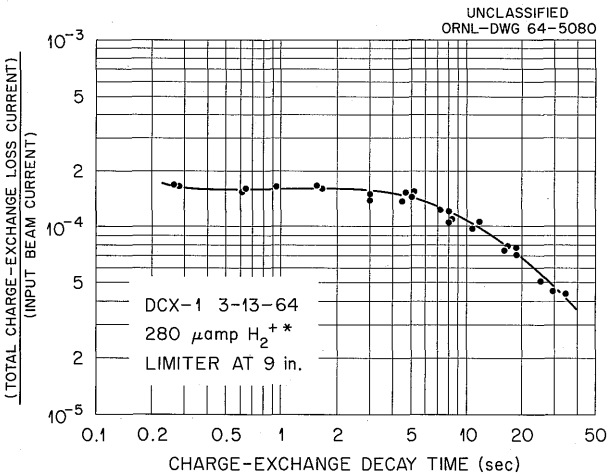

Fig. 1.10. The Ratio of Total Charge-Exchange Loss Current to Input Beam Current as a Function of Charge-Exchange Decay Time.

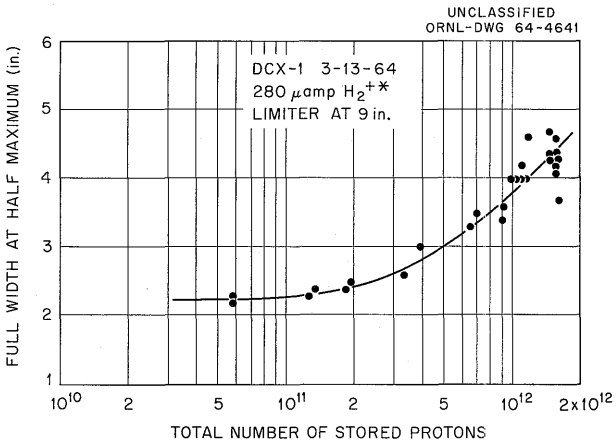

Fig. 1.12. The Full Width at Half Maximum of the Axial Density Profile as a Function of the Total Number of Stored Protons.

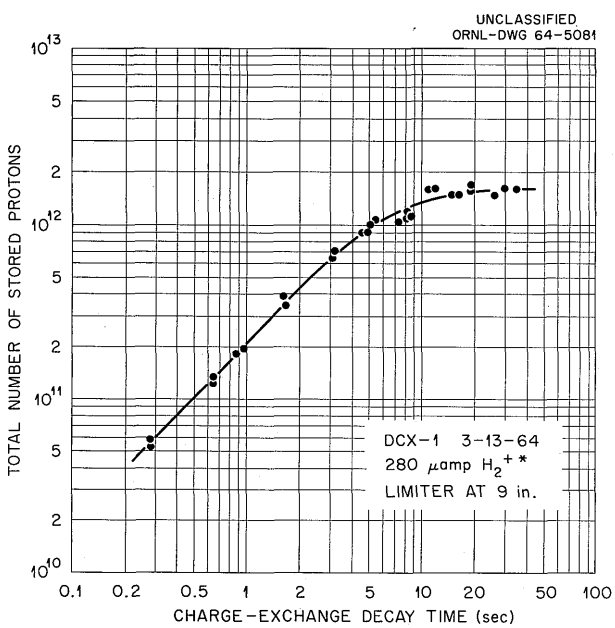

Fig. 1.11. Total Number of Stored Protons as a Function of Charge-Exchange Decay Time.

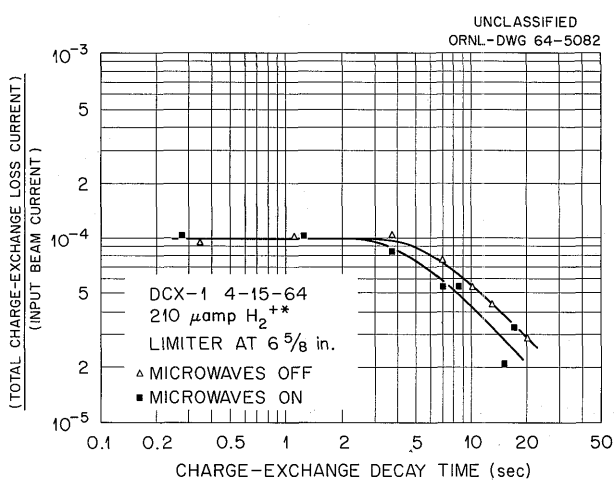

Fig. 1.13. The Ratio of Total Charge-Exchange Loss Current to Input Beam Current as a Function of Charge-Exchange Decay Time.

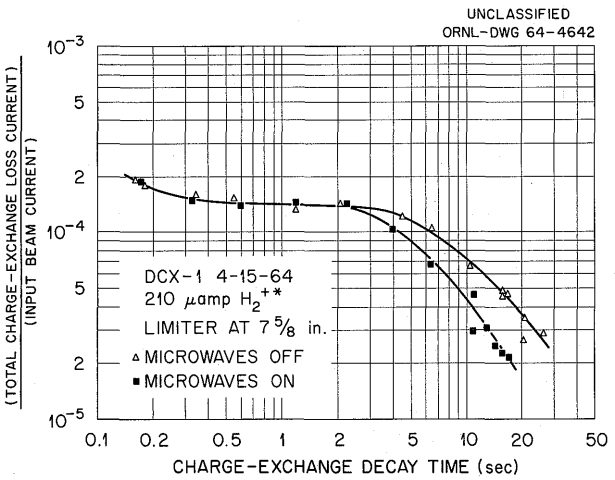

Fig. 1.14. The Ratio of Total Charge-Exchange Loss Current to Input Beam Current as a Function of Charge-Exchange Decay Time.

position were varied while microwave power was continuously applied. The results are shown in Figs. 1.16 and 1.17. At the longer τ values of Fig. 1.17, the charge-exchange currents with the limiter at $6\frac{5}{8}$ in. were actually greater than those with the limiter at $7\frac{5}{8}$ in. That this effect was real was verified by repeated measurements in which the τ was held constant and the limiter position changed.

In the plateau regions of Figs. 1.13, 1.14, and 1.15 the application of microwave power produced essentially no change in the total charge-exchange loss current. In these regions the axial distributions were changed only slightly; the usual observation was that microwave power increased the central loss currents by a few percent. At longer τ values where the microwaves reduced the total loss current, the normalized axial distributions were the same with or without microwaves. With microwave power applied, the current to each detector was reduced by an essentially constant factor.

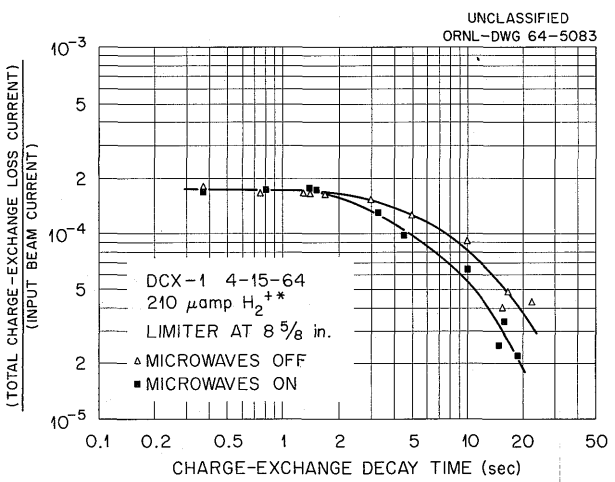

Fig. 1.15. The Ratio of Total Charge-Exchange Loss Current to Input Beam Current as a Function of Charge-Exchange Decay Time.

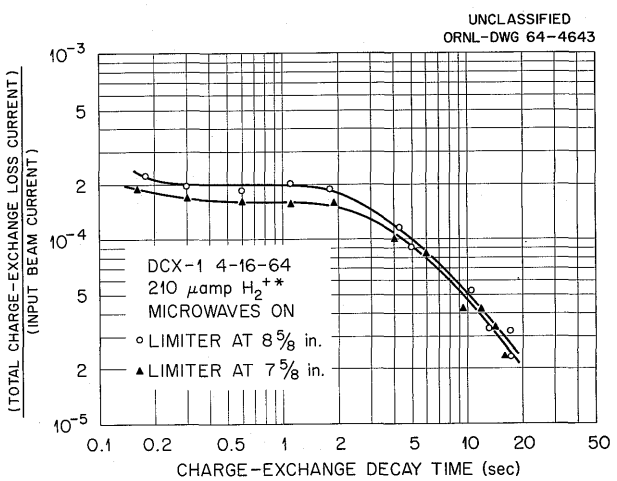

Fig. 1.16. The Ratio of Total Charge-Exchange Loss Current to Input Beam Current as a Function of Charge-Exchange Decay Time and Position of the Radial Limiter.

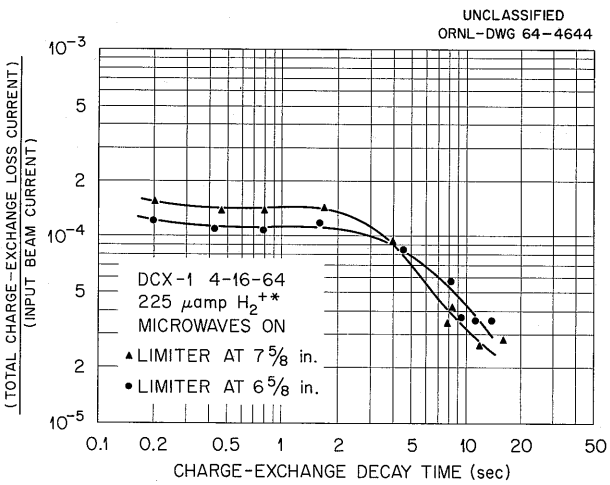

Fig. 1.17. The Ratio of Total Charge-Exchange Loss Current to Input Beam Current as a Function of Charge-Exchange Decay Time and Position of the Radial Limiter.

1.3 EXPERIMENTS WITH MOVABLE END-WALL CONFIGURATIONS

A number of experiments have been performed to investigate the possible stabilizing effects of different types of movable end-wall configurations.

Three sets of end walls were used; each set consisted of two identical walls, one for positive Z and one for negative Z. Each wall was constructed so that the surface presented to the plasma was a plane, parallel to the median plane, of circular cross section greater than the allowed radial extent of the plasma in the median plane. The most simple configuration was a single sheet of copper at ground potential. The two other configurations were patterned after end walls found to have had a marked stabilizing effect on calutron instabilities.[8] In each of these, the surfaces presented to the plasma consisted of sixty 2-in.-square, closely spaced copper plates supported by insulators from a back plate which was grounded. Small coils wound around the insulators produced parallel resonance of each of the elements within the desired frequency range. For one set of end walls this range was 18 to 25 Mc, only slightly higher than the proton cyclotron frequency; for the other set the range was 125 to 150 Mc. The end walls could be moved in Z without disturbing the vacuum, from $Z = \pm 2$ in. to $Z = \pm 6$ in. for the grounded set, and to $Z = \pm 5$ in. for the other two sets.

The experiments were performed with plasmas established by gas dissociation of about 2 ma of H_2^+ current. The usual procedure was to fix the operating pressure and then, as a function of the end wall separation, to measure the charge-exchange currents to the usual array of 12 foil-covered Faraday cups and the rf signals from an electrostatic and two magnetic probes. The probes were mounted in the median plane at radii greater than the allowed radial extent of the fast proton plasma. The electrostatic probe (the E probe) was of the most simple type, a sensitive metallic element connected to wide-band rf amplifiers (Hewlett-Packard type 460 A) through a 50-ohm transmission line. The low-impedance termination restricted the probe response to frequencies above a few megacycles. The magnetic probes were the two loops of the "crown" probe; this probe and the associated electronics have been described previously.[9] One loop (designated θ) was in the median plane and was sensitive to proton clustering signals. The second loop (Z) was at right angles to the first and was, therefore, sensitive to the unstable longitudinal mode. Both a panoramic receiver and oscilloscopes were employed in the rf measurements. The operating pressures were chosen to cover a range of charge-exchange decay times from several seconds (up to 10 sec in a few cases) to about 0.1 sec. The investigation also included observations of the effects of electron cyclotron resonance heating by a few watts of microwave power at 26.6 kMc.

The distributions of the charge-exchange signals showed that the end walls did not stabilize the fast protons against scattering. The plasma did not shrink away from the end walls as they were advanced toward the median plane; instead the plasma appeared to collide with them as it would with any other barrier. The results obtained with the three end-wall configurations appeared to be identical in this respect. The addition of microwave power usually resulted in less axial scattering and a reduction of plasma losses to the

[8]Sect. 4.5, this report.

[9]*Thermonuclear Div. Semiann. Progr. Rept. Oct. 31, 1963,* ORNL-3564, Sect. 1.2, p. 1.

end walls. The magnitude of this effect varied, but the total number of protons stored in steady state was on occasions increased by as much as 25% of the value measured at the largest end-wall separation without microwaves.

The rf measurements, particularly the panoramic observations, proved to be considerably more interesting. As the pressure, the end-wall configuration, and the end-wall separation were changed, there were variations of detail. Variations were also noted in comparing data obtained with symmetrically and asymmetrically displaced end walls. In this report we stress the more consistent features of the observations.

At the widest end-wall separations, the spectra principally consisted of proton cyclotron harmonics

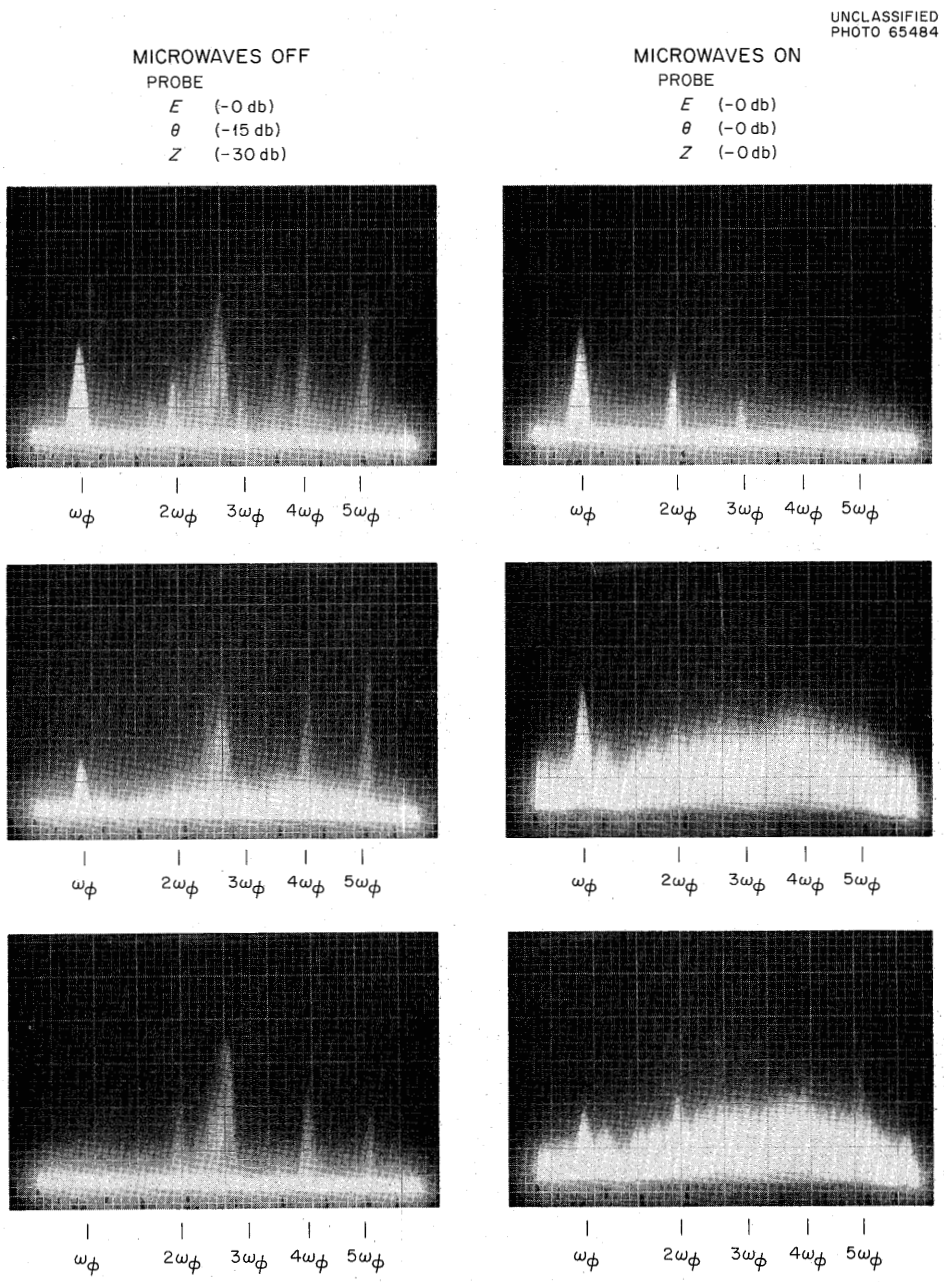

Fig. 1.18. Panoramic Spectra with Grounded End Walls. Data DCX-1, 1-6-64, pictures 25–30, 2.4 ma H_2^+, 2.4×10^{-9} torr, 6-in. wall separation, 10 sec exposure.

(ω_Φ is about 14 to 15 Mc) and considerably less of certain nonharmonic frequencies (major bands at approximately 19, 25, 32, 38, and 50 Mc). The harmonics were most prominent on the θ and E probes, and the nonharmonics were most prominent on the Z probe. As the end walls were advanced, no significant changes in the spectra occurred until the charge-exchange signals indicated that considerable plasma was being lost to the end walls. Then, as the end walls were advanced further, the nonharmonics became more prominent in relation to the harmonics and there were changes in the relative intensities of the signals in each of these two groups. However, the frequencies of the principal bands were not altered.

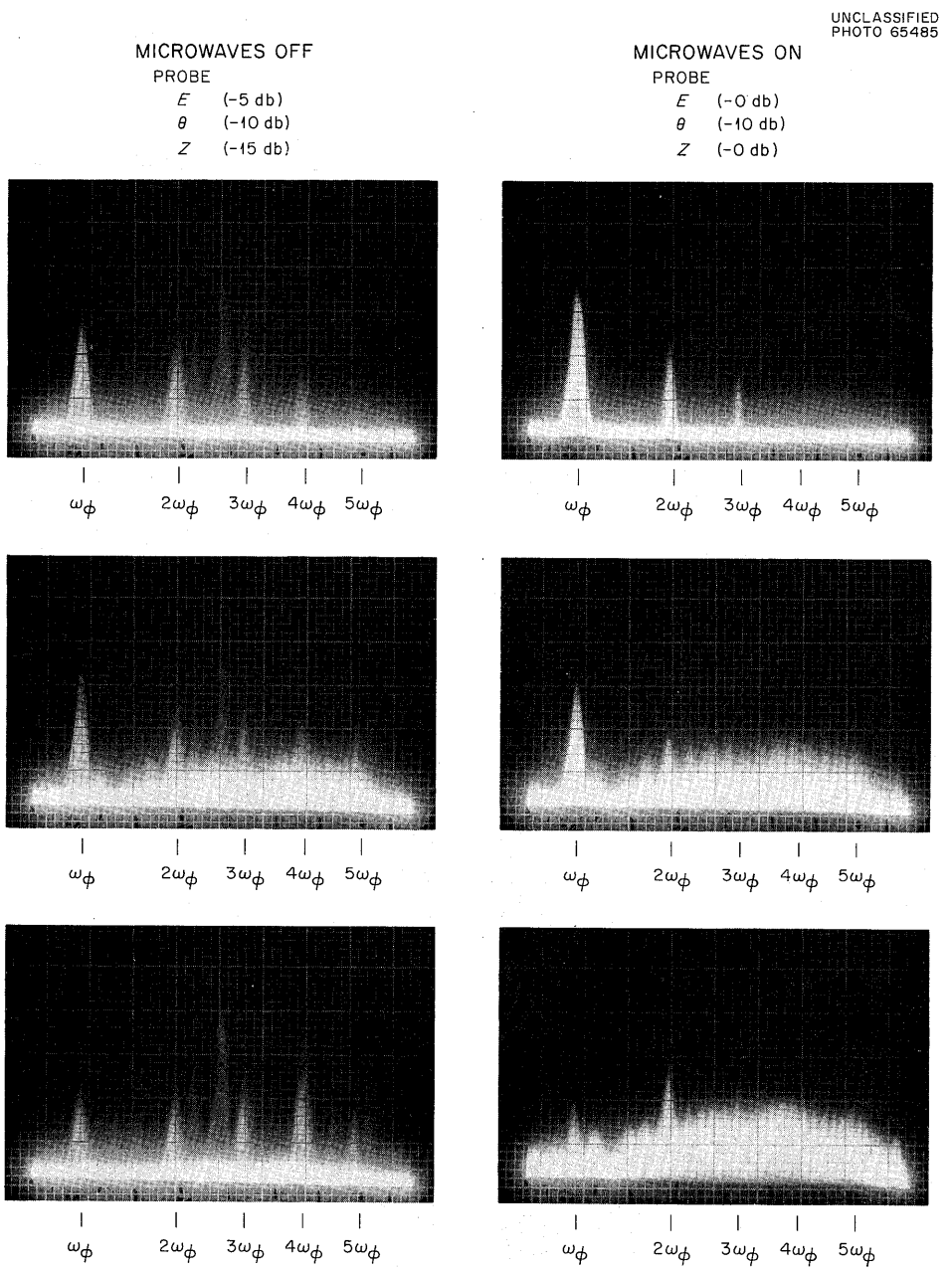

Fig. 1.19. Panoramic Spectra with Grounded End Walls. Data DCX-1, 1-6-64, pictures 7–12, 2.3 ma H_2^+, 2.2×10^{-9} torr, 10-in. wall separation, 10 sec exposure.

The application of microwave power suppressed the nonharmonics but increased considerably (in general by factors of at least 2 or 3) the time-averaged amplitude of the cyclotron harmonics. Since the charge-exchange data indicated that there was a reduction of proton scattering with application of microwave power, we conclude that the unstable longitudinal mode is the more effective in producing axial spreading.

Figures 1.18–1.22 are representative of the panoramic spectra obtained. The db figures are decibels of attenuation required to reduce the rf signals to reasonable levels; the vertical displays are logarithmic with about 5 db per centimeter of

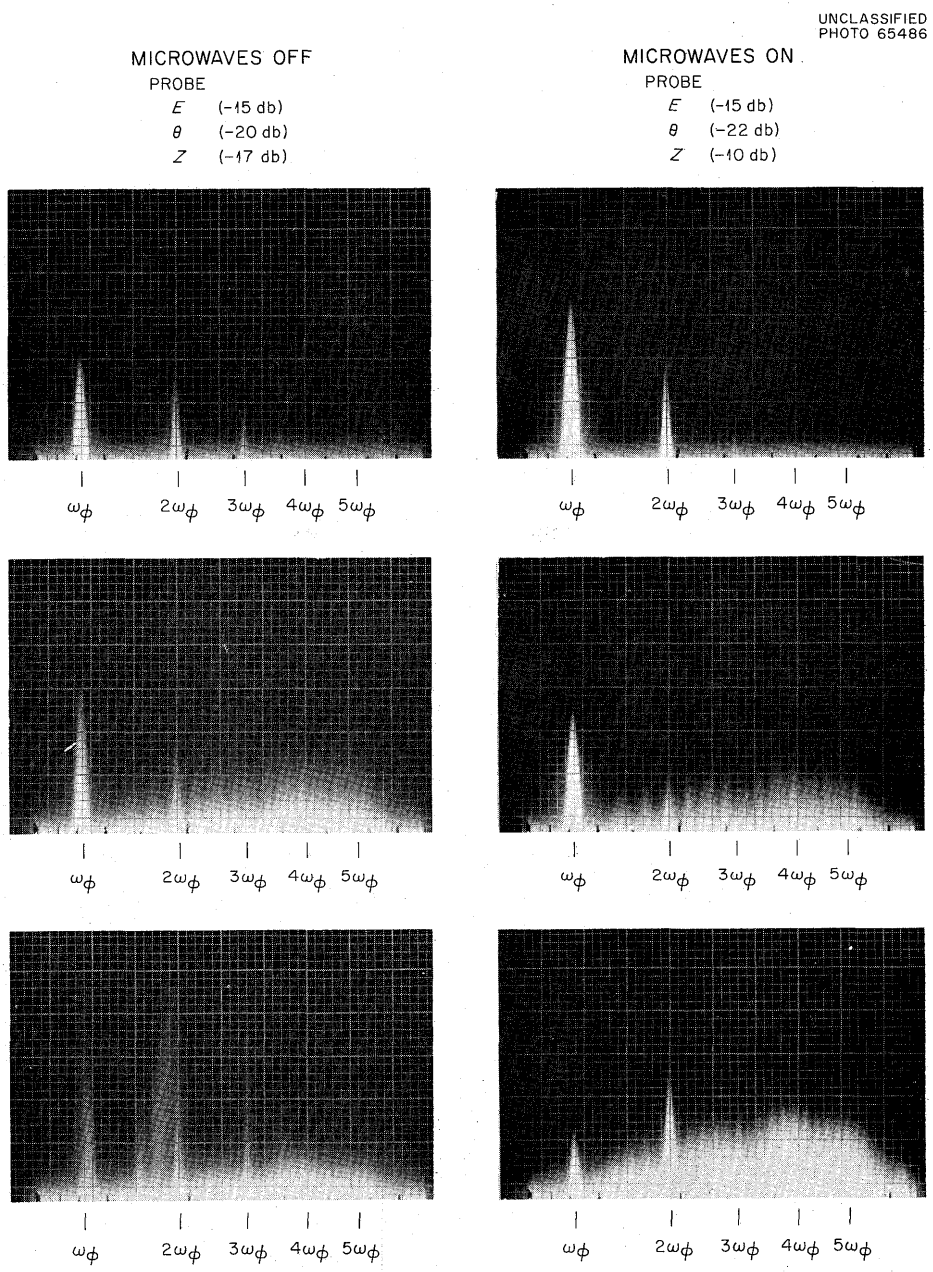

Fig. 1.20. Panoramic Spectra with Grounded End Walls. Data DCX-1, 12-16-63, pictures 27–32, 1.8 ma H_2^+, 6.5×10^{-9} torr, 12-in. wall separation, 10-sec exposure.

displacement. The high background levels on the magnetic probe spectra are the result of instrument noise and do not constitute real signals. The exposure times were 10 sec, so these photographs represent reasonable time-averaged samples of the rf signals. These spectra were obtained with symmetrically displaced end walls.

Spectra obtained with the set of end walls tuned for 125 to 150 Mc were very much like those obtained with grounded walls. The walls tuned for 18 to 25 Mc noticeably suppressed the cyclotron fundamental and, to a lesser extent, the 25-Mc signals.

The oscilloscope scans of the rf signals agreed with the panoramic data on those points for which comparison was possible, that is, for relative amplitudes, frequency composition, and the degree of effect obtained by adding microwave power. The

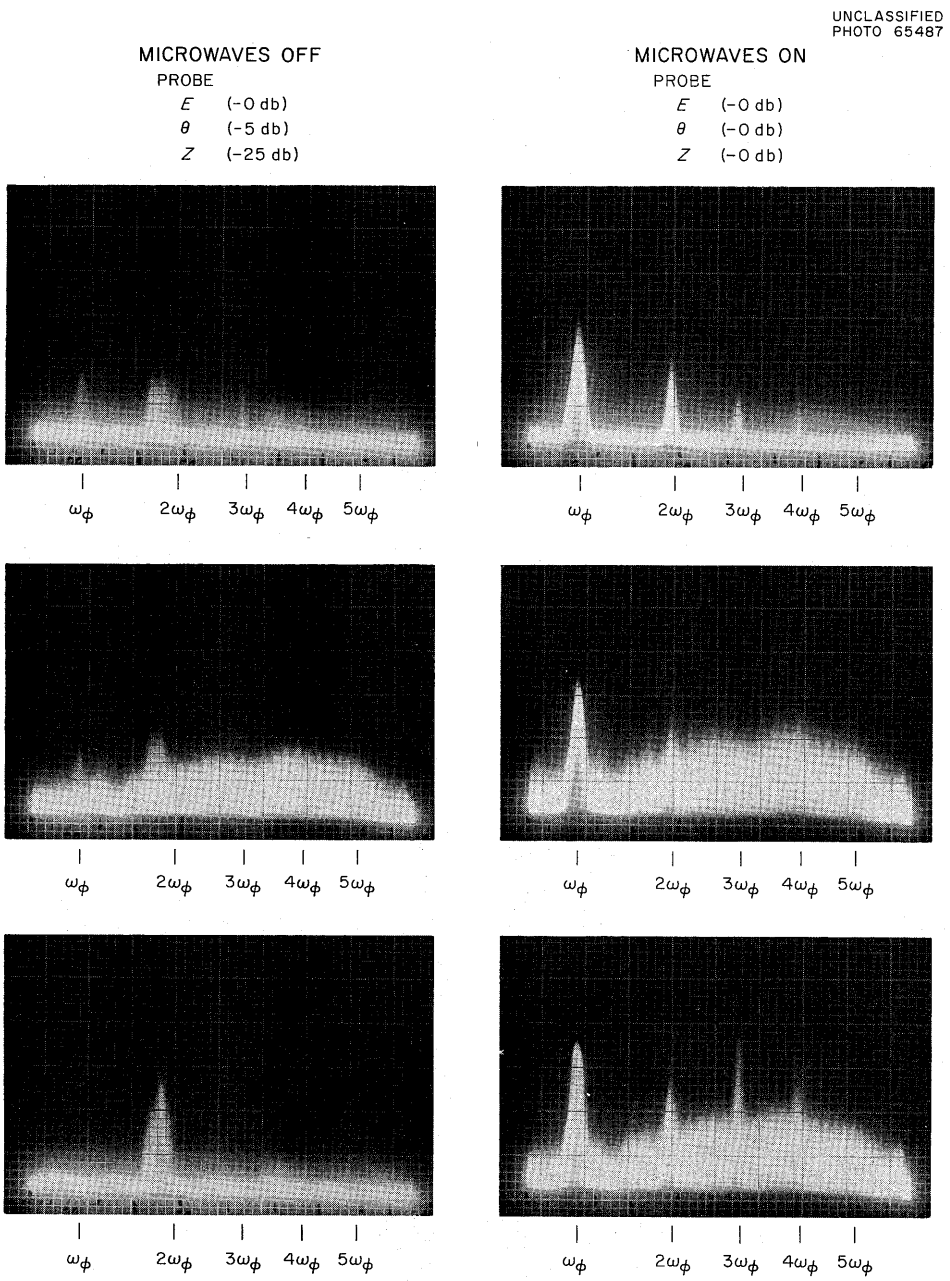

Fig. 1.21. Panoramic Spectra with Grounded End Walls. Data DCX-1, 1-6-64, pictures 72–77, 2.35 ma H_2^+, 1.8×10^{-8} torr, helium leak, 6-in. wall separation, 10 sec exposure.

similarity of the electrostatic probe signal to that of the θ magnetic probe is illustrated in Fig. 1.23.

The most striking feature of the rf data was the frequency composition of the signals associated with the unstable longitudinal mode. The fact that these frequencies were not changed by varying the end-wall configuration or separation, the operating pressure, or the plasma density indicates that the frequencies must be related to periodic proton motion in the magnetic field. In this connection we note that the observed frequencies can be represented as

$$19 \text{ Mc} \approx \omega_\Phi + \omega_z,$$

$$25 \text{ Mc} \approx 2\omega_\Phi - \omega_z,$$

$$38 \text{ Mc} \approx 3\omega_\Phi - \omega_z \text{ or } 2(\omega_\Phi + \omega_z),$$

$$50 \text{ Mc} \approx 2(2\omega_\Phi - \omega_z),$$

$$75 \text{ Mc} \approx 3(2\omega_\Phi - \omega_z),$$

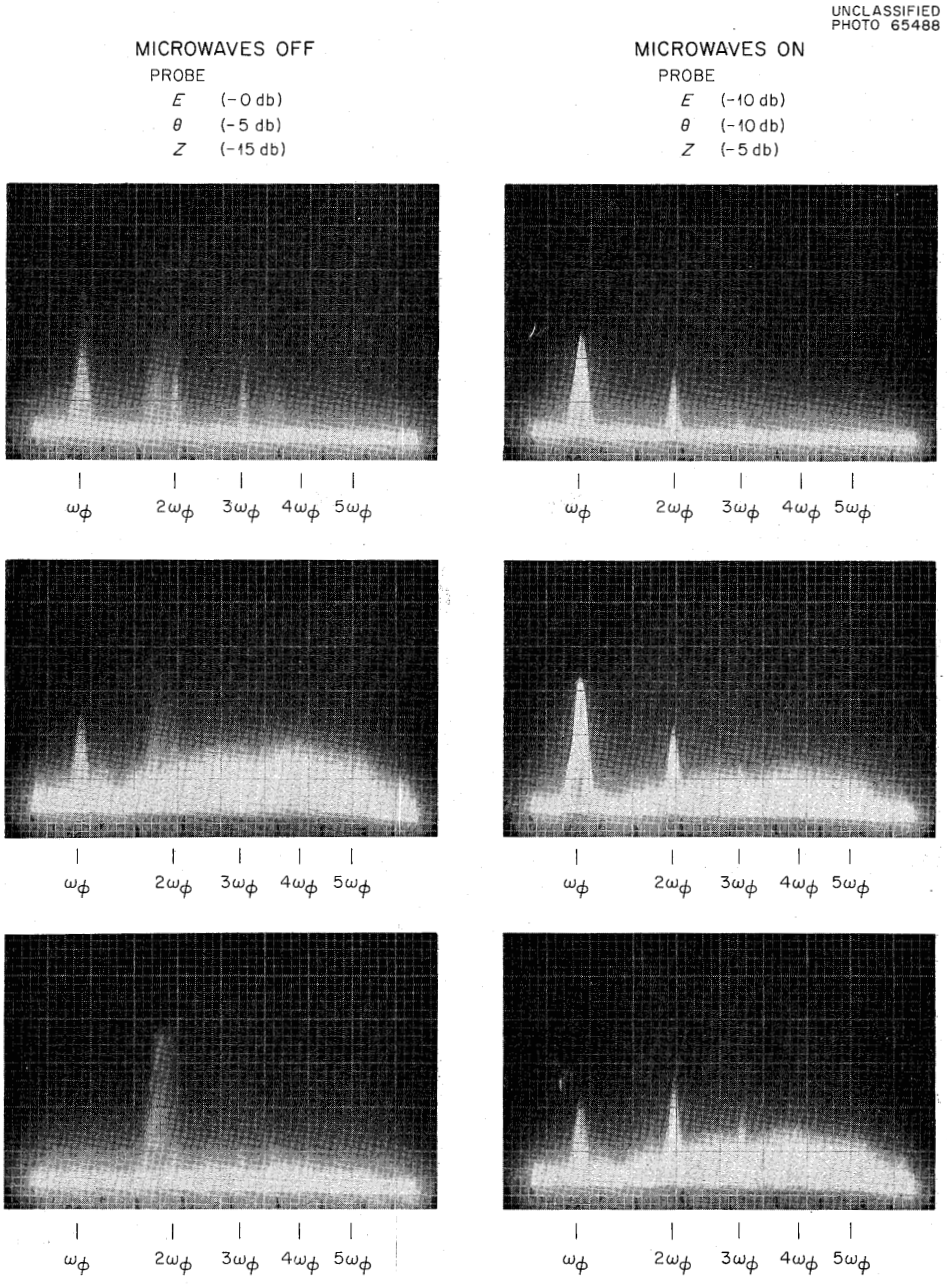

Fig. 1.22. Panoramic Spectra with Grounded End Walls. Data DCX-1, 1-6-64, pictures 54–59, 2.4 ma H_2^+, 2.0×10^{-8} torr, helium leak, 10-in. wall separation, 10 sec exposure.

where ω_Φ is the proton cyclotron frequency and ω_z is the proton axial oscillation frequency (about 5 Mc).

The proton cyclotron signals are evidently due to the azimuthal proton-clustering instability. A theory that accounts for the unstable longitudinal mode and the observed nonharmonic frequencies is given in Sect. 1.7.

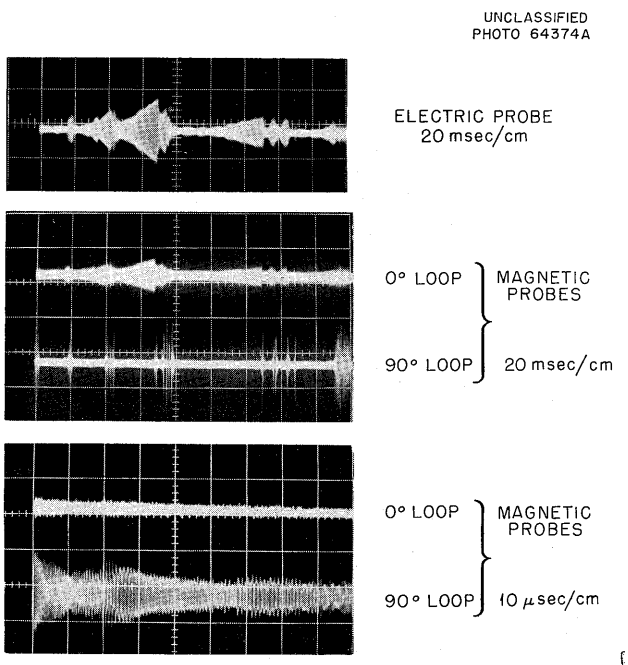

Fig. 1.23. Simultaneously Recorded Signals from an Electric and Two Magnetic Probes, All Mounted in the Median Plane. Data DCX-1, 1-6-64, RF No. 22, 2.4 ma H_2^+, 2.5×10^{-8} torr (helium).

1.4 ADDITIONAL RADIO-FREQUENCY MEASUREMENTS

Radio-frequency measurements similar to those described in Sect. 1.3 were later made with the special end walls removed. The walls surrounding the plasma were then those of the usual high-vacuum liner (Fig. 1.2). These measurements occurred after the realignment of the beam injection system described in Sect. 1.1.

The rf signals both from plasmas established by gas dissociation and from those established by Lorentz-force trapping were examined. The panoramic data were very similar to those obtained with the widest separations of the movable end walls. The most striking feature of the observations continued to be the frequency spectrum of the signals from the unstable longitudinal mode. The investigations included a number of observations with exposure times of 1/25 sec. Figure 1.24 shows such data from the magnetic probes. Aside from the obvious conclusion that a variety of amplitude distributions is possible, there was one consistent feature of these spectra that is probably significant: The band at $\omega_\Phi + \omega_z$ (approximately 19 Mc) was not observed except in conjunction with the cyclotron fundamental.

The oscilloscope data continued to agree with those from the panoramic receiver. However the cyclotron signals were more continuous at low pressures than had been previously noted. A study of the rf data acquired before and after the realignment of the injection system indicates that the realignment was responsible for this change.

Radio-frequency measurements were also made in conjunction with the radial limiter experiments described in Sect. 1.2. Differences of detail were noted as the position of the radial limiter was varied, and some reduction of average amplitudes accompanied reduction of plasma radius; but no new rf phenomena were noted in the τ regime of deficient charge-exchange current.

1.5 LOW-FREQUENCY PHENOMENA

An earlier report[10] described observations of low-frequency (2 to 12 kc) fluctuations in the electron component of slow plasma escaping through a mirror and similar fluctuations in the current transmitted along field lines through the plasma by the lithium ion beam probe. These observations had been made with plasmas established by the gas dissociation of approximately 2 ma of H_2^+ current when operating at base pressures in the 10^{-9} torr range.

[10] *Thermonuclear Div. Semiann. Progr. Rept. Oct. 31, 1963,* ORNL-3564, Sect. 1.3, p. 4.

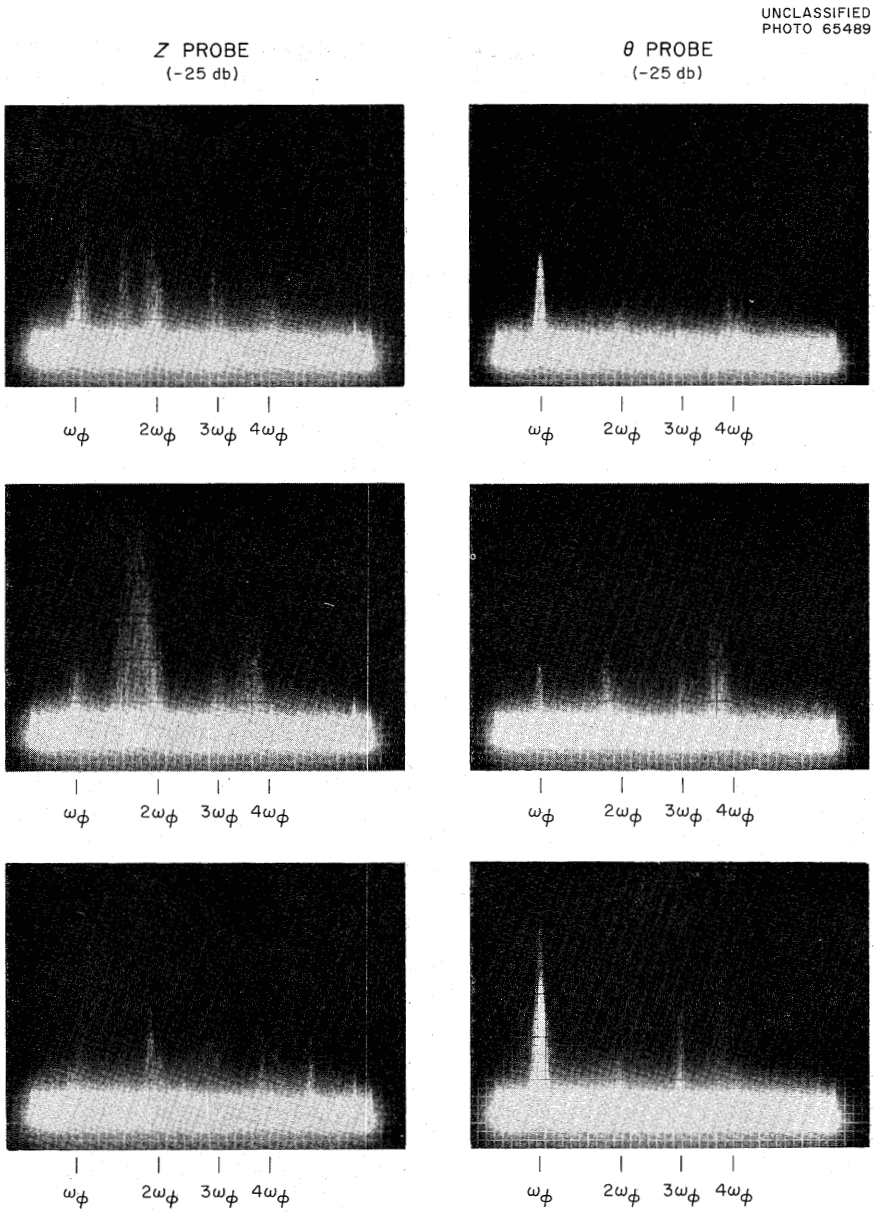

Fig. 1.24. Panoramic Spectra with Normal Liner Configuration. Data DCX-1, 3-24-64, pictures 4, 5, 6, 10, 11, and 13, 210 μa H_2^{+*}, 2.0×10^{-9} torr, $^1/_{25}$ sec exposure.

Additional experiments of this nature were performed during the present report period. The current collector was again a 12-in.-diam plate divided into 60° sectors so that the signals to individual sectors could be compared. The collector had, however, been modified so that one sector could be advanced toward the median plane. Cathode follower couplings between the collectors and oscilloscopes were again employed. Most of the data were obtained with plasma established by Lorentz-force trapping, with 200 to 300 μa of H_2^{+*} current and with base pressures that yielded

charge-exchange decay times of about 10 sec. With the collector located at $Z = 17\frac{1}{2}$ in. (about 2 in. outside the mirror), the current fluctuations were like those described in the earlier report (pulselike ejections of electrons that correlated with the presence of the high-frequency longitudinal instability, and low-frequency modulation of the electron component of slow plasma current) except that now the modulation frequency ranged from 50 to 70 kc and there was less evidence for distinct lower-frequency components. Simultaneous observations of the signals to two sectors 60° apart in mechanical phase usually showed significant differences in the wave patterns both of electron ejection signals and of the modulation. These differences increased as the mechanical phase of the two sectors being compared was increased. From the wave forms accumulated in these comparisons it was not possible to arrive at a consistent interpretation of the modulation signals as a simple disturbance azimuthally rotating either at the observed 50 to 70 kc or, as was the case for a few such comparisons in the earlier work, at a lower frequency. Also, the suggestion of correlations between the modulation signals and modulation of the high-frequency magnetic probe signals that were present in the earlier work was not supported by these later measurements; modulation of the rf signals is often present, but for this modulation to occur at the same frequency as the end collector signals appears to be only coincidental.

As the movable sector was advanced toward the median plane, the 50 to 70 kc signal component to that sector was altered considerably. The wave pattern became more regular; the amplitude increased markedly (by about 4× at $Z = 12$ in., 10× at $10\frac{1}{2}$ in., 20× at 9 in., and 30× at $6\frac{1}{2}$ in.); it became obvious that these signals were continuous and unaltered by the electron ejections; and the signals were also unaffected by ±18 v bias. Advancing the movable sector did not appear to alter the form or magnitude of the electron ejection signal component to that sector, but by the 9 in. position the magnitude of the oscillating component dominated to such an extent that the ejections were no longer visible. Changes in the position of the movable sector did not change the signals to fixed sectors.

Since these data indicated that the advanced sector was responding to fluctuating electric fields in the plasma rather than to particle currents, electrostatic probes were then employed. Initially two probes were mounted in the median plane and about 3 in. beyond the outer radial limit of the trapped energetic plasma. The azimuthal displacement of the two probes was about 40°. The sensitivity of these probes to low-frequency signals was increased by using cathode follower coupling that permitted high-impedance termination of the probes. Figure 1.25 shows the general nature of the signals observed with 10^7 ohms termination. The sharp positive excursions in the 20 msec/cm electric probe trace coincide with signals on the magnetic probe oriented for sensitivity to axial currents (the 90° loop). As previously noted, these axial current fluctuations are associated with the ejection of plasma electrons through the mirrors and with a sharp rise in the plasma potential. The electric probe excursions are responses to these potential fluctuations. The recoveries from these excursions occur with the *RC* time constant (a few milliseconds) of the probe system. Fast sweeps like the one in Fig. 1.25 showed that the frequencies and wave forms of the electric probe signal were similar to those observed with the advanced end plate sector.

UNCLASSIFIED
PHOTO 65402

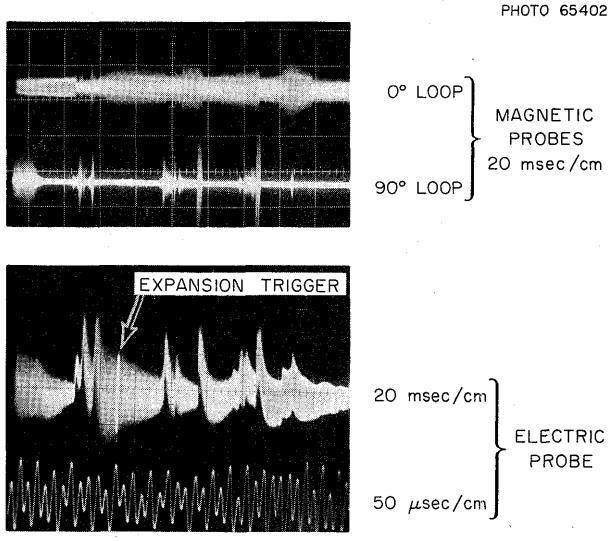

Fig. 1.25. Simultaneously Recorded Signals from Two Magnetic Probes and a Low-Frequency Electric Probe, All Mounted in the Median Plane. Data DCX-1, 4-15-64, picture 50*d*, 200 μa H_2^{+*}, $\tau_{\Sigma DK} = 25$ sec.

Comparisons of the wave form of the electric probe signal and the signals from the magnetic probes confirmed the conclusion, reached during the experiments with the advanced end plate sector, that there does not appear to be any correlation between the low-frequency signals and the magnetic probe signals other than the response of the electric probe to electron ejections.

Numerous oscilloscope scans were made comparing the signals from the two azimuthally displaced electric probes. On slow-speed sweeps the signals appeared to be identical. With sweep speeds fast enough to resolve the wave forms, the results were similar to those that had been obtained with comparisons of the signals to different end plate sectors. The wave forms from the two probes were similar, but not exactly the same except for sinusoidal-like signals, and the phase relations did not permit interpretation as a disturbance in simple azimuthal rotation. There were occasional suggestions of rotation at a frequency lower than the signal frequency, but these were not numerous or consistent enough to give one any confidence in this interpretation.

The frequency of the low-frequency oscillations was examined as a function of the charge-exchange decay time of the plasma. The results obtained for gas dissociation, a helium leak, and the radial limiter positioned at $8\frac{5}{8}$ in. are shown in Fig. 1.26.

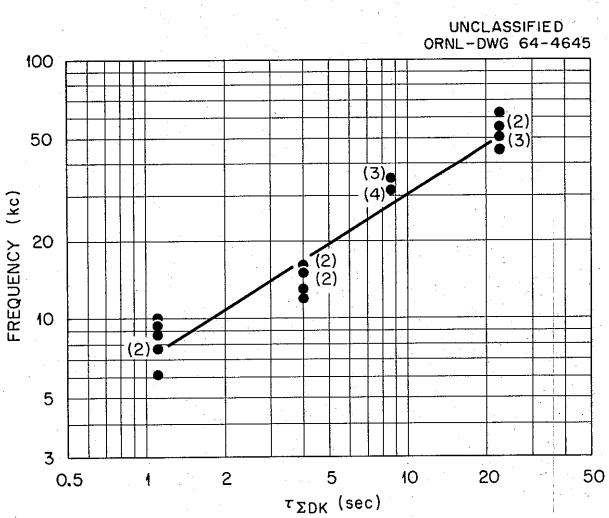

Fig. 1.26. The Frequency of the Low-Frequency Signals as a Function of the Charge-Exchange Decay Time. Data DCX-1, 3-26-64, 2 ma H_2^+, helium gas leak, radial limiter at $8\frac{5}{8}$ in.

There was also a gradual decrease in the amplitude of the signals with decreasing decay time. Similar results were obtained with a nitrogen gas leak, and it was found that the results with either gas were not affected by moving the limiter to $6\frac{5}{8}$ in. Checks made at fixed τ showed that the oscillation frequency varied in the same sense as the injected H_2^+ current. With Lorentz-force trapping it was again found that the frequency varied with the injected current; typical results at about 30 sec τ were 90 kc at 235 μa H_2^{+*}, 68 kc at 150 μa, and 50 kc at 60 μa. The signal amplitudes increased with injected current and were about a factor of 2 higher at 235 μa, than at 60 μa.

With Lorentz-force trapping, the variation of the oscillation frequency with decay time was examined both during normal operation (microwaves off) and during the application of several watts of microwave power at the frequency (26.6 kMc) suitable for resonant heating of electrons in the central plasma region. The results are presented in Fig. 1.27 for the radial limiter at $8\frac{5}{8}$ in., in Fig. 1.28 for the limiter at $7\frac{5}{8}$ in., and in Fig. 1.29 for the limiter at $6\frac{5}{8}$ in. The changes in

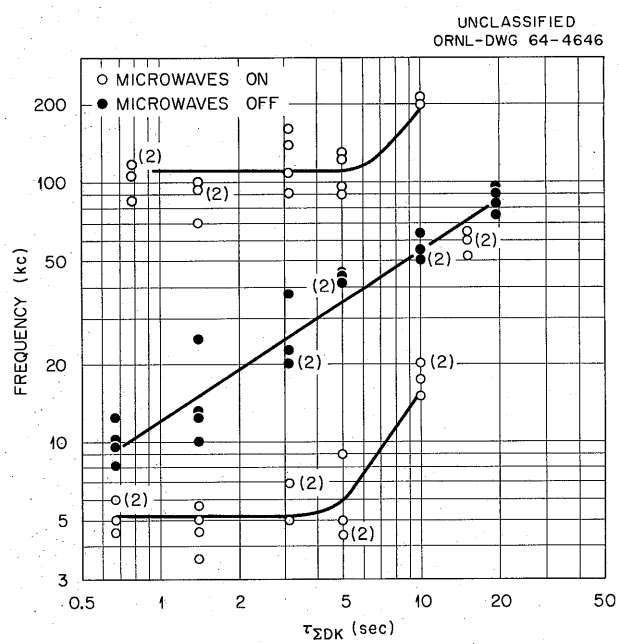

Fig. 1.27. The Frequency of the Low-Frequency Signals as a Function of the Charge-Exchange Decay Time. Data DCX-1, 4-15-64, 200 μa H_2^{+*}, helium gas leak, radial limiter at $8\frac{5}{8}$ in.

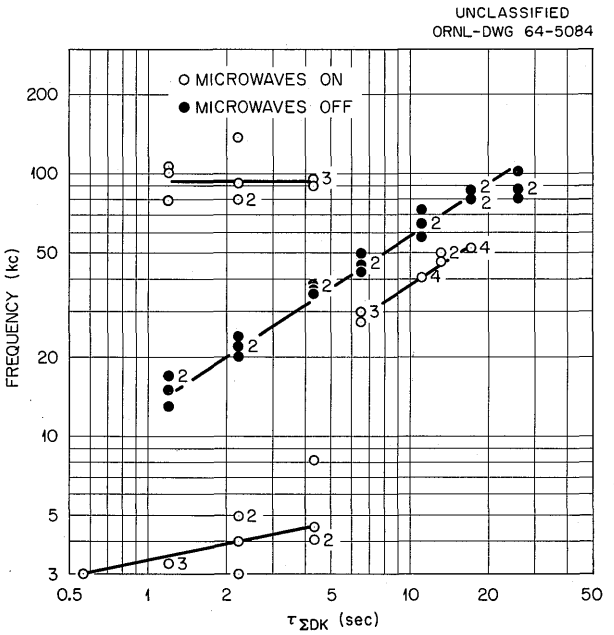

Fig. 1.28. The Frequency of the Low-Frequency Signals as a Function of the Charge-Exchange Decay Time. Data DCX-1, 4-15-64, 200 μa H_2^{+*}, helium gas leak, radial limiter at $7\frac{5}{8}$ in.

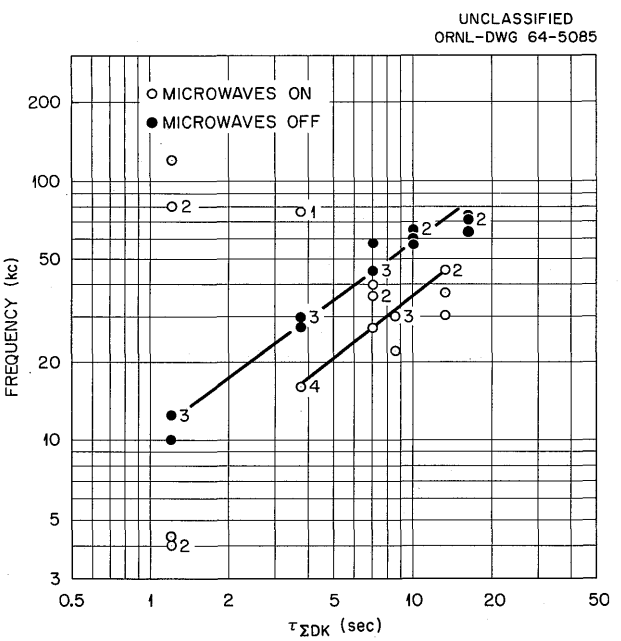

Fig. 1.29. The Frequency of the Low-Frequency Signals as a Function of the Charge-Exchange Decay Time. Data DCX-1, 4-15-64, 200 μa H_2^{+*}, helium gas leak, radial limiter at $6\frac{5}{8}$ in.

the limiter position did not alter the results obtained without microwave heating; in each case the data fit essentially the same curve. That the slope of this curve is about that observed with gas dissociation (Fig. 1.26) suggests that the frequency variation is primarily τ dependent.

The application of microwave power resulted in some rather curious changes. For the points obtained near base pressure the oscillation frequency was simply lowered, but at higher pressures the probe signal showed two frequencies, one above and one below the frequencies obtained with microwaves, and each nearly constant. Figure 1.30 illustrates the changes produced by the microwaves in these two pressure regimes. (With the microwaves on, the longitudinal instability and the associated electron ejections are suppressed, so the electric probe signal is then steadier than without microwaves.) Note that the lower frequency of this double frequency response is not simply a modulation of the higher frequency. For the conditions of Fig. 1.27 (limiter at $8\frac{5}{8}$ in.) only one point in the single-frequency regime was

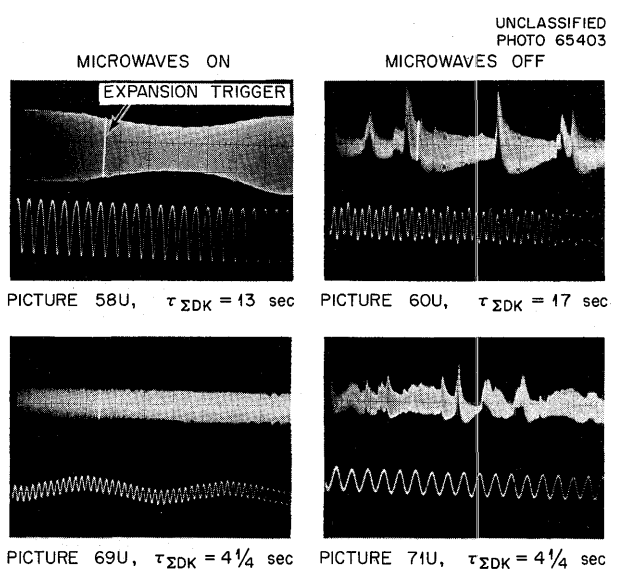

Fig. 1.30. Oscillograms Showing the Effects of Microwaves on the Low-Frequency Signals. Data DCX-1, 4-15-64, 200 μa H_2^{+*}, helium gas leak for lower pair of oscillograms, radial limiter at $7\frac{5}{8}$ in.; horizontal scales are 20 msec/cm and 50 μsec/cm, vertical scales are 5 mv/cm.

obtained. As the limiter was advanced (Figs. 1.28 and 1.29) the transition to the two-frequency regime progressively shifted to shorter decay times, and additional points appeared in the single-frequency regime. It was then apparent that the slope of the data in the single-frequency regime was the same as that of the data obtained without microwaves, and that these data were displaced from those obtained without microwaves by an essentially constant factor. In summary then, varying the position of the radial limiter changed the frequency plots only by changing the point of transition to the two-frequency regime.

Figures 1.31–1.33 show the average amplitude of the low-frequency signals for the data displayed in Figs. 1.27–1.29. On these scales the limit of detection is about 0.1. No low-frequency signals were visible at $\tau = 0.37$ sec for the $8\frac{5}{8}$ in. limiter position, or at $\tau = 0.33$ sec for the $7\frac{5}{8}$ in. position. The high-pressure scan for the $6\frac{5}{8}$ in. position was terminated before the detection limit was reached.

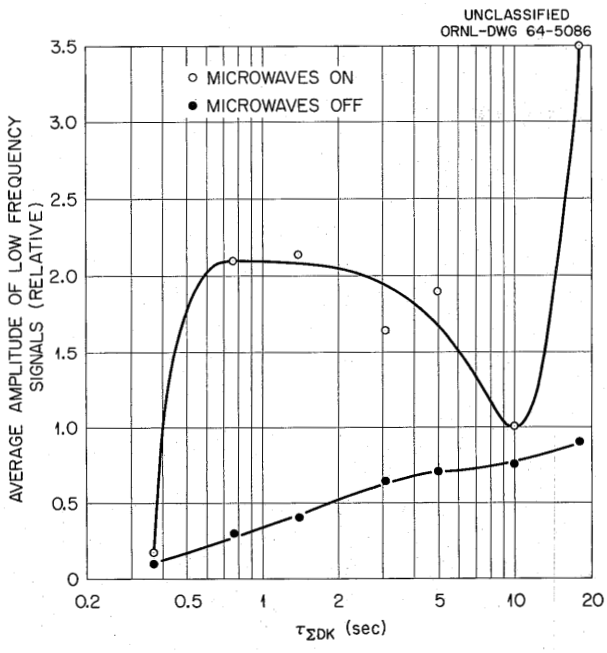

Fig. 1.31. The Average Amplitude of the Low-Frequency Signals as a Function of the Charge-Exchange Decay Time. Data DCX-1, 4-15-64, 200 μa H_2^{+*}, helium gas leak, radial limiter at $8\frac{5}{8}$ in.

Figure 1.34 gives the ratio of the amplitudes of the signals observed in the two-frequency regimes with microwave power applied.

Additional runs similar to those that resulted in Figs. 1.27–1.34 were made utilizing approximately the same values of injected beam current and applied microwave power. The frequency vs τ curve for operation without microwaves was very reproducible. With microwaves the frequencies of the three branches were also reproducible, but

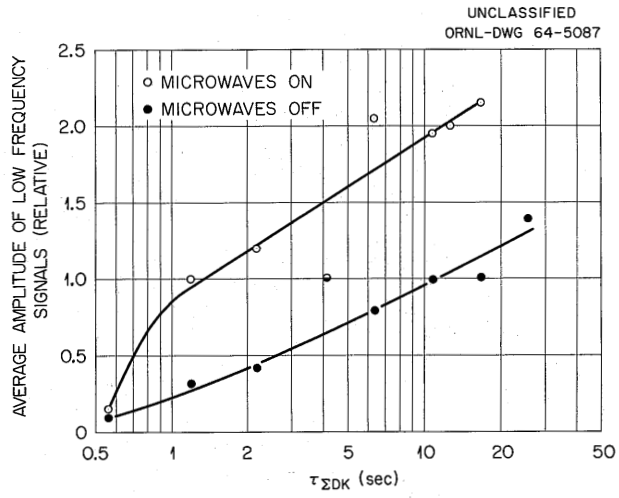

Fig. 1.32. The Average Amplitude of the Low-Frequency Signals as a Function of the Charge-Exchange Decay Time. Data DCX-1, 4-15-64, 200 μa H_2^{+*}, helium gas leak, radial limiter at $7\frac{5}{8}$ in.

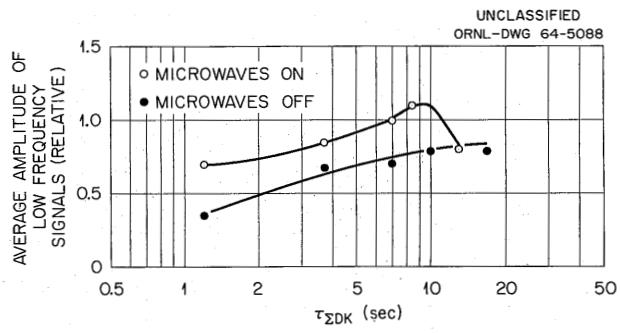

Fig. 1.33. The Average Amplitude of the Low-Frequency Signals as a Function of the Charge-Exchange Decay Time. Data DCX-1, 4-15-64, 200 μa H_2^{+*}, helium gas leak, radial limiter at $6\frac{5}{8}$ in.

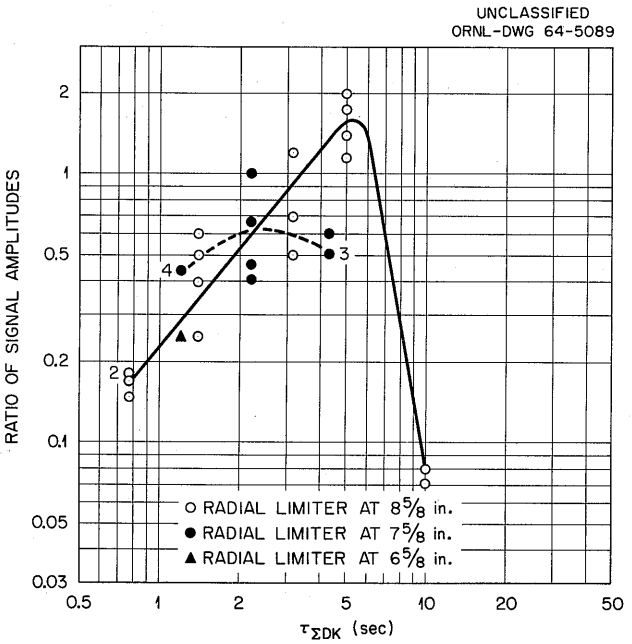

Fig. 1.34. The Ratio of the Amplitude of the High-Frequency Signal to the Amplitude of the Low-Frequency Signal. Data DCX-1, 4-15-64, 200 μa H_2^{+*}, microwaves on, helium gas leak.

with some fluctuations in the data for the longest τ point in the two-frequency regime and in the τ value for transition to that regime (although the trend for the transition to occur at longer τ values for larger radial limits was consistent). The gross behavior of the amplitude curves (amplitudes increasing with τ, with the application of microwave power, and with increasing radial limit) was also consistent.

The preceding observations were all made on steady-state plasmas. The low-frequency signals were also examined during the intervals of plasma accumulation and decay. In operation without the microwaves, the low-frequency signals appeared very early during the buildup interval and disappeared in a small fraction of the charge-exchange decay time during plasma decay. (The high-frequency signals from magnetic probes habitually show similar responses.) The response during buildup was similar with microwaves, but the low-frequency signals persisted for a long time during the decay interval. (The magnetic probe signals still disappeared rapidly.) The amplitude and frequency of the signals were determined a number of times during such a decay at base pressure under conditions which yielded a charge-exchange decay time of 20 sec. Figure 1.35 presents these data. The signals were visible with gradually decaying amplitude for 3 min. Because of the energy dispersion of the trapped proton population and the energy dependence of the charge-exchange loss rate, the fast proton population decays with a time constant that under these conditions might easily be twice the 20-sec decay time measured for the charge-exchange current itself; the amplitude decay of the low-frequency signal is, therefore, probably similar to the decay of the fast protons. Initially there was only a single frequency component which decayed in a fashion similar to the amplitude, but at about 45 sec a high-frequency component appeared and persisted, initially at a constant frequency, for the remainder of the decay. The low-frequency component did not appear as amplitude modulation

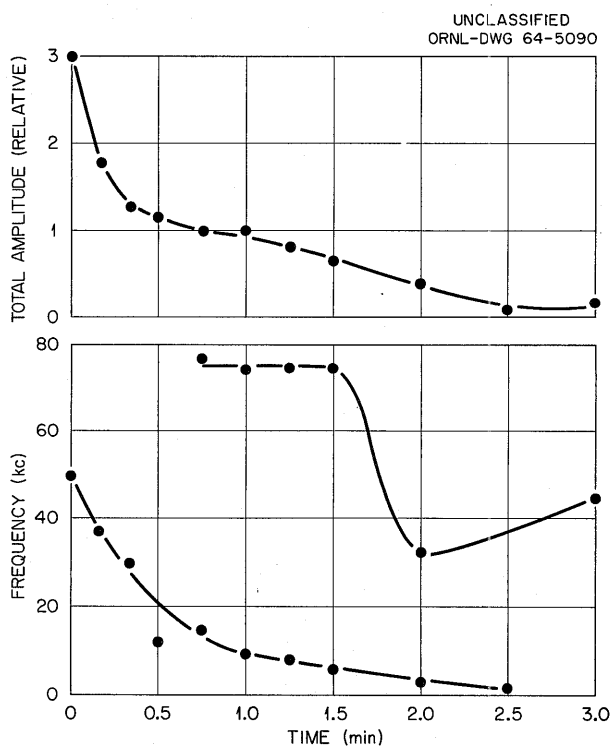

Fig. 1.35. The Variation of Amplitude and Frequency of the Low-Frequency Signals During Plasma Decay with Microwaves On. Data DCX-1, 4-15-64, $\tau_{\Sigma DK}$ = 20 sec, steady-state plasma formed by injection of 200 μa H_2^{+*}, radial limiter at 7⅝ in.

of the higher frequency, but rather the wave forms were similar to those observed in the two-frequency regime of steady-state operation. The amplitude of the high-frequency component was about one-quarter that of the low-frequency component. Cutting the microwaves off during the decay period made the oscillations disappear, but they reappeared if the microwaves were reapplied. Similarly, if the decay was started without microwaves so that the oscillations disappeared, application of the microwaves made the oscillations reappear. Cutting the microwaves off and on a number of times during decay resulted in alternate disappearance and reappearance of the signals. Measurements made during the intervals that the microwaves were on showed that the amplitude and frequency of the oscillations varied as though the microwaves had been applied continuously (Fig. 1.35).

The electric probe system used in these investigations was calibrated by applying oscillating potentials to a set of copper cylinders of different radii. If it is assumed that the probe was responding to potential fluctuations at the surface of the fast-proton plasma, which is fixed by the position of the radial limiter, it is then possible to fix values for the magnitude of the potential fluctuations. For the data obtained with the limiter at $8\frac{5}{8}$ in. (Fig. 1.31) one amplitude unit is equivalent to 85 v potential fluctuation; for data with the limiter at $7\frac{5}{8}$ in. (Figs. 1.32 and 1.35) one unit is equivalent to 125 v; and for data with the limiter at $6\frac{5}{8}$ in. (Fig. 1.33) one unit is equivalent to 190 v.

We do not yet know the origin of these low-frequency oscillations. The inability to obtain a consistent interpretation in terms of an azimuthally rotating phenomenon suggests that the signals may arise from a set of oscillators in azimuthal rotation at different frequencies. Such a situation would account for the difficulties encountered in interpreting the phase differences of signals from azimuthally displaced probes, and also for the differences in wave forms at such probes. The oscillators may involve only slow plasma components (perhaps electrons alone[11]); if the slow plasma then extends beyond the radial limit of the fast-proton plasma, the observed signal amplitudes could represent considerably smaller potential fluctuations than suggested by the calibration data. Whether the low-frequency oscillations contribute to the scattering and the loss of fast protons (described in Sect. 1.2) is not clear. In connection with this phase of the problem, we observe that the amplitude of the oscillations does increase with increases in plasma decay time and with the application of microwave power (both of which under some conditions lead to an enhancement of the apparent proton losses), but that the threshold for observation of the oscillations is well within the pressure regime where the proton losses are by charge exchange.

Further investigations revealed one other low-frequency phenomenon, which was connected with microwave heating but which did not require the presence of fast trapped protons. With a few watts of microwave power applied and the pressure raised about a factor of 2 above that at which the oscillations just described disappeared (to about 4×10^{-8} torr gage pressure, uncorrected for the helium gas leak) periodic burstlike signals were registered by the electric probe. Initially the burst repetition rate was about 60 cps, the dominant frequency in a burst was approximately 10 kc, and the signals were just barely above the detector noise level. The repetition rate, frequency, and amplitude all increased gradually with pressure. Figure 1.36 shows an example of the data obtained at the highest pressure investigated (3×10^{-7} torr, uncorrected). Here the repetition rate was 400 cps, the frequency was approximately 20 kc, and the amplitude was about a factor

UNCLASSIFIED
PHOTO 65490

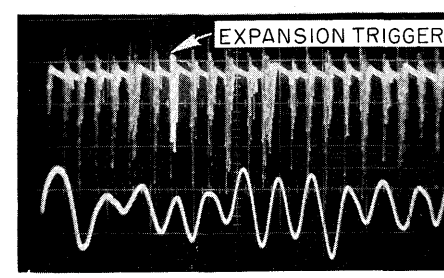

Fig. 1.36. RF Signals from Microwave Generated Plasma as Recorded by a Low-Frequency Electric Probe. Data DCX-1, 4-16-64, picture 39*U*, 3×10^{-7} torr gage pressure, helium gas leak.

[11]R. D. Brown, *Periodic Phenomena in a Plasma in Crossed Electric and Magnetic Fields*, M.S. Thesis, Ohio State University, 1963. (Supported by unpublished recent work of C. E. Nielsen.)

of 30 above the noise level. Since these signals were present without a fast-proton plasma, they were evidently due to a microwave-generated plasma. The phenomenon is probably akin to the unstable "high-temperature, low-density mode" previously observed and reported[12] by the Electron Cyclotron Heating Group.

1.6 CALCULATED RADIAL DENSITY DISTRIBUTIONS OF TRAPPED PROTONS

The radial density distributions of protons trapped in DCX-1 have been calculated for both gas dissociation and Lorentz-force trapping. The following assumptions were made:

1. that the H_2^+ beam path was a line trajectory confined to the median plane,
2. that the point on the trajectory closest to the magnetic axis was at $R = 3.25$ in. (the stable orbit radius for 300-kev protons),
3. that for gas dissociation, the proton currents are equal for equal increments of length along the beam trajectory,
4. that the Lorentz-force dissociation fraction varies as $(v \times B)^{1.93}$ (ref. 13), and
5. that the protons remain at 300 kev and have single-particle orbits confined to the median plane.

Item 5 is the most serious of the assumptions, for the neglect of scattering effects makes the distributions representative of recently trapped protons only.

Studies of the effects of varying the outer radial limit of the proton orbits were included. Limits of $9\frac{1}{2}$, $8\frac{1}{2}$, $7\frac{1}{2}$, and $6\frac{1}{2}$ in. were investigated.

Figure 1.37 shows the normalized distributions resulting from gas dissociation. Figure 1.38 presents distributions for Lorentz-force trapping. In both cases the most significant changes were made when the outer radius was decreased from $7\frac{1}{2}$ to $6\frac{1}{2}$ in.

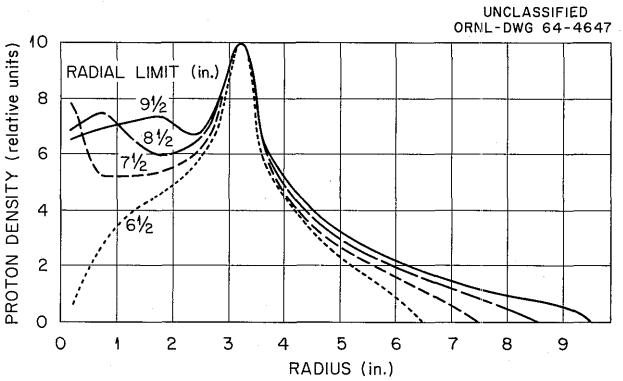

Fig. 1.37. Calculated Radial Density Distributions for Protons Resulting from Gas Dissociation.

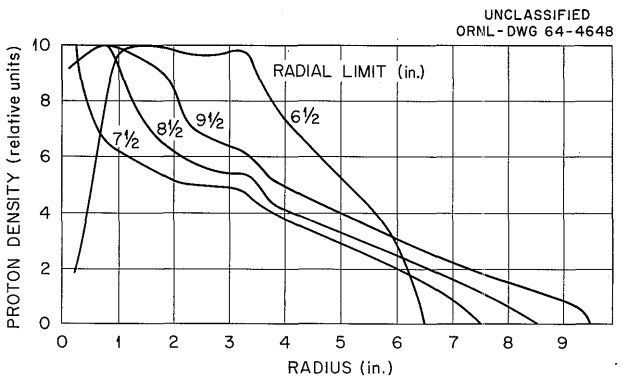

Fig. 1.38. Calculated Radial Density Distributions for Protons Resulting from Lorentz-Force Trapping.

The proton current which can be trapped varies in the same sense as the radial limit. For limits of $9\frac{1}{2}$, $8\frac{1}{2}$, $7\frac{1}{2}$, and $6\frac{1}{2}$ in., this current was found to vary in the ratio 1.0 : 0.835 : 0.67 : 0.51 for gas dissociation and 1.0 : 0.80 : 0.6 : 0.4 for Lorentz-force trapping.

It should be pointed out that the value of central (maximum) proton density, given elsewhere in this report, was not calculated by using these distributions. Instead, allowances for beam divergence and proton scattering were made by assuming that the peak of the radial density was only a factor of 2 greater than the average density in the median plane.

We wish to thank Mozelle Rankin and D. A. Griffin for computer work in connection with this problem.

[12] *Thermonuclear Div. Semiann. Progr. Rept. Oct. 31, 1961,* ORNL-3239, p. 18.

[13] From a curve fitted to data of A. C. Riviere and D. R. Sweetman (Culham Laboratory, England) for the Lorentz-force dissociation of H_2^+ formed from H_3^+. Data received by private communication from J. R. Hiskes (UCRL).

1.7 THEORY OF LONGITUDINAL OSCILLATIONS

C. E. Nielsen

1.7.1 Introduction: Experimental Observations

Magnetic-field probes oriented for sensitivity to oscillating longitudinal currents have been used in numerous investigations of the radio-frequency signals from the DCX-1 plasma. The response of such probes mounted off the median plane is dominated by changes in the B_Φ field component of the azimuthally revolving proton clusters. Longitudinal-current probes mounted in the median plane give signals which vary in character as a function of pressure in the plasma region.[9] At higher pressures the probes respond to the revolution of proton clusters located off the median plane, that is, to axial asymmetries in proton clustering. At lower pressures the probes indicate the presence of a distinctly different longitudinal mode, to which attention will now be confined.

Continuing observations of these low-pressure longitudinal-current signals have demonstrated the following:

1. The longitudinal activity can occur quite independently of the proton-clustering azimuthal mode.[14]
2. The longitudinal mode is suppressed by microwave heating of the plasma electrons,[15] and by traversal of small longitudinal electron currents from an external electron source,[16] as well as by increase of pressure.
3. When longitudinal activity is suppressed by any means, the axial spread of fast protons either decreases or remains constant, while at the same time the azimuthal activity becomes more continuous and thus increases in average amplitude if not in peak amplitude.
4. Each "spike" of longitudinal activity is associated with ejection of electrons out through the mirrors. The spikes have a very complicated structure of amplitude variations; the electrons are ejected in pulses as short as a few microseconds not time-correlated with spike-amplitude variations.[10]
5. Frequencies most prominent in longitudinal activity, observed at various times with various input currents and pressures, are of the form $n\omega_\Phi \pm \omega_z$, ω_Φ being the proton gyrofrequency (about 15 Mc) and ω_z the proton axial oscillation frequency (about 5 Mc).[17]

1.7.2 Current-Ring Model

The frequency spectrum of the longitudinal oscillations was the clue that led to the present interpretation. Independence of plasma density required that the frequencies be related to proton motion in the magnetic field. Frequencies of the form $n\omega_\Phi \pm \omega_z$ could be observed at a fixed point if a ring of protons were oscillating coherently so that axial displacements would have, at any instant, the appearance of a wave with n wavelengths around the ring. A growth of coherent axial oscillation waves has recently been observed at MURA in a uniform circulating electron beam, and at Brookhaven in the Cosmotron; it has been accounted for by interaction between the beam and the adjacent resistive metal walls.[18] Only the waves of frequency $n\omega_\Phi - \omega_z$ will grow from this interaction, and the $n\omega_\Phi + \omega_z$ will be damped.

Is it possible that proton axial oscillation waves may also grow from electrostatic coupling with slow trapped electrons? What is required is that the electrons must act to transfer energy from proton azimuthal motion to coherent axial proton oscillations.

Consider a ring of protons moving in circular orbits in a field B such that there is a restoring force toward the median plane. Let the proton charge be partially neutralized by electrons occupying approximately the same volume, and subject to such restoring forces that their longitudinal oscillations have angular frequency ω_e. Note that ω_e is *not* a plasma frequency, but an oscillation frequency in an equivalent potential well, probably primarily electrostatic, but including also magnetic mirror force. Because of the magnetic field the electron motion is essentially one-dimensional. We ask whether a coherent axial oscillation of the

[14] *Thermonuclear Div. Semiann. Progr. Rept. Oct. 31, 1962*, ORNL-3392, Sect. 1.6, p. 9.

[15] *Thermonuclear Div. Semiann. Progr. Rept. Oct. 31, 1963*, ORNL-3564, Sect. 1.4, p. 8.

[16] *Thermonuclear Div. Semiann. Progr. Rept. Oct. 31, 1962*, ORNL-3392, Sect. 1.6, p. 9.

[17] Sect. 1.3, this report.

[18] L. J. Laslett, V. K. Neil, and A. M. Sessler, *Transverse Resistive Instabilities of Intense Coasting Beams in Particle Accelerators*, UCRL-11090 (1963).

proton ring grows or decays by virtue of electrostatic coupling to the electrons.

As a simple first approximation, suppose that at any given Φ the protons and electrons oscillate in the axial direction without change of distribution over their cross sections. Such oscillations may be characterized by the axial displacements at all Φ specified by the center-of-mass coordinates $Z(\Phi, t)$ and $z(\Phi, t)$ of the proton and electron distributions.

For small oscillations the axial coupling force per unit length (length in the Φ direction) may be considered proportional to relative axial displacement, $F = g(z - Z)$. Denote linear mass densities by μ_p and μ_e. Then, since electrons move only in the axial direction their equation of motion is simply

$$\frac{\partial^2 z}{\partial t^2} + \omega_e^2 z = -\frac{g}{\mu_e}(z - Z).$$

Proton motion is complicated by the revolution of protons about the axis. The protons move through the wave, and the axial acceleration of the wave, $\partial^2 Z/\partial t^2$ at a given Φ, is different from the axial acceleration of a proton, which may be designated, in the usual notation of fluid dynamics for particle-following derivative, by d^2Z/dt^2. We assume axial symmetry of ω_z and g so that axial forces are independent of Φ. In a coordinate system rotating with the protons the proton equation of motion is

$$\frac{d^2 Z}{dt^2} + \omega_z^2 Z = \frac{g}{\mu_p}(z - Z).$$

In order to transform this rotating system to the laboratory coordinate Φ we note that a particle-following (or particle-labeling) coordinate η in the rotating system may be defined by $k\eta = \Phi - \omega_\Phi t$; the initial value Φ_0 is the laboratory position of the η particle at $t = 0$. The value of k may be taken as unity. It is convenient to use the Jacobian notation

$$\frac{dZ}{dt} \equiv \frac{\partial(Z,\eta)}{\partial(t,\eta)},$$

in which the particle-following derivative is explicitly designated as a derivative at constant particle-labeling coordinate η. Since velocity is defined by a particle-following derivative, we write $V_z = dZ/dt$, and consequently

$$V_z = \frac{\partial(Z,\eta)}{\partial(t,\eta)} = \frac{\partial(Z,\eta)}{\partial(t,\phi)} \cdot \frac{\partial(t,\phi)}{\partial(t,\eta)}$$

$$= \left(\frac{\partial Z}{\partial t} \cdot \frac{\partial \eta}{\partial \phi} - \frac{\partial Z}{\partial \phi}\frac{\partial \eta}{\partial t}\right)\left(\frac{\partial \phi}{\partial \eta}\right)_t$$

$$= \left(\frac{\partial Z}{\partial t}\right)_\phi + \omega_\phi \left(\frac{\partial Z}{\partial \phi}\right)_t .$$

Proceeding in this way we obtain

$$\frac{d^2 Z}{dt^2} = \frac{\partial^2 Z}{\partial t^2} + 2\omega_\phi \frac{\partial^2 Z}{\partial t \partial \phi} + \omega_\phi^2 \frac{\partial^2 Z}{\partial \phi^2},$$

and the two coupled equations of motion in laboratory coordinates are

$$\frac{\partial^2 Z}{\partial t^2} + 2\omega_\phi \frac{\partial^2 Z}{\partial t \partial \phi} + \omega_\phi^2 \frac{\partial^2 Z}{\partial \phi^2} + \omega_z^2 Z = \frac{g}{\mu_p}(z - Z),$$

$$\frac{\partial^2 z}{\partial t^2} + \omega_e^2 z = -\frac{g}{\mu_e}(z - Z).$$

We have treated ω_Φ as a constant, which it is nearly enough for small values of proton displacement Z, and for equal coaxial orbits. Any dispersion in ω_Φ over the proton distribution will of course introduce dispersion into the coherent wave and thereby exert a damping or stabilizing influence.

Such a system of coupled equations has solutions of the form

$$Z = \alpha \cos(\omega t - n\phi),$$
$$z = \beta \cos(\omega t - n\phi).$$

Substitution of these solutions transforms the differential equations into a pair of homogeneous algebraic equations for α and β which are soluble only when the determinant of the coefficients vanishes. The condition for vanishing of the determinant is that ω have values satisfying a quartic equation which may be written in the form

$$f(\omega) = \frac{g/\mu_p}{(\omega - n\omega_\phi)^2 - \omega_z^2} + \frac{g/\mu_e}{\omega^2 - \omega_e^2} = 1 .$$

This form is convenient because it facilitates graphical exploration of the roots of the quartic.

We plot $f(\omega)$, and the roots ω_1, ω_2, ω_3, and ω_4 are those values of ω for which $f(\omega) = 1$. A sample plot showing the separate contributions of the two terms is given in Fig. 1.39.

Evidently the roots ω_1 and ω_4 are always real and have values very close to those determined from each term of $f(\omega)$ separately, that is,

$$\omega_1 \approx -(g/\mu_e + \omega_e^2)^{1/2} ,$$

$$\omega_4 \approx n\omega_\phi + (g/\mu_p + \omega_z^2)^{1/2}$$

$$\approx n\omega_\phi + \omega_z \text{ for } g/\mu_p \ll \omega_z^2 .$$

The fact that $g/\mu_p \ll \omega_z^2$ is represented graphically by the closeness of the proton term in $f(\omega)$ to the asymptotes $n\omega_\phi \pm \omega_z$.

As Fig. 1.39 is drawn, the value of $f(\omega)$ exceeds unity throughout the interval $\omega_e < \omega < n\omega_\Phi - \omega_z$, which means that the roots ω_2 and ω_3 are not real but complex, and the wave displacements Z and z, therefore, contain a term that grows exponentially in time. We see that if ω_e should be decreased, a value would soon be reached at which the roots ω_2 and ω_3 would become real; and if ω_e should be increased the roots would become real when $\omega_e > n\omega_\Phi - \omega_z$. There is thus a finite range of ω_e over which coupled axial oscillations grow, and the breadth of this range increases with increase in the value of the coupling constant g, which in turn increases with proton and electron densities. For ω_e in this unstable range the real part of ω_2 and ω_3 is of the order of $n\omega_\Phi - \omega_z$, as is readily ascertained by considering the marginally stable case in which $f(\omega)$ is just tangent to the line $y = 1$.

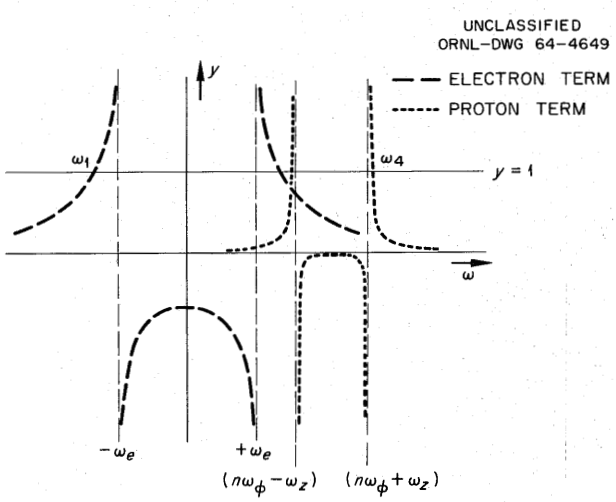

Fig. 1.39. A Sample Plot of the Two Terms of

$$f(\omega) = \frac{g/\mu_p}{(\omega - n\omega_\theta)^2 - \omega_z^2} + \frac{g/\mu_e}{\omega^2 - \omega_e^2} .$$

1.7.3 Extension to a Nonconcentric Orbit Distribution, That Is, to "Interlaced Orbits"

The preceding discussion is based on a model in which proton orbits are approximately concentric and axially centered. Since trapped protons in DCX-1 may occupy a volume of radius exceeding an orbit diameter, one may question whether the model is applicable. But to hope for a solution of the problem employing a realistic proton distribution seems at best an unrealistic hope. Some defense of this real solution of a possibly too unrealistic problem is, however, possible.

Note that restriction to axially centered orbits is not in fact essential. The same analysis applies to coherent axial oscillation of any group of protons with concentric off-axis orbits of nearly enough the same orbit eccentricity and axial amplitude to prevent destruction of the coherent wave by too much spread in gyrofrequency or axial oscillation frequency.

We consider next whether protons more diffusely distributed into interlaced nonconcentric off-axis orbits can cooperate in their axial oscillation. As a simple example we may consider an axisymmetric distribution of orbits with centers lying on an arbitrary circle about the axis. For geometrical analysis it is convenient to think of each orbit as a rigid wave-shaped ring rotated at the wave rotation rate.

It is obvious that the orbit rings may be made tangent at the outside to a circle with arbitrary axial wave shape (but not too high wave number). As they rotate, each point on the tangent circle will oscillate axially. The simplest case is to have the entire circle move axially in phase (if orbits are not too nearly coaxial). If the orbit centers are on a circle of orbit diameter (Fig. 1.40), the point at the axis also will be in phase for all rings when the tangent circle moves in phase. Electron coupling on axis and on the tangent circle would then be possible as indicated by the dotted circles of Fig. 1.40. The preceding remarks apply equally to orbit rings corresponding to any integral number of waves n around the orbit.

UNCLASSIFIED
ORNL-DWG 64-5091

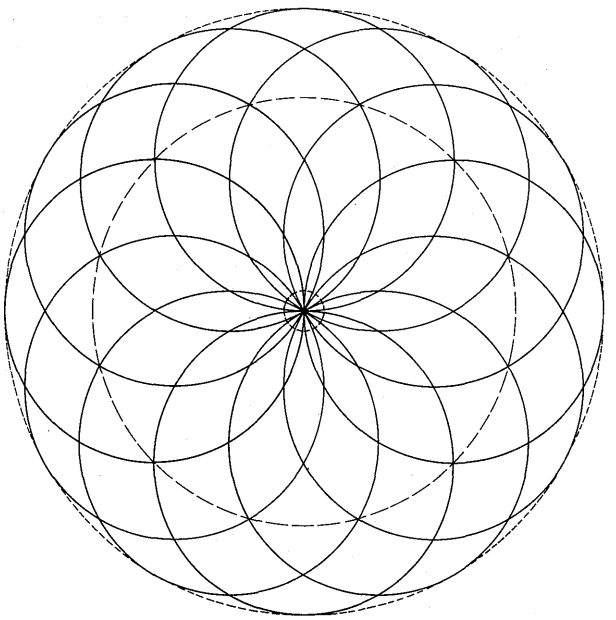

Fig. 1.40. Interlaced Proton Orbits.

For $n = 1$ and the particular eccentricity chosen as an example, orbits can move in phase only on the axis and tangent circle. For $n = 2$ the point on the axis and the tangent circle move in the same direction rather than oppositely as when $n = 1$. At the same time the dashed circle in Fig. 1.40 moves coherently in a direction opposite from the tangent circle and axis. There are then three possible zones of coupling to electrons. It may be that having more zones of possible electron resonance is more favorable to growth of the longitudinal oscillation, because electron oscillation frequency will vary with radius and there is a greater possibility of finding an electron in resonance.

It seems unlikely that, in practice, the plasma potential, the electron oscillation frequency ω_e, or even the proton orbit density will be completely axisymmetric. Since there will be an electron azimuthal drift $(E \times B)/B^2$ and a proton-orbit-center azimuthal drift resulting from the radial gradient of B, the phenomena observed will then be modulated by the rotation and shear of both proton and electron distributions at rates variable with radius.

1.7.4 Discussion of Observations in Terms of the Model

This model of the longitudinal activity appears either to account for, or at least to be consistent with, the various experimental observations cited in Sect. 1.7.1.

1. The model does not require that the proton-clustering azimuthal mode be present for the longitudinal mode to occur.

2. In those cases in which plasma potential was observed, the suppression of longitudinal activity was associated with such a reduction of plasma potential that ω_e could be, as required for stabilization, much less than the characteristic longitudinal frequencies. Other stabilization mechanisms such as increased energy transport by outward flux of electrons may also be important. The self-stabilization implied by the characteristic periodic repetition of short spikes of longitudinal activity requires further study. It seems to have too slow a repetition rate to correspond to alternate electron ejection and replenishment, and perhaps more likely represents the time for accumulation of new ordered protons after the irregular growth of axial oscillation has produced enough disorder in the participating protons to quench their collective motion. The tendency of the $n\omega_\Phi - \omega_z$ longitudinal modes and the azimuthal mode, normally at ω_Φ for any given cluster, to be mutually stabilizing is presumably a special case of the tendency of any disordering process to be stabilizing.

3. Growing coherent longitudinal oscillations would be expected to transmit axial energy to protons much more rapidly than random encounters with the fields of azimuthally revolving clusters. Trapped proton profile data indicate that the longitudinal mode is in fact more effective in producing axial spreading.[17] Numerical comparison of rate of axial spreading with rate expected from growth of longitudinal oscillations has not yet been made; it will be greatly complicated by the fact that during a spike of activity the longitudinal oscillations observed fluctuate wildly in amplitude, probably involving first one and then another group of protons or electrons.

4. Ejection of electrons along magnetic field lines is, like axial proton spreading, a natural consequence of a growing coherent longitudinal oscillation. The process of ejection involves

local plasma potential as well as electron energy and is no doubt complicated in detail by the proton and electron angular drifts mentioned earlier. Departure from axial symmetry as observed in pulses of ejected electrons is consistent with the mechanisms. In those cases in which longitudinal activity is concurrent with a burst of strong proton clustering it may be that the electron resonant response to periodic potential as proposed earlier[19] plays a significant role. Such mixed phenomena appear in any case to be much more complicated.

5. The predication of unstable frequencies corresponding to those observed is one of the most satisfying features of the model, but there remain some mysteries. Frequencies are observed corresponding to $n = 2$ and $n = 3$, but not to $n = 1$. It might have been anticipated that the $n = 1$ mode would be the first to appear as plasma potential rises from a low value, that is, as gas pressure is reduced to the value required for longitudinal activity. The absence of the $\omega_\Phi - \omega_z$ frequency presumably implies that it is more effectively damped or less effectively excited, and we may invoke the conjectured energy loss and excitation mechanisms discussed earlier qualitatively. Landau damping may also be involved. Sometimes there are bands of frequencies in the region of $n\omega_\Phi + \omega_z$. Experimental data suggest that these occur only when azimuthal clustering is present, but we are not certain of this and further study is required.

The longitudinal frequencies tend to be spread over bands of some breadth. Qualitatively this spread can be attributed to the spread in ω_Φ and ω_z resulting from the spread in axial amplitudes and orbit eccentricities. For a given eccentricity, longitudinal frequency is higher when oscillation amplitude is larger. This relation has been strikingly exhibited in some panoramic spectra made with a short enough exposure so that only one spike of activity happened to be included. The shift of frequency with amplitude growth was indicated by the inclination of the 25-Mc peak; the primary cause is presumably the increase in ω_Φ resulting from oscillation of the orbit into regions of increased field away from the median plane.

[19] *Thermonuclear Div. Semiann. Progr. Rept. Oct. 31, 1963*, ORNL-3564, Sect. 1.6, p. 12.

2. DCX-2

P. R. Bell
L. J. Bledsoe
J. S. Culver
R. C. Davis
S. M. DeCamp
J. C. Ezell
R. A. Gibbons
G. G. Kelley
N. H. Lazar
O. B. Morgan
T. F. Rayburn
R. F. Stratton
C. W. Wright
A. J. Wyrick

2.1 INTRODUCTION

Experiments in DCX-2 in which the lithium arc is used for dissociation of the injected 600-kev molecular ion beam have continued. Several independent measurements indicate that the trapped plasma can attain densities in excess of 10^{10} particles/cm^3 averaged over the plasma volume. It was found that the largest values of density occur upon critical adjustment of the magnetic field shape. A reduction in density of a factor of 3 to 10 may occur with field changes amounting to less than 5 gauss in the flat field region with, perhaps, up to a 10-gauss change in the region of the dips.

The lithium arc is operated with about 25 amp at 150 v, and when it is on, the pressure in the liner drops from its base value, approximately 1×10^{-6} mm Hg, to values as low as 1 to 2×10^{-7} mm Hg. Pumping speed measurements with controlled gas flows indicate the arc pumping speed is 3.5×10^4 liters/sec for N_2 and 5×10^4 liters/sec for H_2. The beam current is still limited to approximately 50 ma of 600-kev H_2^+ ions and has been run as low as approximately 0.4 ma by running the source voltage low enough so as not to ignite the source discharge.

2.2 DENSITY MEASUREMENTS

2.2.1 Integral Method

The most direct method of determining the equilibrium number of particles in the machine, assuming all the losses are by charge exchange, is to collect the total number of neutrals produced by charge exchange after the beam has been turned off. This approach has been used by sampling the neutral flux with foil neutral detectors placed in several ports distributed along the axis and around the azimuth. The current to the detector is integrated electronically, and a typical result is shown in Fig. 2.1. A simple geometrical correction is made to account for the total neutral flux. In addition, a correction must be made for the foil transmission. The proper correction is rather difficult since the energy spectrum below 75 kev is not well known, and this is the region of greatest foil attenuation. However, using the best values of the ratio of neutrals to charged particles transmitted through nickel[1] and the known values of energy loss, the estimate for typical spectra is that about one-half of the neutrals striking the foil area are measured. Figure 2.2 shows the transmission as a function of energy.

From the integral shown in Fig. 2.1 we find that the number of particles which decay by charge exchange is approximately 8×10^{14}. As will be discussed below, the approximate mean plasma volume is about 100 liters, yielding a mean density of 8×10^9 particles/cm^3. It may be pointed out that this really represents a lower bound to the density since any particles lost by other means

[1] C. F. Barnett, W. F. Gauster, and J. A. Ray, *Atomic and Molecular Collision Cross Sections of Interest in Controlled Thermonuclear Research*, ORNL-3113 (May 10, 1961).

UNCLASSIFIED
PHOTO 65000A

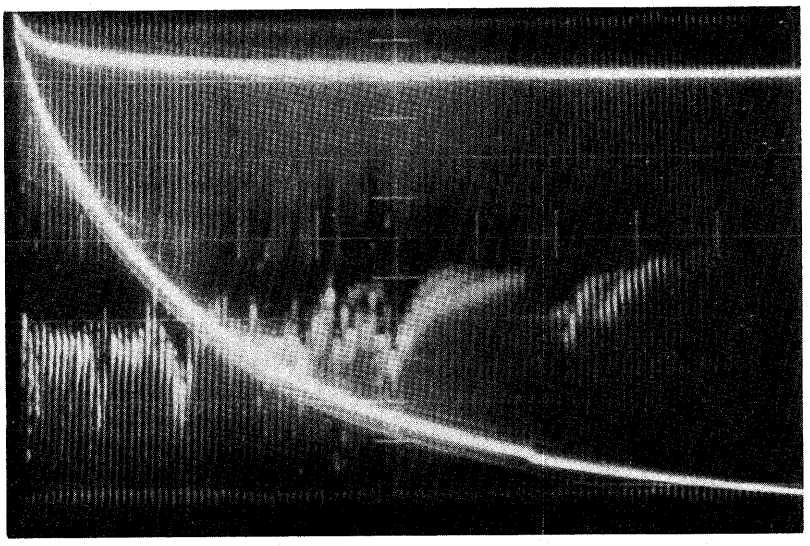

FAST NEUTRAL PARTICLE
INTEGRALS R4P8 AND
R1, 2, 4, 6, 7, P8

FREQUENCY SPECTRUM
18.0 – 18.5 Mc 0.1 sec/cm
4/10/64 – P25

Fig. 2.1. RF Spectrum and Foil Neutral Detector Integrals vs Time. Sweep speed 0.1 sec/cm. Upper trace, integral from ring position 8 with 3.3×10^{-10} coulomb/cm. Lower trace, integral of the sum of five detectors along the machine axis with 10^{-9} coulomb/cm. Radio-frequency has same frequency spread as Fig. 2.3.

contribute to the density but not to the charge-exchange flux. Also, the errors at the very low energy are likely to result in an underestimate in the density but cannot result in a significant overestimate.

2.2.2 Density Measurements Based on $I_x\bar{\tau}_x$

It was pointed out in the previous semiannual report[2] that a measurement of the energy spectrum of the neutral flux yields sufficient information to determine the mean lifetime for charge exchange provided the density and composition of charge-exchange centers are known. The energy analyzer which is used was described previously.[2] It consists of a silicon barrier detector collimated by means of a combination of a 5- to 10-μ slit and a 0.003-in. pinhole in a gold foil. The collimation is designed to sample all the particles emitted in a fan $0.2° \times 40°$.

A typical spectrum which was obtained by sweeping the energy analyzer so as to sample all plasma particles is shown in Fig. 2.3. Also shown in Fig. 2.3 is the spectrum of contained particles obtained by correcting for the charge-exchange rate as a function of energy (proportional to $1/\sigma_x v$). The energies observed are considerably higher than expected. In fact, the cross sections for charge exchange have not been measured for proton energies above 1 Mev. The values of charge exchange in nitrogen are used for lack of accurate gas composition measurements. The pressure is higher than is expected from the measured pumping speed of H_2 and the quantity of gas in the input beam, and most of the heavier gas constituents have cross sections not too different from nitrogen at these energies. The extrapolation to higher energies is done using the best fit to the data at lower energies. The result of careful fitting to the data of Barnett[1] is shown in Fig. 2.4; the analytic function used is

$$\sigma = \frac{8.64 \times 10^{-10}}{\sqrt{E}\,(E^3 + 6.46 \times 10^5)},$$

where E is the energy in electron volts. Unfortunately, theories for charge exchange of protons are in such poor state as to yield very little assistance in the extrapolation except in the case of charge exchange in H_2, and even here questions related to the effect of the molecular

[2]P. R. Bell *et al.*, *Thermonuclear Div. Semiann. Progr. Rept. Oct. 31, 1963*, ORNL-3564, p. 16.

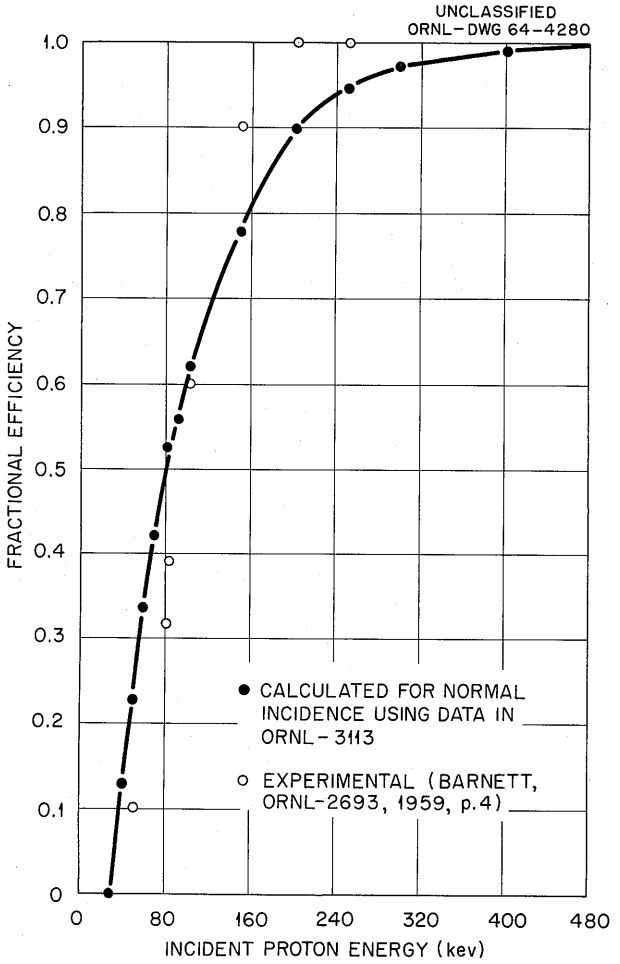

Fig. 2.2. The Efficiency of 10-μ in. Nickel Foil Neutral Particle Detectors as a Function of Energy.

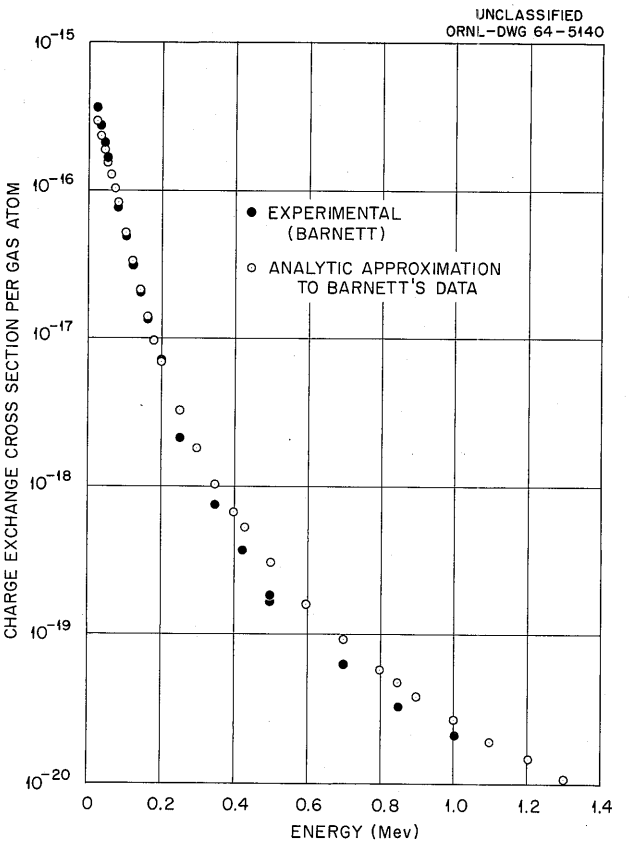

Fig. 2.4. Charge-Exchange Cross Section vs Energy for Protons in N_2. The solid circles represent experimental data of Barnett.[1] The open circles show points on the analytic fit $\sigma = 8.64 \times 10^{-10} [\sqrt{E}\ (E^3 + 6.46 \times 10^5)]^{-1}$.

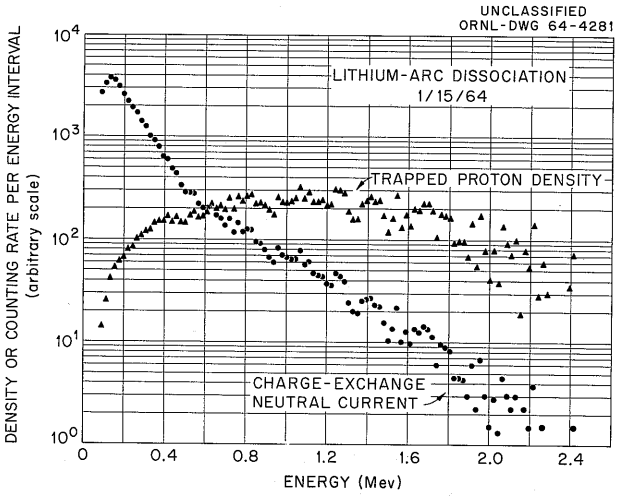

Fig. 2.3. The Spectrum of Charge-Exchange Neutral Particles from the DCX-2 Plasma and the Corresponding Energy Distribution of the Trapped Plasma.

state have been raised in the literature.[3] The mean value of $\bar{\tau}_x$ from the spectrum in Fig. 2.3 is 0.15 sec, using the pressure as measured on the ion gage as a measure of the charge-exchange-center density. With this value of $\bar{\tau}_x$ one obtains a density of 2×10^{11} particles/cm^3 over the same mean volume as used in the integral measurement. The charge-exchange neutral flux was corrected for geometry and foil efficiency in the same way as in the integral measurement. This estimate of density is probably too high because it is clear from the radial scan of the energy analyzer that there is an increased density of charge-exchange centers near the axis (see below).

2.2.3 Diamagnetic Measurements

Several independent measurements have been made in which the effects have been associated with the diamagnetism of the plasma. The most direct was a measurement made with two Hall probes. The probes were placed so that one was inside the liner and the other outside. If the time constant for the field penetration through the liner is sufficiently long, then, upon beam turnoff, the difference between the Hall probe signals is a measure of the flux displaced by the diamagnetism of the plasma, and for a long plasma

$$\Delta B_{\text{diamag}} = \Delta B_{\text{obs}} \cdot \frac{A_{\text{liner}}}{A_{\text{plasma}}} ,$$

where A_{liner} and A_{plasma} are the cross sectional areas of the liner and the plasma. Unfortunately, the time constant of the plasma is somewhat longer than the time constant of the liner. The value obtained has not been corrected for the leakage, and the result (1.5×10^9 ions/cm^3 for 600 kev average energy) is too low. Better results are expected for the next report period. A coil placed in the liner with a current having a proper rise and fall time will be used to provide the proper normalization.

Two other effects which have tentatively been ascribed to diamagnetism will be discussed more fully in following sections. These are a shift in frequency of the fundamental of the proton cyclotron frequency, and a change of the pitch angle of the injected beam. They both imply a density of about 8×10^{10} ions/cm^3 and a β of 0.016 at a mean energy of 700 kev.

[3]T. F. Tuan and E. Gerjuoy, *Phys. Rev.* **117**, 756 (1960).

2.3 PLASMA DISTRIBUTION

The method reported in the last semiannual report[2] which was worked out to determine radial density distribution using information from the scanning neutral-particle spectrometer cannot be applied at the higher densities obtained using a lithium arc. The method depended on the assumption that the distribution of charge-exchange centers did not vary throughout the plasma except for a localized high-density region at the position of the arc. There are at least two reasons to believe that the distribution of charge-exchange centers is no longer uniform but rather is much greater at the axis than at the edge of the plasma. Neutral-particle spectrometers in different port locations receive dissociation neutrals from the molecular ion beam resulting from dissociation at different depths in the plasma (Fig. 2.5). The results of scans at two port positions are shown in Fig. 2.6. It may be seen that the dissociation current reaching the detector at port position 6-3 is much greater in absolute quantity than that at port position 4-4. Figure 2.1 in ORNL-3472 gives a key to port locations; position 6-3 means ring 6, position 3, etc. When these scans are corrected for geometry factor and for the attenuation of the beam between locations 4 and 6, the dissociation rate at *a* in Fig. 2.5 is found to be 7.2 times the

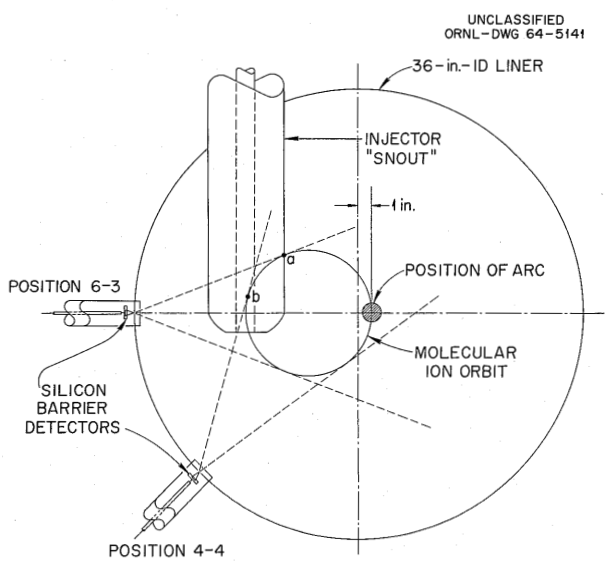

Fig. 2.5. A Transverse Section of DCX-2 Showing the Location of Energy-Sensitive Detectors.

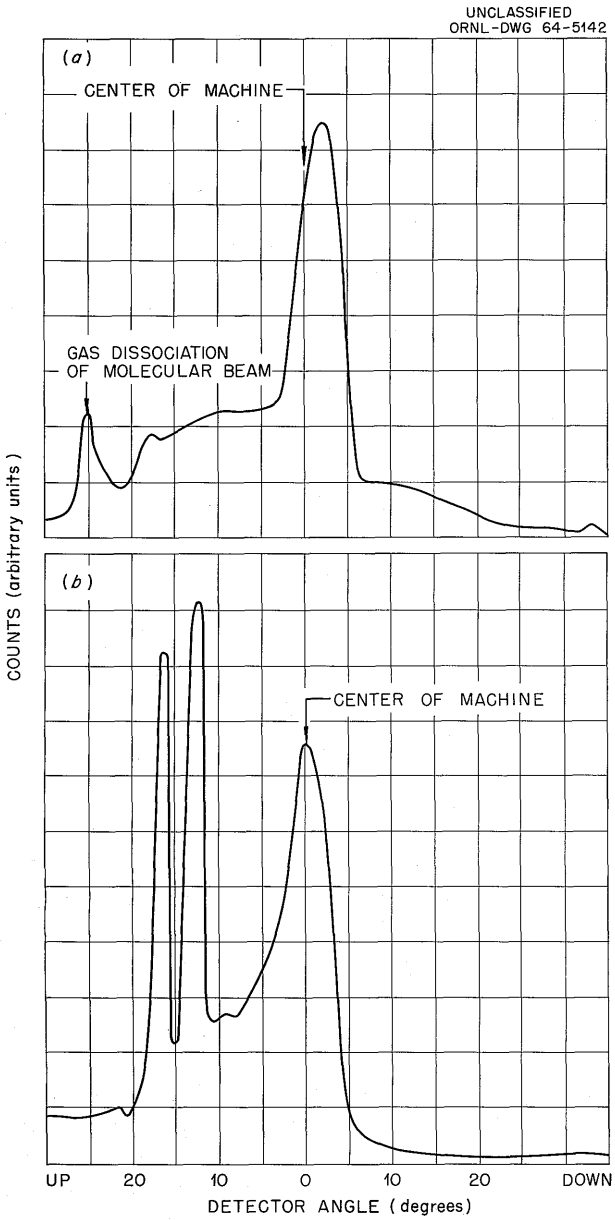

Fig. 2.6. The Angular Distribution of Charge-Exchange Current as Seen (*a*) from Port Position 4-4 and (*b*) from Port Position 6-3. See Fig. 2.5 for position locations. The detector labeled 4-4 is in the midplane. The detector labeled 6-3 is 27 in. from the midplane. The peaks are the response of the energy-sensitive detectors to the background-produced dissociation of the initial and reflected molecular ion beams. An *X-Y* recorder was used with vertical input from a count-rate meter and horizontal input from a voltage proportional to the angular position of the detector.

rate at *b*. It probably is safe to assume that there is also a large difference between the rates of charge exchange at these two positions.

Scans of the type shown in Fig. 2.7 give a further indication that the distribution of charge-exchange centers is not uniform with respect to radius. This figure shows a number of scans through a plasma with lithium arc dissociation made with a single-channel analyzer selecting energies in relatively narrow intervals. In order to reduce the effect of arc dissociation and charge exchange relative to the background, the pressure was raised by means of a controlled hydrogen leak from a gage reading of 4×10^{-7} mm Hg to 2×10^{-6} mm Hg. It can be shown that if the background gas density is independent of position, then for a single energy the distribution of current from charge exchange in the background gas should be exactly symmetric about a line having an impact parameter one Larmor radius from the axis. In these actual scans it is not possible to obtain a symmetric distribution with any reasonable subtraction of the localized contribution from the arc.

Because of a lack of information on the distribution of charge-exchange centers, it is possible to draw only qualitative conclusions about the distribution of the plasma. The tendency of the background density to increase toward the axis means that the response of the spectrometer to charge exchange from the hot plasma near the axis is relatively greater, and the currents at large angles must be weighted more heavily accordingly. The distributions do show that hot plasma exists out to an angle of 32°, corresponding to an impact parameter of about 13 in. with respect to the axis. The tendency reported previously[2] for the high-energy particles to be found more frequently circulating symmetrically about the axis apparently is not present under these circumstances.

The energetic plasma density varies in the axial direction with the exact shape of the magnetic field but is approximately uniform from port positions 2 to 6 (27 in. either side of the midplane) when the field is set for maximum plasma density. Foil neutral detectors at the same θ positions indicate currents which do not vary by more than a factor of 2 along the axis.

The maximum density of the plasma has been found to be very sensitively dependent on the shape of the magnetic field. This characteristic

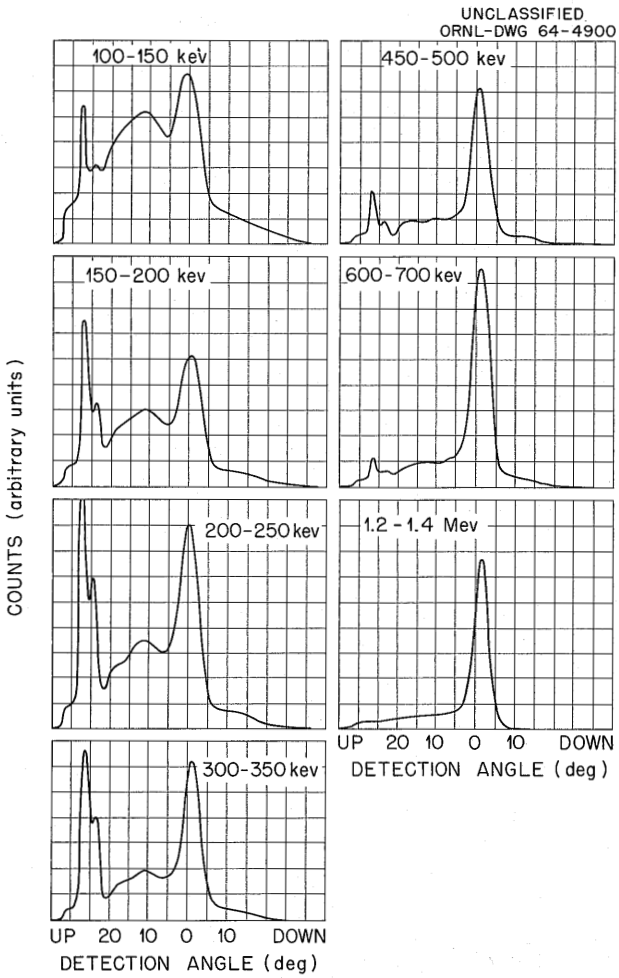

Fig. 2.7. Energy-Resolved Vertical Scans at Port Position 4-4.

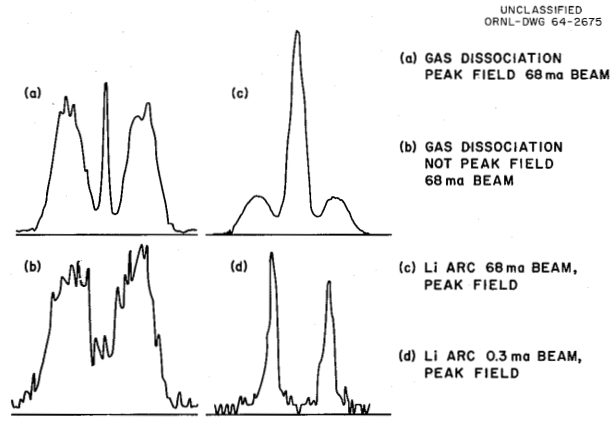

Fig. 2.8. The Horizontal Angular Distribution of Charge-Exchange Neutrals as Seen at Port Position 4-4 Under Various Conditions.

was discovered when an integrating amplifier was used with one of the foil neutral detectors. It became easy to optimize the machine parameters for maximum density using this signal. It was found that at the optimum field adjustment a feature which previously had been noticed in the shape of horizontal scans using the energy-sensitive detector became quite prominent. This effect is shown in Fig. 2.8. The central peak which was found occasionally in the angular distribution is the dominant feature of the distribution at the highest density. When the injected current was decreased to 0.4 ma, this central peak disappeared. There remained only the two side lobes at $\sim \pm 4°$, which are identified with the angles of the initial and reflected molecular ion beam. Protons coming from dissociation in the beam retain the same approximate pitch angle at low plasma density until they are lost. The side lobes move outward as the plasma density is increased. The amount of the shift corresponds to the same diamagnetic depression of the field as was found by the frequency shift of the proton cyclotron frequency.

The spectrum of the charge-exchange particles coming from this peak, that is, straight ahead, is approximately the same as that in the wings. The mechanism for population of this class of particles with small z momentum is not understood, but it is clear that the particles are held between the slight field maxima which occur just inboard of the field dip and have, therefore, no precessional loss to the snout.

The current of energetic neutrals from dissociation of the molecular ion beam in the arc was measured by means of a foil neutral detector which could be scanned transversely near the vacuum liner wall above the plasma. This detector measures the total neutral current striking it. It was mounted on the end of a short horizontal arm and could be swung to about 7 in. either side of the longitudinal midplane. A typical result is shown in Fig. 2.9. The distribution appears to be made up of a broad component produced by background dissociation and two peaks corresponding to arc dissociation of the incident and reflected molecular ion beams. It was not possible to get an absolute estimate of the total dissociation current from this scan because the foils were severely damaged by the high energy density. Secondary-emission detectors are being made for use where the energy density is too great for foil detectors.

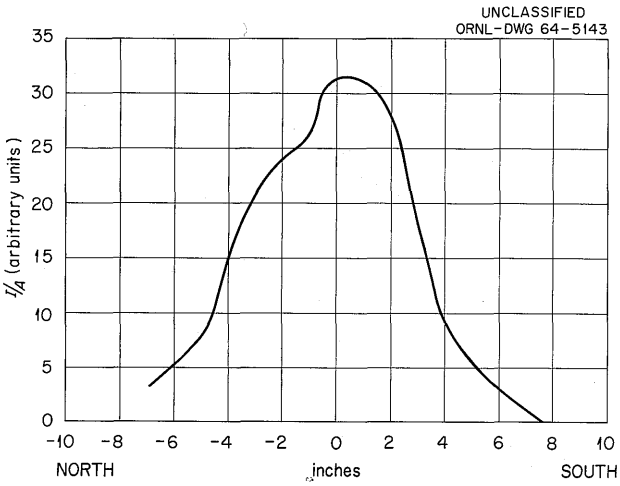

Fig. 2.9. Spatial Distribution of the Dissociation Neutrals as Seen from Port Position 4-1. The abscissa is the distance in inches either side of the vertical midplane at a position near the top of the central vacuum chamber.

2.4 SECONDARY PLASMA MEASUREMENTS

A plane, multi-gridded probe was inserted radially at the west end of the machine (opposite the injection point) outside of the mirror to measure the electron and ion currents streaming out along flux lines which passed about 3 to 7 in. from the axis in the hot plasma. The intermediate grid of this probe was biased either to suppress all electron current or all ion current, and the collector was varied sinusoidally at about 200-cps rate over a range of ±200 v. Figure 2.10 shows the results of measurements with electrons suppressed and with ions suppressed. As illustrated, the ion current begins to fall at about zero potential. When this fall of current is analyzed, it corresponds roughly to a Maxwellian distribution with a temperature of ~150 ev. The fact that the current begins to fall at zero potential is an indication of a plasma potential very near zero – certainly less than 30 ev. When the electron repulsion curve is analyzed, the electron distribution also appears to be Maxwellian and corresponds to a temperature of

UNCLASSIFIED
PHOTO 64999A

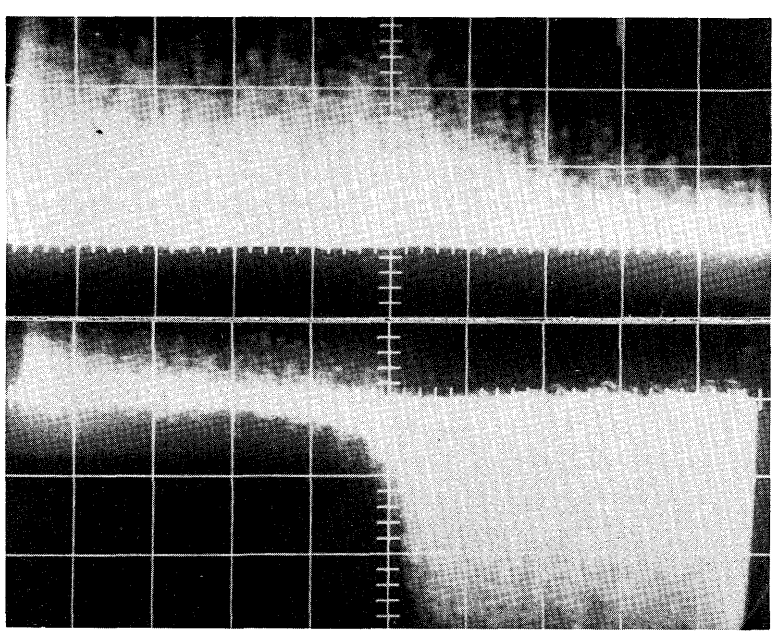

ION CURRENT 0.2 ma/cm
$G_2 = -250$v, 6.5 in. FROM AXIS, RING 9

ELECTRON CURRENT 0.1 ma/cm
$G_2 = +250$v, 4/10/64 P7, 4
±200v SWEEP

Fig. 2.10. The Response of a Multi-Gridded Probe to the Cold Plasma Streaming Through the Mirrors Along a Flux Line Passing About 3 in. from the Axis in the Hot Plasma Region. The upper signal is the ion current at 0.2 ma per major division with the intermediate grid biased to −250 v. The lower trace is the electron current at 0.1 ma per major division with the intermediate grid biased to +250 v. The horizontal sweep is ±200 v for both pictures.

about 33 ev. The breaks in the two curves correspond to those found in very cold plasma. They do not occur at zero potential because of faults in the probe.

The ion saturation current due to the cold plasma has been measured on a negatively biased plate which was scanned radially at the end of the cylindrical section of the central plasma region. This position is well inside the mirror maximum but outside the region in which hot plasma is found. The result of one such scan is shown in Fig. 2.11. Mechanical limitations prevented a scan to the axis. The maximum current recorded corresponds to a density of $3.7 \times 10^9/\text{cm}^{-3}$ of 150-ev ions.

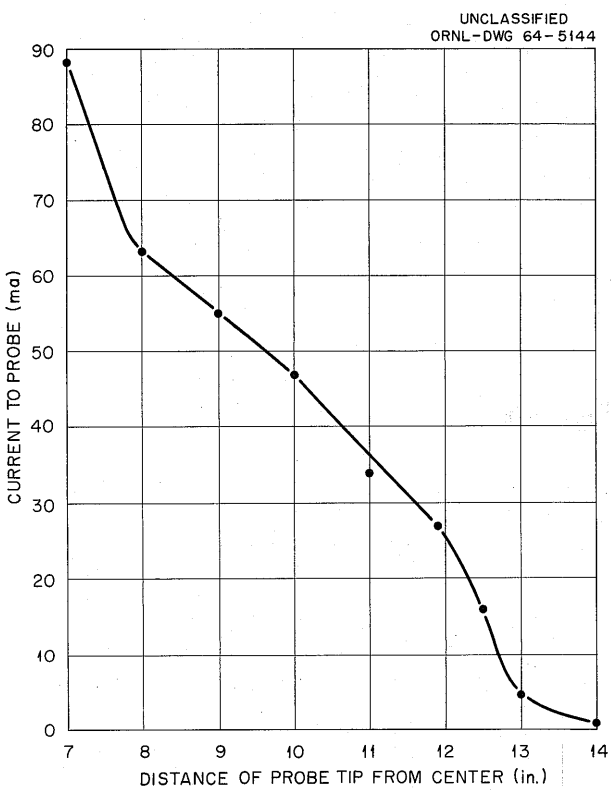

Fig. 2.11. Ion Saturation Current to a Biased Plate as a Function of Radius. The plate was scanned radially at the end of the central vacuum container.

2.5 PARTICLE LOSSES

At low densities with gas breakup it was found that within a factor of 2 all the particles produced by dissociation were lost to the wall as neutrals from charge exchange. Because the lithium arc dissociates a sizable fraction of the total beam, it is possible to measure the dissociation directly by means of the energy-sensitive detectors. The detector in position 4-4 resolves the peaks due to gas dissociation from the incident and reflected molecular ion beams. It is found that the area under the reflected peak is about one-third that of the incident peak. When these differences are extrapolated to the input position, it is found that approximately eight-ninths of the beam is dissociated. At the same time, calorimetric measurements on the snout target show that 60% of the power of the injected beam is being returned to the snout.

Since

$$W_{ps} = W_s - (1 - \alpha)W_b$$

and

$$W_p = \alpha(1 - \delta)W_b ,$$

where

W_{ps} = plasma power returned to the snout,

W_p = plasma power input,

W_s = total power returned to the snout (typically $0.6W_b$),

W_b = beam power input,

α = fraction of the beam dissociated (typically 8/9), and

δ = fraction of neutral particles produced in the dissociation process,

the fraction of the power lost from the plasma by protons striking the snout is

$$\frac{W_{ps}}{W_p} = \frac{0.6 - 0.111}{0.889 \times 0.83} = 0.66 .$$

The value of 0.17 chosen for δ is that appropriate for N_2 gas background.

The power balance equation for the plasma is

$$W_p = W_{ps} + W_{pw} + W_{pa} ,$$

where w refers to wall loss and a to arc loss. Substituting measurable quantities yields

$$\alpha(1 - \delta)W_b = W_s - (1 - \alpha)W_b + W_{pw} + W_{pa} ,$$

and rearranging

$$W_{pw} + W_{pa} = (1 - \alpha\delta)W_b - W_s .$$

For typical values,

$$W_{pw} + W_{pa} = 0.25W_b \, .$$

At a particular time the total charge-exchange current inferred from the foil neutral detector signals was 5.4 ma. The mean energy of the escaping neutrals was not measured simultaneously but is typically about 250 kev. Then

$$W_{pw} = 250 \times 5.4 \times 10^{-3} = 1.35 \text{ kw}$$

and

$$W_b = 600 \times 30 \times 10^{-3} = 18 \text{ kw} \, ,$$

leaving as the power lost in the arc

$$W_{pa} = 0.25 \times 18 - 1.35 = 3.1 \text{ kw} \, .$$

At a fast ion density of 10^{10} the average rate of energy loss to the arc per ion is

$$\frac{dE}{dt} = \frac{W_{pa}}{1.6 \times 10^{-19} \times nV}$$

$$= \frac{3.1 \times 10^3}{1.6 \times 10^{-19} \times 10^{15}} = 1.9 \times 10^7 \text{ ev/sec} \, ,$$

where E is the proton energy in the plasma, n is the average hot-ion density, and V is the plasma volume.

If it is assumed that all of the particles are accounted for by

$$2\alpha(1 - \delta)I_b = I_s + I_w \, ,$$

where

I_b = current of molecular ions entering the machine,

I_s = proton current to the snout, and

I_w = proton current to the wall,

then since I_w can be measured, I_s can be determined. In the case considered

$$I_w = 0.18I_b$$

and

$$I_s = (1.47 - 0.18)I_b = 1.29I_b \, .$$

(The total influx of atomic particles is $2I_b$.) Then,

$$\bar{E}_s = \frac{W_s}{I_s} = \frac{0.6I_bE_b}{1.29I_b} = 280 \text{ kev}$$

for 600-kev molecular ion injection. Here $\bar{E}_s$ is the average energy of particles returning to the snout. Therefore, the percentage particle loss to the snout is equal to $300/280 \times W_{ps}/W_p$, and about 70% of the trapped particles are lost to the snout. Charge exchange accounts for the remaining 30%.

2.6 RADIO-FREQUENCY EMISSIONS

The increase of plasma density obtained with optimum adjustment of the magnetic field shape has further modified the radio-frequency spectrum from that reported in the previous semiannual report.[2] As shown in Fig. 2.12 the spectrum of

UNCLASSIFIED
PHOTO 64742

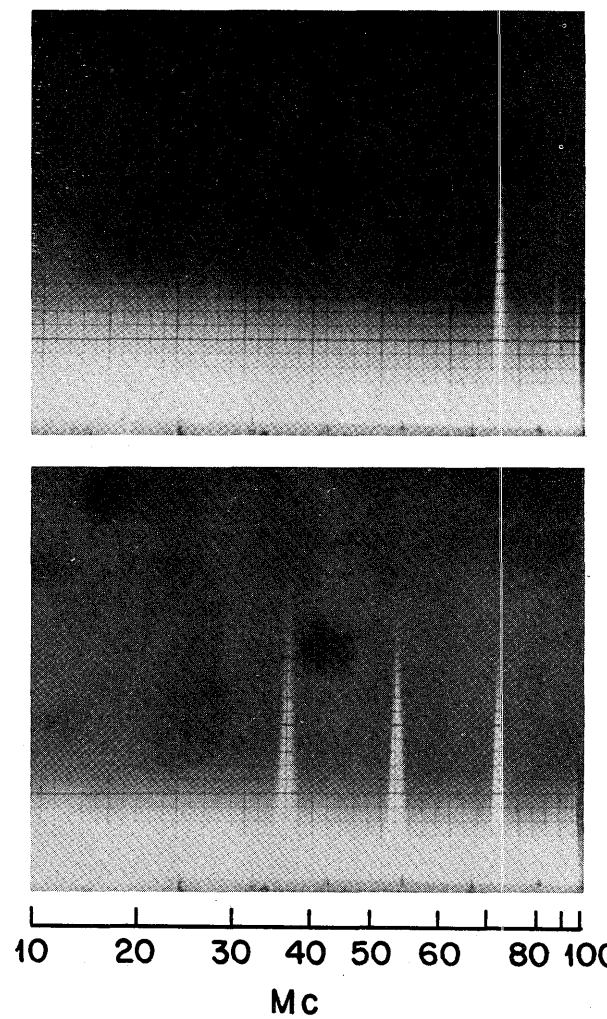

Fig. 2.12. DCX-2 RF Spectra with 0.3-ma H_2^+ Beam (Upper) and 40-ma Beam (Lower). Lithium arc current 30 amp and magnetic field tuned to optimum integral.

UNCLASSIFIED
PHOTO 64740A

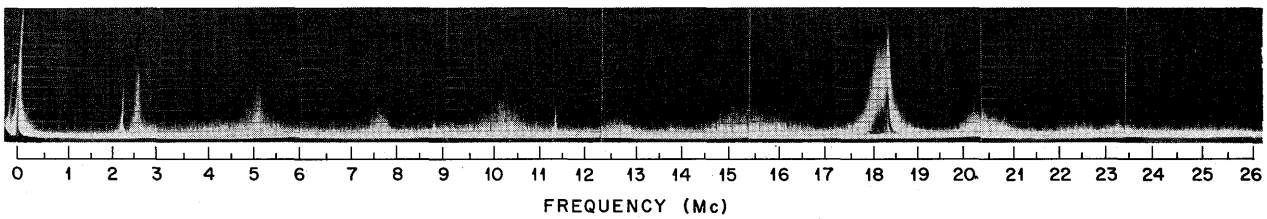

Fig. 2.13. DCX-2 RF Spectrum, Lithium Arc 18 amp, H_2^+ Beam 30 ma, Pressure 4×10^{-7} mm Hg, Optimum Field.

emission is principally the second, third, and fourth proton cyclotron harmonics and a considerable amount of white noise. The increased plasma at large radius in the machine has forced a withdrawal of the radial electric rf probes from their former position at 14 in. from the machine axis to 18 in. (flush with the liner wall) to prevent damage by excessive heating. This position at larger radius may account for the relatively increased white noise. When the H_2^+ injected beam is reduced to a very low value (0.4 ma), only the white noise and the fourth harmonic of the proton cyclotron frequency remain. Although not visible in the spectra of Fig. 2.12 because of the wide band width of this spectrometer, there are very weak emissions at lower frequencies. Figure 2.13 shows the spectrum from 0 to 26 Mc. The line at zero frequency is an artifact of the spectrometer, and the sharper lines at 2.2 and 11.4 Mc are also false responses at spectrometer oscillator harmonics (birdies). The remaining lines are the proton cyclotron fundamental and lines corresponding to $^7Li^+$, $^7Li^{2+}$, and $^7Li^{3+}$ and their harmonics. Very weak lines corresponding to the ^6Li ions can be seen on close inspection, but these are hard to see since the lithium used for the arc was depleted in ^6Li. The H_2^+ line at 9.1 Mc is barely detectable, and since it is coincident with the $^6Li^{3+}$ line, the response may be largely due to the latter. The lithium ion cyclotron lines are excited by the action of the proton plasma of DCX-2, since they are completely absent when the arc is run without any H_2^+ beam injected. The H^+ line has a strange shape which is due to the presence of a broad line while the beam is on and a much narrower line at a different and variable frequency present after the beam has been turned off. Some frequency spectra near this proton cyclotron fundamental are shown in Figs. 2.1 and 2.14. Here frequency is displayed vertically with time horizontally, and the brightness corresponds to intensity of rf. Each vertical stripe corresponds to a new measurement of the spectrum. The H_2^+

UNCLASSIFIED
PHOTO 64743

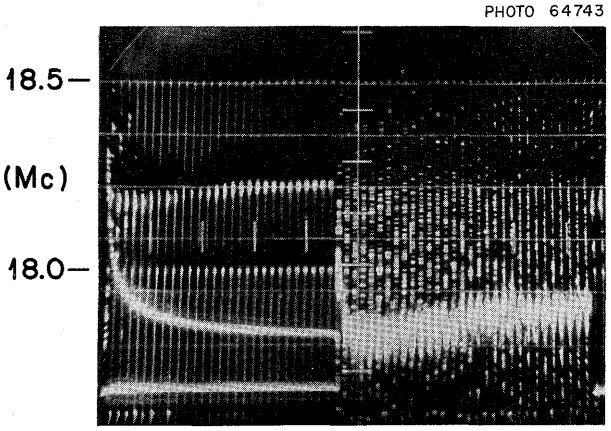

Fig. 2.14. RF Spectrum, Foil Neutral Detector Signal Integral, and Dissociation Current vs Time. The trace beginning at the top line at the left and sweeping down to the lower part of the figure at the middle and disappearing there is the integral of the foil neutral detector current at position 4-8 with a scale of 10^{-10} coulomb/cm increasing downward. The trace at the bottom, rising several centimeters and oscillating slightly while the beam is on, is the dissociation current from a foil detector at position 4-1. The pattern of dots is the rf spectrum. The horizontal rows near the center and upper edge are the frequency markers at 18.0 and 18.5 Mc respectively. The time scale is 0.1 sec/cm, and the machine conditions are: H_2^+ beam 38 ma, lithium arc 50 amp. The magnetic field is tuned for maximum integral.

beam has just been turned off at the left edge of Fig. 2.14 and is turned on again a little less than 0.5 sec later at the center of the figure. The horizontal rows of dots near the center of the figure and at the upper edge are fixed frequency markers at 18.0 and 18.5 Mc respectively. The broad distribution of dots on the right side of the figure is the broad line produced while the H_2^+ beam is on. After beam turnoff at the left edge of the figure, two relatively narrow lines can be seen – one is rather constant and merges with the other line at about 0.1 sec. The second line begins at about 18.07 Mc and changes frequency with time, approaching 18.22 Mc asymptotically. If this second line is interpreted as the proton cyclotron line perturbed by the diamagnetic reduction of the magnetic field by the presence of the plasma, a value for the plasma density can be obtained.

Equating the pressure inside and outside the plasma, and since the cyclotron frequency is proportional to field,

$$\frac{2\,\Delta B}{B_o} = \frac{2\,\Delta f}{f} \approx \frac{nkt}{B_o^{\,2}/8\pi} = \beta\,.$$

Assuming an average plasma ion energy of 700 kev,

$$\frac{2(0.15)}{18.22} = 0.016 \approx \frac{n^+(7\times 10^5)\,1.6\times 10^{-12}}{(1.2\times 10^4)^2/8\pi}\,,$$

$$n^+ = 8\times 10^{10}\ \text{ions/cm}^3\,.$$

This value of ion density is comparable with that obtained above from the pitch angle shift.

It is possible, of course, that the frequency shift is complicated by plasma wave effects to such an extent that it is not proper to interpret it as a simple diamagnetic shift. The frequency pattern is certainly complicated under some conditions. Figure 2.1, for example, shows one turnoff obtained during a period of maximum foil neutral detector current integral. Here the region of relatively constant frequency is extended nearly to 0.5 sec before a frequency shift is seen, and a second interval of shift is also seen. This might be supposed to be radiations emitted from different sections of the plasma but may well be some more complex plasma behavior.

The sporadic appearance of hot ions at large radii in the machine that was previously reported as a sort of vaguely flutelike behavior still occurs but is still rather weak and does not seem to account for any appreciable amounts of plasma. Figure 2.15 shows an example of these pulses. The upper trace is that from a radial electric probe at the liner wall with 18-Mc and higher frequencies filtered out. The amplitude of these pulses is very small; the vertical scale represents 10^{-5} amp/cm with a probe area of several square centimeters. The lower trace is a foil neutral detector signal with a sensitivity of 10^{-7} amp/cm. The traces cover the first millisecond after beam turnon.

UNCLASSIFIED
PHOTO 65001A

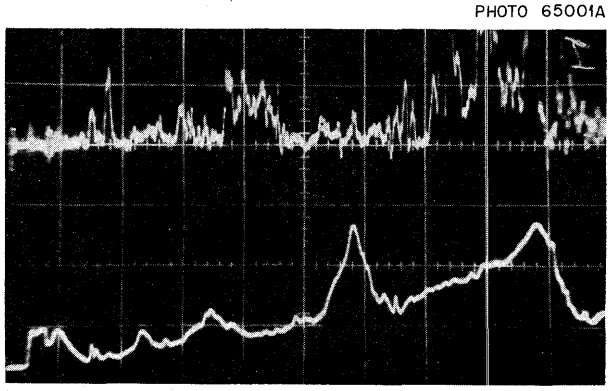

Fig. 2.15. Upper Trace: Radial Probe at Liner Wall 10^{-5} amp/cm at Ring 5, Position 3; Lower Trace: Foil Neutral Detector Signal 10^{-7} amp/cm at Ring 4, Position 8. Sweep speed 100 μsec/cm, 4/10/64, G-10.

3. Electron-Cyclotron Heating

3.1 ELECTRON-CYCLOTRON HEATING EXPERIMENTS IN THE EPA FACILITY

W. B. Ard
M. C. Becker[1]
R. A. Dandl[1]
H. O. Eason
A. C. England
H. C. Hoy
R. L. Knight
N. H. Lazar
R. L. Livesey
O. D. Matlock
M. W. McGuffin

3.1.1 Introduction

The electron-cyclotron plasma (ECP) in the EPA Facility, first described in the last semiannual report (ORNL-3564),[2] has been studied with an x-ray pinhole camera. The plasma volume and shape as determined by this technique are in good agreement with previous indirect measurements.

The EPA Facility has been under extensive modification for experiments involving an energetic neutral beam. The problems associated with the incorporation of the beam into this experiment are described in Sect. 3.1.3, while the construction and development of the beam are described elsewhere.[3]

3.1.2 Pinhole-Camera X-Ray Photographs

With use of an x-ray pinhole camera, described briefly in the last semiannual report, excellent x-ray photographs were taken of the electron-cyclotron plasma (ECP). The pinhole camera consisted of a thick lead box with a gold plug into which a 1/4-in.-diam pinhole was drilled. The pinhole was in the midplane of the magnetic mirror configuration, and the distance from the EPA axis to the pinhole divided by the distance from the pinhole to the film plane was approximately 8. This provided a measured ~5-cm resolving power at the axis of the machine. The x rays had to pass through two 0.009-in. aluminum windows, one on the cavity (to contain the microwaves) and one vacuum window.

In the last semiannual report,[2] Polaroid film was used to make qualitative observations of the plasma. To make detailed measurements, we changed to regular x-ray film. The photographs were taken in sets of four pictures with variable exposure times on Eastman Kodak type AA film. Manufacturer's recommendations were strictly followed in the development and fixing. Using the measured sensitometric properties of the film,[4] and the fact that the reciprocity law[5] is known to hold for x-ray film, the measured film density was converted to incident x-ray intensity (energy per unit time per unit area).

Figure 3.1 shows a contour plot of the measured relative intensity of x rays on a typical film. Superimposed on the plot is a scale on a plane passing through the axis of the EPA machine normal to the camera axis. From this picture the radius to the half-maximum contour appears to be ~23 cm and the total axial length (to the half-maximum points) is estimated to be ~30 cm. The axial extent cannot be measured because of interfering film exposure due to x rays emanating from the cavity wall where it "necks down" at the mirror throat. These dimensions give a plasma

[1]Instrumentation and Controls Division.

[2]W. B. Ard *et al.*, *Thermonuclear Div. Semiann. Progr. Rept. Oct. 31, 1963*, ORNL-3564, p. 28.

[3]Section 7.5 of this report by N. H. Lazar *et al.*

[4]*Radiography in Modern Industry, Supplement #2*, Eastman Kodak Company, X-Ray Division, 1959.

[5]The reciprocity law is an example of a general photochemical law that states that the same effect is produced for It = constant, where I is the intensity of radiation and t is the time of exposure.

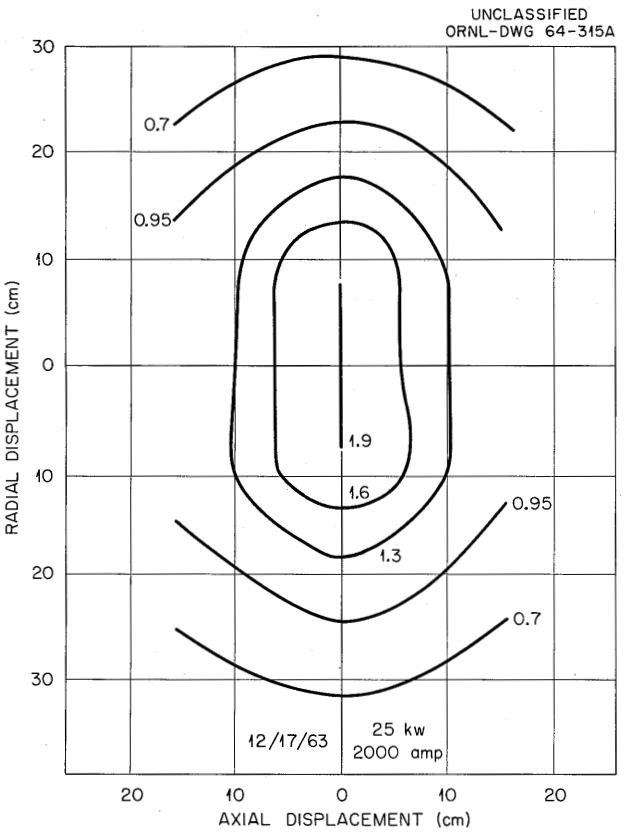

Fig. 3.1. Contour Plot of Relative Intensity from X-Ray Pinhole Camera Photograph.

volume of ~50 liters for a microwave power input of 25 kw and a magnetic field coil current of 2000 amp.

As explained in the last semiannual report,[6] the spectral intensity of bremsstrahlung radiation from the plasma is given by

$$I(E) = (\text{Const}) \frac{Z^2 n_+ n_-}{T^{1/2}} e^{-E/T} \text{ sec}^{-1} \text{ cm}^{-3} .$$

The intensity of x radiation in the 1/4-in.-diam area at the center of the film can be calculated from the solid angle, the volume of plasma visible to this area through the pinhole, the measured plasma density of $5 \times 10^{11}/\text{cm}^3$, and plasma "temperature" of ~120 kev. This intensity is proportional to $Z^2 n_+ n_- T^{1/2}$. Computing the absorption of the two 0.009-in. Al windows as a function of energy, the amount of energy per unit area per unit time per unit photon energy was calculated (in ergs cm^{-2} min^{-1} kev^{-1}). The time unit of 1 min was chosen as this is the time used in the measurement of Fig. 3.1. Using the measured spectral sensitivity (in ergs/cm^2 unit density) of a similar type of film[7] and dividing the spectral intensity by the spectral sensitivity, we arrived at a figure of merit which we called the "specific density" for this kind of film and spectral distribution. This specific density (density per kev) is plotted in Fig. 3.2 as a function of photon energy.

The total area under the curve in Fig. 3.2 is proportional to the film density, and if the spectral sensitivity of the film actually used were known, the area would be equal to the film density. The important point to be noted from the figure is that the highest specific density peaks are at photon energies just above the $K\alpha$ absorption edges of silver and bromine. Moreover, half the total area of the curve shown here is below 25 kev, that is, the film is most sensitive to low-energy photons. The spectral sensitivity has not been measured above 65 kev, so that the specific density is unknown in the region of interest near 100 kev. However, it is clear from the figure that most of the area of the curve is well below 100 kev. Thus, the film image is not representative of the higher-energy photons.

[6] *Thermonuclear Div. Semiann. Progr. Rept. Oct. 31, 1963,* ORNL-3564, Sect. 3.1.

[7] H. E. Seemann, *Rev. Sci. Instr.* **21**, 314 (1950).

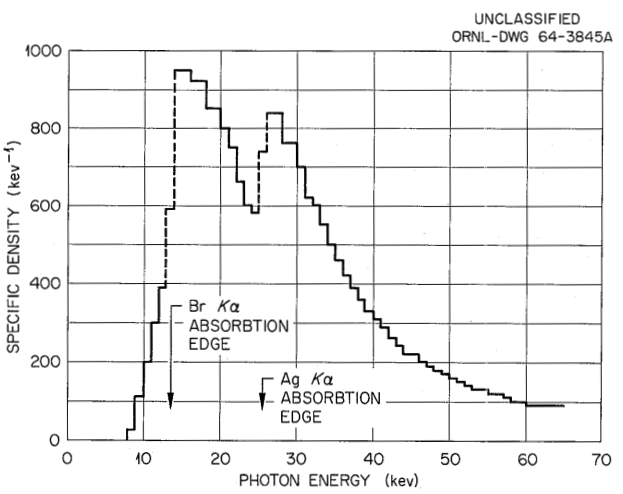

Fig. 3.2. Plot of "Specific Density" vs Photon Energy.

The observed x-ray intensity incident on the film has been transformed back into a radiance coefficient (energy per unit time, unit volume, and unit solid angle) in the plasma by an inversion procedure resembling the Abel inversion schemes used in certain optical problems.[8] The results have shown that while the plasma shape as determined by this technique is changed somewhat from the apparent film image shape, the radius determined by this technique is changed by less than 20% from that measured from the film, that is, the picture on the film can be used to determine the approximate dimensions, and hence an inversion procedure is not required to determine the plasma volume in this case. Inasmuch as the x-ray photographs may not give a representative picture of the 120-kev plasma, for the reasons mentioned above, it is felt that this technique has reached the logical limit of its precision. Also, since the calculated radiance coefficient is proportional to $Z^2 n_+ n_- T^{1/2}$, it is not clear that the radiance coefficient is truly representative of the radial electron density distribution.

Attempts were made to "harden" the spectrum of photons arriving at the film by using absorbers between the plasma and film plane. Unfortunately, while this technique is successful in many other applications, there is no place for the absorbers in this experiment. The absorber cannot be used next to the film because not only does it absorb low-energy photons, but it also produces low-energy photoelectrons, which further blacken the film in a way that cannot be calculated. Attempts were made to put the absorbers near the pinhole; however, due to the very large flux of photons incident on this pinhole, the production of fluorescence radiation in the absorber was enough to cause enough film blackening to mask the effects of the hardened spectrum. The optimum place to put the absorber is near the source of x rays; however, as this requires the absorber to be in the microwave cavity, it was not practical in this case.

The radiance coefficient radius determined by this technique is in approximate agreement with the plasma radius measured by other techniques, for example, the Hall probe and $d\phi/dt$ measurements. The plasma volume measured here is also in approximate agreement with that calculated from a correlation of the bremsstrahlung measurement and the $d\phi/dt$ measurement.

[8]One of many references is: K. Bockasten, *J. Opt. Sci. Am.* **51**, 943 (1961).

3.1.3 EPA Cavity – Neutral Injection Entry

Injection of a beam of energetic neutrals into the EPA plasma required that a beam tube of 3-in. minimum diameter be connected directly to an opening of up to 3-in. diameter in the microwave liner (cavity). Leakage of 10.6 Gc microwave power through an opening of this size was of serious concern in several major areas. Among these were: (1) the potential microwave radiation hazard to personnel, (2) the possibility of adverse effects on the performance of the neutral beam source, and (3) the possibility of a serious decrease in the microwave efficiency of the system due to loss of a significant fraction of the microwave input power. These considerations prompted experiments to determine the extent of the problem and the effectiveness of corrective measures.

A high-power microwave termination which mated with the beam tube was fabricated and tested. The termination consisted of a conical glass "spear" mounted in a tapered copper cylinder as shown in Fig. 3.3. The entire assembly was vacuum-tight. Water was circulated in the spear to absorb the microwave leakage energy, and power was measured calorimetrically. Metal plates having holes of various sizes were placed between the termination and the cavity wall to determine leakage power as a function of the size of the opening. Typical results are given in Table 3.1 for both optimum and high-pressure gas feed conditions.

Table 3.1 Results for Optimum and High-Pressure Gas Feed Conditions

Orifice Diameter (in.)	Gas Feed	Microwave Leakage Power[a] (w)
3	Optimum	750
	High-pressure	1200
2	Optimum	445
	High-pressure	940
1½	Optimum	170
	High-pressure	350

[a]Input power to cavity = 40 kw under all conditions.

UNCLASSIFIED
ORNL-DWG 64-3870A

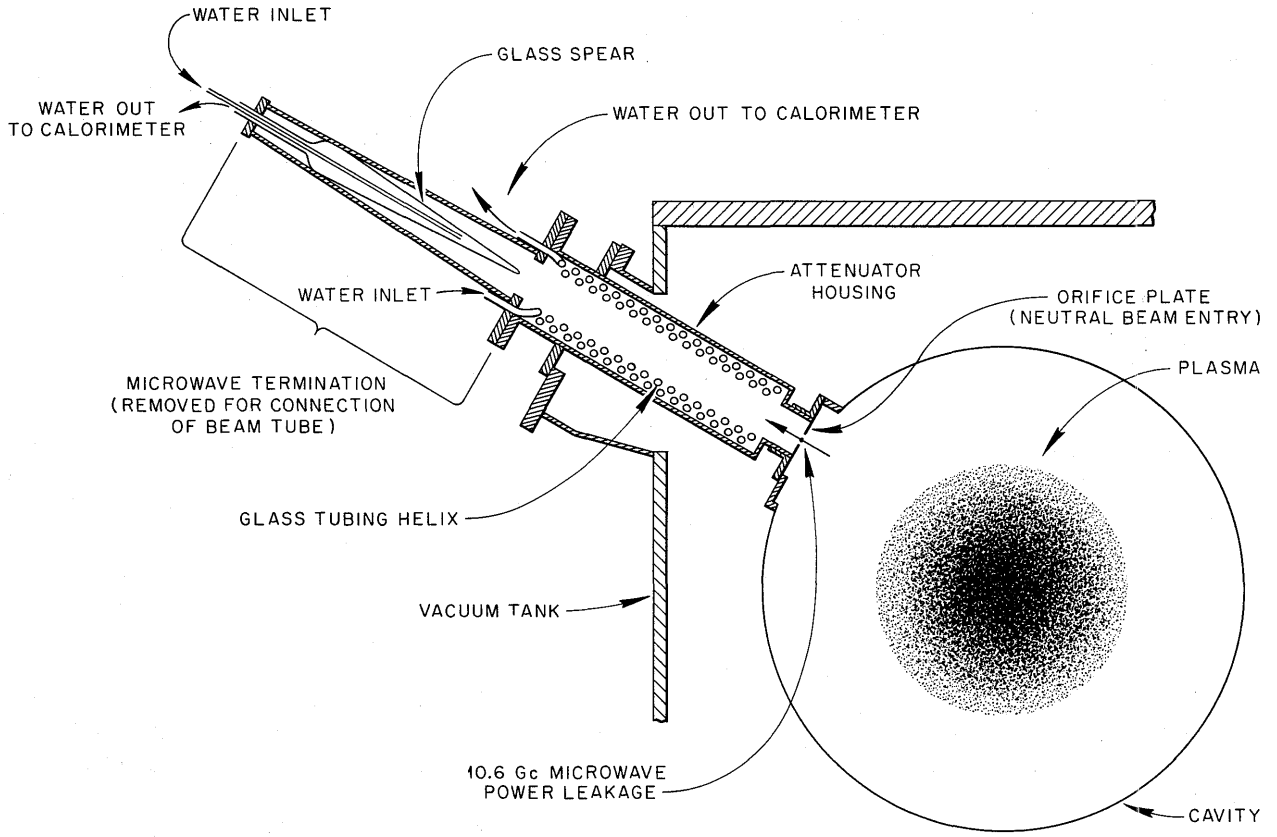

Fig. 3.3. Apparatus for Measuring and Attenuating Microwave Leakage in the Neutral Beam Entry Tube.

These results were favorable in that the maximum leakage power measured under any gas feed condition represented less than 5% of the input power with a 3-in.-diam opening in the cavity wall. Variation of leakage power with gas feed rate at a given power input level indicates a variation in microwave absorption efficiency of the plasma. "Optimum" gas feed corresponds to maximum microwave noise radiation from the plasma at 1.25-cm wavelength.[6] This is also the condition at which microwave leakage power is minimum. Leakage under "optimum" feed conditions is roughly proportional to the area of the aperture and to the input power.

Once the magnitude of the leakage power became known, an attenuator was fabricated for insertion in the beam entry tube. This attenuator is also shown in Fig. 3.3. It consists of a two-layer close-wound helix of Pyrex tubing through which water is circulated. The helix bore is 3 in. and the length is 24 in. Power absorbed by the attenuator is also measured calorimetrically. The helix is mounted inside a 6-in.-diam length of metal tubing and is located near the cavity wall. The attenuation of this unit at 10.6 Gc is approximately 25 db as measured with the arrangement shown in Fig. 3.3. This is sufficient to reduce the microwave leakage into the neutral beam source to approximately 5 w under the worst conditions yet encountered. Water flow in the helix attenuator is interlocked with the vacuum system for safety. The attenuator has been in use for several months and no difficulties have been encountered through its use.

3.2 ELECTRON-CYCLOTRON HEATING EXPERIMENTS IN THE PHYSICS TEST FACILITY (PTF)

W. B. Ard
M. C. Becker[9]
R. A. Dandl[9]
H. O. Eason
A. C. England
G. M. Haas
R. L. Livesey
M. W. McGuffin

3.2.1 Introduction

The plasma density has been studied with the aid of a new microwave interferometer. Also, further studies have been made of the plasma by means of a new improved x-ray pinhole camera, similar to the one used with the EPA. Some preliminary investigations of the neutral hydrogen atoms leaving the cavity have been made in order to determine where the ionization is taking place.

3.2.2 Microwave Interferometer

A new 4-mm microwave interferometer has been constructed in order to investigate the discrepancy between previous interferometer measurements[10,11] and the mass of other data on the Physics Test Facility. The present system is shown schematically in Fig. 3.4. It differs from the previous system in two respects. First, only a single lens and horn are used in conjunction with a reflector, thereby doubling the path through the plasma, and second, a balanced detector is used to provide increased sensitivity for small phase shifts. The carrier is modulated at 400 kc. The reflected signal is mixed in the ring hybrid, and the outputs from the detectors are fed into a tuned differential amplifier. The output from the differential amplifier thus exhibits a null for a 90° phase shift, and this output is linear up to a 20° phase shift about a null. With this system, phase shifts of 1° are readily observable.

The radiation pattern for the present antenna system is shown in Fig. 3.5. The arrows indicate the signal at the edges of the reflector. Measurements in the PTF cavity indicate that there is no (measurable) coupling to the cavity with the new system, whereas the previous system[10] did exhibit coupling to the cavity.

Proper operation of this interferometer requires that the isolation of the directional couplers be high (>30 db) and that the detectors have a low VSWR (<1.3).

Preliminary measurements have been performed with this system and the following have been noted.

1. There is a close relation between the decay of the interferometer signal, microwave noise,

[9]Instrumentation and Controls Division.

[10]*Thermonuclear Div. Semiann. Progr. Rept. Oct. 31, 1963*, ORNL-3564, Sect. 3.1.

[11]*Thermonuclear Div. Semiann. Progr. Rept. April 30, 1963*, ORNL-3472, Sect. 3.1.

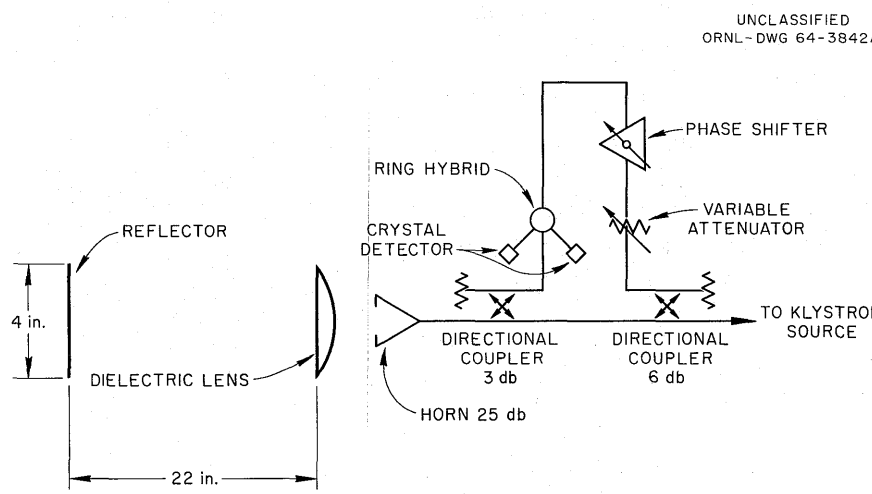

Fig. 3.4. Schematic Diagram of the Present 4-mm Microwave Interferometer.

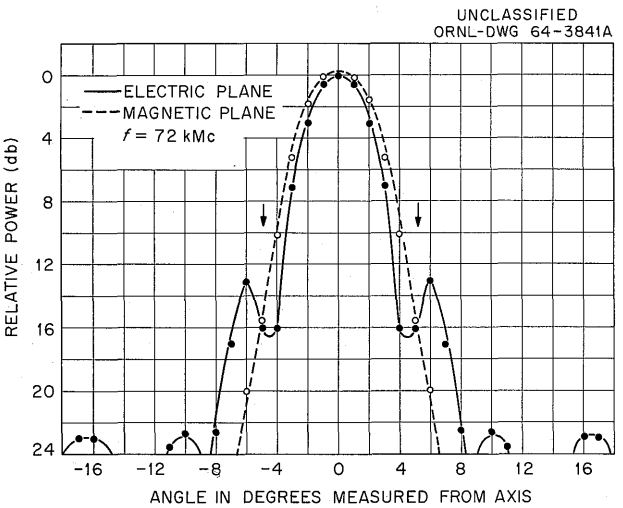

Fig. 3.5. Radiation Pattern from Present 4-mm Microwave System. The arrows indicate the edges of the reflector.

and the electron current out through the mirrors.

2. For a fixed heating power, as the microwave noise is increased (by controlling gas pressure) an instability develops during turnoff, causing a large increase in the microwave noise, which obscures the interferometer signal, making interpretation impossible.

Systematic measurements using the microwave interferometer in conjunction with probes, x rays, etc., are being pursued in order to attempt to resolve the aforementioned discrepancies.

3.2.3 X-Ray Pinhole Photographs

An improved x-ray pinhole camera has been constructed for studies of the PTF plasma. The camera is very similar to the pinhole camera used in the EPA Facility and described in the last semiannual report.[10] The new camera was designed so that careful measurements could be made similar to those described in Sect. 3.1.2 of this report.

The pictures obtained to date at 3-kw power input show a plasma with a radius of ~10 cm and an axial length of ~10 cm, hence a volume of ~3 liters. These measurements are in fair agreement with other measurements based on energy density and thermal neutral beam attenuation.

3.2.4 Pinhole Photographs of Atomic Hydrogen Emission

A pinhole camera was constructed to study the emission of atomic hydrogen from the PTF plasma. Such a technique was first reported by E. S. Chambers.[12]

There are several sources of fast atomic hydrogen atoms from a hot-electron plasma. In the process of ionization by electrons, one reaction which can occur is $H_2 + e \rightarrow H^0 + H^0 + e$. Both neutrals are emitted with ~2.2-ev kinetic energy as a result of the Franck-Condon principle when the molecule is excited into the $1^3\Sigma_u$ state.[13] This can occur either as a result of a direct transition from the ground state, $1^1\Sigma_g$, or as a result of excitation to the $2^3\Sigma_g$ state and subsequent de-excitation to the $1^3\Sigma_g$ state. A more important process is the dissociation of H_2^+ molecules from the $^2\Sigma_u$ repulsive state. Both the proton and neutral hydrogen atom come off with ~5 ev on the average, but each can have as much as 10 ev.[13] The mean free path for all of these fast neutrals is at least an order of magnitude more than the mean free path for H_2 molecules. Hence, atomic hydrogen from both processes can easily penetrate the ~20-cm-diam PTF plasma. All other ionization reactions produce near-thermal atoms and ions.

Another source of fast atomic hydrogen is the charge-exchange atoms which come from hot ions in the PTF. These ions would have to have at least ~10 ev before the charge-exchange cross section on atomic hydrogen in the plasma would be large enough to give an appreciable reaction rate. Hence, such fast atomic hydrogen would penetrate the plasma easily.

There are a number of specific detectors of atomic hydrogen.[14] The current experiments use MoO_3, first used in the 1920's.[15] The technique is to deposit a film of white or yellow MoO_3 on a glass or metal plate and to expose it to the hydrogen flux behind the pinhole, which chemically reduces the

---

[12] E. S. Chambers, UCRL-6793 (Feb. 20, 1962) (unpublished).

[13] H. S. W. Massey and E. H. S. Burhop, *Electronic and Ionic Impact Phenomena*, 1st ed., chap. 4, p. 229 ff, Clarendon Press, Oxford, 1956.

[14] G. Glockler and S. C. Lind, *The Electrochemistry of Gases and Other Dielectrics*, chap. 6, p. 119, Wiley, New York, 1939.

[15] E. Wrende, *Z. Physik* **41**, 569 (1927).

surface to "molybdenum blue." This material has approximately the formula $MoO_{2.5-3} \cdot xH_2O$.

Figure 3.6 shows a photograph of one of the pinhole H^0 "photographs." In the figure, there is a horizontal light streak caused by the shadowing effect of an ion-cyclotron rod on the axis of the machine. The ion-cyclotron power was not on at the time. The two curved lines on the image are probably caused by the emission of H^0 from the cavity walls where they "neck down" at the mirror throats.

The size reduction on the plate is 8 to 1 for a source at the axis of the cavity. Using this figure, a plasma radius of ~10 cm and an axial length of ~10 cm are obtained. These figures are in close agreement with those obtained from x-ray photographs.

When these plates are exposed to the plasma fed with pure helium gas or pure argon gas, patterns are also obtained. However, the patterns are different in shape, are much fainter for equal exposure times, and do not have the characteristic blue color of the patterns obtained with hydrogen plasmas. These patterns may be caused by reduction of the MoO_3 to other oxides (such as MoO_2 and Mo_2O_5) by ultraviolet light.

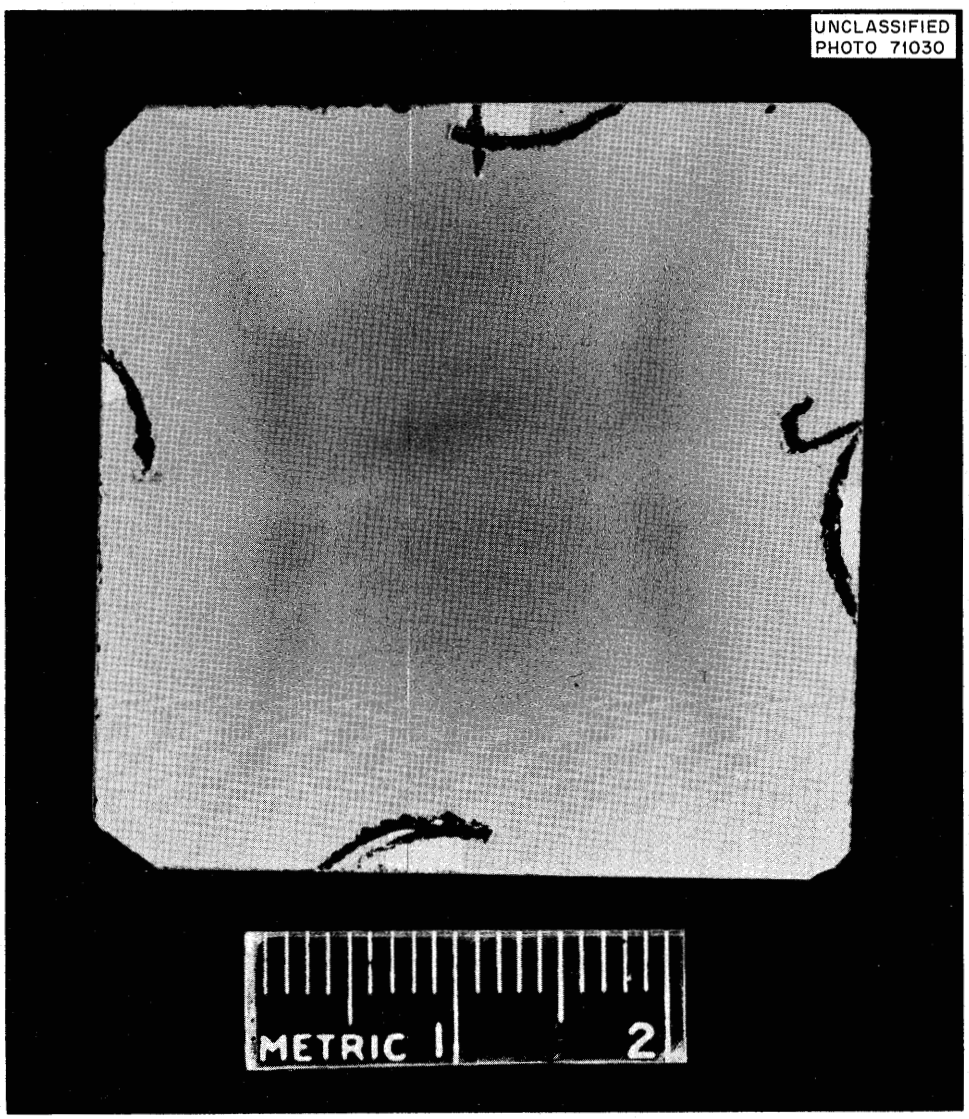

Fig. 3.6. Photograph of an H^0 Pinhole "Photograph" of the Plasma in the PTF Cavity. The size reduction is 8 to 1 for a source on the axis of the cavity.

4. Plasma Physics

4.1 OBSERVATION OF BURNOUT IN A STEADY-STATE PLASMA

Igor Alexeff R. V. Neidigh W. F. Peed

4.1.1 Identification of the Burnout Phenomena

Experimental observations have been made which support our theoretical model[1] that predicts the conditions for burnout in a steady-state plasma. The model assumes that in the normal plasma, the electron temperature is limited by excitation processes in the un-ionized gas; in other words, by radiation cooling. As the gas input is reduced, or the applied power increased, the excitation processes finally can no longer dissipate the applied power. Beyond the critical point the electron temperature suddenly rises, the gas becomes almost completely ionized, the plasma potential becomes quite positive, and energetic positive ions are ejected from the plasma. The ejection of high-energy ions from various plasmas has been noted before,[2] and various mechanisms have been proposed for the phenomena.[3]

The apparatus used in this study is the pressure-gradient arc, shown schematically in Fig. 4.1. In this apparatus, electrons from a hot tantalum cathode flow along lines of magnetic force into a hollow copper anode. Gas is fed into the hollow anode, forming a local high-pressure region, and a localized plasma is formed in the hole. At modest power inputs, a quiescent stream of plasma flows from the opening opposite the cathode. At higher power inputs, a "bursting" effect is observed, and high-energy ions are ejected, as shown in Fig. 4.2.

In our theoretical analysis of the phenomena, we make several crude assumptions to get a first approximation to reality. First, we assume that the incident electron beam transfers its energy to the plasma electrons with 100% efficiency. Such an assumption is reasonable in light of the various experiments showing strong plasma-beam interactions.[4]

Second, we assume that in the non-burned-out case, the major loss of electron energy is by excitation processes in the un-ionized gas. Thus, the power balance equation, to a first approximation, is:

$$W = n_e n_g \sigma_{ex} v_e \Delta E V . \qquad (1)$$

Here, W is the power input to the plasma (ergs/sec), n_e is the electron density (cm^{-3}), n_g is the gas density (cm^{-3}), σ_{ex} is the excitation cross section (cm^2), v_e is the mean electron velocity (cm/sec), ΔE is the energy lost per excitation (ergs), and V is the plasma volume (cm^3).

Since the plasma is assumed to be dense, we replace the electron density n_e with the ion density n_i. (Single ionization is assumed.) Now, we assume that in this apparatus,

$$n_i + n_g = n_{g0} , \qquad (2)$$

[1] I. Alexeff and R. V. Neidigh, *Bull. Am. Phys. Soc.* **9**, 469 (1964).

[2] R. V. Neidigh and C. H. Weaver, *Proc. UN Intern. Conf. Peaceful Uses At. Energy, 2nd Geneva, 1958*, **31**, 315 (1959); E. R. Harrison, *Nature* **184**, 245 (1959); M. Fumeli, Association Euratom-CEA, Fontenay-aux-Roses (Seine), France, private communication, 1963; M. V. Nezlin and A. M. Solntsev, *Zh. Eksperim. i Teor. Fiz.* **45**, 840 (1963).

[3] G. Guest and A. Simon, *Phys. Fluids* **5**, 503 (1962); M. V. Nezlin and A. M. Solntsev, *Zh. Eksperim. i Teor. Fiz.* **45**, 840 (1963).

[4] L. D. Smullin and W. D. Getty, *Phys. Rev. Letters* **9**, 3 (1962); I. F. Kharchenko *et al.*, "Proceedings of the Conference on Plasma Physics and Controlled Nuclear Fusion Research, 4–9 September 1961, Salzburg, Austria," *Nucl. Fusion*, 1962 Suppl., Part 3, p. 1101; also, AEC TR-5589, p. 463; I. Alexeff *et al.*, *Phys. Rev. Letters* **10**, 273 (1963).

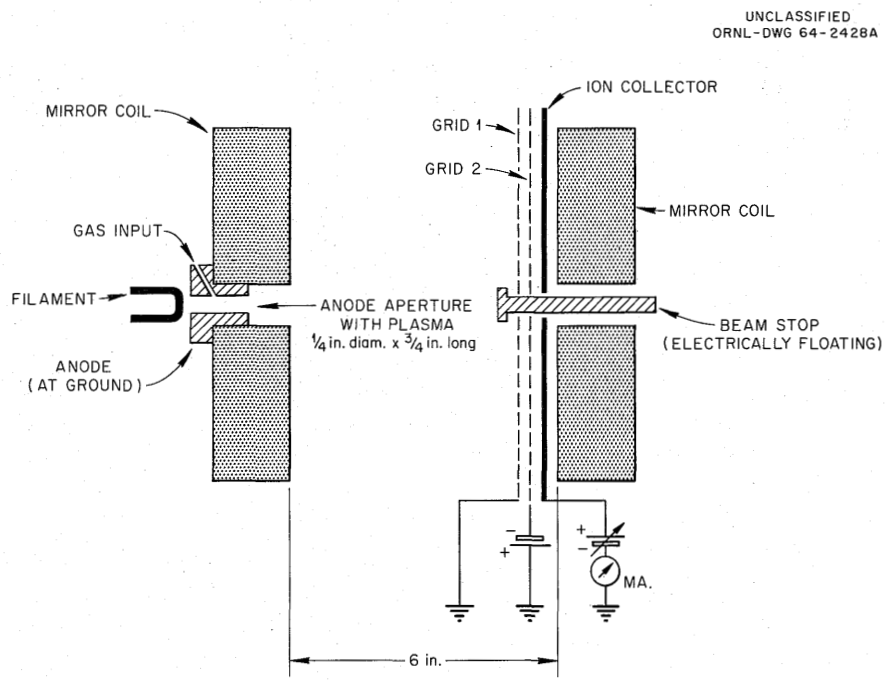

Fig. 4.1. Schematic of Apparatus Showing Gridded Probe Used to Measure Positive Ion Flux. Grid 2 repels electrons. Grid 1 prevents electric field lines from grid 2 from leaking into the main volume. Operating conditions: pressure in the main volume is about 10^{-5} torr; the magnetic field is about 4500 gauss in the mirrors and 1500 gauss in the midplane. The mirror configuration is not needed for the "bursting" phenomenon to occur, but was used merely for convenience in this case. The gas used was argon, and the cathode voltage was −135 v.

where n_{g0} is the gas density in the plasma region before any power is applied. We can substitute Eq. (2) into Eq. (1) to obtain a formula for the gas density in the plasma as a function of power input:

$$n_g = \frac{1}{2} n_{g0} \times \left[1 + \left(1 - \frac{4W}{n_{g0}^2 \sigma_{ex} v_e \Delta E V} \right)^{1/2} \right] . \quad (3)$$

The equation predicts that as the power input is increased, n_g gradually decreases until the quantity in the radical becomes zero. Increasing the power input beyond this point causes the radical to become imaginary. Further analysis shows, actually, that n_g discontinuously drops to zero. At the transition, we find the following relationship:

$$n_{g0} = 2 \left(\frac{W}{\sigma_{ex} v_e \Delta E V} \right)^{1/2} . \quad (4)$$

Physically, what occurs at the transition is that an increase of input power causes n_e to grow, but n_g shrinks faster, so that the product $n_e n_g$ decreases. Thus an increase of input power causes a decrease of excitation loss, n_e further grows, n_g further shrinks, and a runaway condition occurs which ends with $n_g = 0$, or burnout. In multielectron atoms such as argon, a similar burnout phenomenon should occur, except that a multielectron atom would probably end up in a multiply ionized, difficult-to-excite state, but not necessarily be stripped of electrons.

Experimental verification of the above theory has been obtained both from old data (predating the theory) and from recent experiments. The old data show that the theory approximately predicts the gas pressure at which the plasma transition occurs. The new data show that: (1) the gas density at which the observed "burnout" transition occurs has the correct functional dependence on power input; (2) in the burnout condition many, if not all, gas atoms are ionized; (3) in the burnout

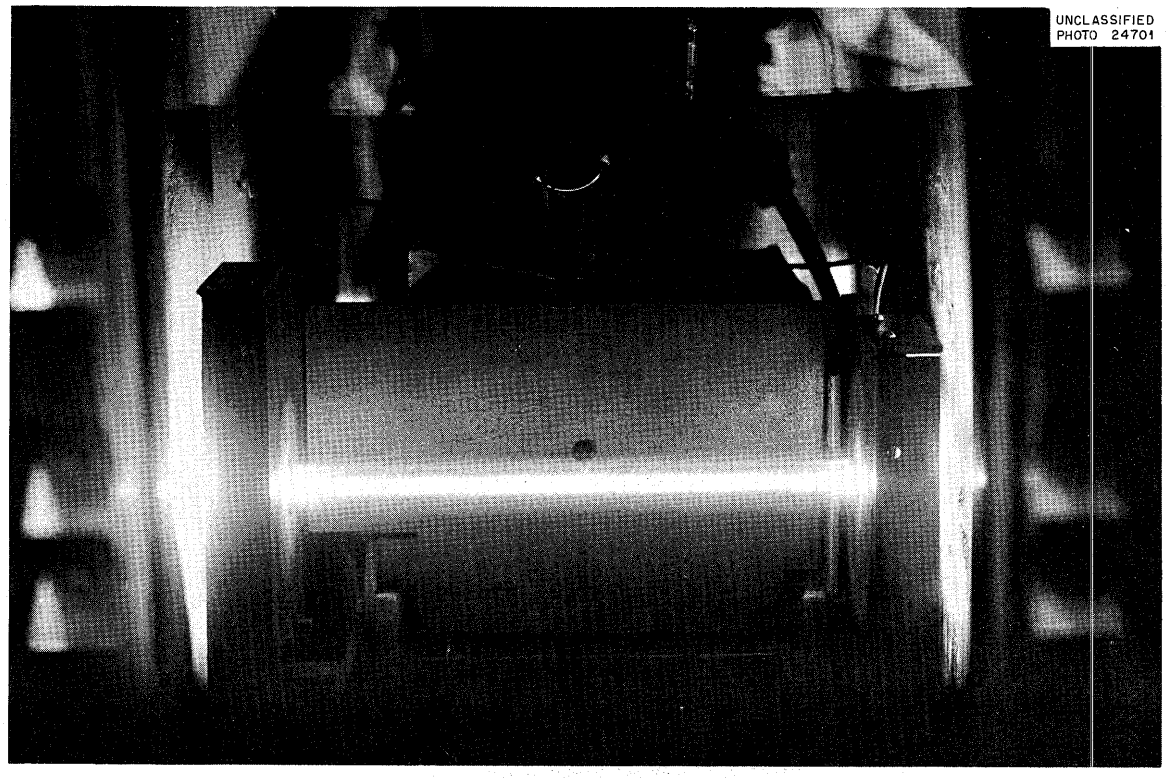

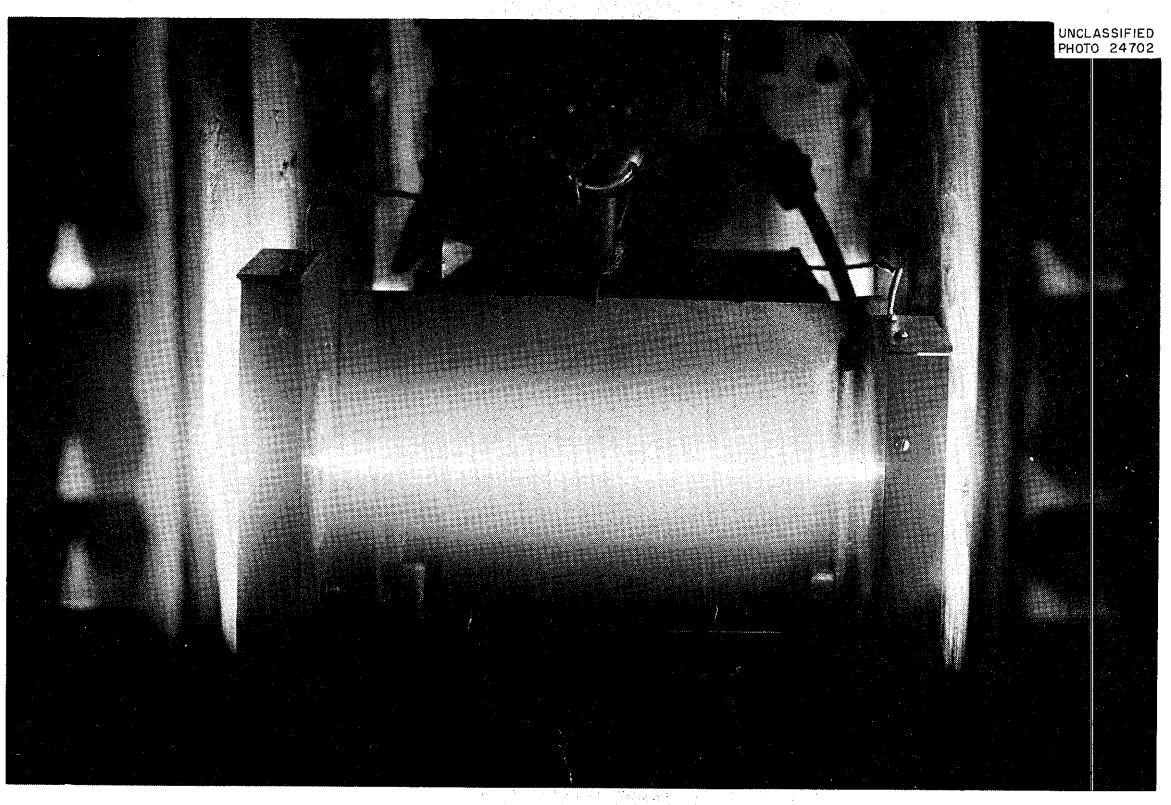

Fig. 4.2. Top – Normal, Quiescent Plasma; Bottom – Ion Emitting Plasma. Note in the lower picture the broad band of light which is due to energetic ions ejected across the magnetic field. The axial magnetic field runs left to right. In these pictures, there is a plasma source at both ends of the plasma column.

condition, the emission of spectral lines in deuterium and helium plasmas virtually ceases.

The dependence of gas input to the anode vs power input required for the transition is shown in Fig. 4.3. Gas density in the anode, n_{g0}, is assumed to be proportional to gas flow rate. As predicted by Eq. (4), n_{g0} should be proportional to $W^{1/2}$, since σ_{ex}, v_e, ΔE, and V in this case are constants. The plotted curve is for argon, since the blowup phenomenon, shown in Fig. 4.2, was easy to observe in this gas. The experimental curve shows the correct functional form, supporting the model.

Verification that many of the gas atoms in the plasma were indeed ionized in the burnout case was accomplished by means of particle accountability. Most of the ions escaping from the anode aperture (shown in Fig. 4.2) were collected on a large gridded probe (shown in Fig. 4.1), and the steady-state current was measured. Assuming that an equal number of ions stream from the hole facing the cathode, and assuming that the argon was singly ionized, we find that 70% of the gas atoms fed into the apparatus reach the collector plate as ions. Thus, at the least, we can say that percentage of ionization is high.

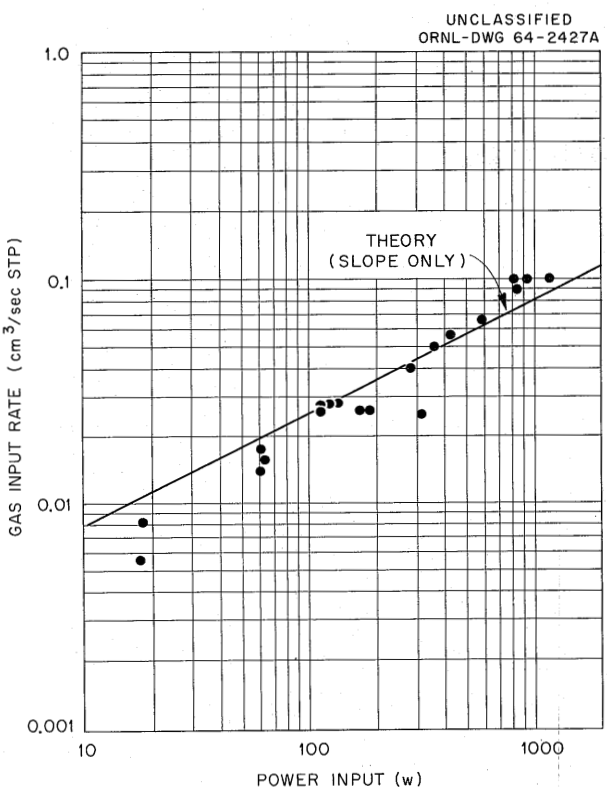

Fig. 4.3. Dependence of Plasma Transition from Normal to Ion-Emitting State as a Function of Gas Flow and Applied Power. Argon gas was used.

If we follow Eq. (2) of our model, or if we assume that the ion loss rate after burnout is approximately the same as the gas atom loss rate before burnout, we find that the ion density *after burnout* should be the same as the gas density *before power* is applied. In this particular run, we have not measured the gas density directly, but we can estimate it from the dimensions of the apparatus and the input flow rate. The density, n_{g0}, is greater than 10^{14} cm^{-3}. Assuming an ionization cross section of 10^{-16} cm^2 for argon, and an electron density of 10^{14} cm^{-3}, occurring after burnout, neutral argon atoms entering the plasma would be reduced to e^{-1} of their flux by ionization in about 0.05 cm. This distance is small compared with the dimensions of the apparatus. Thus, our model is at least self-consistent, and burnout is possible.

Spectroscopic studies also strongly suggest that burnout has occurred and the measured energy of the ions emitted from the hollow anode also supports the burnout model.

4.2 STABILIZED PLASMA

I. Alexeff R. V. Neidigh W. F. Peed

4.2.1 Hot-Electron Plasmas

A previous report[5] of the experiments with the hot-electron plasma generated by beam-plasma interaction observed that the plasma decayed with a constant e-folding time, τ(sec), predictable from the multiple scattering equation,

$$\tau = \frac{\theta^2 E^2}{2\pi n_0 v e^4 \ln (A_0 E/e^2)} .$$

Here, θ (radians) is the angle through which the velocity vector of an electron initially rotating about the axis must change to reach the loss cone, E is the electron energy (ergs), n_0 is the gas density (cm^{-3}), v is the electron velocity (cm/sec), e is the electronic charge (esu), and A_0 is

[5] *Thermonuclear Div. Semiann. Progr. Rept. Oct. 31, 1963*, ORNL-3564, sect. 4.1.5, p. 51.

the Bohr radius (cm). This equation assumes that electron-neutral collisions are the dominating loss mechanism. Therefore the plasma was not thought to be dissipated by instabilities, at least during its decay. The data presented are shown again in Fig. 4.4 where the decay time is plotted as a function of electron temperature. The lower solid line is the calculated decay time for a neutral density of 3.5×10^{12} cm^{-3}. The data points were normalized to this neutral density. We think the scatter above and below the line indicates errors in our measurement of n_0 and of τ.

A better case for the stability of the hot-electron plasma could be made if the neutral density were reduced and the decay time found to be proportionately longer. We did this and the data are also given in Fig. 4.4. The family of curves are the calculated decay times vs electron temperature for the neutral densities indicated. The three points are the measured values of electron temperature and the e-folding time, τ, of the decay. In general, we see the decay time is proportionately longer as expected, but again the agreement with the scattering equation depends on the accuracy of the n_0 and τ measurements.

Actually, we think the data are in excellent agreement with the value predicted by the multiple-scattering equation, and therefore the plasma shows stability during the decay. In order to determine n_0 and τ, it is necessary to understand the method of reducing the neutral pressure.

The method is shown schematically in Fig. 4.5. An air-driven plunger accelerates over a 3-in. travel and plugs the gas flow at the end of its stroke. The location of the gas-turnoff point is adjacent to the defining slot in the mirror throat. Gas flow is stopped in less than a millisecond. Gas flow through the leak valve is not changed, but this gas simply fills the reservoir. The reservoir capacity is large enough to absorb gas for several seconds. Power turnoff is simultaneous with gas turnoff. At turnoff the 20-in. diffusion pump on the vacuum chamber begins removal of the neutral gas.

If the pumps were able to drop the pressure in the apparatus to a very low value, an appreciable part of the hot-electron plasma would be trapped and confined for very long times. This trapping factor can be expressed mathematically as follows: Let τ_a be the time in which the plasma density would drop to e^{-1} of its initial value if the gas pressure were kept constant. Let τ_b be the time in which the background gas density drops to e^{-1} of its value after the gas-feed valve is turned off. Then the trapped plasma density n at very long times after gas turnoff (ignoring ion-electron and electron-electron scattering and instabilities) is given by the following equation:

$$n = n_0 e^{-\tau_b/\tau_a} ,$$

where n_0 is the initial plasma density. Thus, under ideal conditions, $\tau_b \ll \tau_a$, most of the hot-electron plasma could be trapped and studied in a high-vacuum environment. Actually, we did not have a low enough ultimate pressure to get very long confinement times, but a big improvement was noted.

The overall pumping speed of a vacuum system is partly dependent on the history of the system and may vary from run to run. The pumping speed was measured before each of the three runs, and since the pressure could not be measured during a run, the pressure drop during a trial without plasma was obtained.

Neutral density, n_0, vs time after turnoff could now be estimated for the three runs and is shown in Fig. 4.6. Note how closely the density at which τ was measured agrees with the density in

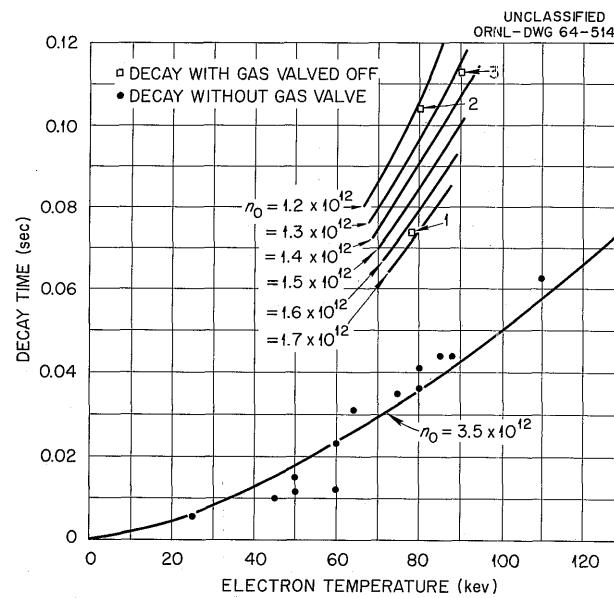

Fig. 4.4. Decay Time vs Electron Temperature of Hot-Electron Plasma. Solid lines are for different values of neutral density.

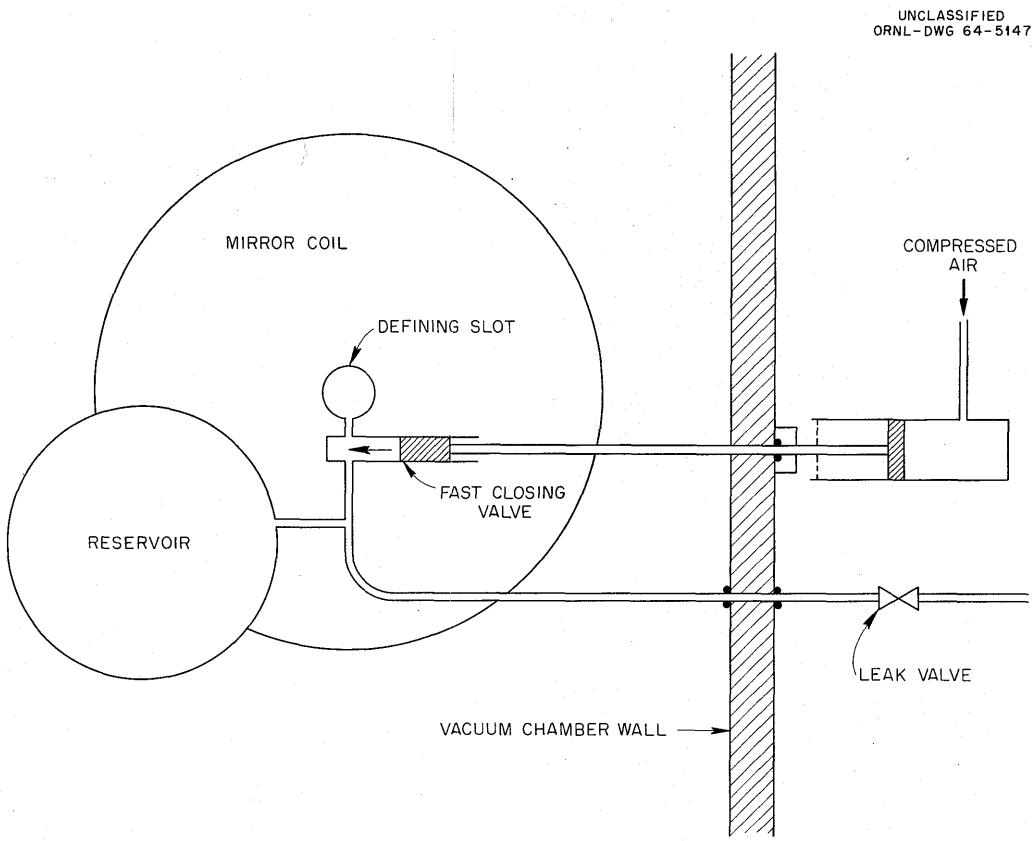

Fig. 4.5. Schematic Diagram of Fast-Closing Gas Valve. *An air-driven plunger cuts off gas flow at the defining slot. The reservoir collects gas during a plasma decay.*

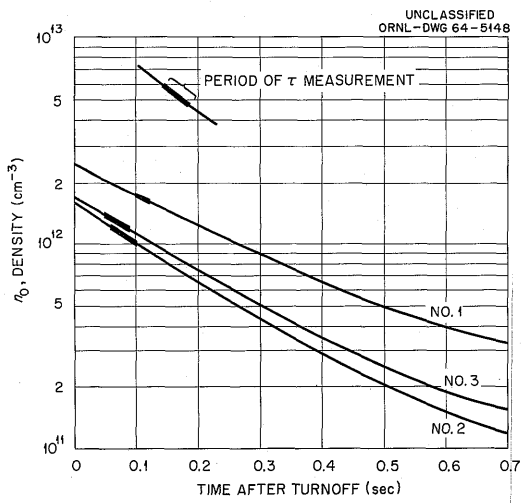

Fig. 4.6. Neutral Density vs Time After Turn-Off. *Since the pressure could not be measured during a run, the curves were obtained from measured pumping speeds before each run, a typical pressure vs time curve without plasma, and pressure measurement before and after the run.*

the family of curves of Fig. 4.4. The τ continued to increase with time, as it should, and for run 3 there was sufficient x-ray flux to determine a τ of 0.350 sec after 0.3 sec and the x-ray flux remained above background for 0.8 sec.

The three runs shown were the most stable observed. We noted that for some combinations of gas feed rate, magnetic field strength, mirror ratio, and power input, the x-ray output came in bursts during the steady state. We did not consider this a good adjustment of the parameters. Decay of the plasma from this "not so steady," steady-state condition was much more rapid and the x-ray bursts continued during the decay. Two extremes in x-ray output during the decay are shown in Fig. 4.7. There was some variation in the decay time with the best adjustment of parameters which led us to believe that the decay τ was in some way dependent on the condition of the plasma at turnoff.

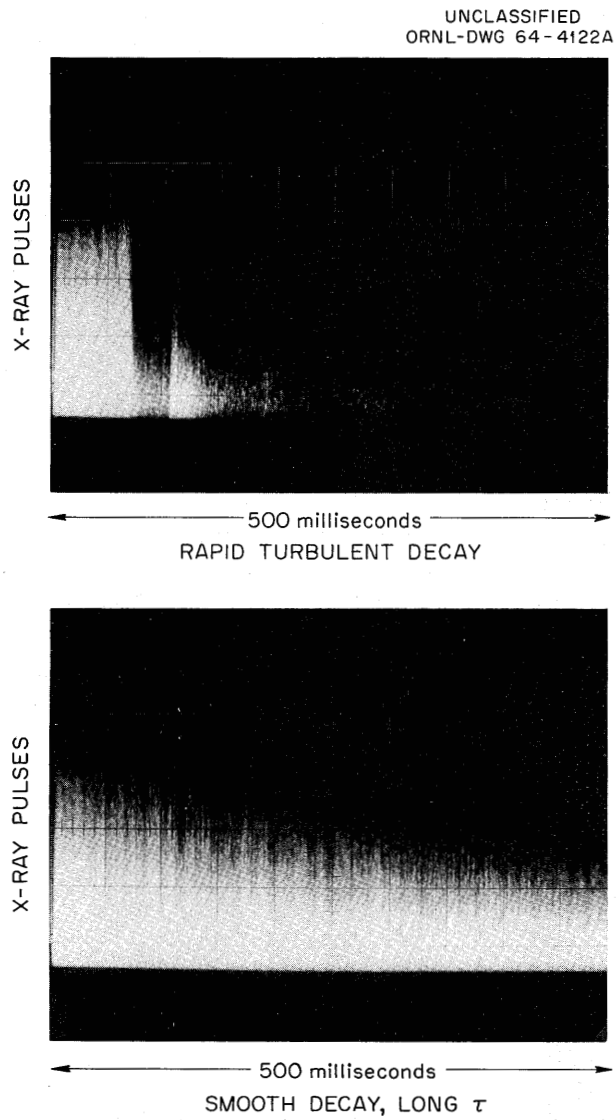

Fig. 4.7. X-Ray Flux Decay After Turn-Off. Upper photo shows a rapid, turbulent decay. Lower photo shows smooth decay, lasting well over 0.5 sec.

4.3 MEASUREMENT OF PLASMA DENSITY IN HOT-ELECTRON PLASMAS BY X-RAY FLUX – IMPURITY CONSIDERATIONS

I. Alexeff

In previous experiments,[6] we measured the density of a hot-electron plasma by measuring the energy emitted in the form of bremsstrahlung x rays. These measurements are in excellent agreement with density measurements made with a diamagnetic probe and with a neutral beam.[7] However, for the x-ray measurements to be meaningful, we had to assume that the plasma contained little contamination of materials of high atomic number. In this present discussion, we now prove that the impurity content was too small to have any serious effect on the density measured by the x-ray flux.

We show that the measurements of plasma density by x rays is accurate by examining the decay time for the plasma caused by electron-neutral collisions. Both the x-ray flux yield and the decay time depend essentially on Z^2n, where Z is the atomic number and n is the density of the unionized gas in the system. Now, if the decay time, τ, found experimentally agrees with the decay time computed from the measured deuterium gas pressure in the system, then high-Z contaminants did not appreciably affect the decay measurement. Since the decay time and the x-ray flux yield have essentially the same functional dependence on Z and n, we can infer that in this given run the contamination was sufficiently low as not to affect the electron density measurement obtained by the x-ray flux.

The above argument is easily put into a quantitative form. The x-ray rate of energy emission, ϵ, is given as follows:[8]

$$\epsilon = 1.42 \times 10^{-27}\, n_e n_g Z^2\, T_e^{\,1/2} .$$

Here ϵ is in ergs cm^{-3} sec^{-1}, n_e is the plasma electron density (cm^{-3}), n_g is the gas density (cm^{-3}), Z is the atomic number of the gas, and T_e is the electron temperature (°K). We assume that most of the photons are produced by electron-atom collisions rather than electron-ion collisions, or, equivalently, that $n_e < n_g$. Next we find the expression for the reciprocal of the decay time – that time (seconds) in which the plasma density drops to e^{-1} of its initial value by electron–gas-atom collisions. This time is given by the following equation:[7]

$$\tau^{-1} = \frac{2\pi n_g V e^4 Z^2}{\theta^2 E^2} \ln_e \frac{A_0 E}{e^2 Z^{4/3}} .$$

[6] I. Alexeff *et al.*, *Phys. Rev. Letters* **10**, 273 (1963).

[7] I. Alexeff *et al.*, *Thermonuclear Div. Semiann. Progr. Rept. April 30, 1963*, ORNL-3472, p. 31; *Thermonuclear Div. Semiann. Progr. Rept. Oct. 31, 1963*, ORNL-3564, p. 44.

[8] L. Spitzer, Jr., *Physics of Fully Ionized Gases*, 1st ed., chap. 5, p. 88, Interscience, New York, 1956.

Here n_g is the gas density (cm^{-3}), V is the average electron velocity (cm/sec), e is the electron charge (esu), Z is the atomic number of the gas, θ is the angle through which the velocity vector of an electron initially rotating about the axis must change to reach the loss cone, E is the electron energy, and A_0 is the Bohr atomic radius, Thus, if a small amount, Δn_g, of a high-Z contaminant were added to a hot-electron plasma, both ϵ and τ^{-1} would suffer the same percentage change, as long as the effect of the $\ln_e$ term in the formula for τ^{-1} is small. This logarithmic term, unfortunately, also contains Z.

Examination of the logarithmic term shows that at the high electron energies being studied, 100 kev and more, the logarithmic term varies only slowly with Z. Let us compare the worst possible cases – hydrogen with uranium:

$$\frac{\ln_e(U)}{\ln_e(H)} = 3.7 \ .$$

Thus, even if the logarithmic term has the largest variation permitted by the periodic table, this variation results in only a factor of 3.7.

What the above factor of 3.7 means experimentally is as follows: Suppose that our experimentally measured decay time is 20% shorter than the decay time computed from the gas pressure measured in the system. If we assume that this 20% discrepancy is due to contamination of the gas, and if we assume that the contaminant is the worst possible – uranium – then our plasma density measurement made by the x-ray flux is too high by $3.7 \times 20\% = 74\%$. Thus, we are off in density by less than a factor of 2 in this worst possible case. The agreement between the measured and the computed decay times for the hot-electron plasma thus shows that our density measurements based on the measured x-ray flux were not grossly in error.

4.4 BEAM-PLASMA STUDIES

V. J. Meece W. L. Stirling

Investigation of previously reported beam-plasma interactions[9] has been continued. In this experiment, the secondary plasma is created by the primary dc electron beam through ionization of the background gas. Under certain conditions, the beam and plasma interact in a manner to heat the plasma electrons as indicated by the x rays produced. A plot of the logarithm of the x-ray intensity vs energy yields an electron temperature.[10] Temperatures determined in this manner are always approximately equal to the beam energy, which lies in the range of 15 to 30 kev. Densities in the range of 10^{10} to 10^{11} e/cm^3 are calculated from an estimate of the total amount of energy radiated.

Study of the low-intensity x-ray mode reported in ref. 9 shows that the low-frequency rf spectrum is a weak function of the magnetic field between about 1500 and 3000 gauss, and very similar patterns can be obtained independent of the type of gas admitted into the interaction region.

Figure 4.8 shows a typical picture made with a panoramic spectrum analyzer. Fig. 4.9 shows the rf patterns of two identical probes, one on either end of the interaction region. Each probe is a single-turn grounded loop oriented with its plane parallel to the magnetic field. The scope sweep speed is 20 μsec/cm, which yields a repetition frequency of about 40 to 50 kc. A comparison of

[9] E. Earley *et al.*, *Thermonuclear Div. Semiann. Progr. Rept. Apr. 30, 1963*, ORNL-3472, p. 37.

[10] L. Spitzer, Jr., *Physics of Fully Ionized Gases*, 1st ed., chap. 5, p. 89, Interscience, New York, 1956.

UNCLASSIFIED
PHOTO 65511

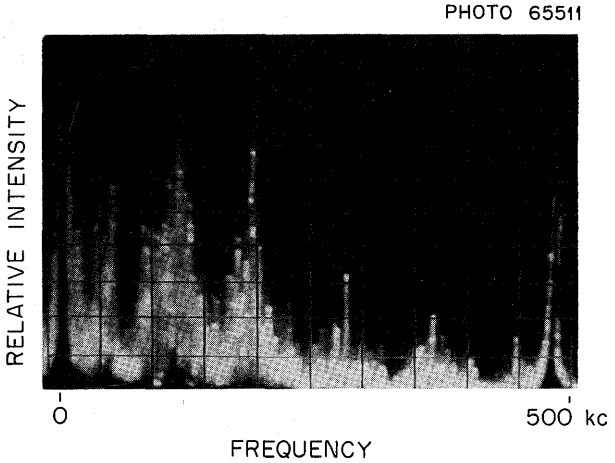

Fig. 4.8. Low-Frequency Spectrum from Panoramic Analyzer. Beam current = 650 ma; beam voltage = 25 kv; field = 2200 gauss; argon flow = 15 sec/cc in the interaction region and 30 sec/cc in the gun.

UNCLASSIFIED
PHOTO 65512

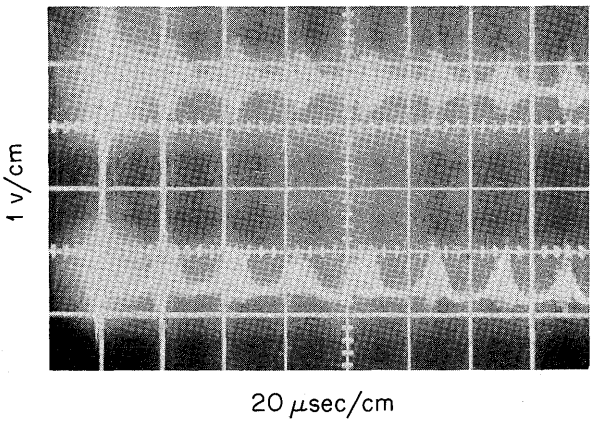

Fig. 4.9. Oscilloscope Display of Probe Signals.

UNCLASSIFIED
PHOTO 65513

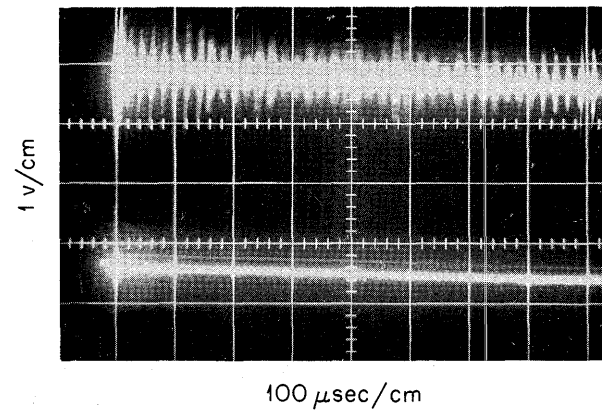

Fig. 4.10. Oscilloscope Display of Probe Signal, Slow Sweep.

Figs. 4.8 and 4.9 shows that the beam-plasma interaction is pulsing at a uniform repetition rate of 40 to 50 kc, and that the panoramic spectrum analyzer is displaying a Fourier analysis of the pulse. The predominant frequency emitted during the pulse is about 10 Mc and it has been seen on both the analyzer and the scope. Higher-frequency measurements have not been made. The upper trace of Fig. 4.10 was taken at a scope sweep of 0.1 msec/cm, and shows that the pulsing is very steady over long periods of time. Repetition frequencies as high as 120 kc have been obtained with argon gas. The exact frequency depends on both gas feed and the electron-gun parameters. The pulsing has been observed at zero gas feed into the interaction region and at beam accelerating voltages as low as 5 kv.

An unexpected observation occurred when the beam port on the target end of the localized high-pressure region fell off. Investigation of the entire end wall depicted an erosion pattern like that shown in Fig. 4.11. The wear pattern is approximately an exponential function of the radius with slightly more than 50 g of copper missing. An identical wear pattern was found on the other end of the cylinder. A crude estimate of the sputtering ratio can be made by estimating the total operation time and an average ion current from the meter readings. The resultant value yields an ion velocity of about 100–300 v for argon on copper. Further study of the system showed that there is no erosion on the inner surfaces of the beam ports and no erosion on the target which is a 0.030-in.-thick piece of copper. Thus the only ions of appreciable energy are those in the secondary plasma around the primary beam inside the interaction region. A study of the ion velocity distribution is now under way.

From the work of other authors,[11,12] one might expect that the conditions prevailing in this experiment are right for supporting a helical or screw instability. The results of efforts to determine if the plasma is rotating are inconclusive. Probes of the type developed for use in DCX-1[13] will be employed to improve these measurements.

There is a striking similarity between this experiment and that of Nezlin on the electrostatic instability of an intense electron beam in a plasma.[14] Nezlin postulated the formation of a virtual cathode in the beam which interrupted the passage of the beam to the anode or target. The condition he quotes for such an effect is $j_b \approx 0.7\, j_{ep}$ where j_b is the beam density and j_{ep} is the plasma electron density. Nezlin's model for the explanation of his results is that the virtual cathode alternately appears and disappears at a frequency of 10 Mc during which time the beam

[11] G. Guest and A. Simon, *Phys. Fluids* **5**, 503 (1962).

[12] F. C. Hoh, *Phys. Fluids* **5**, 22 (1962).

[13] J. L. Dunlap *et al.*, *Thermonuclear Div. Semiann. Progr. Rept. Oct. 31, 1963*, ORNL-3564, p. 2.

[14] M. V. Nezlin, *Soviet Phys. JETP* **14**, 723 (1962).

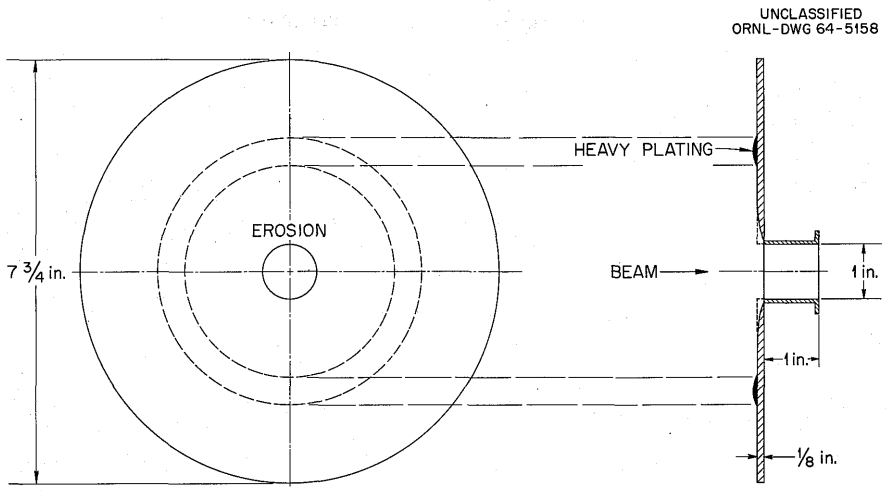

Fig. 4.11. Wear Pattern on Wall of Interaction Chamber.

interacts with the plasma and heats the plasma electrons. The plasma electron density thereby increases until the condition for instability is destroyed. The system then relaxes while the plasma cools off; the beam can now pass uninterrupted until the critical condition again prevails. His measurements of the relaxation time lie between 10^{-4} and 10^{-3} sec. A later report[15] states that ions (lithium) with energies of several hundred ev are emitted transversly when the beam is unstable. A direct comparison to this experiment would set our relaxation time between 3 and 20 μsec. We have observed x rays due to heating of the plasma electrons and have observed erosion of the interaction chamber walls. Several experiments are under consideration to test this model.

4.5 ION BEAM STABILIZATION

E. D. Shipley
O. C. Yonts
A. M. Veach[16]
R. N. Goslin[17]
W. A. Bell[16]
K. A. Spainhour[16]

It is assumed that progress of the DCX program is related directly to the ability to achieve stabilization of the wrapped-up beam. In many respects the calutron ion beam presents a simplified but similar ion beam configuration, and it is probable that treatments which improve calutron beams can be adapted (even though not fully understood) to the solution of DCX problems. This work is conducted as a joint effort with the Electromagnetic Isotope Separation Department of the ORNL Isotopes Division.

The standard calutron used in isotope separation exhibits regions of unstable operation as shown by the inverse beam quality curve in Fig. 4.12. Beam quality is defined as the ratio of collector current to collector plus face-plate current. Increase in ion-beam current decreases the region of stable operation as does the presence of more than one ion beam.

The region of stability can be extended by use of flat plates placed near the ion beam or extended even further if the plates are segmented and electrically isolated by an impedance to ground. This is shown in Fig. 4.13.

In practice, the use of plates and segmented walls has resulted in a single ion beam of 250 ma which maintains focus and stability at pressures down to 3×10^{-7} torr – the base pressure of the particular system. Recently, under improved vacuum conditions and with a somewhat smaller ion source, a 125-ma beam was run at a pressure of about 6×10^{-8} torr.

In the past, use of two ion sources in a single tank has been limited to heavy elements over a very restricted pressure range. Recently two calcium ion beams of 150 ma each have been run

[15] M. V. Nezlin and A. M. Solntsev, *Soviet Phys. JETP* 18, 576 (1964).

[16] Isotopes Division.

[17] Consultant from Oglethorpe University, Atlanta, Ga.

at pressures of 10^{-6} torr with no interference between beams and no defocusing due to reduced pressure. Without wall treatment, beams of this intensity and quality are unobtainable.

This work has progressed through the use of a succession of models upon which experiments were formulated and performed. Experimental results frequently necessitated revision of postulated models to maintain agreement of working concepts and observed data. At this time beam stability appears to be related to the stabilizing action of certain electrons as discussed in Sect. 8.4.

Present experiments involve determination of the real difference, if any, which exists between properly positioned flat plates and the segmented plates with associated inductances to ground.

The authors wish to express their appreciation to J. P. Wood, H. L. Huff, and R. L. Johnson for the design, construction, and operation of equipment, and to H. C. Hoy and R. A. Strehlow for many helpful discussions.

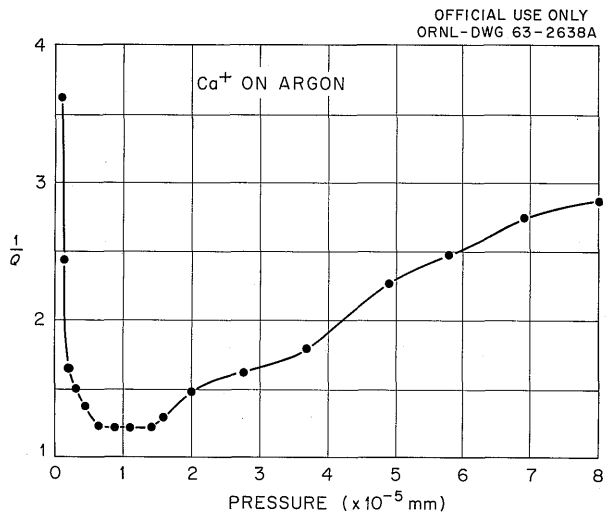

Fig. 4.12. Inverse Beam Quality Curve in Standard Calutron.

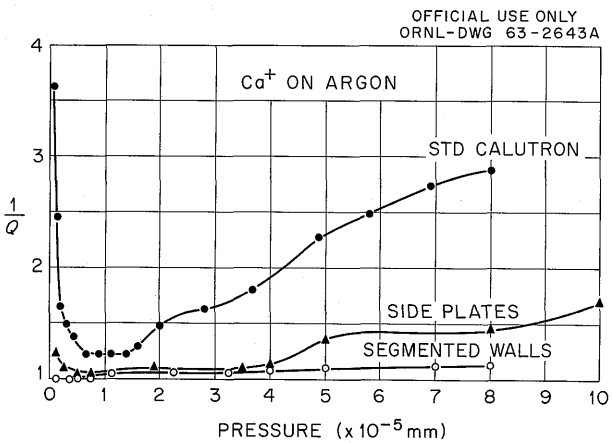

Fig. 4.13. Inverse Beam Quality Curves.

4.6 VELOCITY OF MOVING STRIATIONS IN DISCHARGE TUBES AS A FUNCTION OF GAS PRESSURE

I. Alexeff W. D. Jones

4.6.1 Introduction

Previously,[18,19] we reported on image-converter studies made of moving striations in the inert gases at low pressures. We describe here further studies, both experimental and theoretical, made of moving striations in the inert gases.

Experimentally, the velocities of moving striations have been measured, as a function of background gas pressure, in the positive columns of both cylindrical and tapered discharge tubes. For the most part, only the so-called positive striations, moving from the anode toward the cathode, have been studied. Theoretically, the theory of ionic sound waves has been modified to include the effects of ion–gas-atom collisions. The modified theory predicts that the ion waves should be slowed down, as well as strongly damped, by the collisions. The theory has no adjustable parameters. Over a pressure range of from a few microns to several millimeters of mercury and a velocity range of roughly 10^3 to 10^6 cm/sec, quantitative agreement is found between the ionic sound wave velocities predicted by the modified theory and the experimentally observed average velocities of the moving striations. Experimentally, the strong damping is not observed. A simple, cavity-type oscillation involving the

[18] Igor Alexeff, W. D. Jones, and R. V. Neidigh, *Thermonuclear Div. Semiann. Progr. Rept. Oct. 31, 1963*, ORNL-3564, p. 59.

[19] Igor Alexeff, W. D. Jones, and R. V. Neidigh, *Bull. Am. Phys. Soc.* **9**, 323, paper L-8 (1964).

radial dimensions of the tube, and supported qualitatively by experimental evidence, is suggested as a possible source of the observed oscillations.

Although several people have considered the obvious possibility of interpreting moving striations in terms of ion waves, few have bothered to proceed very far along this line. This reluctance has stemmed largely from the fact that the changes in plasma density and space potential accompanying moving striations are often so large that, a priori, any agreement between experiment and a linear plasma theory would seem almost fortuitous. Perhaps the most serious effort to derive a plasma theory, suitable for correlation with moving striations, has been made by Armstrong, Emeleus, and Neill.[20] Although these authors went so far as to include the effects of ion–gas-atom collisions in the theory, and even wrote down an "appropriate" solution, they had little faith in the overall applicability of the theory to moving situations, and thus did not pursue this line of attack further.

Despite the strong objections, on theoretical grounds, to trying to interpret nonlinear wave phenomena in plasmas in terms of a linear theory, there is evidence which seems to indicate that the nonlinear effects do not introduce much change in the observed results. Little,[21] for example, has done experiments with plasmas expanding into a vacuum. He found that the observed velocities did not differ greatly from the results predicted by a linear theory, even though extremely large density gradients were present in these experiments.

Although not done for the purpose of trying to explain moving striations, a more complete modification of the theory of ionic sound waves, allowing for collision effects with the background gas atoms, has been made by Hatta and Sato.[22] This modified theory includes not only the effects of ion–gas-atom collisions, but also of electron–gas-atom collisions and of a finite ion temperature. These authors derived an ionic sound wave velocity expression which, under the assumptions made in Sect. 4.6.2 below, is almost identical to the corresponding velocity expression derived in that section.

The mathematical treatment given below is approximate in that it is one-dimensional. The treatment does not take into account the finite diameter of the discharge tube. One problem in trying to account for the finite tube diameter is that it is not known what boundary conditions should be imposed on the ion wave at the tube wall. If it is assumed that the wave has a pressure antinode at the boundary, then the wave can progress down the tube in a one-dimensional, "speaking tube" manner. For this mode of propagation, the tube diameter is unimportant. If the wave has a pressure node at the tube wall, the wave will still progress at essentially the one-dimensional velocity, as long as the wavelength is less than about twice the tube diameter. For longer wavelengths, the wave velocity increases. In general, the striation spacing observed was not much greater than twice the tube diameter, so that, hopefully, the effects of the finite tube diameter were not serious.

The failure to observe, experimentally, the strong damping predicted by the modified theory would seem to indicate that some mechanism is operative at the higher pressures which restores energy to the waves as they propagate down the tube. Therefore, at the higher pressures, the theory is incomplete to the extent that it does not provide for the energy-restoring mechanism.

Although further note of the fact will not be made in the present writeup, it is interesting to note that the data of the present experiment are not the only ones accurately predicted by the modified theory. In at least 80% of the striation literature which has been reviewed, the velocity data reported are accurately predicted, within a factor of 2 or 3, by the present theory.

4.6.2 Theoretical Properties of Ionic Sound Waves

Even though, as intimated above, the modified form of the differential equation of motion for longitudinal compression waves propagating in a gaseous medium is known, the following derivation is sufficiently elementary that its presentation here is considered to be worth while.

[20] E. B. Armstrong, K. G. Emeleus, and T. R. Neill, *Proc. Roy. Irish Acad., Sect. A* **54**, 291 (1951).

[21] P. F. Little, *J. Nucl. Energy: Pt. C* **4**, 15 (1962).

[22] Y. Hatta and N. Sato, *Proc. Intern. Conf. Ionization Phenomena Gases, 5th Conf., Munich, 1961*, vol. I, p. 478 (1962).

In the derivation, the following plasma model is assumed: (1) the working medium is an electrically neutral mixture of electrons, positive ions, and gas atoms, with only one species of singly charged positive ions present, (2) the temperature of the electrons is much higher than the temperature of the ions, (3) the ion and gas atom temperatures are equal, (4) the masses of the ions and gas atoms are equal, (5) the electrons obey the ideal gas law, and (6) electron-ion and electron-neutral collisions are unimportant.

In the derivation it is assumed that there is conservation of linear momentum and of particles, and that the processes associated with the ionic sound wave motion take place rapidly enough to be considered as adiabatic processes. For simplicity, wave motion in only one direction is considered.

In the first part of the derivation it is assumed that no ion–gas-atom collisions occur. The results obtained are then easily and straightforwardly modified to include the effects of ion–gas-atom collisions.

Consider a slab of plasma of thickness Δx, as shown in Fig. 4.14, and assume that a pressure differential exists across the width of the slab. Denoting the pressures at x_0 and at $x_0 + \Delta x$ as $P(x_0)$ and $P(x_0 + \Delta x)$, respectively, and making the approximation that $P(x_0 + \Delta x) \approx P(x_0) + (\partial P/\partial x)\Delta x$, the pressure difference on the slab is given by

$$\Delta P = \frac{\partial P}{\partial x} \Delta x \ . \tag{1}$$

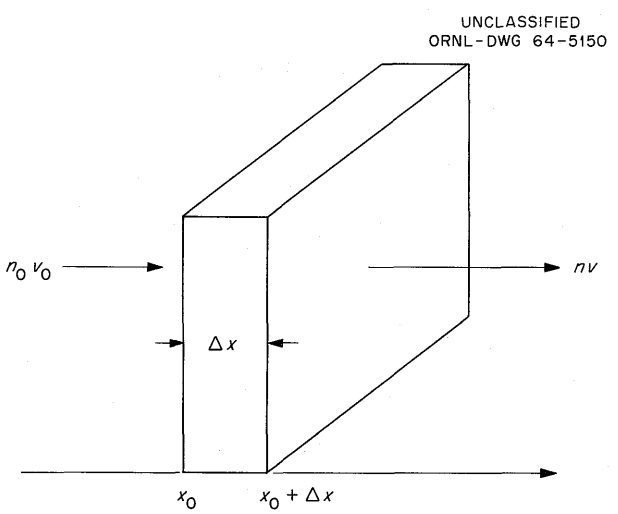

Fig. 4.14. Slab of Plasma.

According to Newton's second law, this pressure difference must equal the rate of change of linear momentum stored in the slab per unit area.

Case of No Ion-Neutral Collisions. – For this case, to a good approximation, the momentum stored in the slab, per unit area, is given by $mvn\ \Delta x$, where m is the mass of the ion, v is the speed of the ion, and n is the ion number density. Thus, the rate of change of momentum in the slab is

$$\frac{\partial}{\partial t}(mvn\ \Delta x) = m\ \Delta x \frac{\partial}{\partial t}(nv) = \Delta P \ , \tag{2}$$

where ΔP is the thermal pressure of the electrons. The equating of the pressure of the electron gas to the rate of change of momentum of the ions is justified because, under the conditions of ionic sound wave motion, the electron and ion fluids are constrained to move as one by the electrostatic forces.

To obtain a suitable expression for ΔP, we utilize the following three equations:

the equation for adiabatic processes,

$$PV^{\gamma} = \text{constant} \ , \tag{3}$$

the equation of state for an ideal gas,

$$PV = RT \ , \tag{4}$$

and the equation relating the thermal pressure of electrons and electron temperature,

$$P = nkT \ . \tag{5}$$

In these three equations, P, V, T, n, and γ are thermal pressure, volume, temperature, density, and adiabatic compression coefficient, respectively, of the electron gas.

Substituting from Eq. (5) into Eq. (4) gives

$$V = \frac{R}{nk} \ . \tag{6}$$

Substituting from Eq. (6) into Eq. (3) gives, after differentiation,

$$\Delta P = \gamma P n^{-1}\ \Delta n \ . \tag{7}$$

Substituting from Eq. (5) into Eq. (7) gives the desired expression for ΔP,

$$\Delta P = (\gamma kT)\ \Delta n \ . \tag{8}$$

We now equate the rate of change of momentum, given by Eq. (2), to the above pressure differential (noting that a minus sign is required) to obtain

$$\Delta P = \Delta n\,(\gamma kT) = -m\,\Delta x\,\frac{\partial}{\partial t}\,(nv)\,, \qquad (9)$$

or, by dividing both sides of Eq. (9) by $m\,\Delta x$, we obtain

$$\frac{\Delta n}{\Delta x}\left(\frac{\gamma kT}{m}\right) = -\frac{\partial}{\partial t}\,(nv)\,. \qquad (10)$$

A second needed equation is obtained by requiring conservation of particles. Referring to Fig. 4.14, let $n_0 v_0$ and nv be the number of particles entering and leaving the slab, respectively, per unit area per unit time. The difference between these two quantities, divided by the thickness of the slab, is the increase in the number density in the slab per unit time, or

$$\frac{\partial n}{\partial t}\,\Delta x = n_0 v_0 - nv = n_0 v_0 - nv_0 + nv_0 - nv\,,$$

or

$$\frac{\partial n}{\partial t} = -\frac{v_0(n-n_0)}{\Delta x} - \frac{n(v-v_0)}{\Delta x}\,. \qquad (11)$$

If we let $\Delta x \to 0$, $v \to v_0$, and $n \to n_0$, then Eq. (11) becomes

$$\frac{\partial n}{\partial t} = -\,v\frac{\partial n}{\partial x} - n\,\frac{\partial v}{\partial x}\,,$$

or

$$\frac{\partial n}{\partial t} = -\frac{\partial}{\partial x}\,(nv)\,. \qquad (12)$$

Differentiating both sides of Eq. (12) with respect to time gives

$$\frac{\partial^2 n}{\partial t^2} = -\frac{\partial^2}{\partial t\,\partial x}\,(nv)\,. \qquad (13)$$

Differentiating both sides of Eq. (10) with repect to x gives

$$\frac{\partial^2 n}{\partial x^2}\left(\frac{\gamma kT}{m}\right) = -\frac{\partial^2}{\partial x\,\partial t}\,(\mathrm{nv})\,. \qquad (14)$$

We now assume that $\partial^2/\partial x\,\partial t = \partial^2/\partial t\,\partial x$. (This places some minor restrictions on the function nv that are of negligible importance here.) Combining Eqs. (13) and (14), then, we obtain the desired equation,

$$\frac{\partial^2 n}{\partial x^2}\left(\frac{\gamma kT}{m}\right) = \frac{\partial^2 n}{\partial t^2}\,. \qquad (15)$$

Equation (15) represents the propagation of a one-dimensional, longitudinal compression wave in a medium, with a speed $v = (\gamma kTm^{-1})^{1/2}$. This is the same as the Langmuir-Tonks expression for long-wavelength ionic sound waves propagating in a plasma.[23] This case is for "free space" (no ion–gas-atom collisions) propagation, and we will denote this velocity by

$$v_0 = (\gamma kTm^{-1})^{1/2}\,. \qquad (16)$$

Thus Eq. (15) can be rewritten as

$$v_0^2\,\frac{\partial^2 n}{\partial x^2} = \frac{\partial^2 n}{\partial t^2}\,. \qquad (17)$$

Case of Ion-Neutral Collisions. – If collisions between ions and the background gas atoms occur, some of the momentum added to the plasma system by the pressure term will be lost to the neutrals, and thus be removed from the momentum term [see Eq. (10)].

In order to calculate the collision rate of a given ion with the gas atoms, the assumption is made that the coherent velocity of the ions due to the ionic sound wave motion is small compared to the thermal, random velocity of the ions. Under this assumption the average rate of collision is independent of the ionic sound wave motion, and can be expressed as[24]

$$\nu_c = n_g v_T\,\sigma\sqrt{2}\,, \qquad (18)$$

where n_g is the gas atom density, v_T is the thermal speed of atoms and ions, and σ is the collision cross section.

The further assumption is made that every time an ion collides with a gas atom, the ion loses

[23] Igor Alexeff and R. V. Neidigh, *Phys. Rev.* **129**, 516 (1963).

[24] G. Joos, *Theoretical Physics*, pp. 559, 585, Hafner Publishing Co., New York, 1950.

all the directed ion-wave momentum which it had before the collision. This assumption, while not strictly true, is not too unrealistic because the fraction of directed energy lost per collision is large.[23] Thus Eq. (9) becomes, for the case of ion–gas-atom collisions,

$$\Delta P = \Delta n\,(\gamma kT) = -m\,\Delta x\,\frac{\partial}{\partial t}(nv) - mv\nu_c n\,\Delta x\ , \quad (19)$$

or

$$\frac{\partial n}{\partial x}\left(\frac{\gamma kT}{m}\right) = -\frac{\partial}{\partial t}(nv) - v\nu_c n\ . \quad (20)$$

Differentiating both sides of Eq. (20) with respect to x gives

$$\frac{\partial^2 n}{\partial x^2}\left(\frac{\gamma kT}{m}\right) = -\frac{\partial^2}{\partial x\,\partial t}(nv) - \nu_c\frac{\partial}{\partial x}(nv)\ . \quad (21)$$

Substituting from Eqs. (12), (13), and (16) into Eq. (21) gives

$$v_0^2\frac{\partial^2 n}{\partial x^2} = \frac{\partial^2 n}{\partial t^2} + \nu_c\frac{\partial n}{\partial t}\ . \quad (22)$$

Equation (22) is the desired differential equation of motion, representing the propagation of ionic sound waves in a plasma, taking into consideration loss of wave energy due to collisions between ions and background gas atoms.

Dispersion Relation. – Suppose we choose a solution for Eq. (22) of the form

$$n = n_0 + n'\exp i(kx - \omega t)\ . \quad (23)$$

If $n' \ll n_0$, then Eq. (23) represents a small-amplitude density wave propagating along the plasma column, where k and ω are the propagation constant and angular frequency, respectively, of the density wave. (Note that we now have two meanings for k; however, Boltzmann's constant always appears with T.) Substituting Eq. (23) into Eq. (22) gives the dispersion relation,

$$\omega^2 + i\nu_c\omega - v_0^2k^2 = 0\ , \quad (24)$$

where, in general, ω and k are both complex. In practice, one usually requires one of these quantities to be real and then solves the dispersion relation for the other one in terms of the real one.

If we require ω to be real, then we can solve Eq. (24) to determine what values of k will be allowed if Eq. (22) is to have a solution of the form given in Eq. (23). Doing this we find that

$$k = \pm\frac{\omega}{v_0}\left[\frac{1}{2}+\frac{1}{2}\sqrt{1+(\nu_c/\omega)^2}\right]^{1/2} + \frac{i\nu_c}{2v_0}\left[\frac{1}{2}+\frac{1}{2}\sqrt{1+(\nu_c/\omega)^2}\right]^{1/2}\ . \quad (25)$$

Similarly, if we require that k be real, we find that

$$\omega = \pm kv_0\left[1+\frac{1}{4}(\nu_c/\omega)^2\right]^{-1/2} - \frac{i\nu_c}{2}\ . \quad (26)$$

If we substitute Eq. (25) into Eq. (23), then we find that the speed, v_s, and the damping factor, d.f., of the propagating density disturbance are given by

$$v_s = v_0\left[\frac{1}{2}+\frac{1}{2}\sqrt{1+(\nu_c/\omega)^2}\right]^{-1/2}\ , \quad (27)$$

$$\text{d.f.} = \exp\left\{-\frac{c}{2v_0}\left[\frac{1}{2}+\frac{1}{2}\sqrt{1+(\nu_c/\omega)^2}\right]^{-1/2}x\right\}\ . \quad (28)$$

Similarly, for the k-real–ω-complex case, we find that

$$v_s = v_0\left[1+\frac{1}{4}\left(\frac{\nu_c}{\omega}\right)^2\right]^{-1/2}\ , \quad (29)$$

$$\text{d.f.} = \exp\left(-\frac{\nu_c}{2}t\right)\ . \quad (30)$$

Thus, it is seen that the effects of the ion–gas-atom collisions on the propagating density wave are twofold. In both cases, not only is the wave exponentially damped (spacewise for ω real, timewise for k real), but also the wave propagates at less than the free-space velocity, v_0.

In Fig. 4.15 plots of v_s/v_0 vs ν_c/ω are shown for the two cases. For low values of ν_c/ω, the velocities predicted by the two cases are roughly the same. At large values of ν_c/ω, however, the

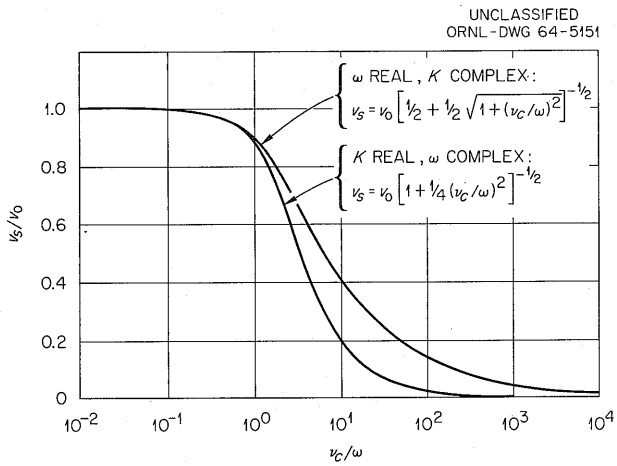

Fig. 4.15. Retardation of Ionic Sound Waves Due to Ion–Gas-Atom Collisions.

velocity predicted by the k-real case is much smaller than that predicted by the ω-real case.

Equation (27) is found to be almost identical to the corresponding equation given by Hatta and Sato,[22] if the assumptions made in the present derivation (i.e., that the electron temperature is much larger than the ion temperature, and that electron–gas-atom collisions are unimportant) are incorporated into that equation. (In their derivation, these authors first solved a set of linearized equations obtained from Poisson's equation, and the ion and electron equations of motion and continuity. They then assumed an isothermal plasma and a sinusoidal density disturbance to obtain a dispersion relation. Upon making certain other assumptions, including the one that ω be real, they obtained the discussed phase-velocity expression.)

4.6.3 Experimental Apparatus and Procedures

Figure 4.16 shows the types of discharge tubes used. Most of the measurements were made in a cylindrical tube about 50 cm in length and 4 cm in diameter, as shown in Fig. 4.16(*a*). Some measurements were also made in cylindrical tubes having smaller and larger diameters, as well as in a tapered discharge tube as shown in Fig. 4.16(*b*).

The tubes were operated in the ordinary glow mode, under both space-charge-limited and non-space-charge-limited conditions of the hot-filament cathode. Direct-current potentials across the tubes normally ranged from about 50 to 250 v. Discharge currents ranged from a few milliamperes to approximately 300 ma. Background gas pressures ranged from a few microns to several millimeters of mercury.

Several diagnostic tools were used to study the glow discharges. These included "floating" probes, an ordinary Langmuir probe with an automatic converter circuit,[25,26] "double" probes, a photomultiplier tube, a fast stroboscopic device,[19,27] and a double-beam oscilloscope.

---

[25]See, for example, R. S. Harp, *Rev. Sci. Instr.* **34**, 416 (1963); H. W. Jones and P. Saunders, *J. Sci. Instr.* **37**, 457 (1960).

[26]Igor Alexeff and W. D. Jones, *Thermonuclear Div. Semiann. Progr. Rept. Apr. 30, 1963*, ORNL-3472, p. 47; I. Alexeff and W. D. Jones, *Thermonuclear Div. Semiann. Progr. Rept. Oct. 31, 1963*, ORNL-3564, p. 62.

[27]Igor Alexeff and R. V. Neidigh, *Thermonuclear Div. Semiann. Progr. Rept. Oct. 31, 1962*, ORNL-3392, p. 41.

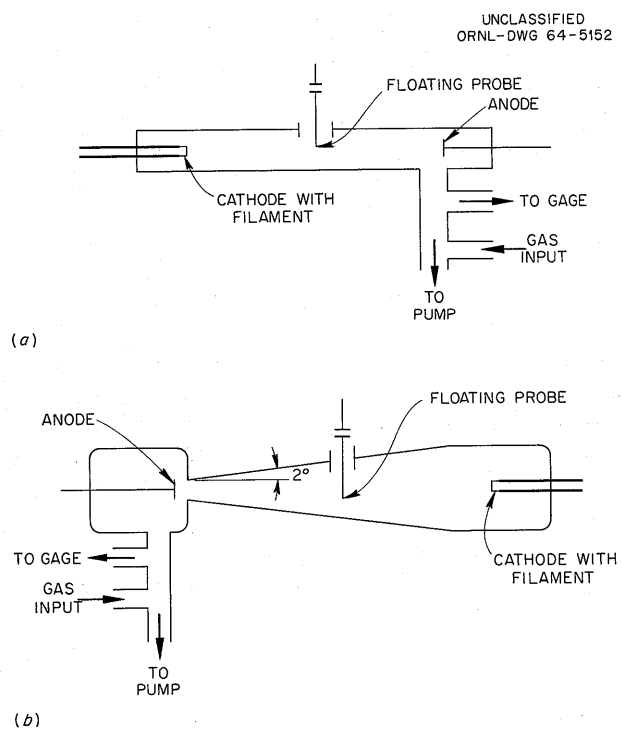

Fig. 4.16. Types of Discharge Tubes Used: (*a*) Cylindrical, (*b*) Tapered.

The "floating" probe consisted of a small, cylindrical wire protruding into the discharge, being isolated from ground (with respect to direct current) by a series condenser. The main uses of such a probe were to monitor the changes in potential of the discharge (the signal from the probe being fed directly to an oscilloscope) and to provide a synchronizing signal for the oscilloscope.

The "double" probes system consisted of two small, parallel, cylindrical wires protruding into the plasma. Such a probe could be used to measure either electric fields or plasma ion density. By connecting the leads to the two probes directly into a Tektronix type G plug-in unit (a differential preamplifier), both dc and transient electric fields could be measured. By properly biasing the probes, relative to each other, and feeding the voltage developed across a connecting resistor into the type G plug-in unit, relative ion density fluctuations could be measured.

The standard photomultiplier tube was mounted inside a light-tight box, with a collimator leading to the tube window. The photomultiplier tube could be used either in conjunction with the oscilloscope to measure the light output of the plasma at a given point as a function of time, or the output of the tube could be used to provide a synchronizing signal for the oscilloscope. Also, at low pressures where the moving striations were too faint to be seen by use of the stroboscope, the photocell could be moved along the tube to make phase-shift measurements,[28] thus allowing the striation velocities to be calculated from the measured wavelengths and observed frequencies.

The stroboscope, whose operation in connection with the study of moving striations has been discussed previously,[18,19] was used primarily to measure the velocity of the moving striations. Under normal conditions the moving striation originated at the anode and propagated in the direction of the cathode. At the higher pressures the striations could be observed to propagate all the way to the Faraday dark space. At the lower pressures, however, the striations sometimes propagated only a short distance before the light fluctuations became too dim to be seen. In general, the velocity measurements were made over as large a distance as the striations could be seen to move. Thus, for the most part, only average velocities of the moving striations were measured.

As is indicated by the design of the tubes shown in Fig. 4.16, the system was continuously flushed with new gas, as well as continuously pumped. This procedure greatly reduced contamination problems arising from slow degassing of the walls, electrodes, etc., such as can occur with the sealed discharge tubes which are often used for such studies.

4.6.4 Data and Interpretation

Cylindrical Discharge Tubes. – Below are shown plots of the moving-striation velocity measurements which have been made in the inert gases in cylindrical discharge tubes, as a function of background gas pressure. In Figs. 4.17 and 4.18, the discharge tubes were about 50 cm in length and 4 cm in diameter. The interelectrode spacing ranged from about 20 to 40 cm. In Fig. 4.19, the discharge tube was about 150 cm in length and 7.5 cm in diameter. The interelectrode spacing ranged from 20 to 100 cm. In none of the tubes was a dependence of the striation velocity upon interelectrode spacing found.

Some velocity measurements were also made in tubes down to 1 cm in diameter, though a complete set of such measurements (as a function of pressure) was not made. For the few measurements made, no dependence on tube diameter was observed.

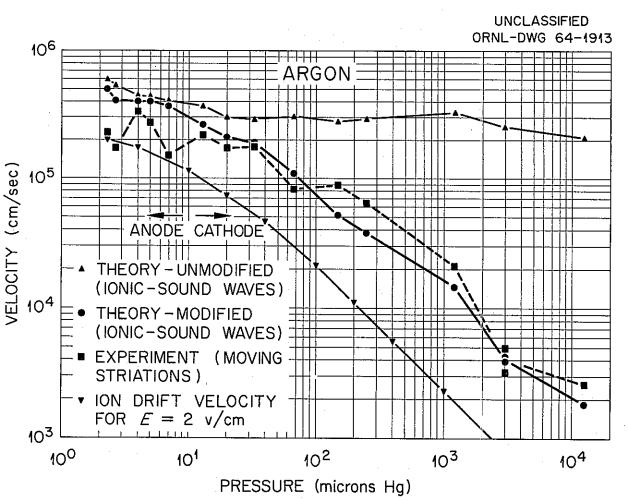

Fig. 4.17. Comparison of Experiment and Theory for Striations in a 4-cm-diam Tube – Argon.

[28]See, for example, T. Donahue and G. H. Dieke, *Phys. Rev.* **81**, 248 (1951).

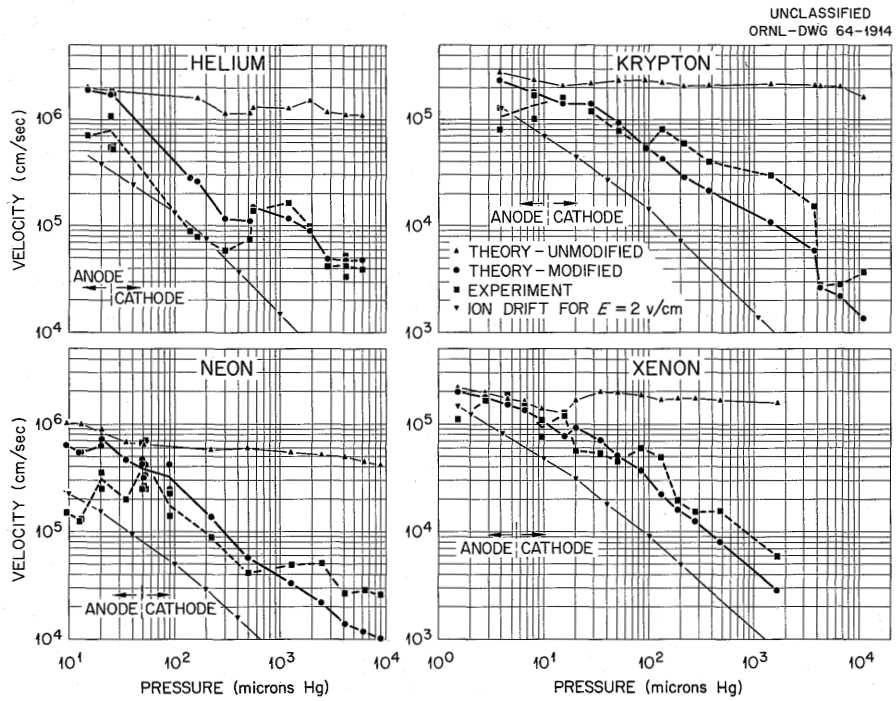

Fig. 4.18. Comparison of Experiment and Theory for Striations in a 4-cm-diam Tube – Helium, Neon, Krypton, and Xenon.

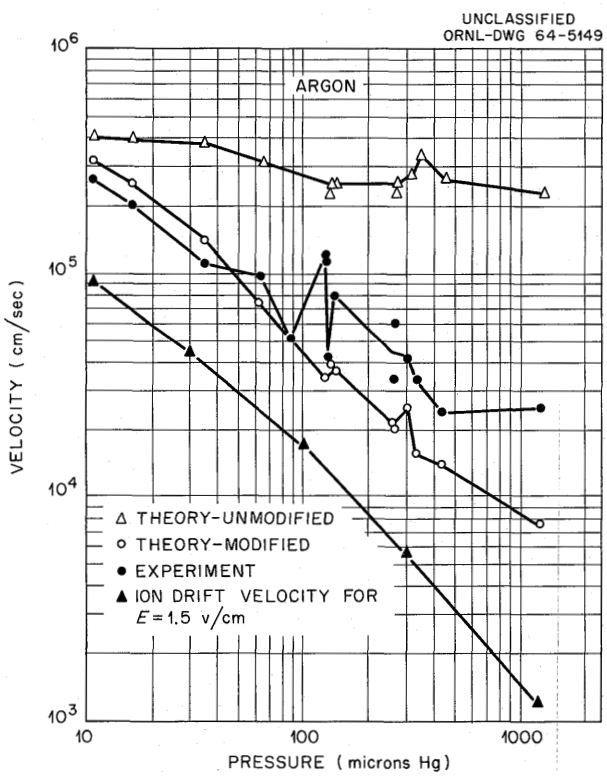

Fig. 4.19. Comparison of Experiment and Theory for Striations in a 7.5-cm-diam Tube – Argon.

Figures 4.17–4.19 also show the velocity curves predicted by the modified ionic sound wave theory. [It was found that, even though the predictions of both cases (see Fig. 4.15) were in agreement with experiment at low pressures, only the predictions of the ω-real–k-complex case were in agreement with experiment at high pressures. Thus, the theoretical curves shown in the figures were calculated for the ω-real–k-complex case.] For the purpose of comparison, velocities predicted by the unmodified theory are also shown. The bottom curve in each figure shows the approximate drift velocities of the discharge ions, based on measured values of the pressure and the average electric field in the positive column of the discharge, and on the drift-velocity curves given by Brown.[29]

The striation velocity data shown in Figs. 4.17–4.19 are uncorrected for the ion drift velocities. As is indicated in the figures, at the lowest gas pressures the direction of propagation of the moving striations was found to be reversed, that is, from cathode to anode. Thus, at the lowest

[29] S. C. Brown, *Basic Data of Plasma Physics*, pp. 65, 72, Wiley, New York, 1959.

pressures, the ion drift velocities should be added to the experimentally measured striation velocities, whereas at the higher pressures the drift velocities should be subtracted from the striation velocities. Even without these corrections, however, which are around 10% at the high pressures but as much as 100% at the low pressures, the agreement between the observed striation velocities and the wave velocities predicted by the modified ionic sound wave theory is remarkably good. For example, in the case of argon, over a pressure range of almost 10,000 to 1 and a velocity range of over 200 to 1, theory and experiment disagree at most by a factor of 3.

Also apparent from the figures is the inability of the unmodified theory to predict accurately the observed velocities. Equally clear is the fact that the striations cannot be interpreted in terms of ions drifting in the average electric field, especially at the higher pressures.

The striations noted at low pressure, which move in the direction of the anode, may represent a heretofore unreported variety of the so-called negative striations. Other people who have seen negative striations, as originally Donahue and Dieke,[28] have reported their velocities to be considerably higher than the velocities of the corresponding positive striations. Here, except for the effect of the ion drift, the two velocities appear to be equal.

In the theoretical calculations, the value of γ in the Langmuir-Tonks velocity equation was taken to be $\frac{5}{3}$. The T_e value used was the one measured experimentally by use of the swept Langmuir probe. Due to the relatively low sweep rate, the T_e value measured is an average value. The angular frequency, ω, required by the modified theory was taken to be 2π times the gross plasma oscillation frequency measured experimentally. In the calculation of ν_c [see Eq. (18)], the thermal velocity, v_T, of the ions and gas atoms was calculated from $v_T = (3kTm^{-1})^{1/2}$, where T was taken to be room temperature ($\sim \frac{1}{35}$ ev). Since values of σ for these low energies are not known, simple calculations (see Appendix), based on known ion drift velocity data,[29] were made for this parameter.

Electron-density measurements were performed in the usual manner, utilizing the saturation current obtained from the Langmuir probe characteristic. Densities in the range 5×10^8 to 1×10^{10} were found. It might be emphasized that these rather large variations in density arise primarily from the large ranges of discharge currents used, rather than being any indication of the density modulations which accompany moving striations, and which were not measured in these experiments. Some relative ion-density measurements were made, however. Although measurements were not made for all the gases studied, the relative ion-density fluctuations, as measured by the double-probe technique, were found to be never greater than about 30% in argon. The approximate ranges of some of the other parameters observed and calculated for each gas are shown in Table 4.1.

In Fig. 4.20 are shown some data which have been reported previously.[18,19] These observations were made at pressures ranging from 10 to 50 μ Hg, before the modified theory of ionic sound waves had been developed. The figure shows a plot of the average experimental velocity of the moving striations as a function of ionic mass of the inert gases. Here the experimental velocities have been normalized to an electron temperature of 1 ev, the normalization being made in accordance with the Langmuir-Tonks ionic sound wave velocity equation. The straight lines give the theoretical velocity dependence of ionic sound waves on ionic mass for the same electron temperature normalization, again, as given by the Langmuir-Tonks equation. The agreement of the experimental points with the theoretical lines shows that the striation velocities exhibit the same dependence on ion mass as do ionic sound waves. A calculation for these data showed that the electron-temperature

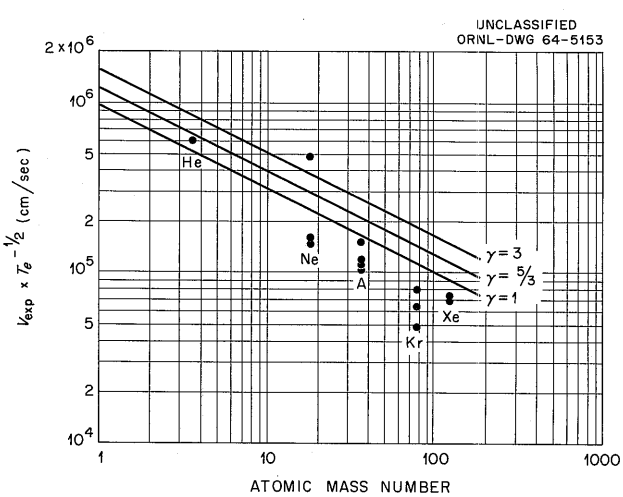

Fig. 4.20. Striation Velocity vs Ionic Mass for a Velocity Normalization to $T_e = 1$ ev.

Table 4.1. Approximate Values of Some of the Parameters Observed and Calculated

Gas	Pressure (μ Hg)	T_e (ev)	σ (cm^2/atom)	$\nu_c^{(a)}$ (sec^{-1})	ω (sec^{-1})	ν_c/ω
			$\times 10^{-15}$	$\times 10^7$		
He	15–6200	2.8–8.8	4	$2.56P^{(b)}$	4.7×10^4–1.1×10^6	0.7–1400
Ne	9.5–9000	2.1–12.5	4.7	$1.39P$	1.9×10^4–6.3×10^5	1.8–4500
Ar	2.3–12,600	1.0–8.5	7.8	$1.59P$	5.7×10^3–3.1×10^5	1.2–36,000
Kr	3.8–11,000	1.3–3.8	8.8	$1.23P$	4.2×10^3–1.2×10^5	2.6–51,000
Xe	1.5–1650	1.3–3.8	10.8	$1.23P$	3.9×10^3–1.4×10^5	2.0–13,000

[a] For pressures below the "critical" pressures, the expressions here were multiplied by $\nu_{drift}/\nu_{thermal}$.
[b] P is in mm Hg.

normalization caused the rms scatter in the experimental points to decrease by more than a factor of 2, thus indicating that the striation velocities also have the same temperature dependence as do the ionic sound waves.

At the time the data in Fig. 4.20 were reported, the assumption of a group velocity was made to explain why the observed velocities fell somewhat below the theoretical ("free-space") lines. The present theory predicts the observed velocities to be somewhat less than the free-space velocities, so that the assumption of a group velocity is no longer needed.

Were it not for one factor which as yet has not been discussed, the interpretation of the observed close agreement between experiment and theory would be obvious: that moving striations in the inert gases are simply manifestations of propagating ionic sound waves. The important factor which has not been discussed is damping. According to both Eqs. (28) and (30), the ionic sound waves should be strongly damped by the ion–gas-atom collisions. For some of the runs at higher pressures, it is not unusual for the damping factor to be of the order of 10^{-4}, for the observed propagation distance. Experimentally, this strong damping is not observed. In fact, the higher the gas pressure the less damping there appears to be. This would seem to suggest that some mechanism may be operative at the higher pressures which restores energy to the waves as they propagate down the tube. Energetically, this is quite possible, since the power input to the discharge tubes is always much greater than the predicted energy loss rate of the waves to the background gas atoms.

If the association of moving striations with ionic sound waves is correct, then it follows from the preceding discussion that the theory cannot be complete at the higher pressures, since it contains no mechanism allowing for energy to be returned to the waves as they travel down the tube. Thus, the interpretation must be tempered by the realization that the good agreement of experiment and theory at the higher pressures may be fortuitous. At the low pressures, however, where the velocity curves exhibit obvious leveling-off tendencies near the free-space ionic sound wave velocities, the evidence in favor of the proposed interpretation is more convincing.

Tapered Discharge Tubes. – Kenjo and Hatta[30] have recently made observations of moving striations in neon in tapered discharge tubes similar to the one shown in Fig. 4.16(*b*). These workers reported that at constant gas pressure the distance, λ, between striations was proportional to d^{β}, where d was the tube diameter and β ranged from 1.5 to 2.0.

[30] T. Kenjo and Y. Hatta, *J. Phys. Soc. Japan* **18**, 910 (1963).

It is well known,[31] empirically, that the following relation holds in positive columns (for cylindrical geometry) having moving striations:

$$v = \nu\lambda \ , \tag{31}$$

where v and λ are the observed striation velocity and interstriation distance, respectively, and ν is the observed plasma oscillation frequency.

Since the observations of Kenjo and Hatta were made at constant ν, their results, when combined with Eq. (31), would indicate that the velocity of the moving striations showed a rather large, systematic variation along the length of the tapered tubes. But the present theory [see Eqs. (27) and (29)] would predict that at constant pressure and constant plasma oscillation frequency (i.e., constant ν_c and constant ω), the striation velocity should be constant along the length of the tubes.

In Fig. 4.21 are shown the results of the present experiment, using argon in a tapered tube. The case with the anode at the small end of the tube will be discussed first. For this case the frequency of oscillation was found to be constant along the tube, and the wavelength, λ, was found to increase with increasing diameter; however, the rate at which λ changes with diameter seems to vary with pressure. At the lowest pressure, λ changes relatively little with tube diameter, whereas at the higher pressures it appears to be approaching a linear relationship with the diameter. These results are in qualitative agreement with the results Kenjo and Hatta found using neon, though the dependence is not as strong. The velocities predicted by the modified theory, while not agreeing with the individual velocities measured, agree within a factor of 2 with the *average* velocity of the moving striations at the different pressures.

Except for one isolated case, the observations made with the anode at the large end of the tube (i.e., reversed current flow) are not even in qualitative agreement with the corresponding ones of Kenjo and Hatta in neon. The following differences were noted:

1. Moving striations could be observed over the *same* current ranges as were observed for the anode at the small end of the tube, whereas Kenjo and Hatta were able to see striations only at relatively low currents, compared to those for which striations could be seen with the anode at the small end.

2. The frequency of oscillation was not constant along the length of the tube, but rather increased toward the small end.

3. The striation velocities generally increased with decreasing tube diameter, rather than with increasing diameter. [Kenjo and Hatta did not actually make velocity measurements; we are here deducing, by means of Eq. (31), what they would have observed had they made measurements.] Also, at the lowest pressure, it was found that positive or negative striations could be produced at will by varying the discharge current between the space-charge-limited value and a less-than-1%-smaller value at non-space-charge-limited conditions of the cathode. The difference between the two velocities was in good agreement with that expected from the ion-drift effect. (In one isolated case, when the tube was being operated far from space-charge-limited conditions of the hot cathode, the plasma oscillation suddenly became quite constant and sinusoidal throughout the tube. At this time the observations qualitatively resembled those of Kenjo and Hatta, though the

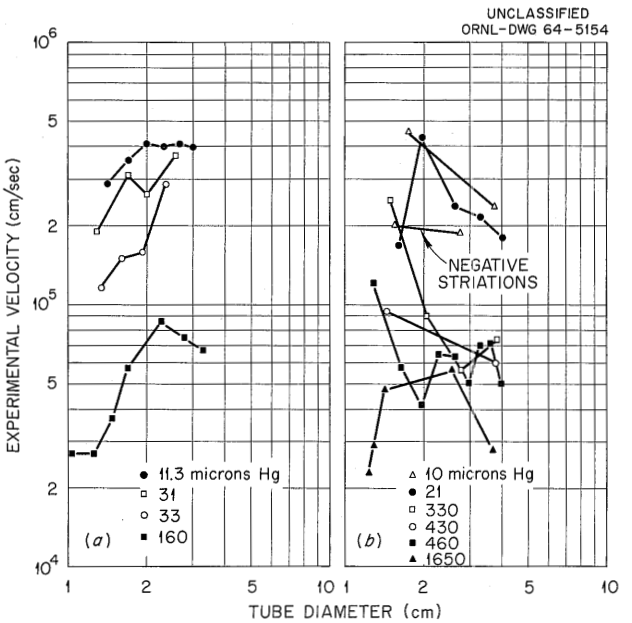

Fig. 4.21. Moving Striations in Argon in a Tapered Tube: (*a*) Anode at the Small End, (*b*) Anode at the Large End.

[31] G. Francis, *Handbuch der Physik*, vol. 22, p. 137, 1956.

change in wavelength along the tube was much less than that observed by them.) Again, the predictions of theory were usually in good agreement with experiment, though in a few instances disagreement by as much as a factor of 5 was found.

Perhaps the first thing to be concluded from the present experiment is that our observations sometimes differ from the observations of Kenjo and Hatta – that is, moving striations do not always propagate faster in the larger section of the tube. Thus, the observed velocity variations may be due to secondary effects of some kind, related perhaps to the tapered walls. Cooper and Oleson[32] and Coulter *et al.*,[33] for example, have noted unusual effects at junctions in tubes where sections of unequal diameter meet; and Crawford and Pagels[34] have discussed the formation of local double sheaths in constricted discharge tubes.

A second important factor to be noted is that the striation velocities are never significantly greater than the predicted free-space velocity. In fact, in Fig. 4.21(*a*), at the lowest pressures there seems to be a tendency to approach the free-space velocity along the entire length of the tube, as might be expected from the theory. In Fig. 4.21(*b*) this same tendency seems to be present, though it is somewhat less unambiguous.

By means of a series of double-probe systems positioned along the length of the positive column, measurements were made to determine if variations in the dc electric field strength along the column might be responsible for the velocity variations observed in the tapered tubes. The dc electric fields were found to remain remarkably constant, with respect both to position along the column and to changes in the background gas pressure.

Another factor which could produce a velocity variation along the length of the tube would be a variation of gas pressure along the column. According to the modified ionic sound wave theory, an increase in pressure (i.e., an increase in ν_c), for a given value of ω, leads to a slower wave. Measurements in argon discharges by McGuckin[35] have shown that, indeed, pressure gradients can exist in positive columns, with the pressure being greatest at the anode end. While the predicted velocity variations due to such pressure variations along the column would be in qualitative agreement with those observed in the present set of experiments (except for the isolated case noted above), they would be in disagreement with all of the (inferred) velocity measurements made by Kenjo and Hatta for the anode at the large end of the tube. In any event, the pressure differences would not be expected to be large enough to produce the velocity differences observed.

Thus, even though there appears to be a general agreement of experiment and theory for the tapered tubes, the agreement does not seem to be as systematic as that observed for the cylindrical tubes. Again, the strong damping predicted by the theory was not observed.

It should be pointed out that, while only small velocity variations were seen along the axis of the cylindrical tubes in the present work, other workers[28,36] have reported variations of velocity in cylindrical tubes as large as those observed here in the tapered tubes.

A Possible Source of the Observed Frequencies. – In the effort to correlate moving striations and ionic sound waves, it was speculated that the observed frequencies are connected in some way with a simple, cavity-type oscillation involving some part of the discharge tube. In order to see if the interstriation distance, λ, might be constant enough to be roughly correlatable with some dimension of the discharge tube, calculations of λ for some of the experimental data were made (by dividing the observed velocities by the corresponding observed plasma oscillation frequencies). At the time the calculations were made, only positive striations had been seen. Also, velocity measurements had been made by use of the stroboscopic technique only. For the data shown in Figs. 4.17 and 4.18, the following average values were obtained: $\lambda_{He} = 7.0$ cm; $\lambda_{Ne} = 8.3$ cm; $\lambda_{Ar} = 7.0$ cm; $\lambda_{Kr} = 8.9$ cm; and $\lambda_{Xe} = 13.4$ cm.

[32] A. W. Cooper and N. L. Oleson, *Proc. Intern. Conf. Ionization Phenomena Gases, 5th Conf., Munich, 1961*, vol. I, p. 566 (1962).

[33] J. Coulter, N. Armstrong, and K. G. Emeleus, *Proc. Phys. Soc. (London)* **77**, 476 (1961).

[34] F. W. Crawford and H. R. Pagels, Microwave Lab. Rept. No. 962, p. 13 (1962) (W. W. Hansen Laboratories of Physics, Stanford University, Stanford, Calif.).

[35] J. P. McGuckin, *Brit. J. Appl. Phys.* **14**, 528 (1963).

[36] M. K. Pigg, J. B. Burton, and N. B. Oleson, *Proc. Intern. Conf. Ionization Phenomena Gases, 3rd, Venice, 1957*, pp. 833–49.

Thus, it would appear that the average interstriation distance for these data is roughly a constant, independent of the type gas used. To a first approximation, this is what might be expected if a cavity-type oscillation is the source of the moving striations. It is also noted that this distance is roughly of the order of the dimensions of the discharge tube, ranging from two to three times the tube diameter.

The calculations also suggested that λ is somewhat pressure dependent, seemingly showing a tendency to be larger for the intermediate ranges. This tendency seemed more pronounced the heavier the gas atom. Both of these tendencies can be seen from Fig. 4.22. It is not possible, using the present data, to be certain of the exact pressure dependence of λ, since no effort was made to keep constant other parameters which may also affect λ. For example, the discharge currents at which moving striations could be seen sometimes varied radically from one pressure to the next. Thus, Fig. 4.22 may include the effects of other parameters being varied independently of the pressure.

Taking an average of the λ's for *all* of the gases gave $\lambda_{av} = 9.1 \pm 4.1$ cm, where the deviation is the statistical rms scatter. In Figs. 4.23 and 4.24 are shown the experimental velocity curves given

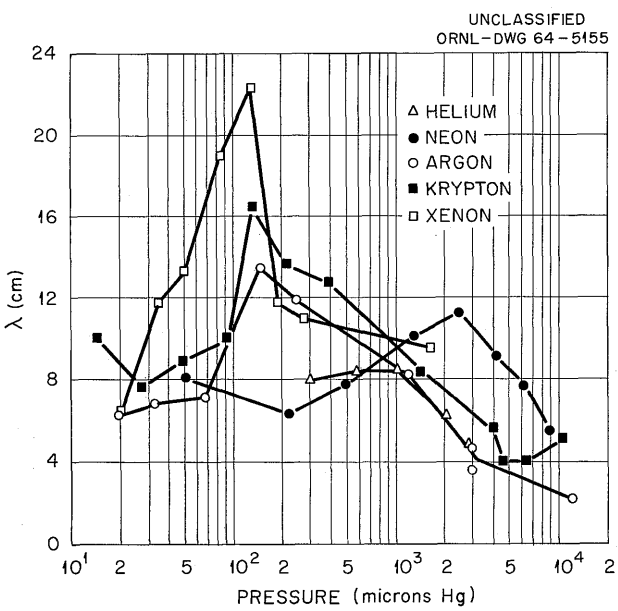

Fig. 4.22. Calculated Interstriation Distance vs Pressure for Measurements Made in a 4-cm-diam Tube.

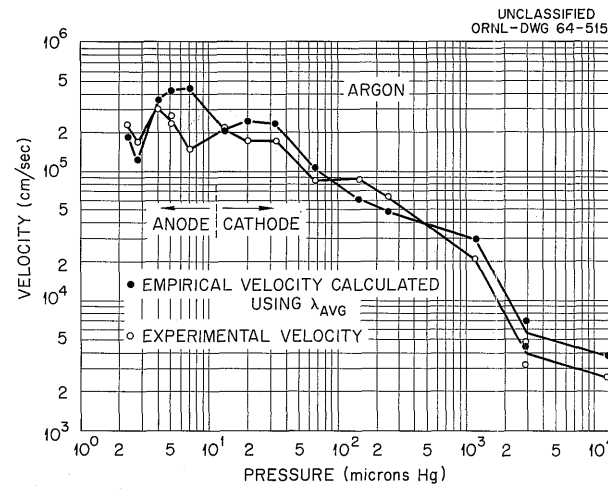

Fig. 4.23. A Comparison of Experimental Striation Velocities and Velocities Calculated Empirically Using a Constant, Average Interstriation Distance — Argon.

in Figs. 4.17 and 4.18. Also shown in these two figures is a second set of curves based on the above grand-average wavelength, λ_{av}. This second set of velocity curves was calculated according to Eq. (31), with λ_{av} replacing λ in the equation and with the experimentally observed plasma oscillation frequencies being used for ν. Velocities were calculated for all of the experimental data, even though λ_{av} was obtained (as noted previously) from only part of the experimental measurements. Comparison of the experimental curves with the calculated curves shows, for the most part, both quantitative and qualitative agreement. This agreement over such wide ranges of pressure and velocity is certainly suggestive that a characteristic dimension is a rather basic property of the moving striations, independent of the gas used.

If the striation wavelength depends upon the diameter of the tube, then longer wavelengths would be expected for a larger tube. Although only argon was used in the 7.5-cm-diam tube used to obtain the data shown in Fig. 4.19, it was found that, indeed, for this gas the striation wavelength was increased. The average wavelength found for these data was $\lambda_{av} = 18.5$ cm which, again, is between two and three times the tube diameter. The distances between the electrodes, between the electrodes and the tube ends, and between the electrodes and the probe were varied appreciably without any dependence of the striation wavelength upon any of these dimensions being observed. As

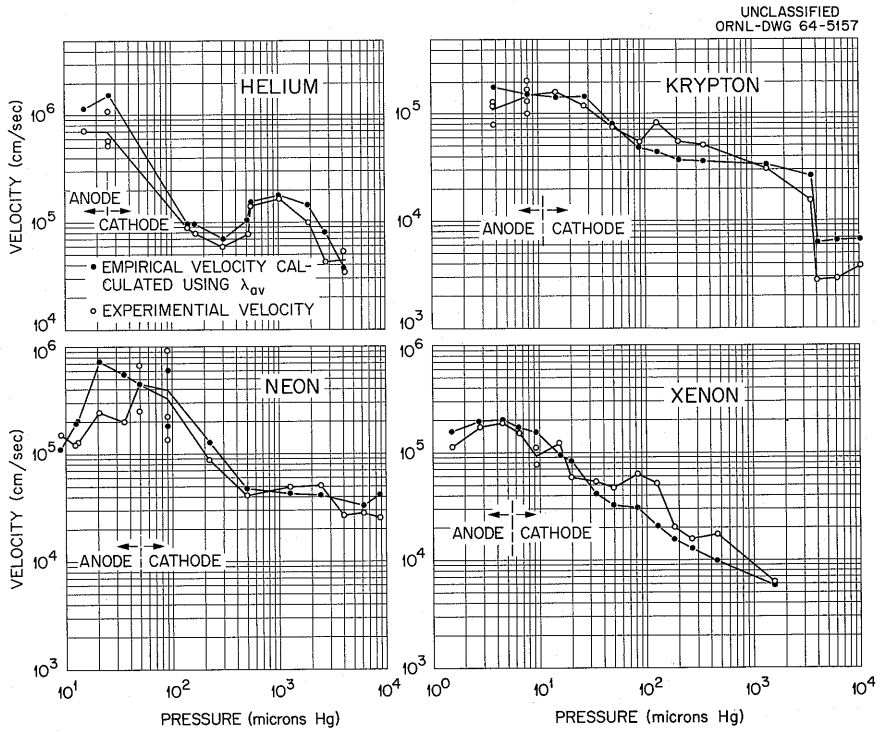

Fig. 4.24. A Comparison of Experimental Striation Velocities and Velocities Calculated Empirically Using a Constant, Average Interstriation Distance – Helium, Neon, Krypton, and Xenon.

for the smaller tube, the wavelength showed some pressure dependence. Instead of there being a general tendency to increase at the intermediate pressures, however, there seemed to be a tendency to fluctuate erratically from relatively large to relatively small values in this range.

Thus, in view of the results of the limited study which has been made, there would appear to be a rough dependence of the wavelength upon the diameter of the discharge tube. This may imply that some cavity-type oscillation involving the radial dimensions of the tube is involved in the production of the observed frequencies. Lord Rayleigh[37] has shown that for a pressure maximum at the wall, the longest wavelength which will exist as a radial oscillation is approximately 1.7 times the diameter; for a pressure minimum at the wall, the longest wavelength is approximately 1.3 times the diameter. The present calculations would thus suggest a pressure maximum at the tube wall. For this case, the velocity of the wave is independent of boundary conditions at the wall.

This is not the first time that it has been suggested that discharge oscillations and moving striations are intimately related. Armstrong *et al.*,[20] for example, have reviewed the connection between moving striations and electrical oscillations. Zaitsev,[38] also, has advanced the hypothesis that discharge oscillations produce moving striations.

4.6.5 Appendix: Calculation of σ

The rate of collision of an ion with the background gas atoms depends upon the velocity of the ion. For a given electric field, the dominant ion velocity will be determined by the collision rate. At high pressures, where the average ion travels only a short distance between collisions, the ion drift velocity will be small, so that the dominant velocity will be the thermal velocity of the ions. At low pressures, however, the ion drift velocity may exceed the thermal velocity, in which

[37] J. W. S. Rayleigh, *The Theory of Sound*, vol. I, p. 331; vol. II, p. 161, Dover Publishing Co., New York, 1945.

[38] A. A. Zaitsev, *Proc. Acad. Sci. USSR* (English Transl.) **79**, 779 (1951).

case the dominant velocity will be the drift velocity.

In the present calculations it is assumed that the ions have a thermal velocity corresponding to room temperature. It is further assumed that a uniform electric field of 2 v/cm is present in the positive column, this being the approximate value observed experimentally. Making these assumptions and using known drift velocity curves,[29] it can be shown easily that the critical pressures for the rare gases vary from about 100 μ Hg for helium to about 25 μ Hg for xenon. Here, critical pressure is defined as that pressure at which the thermal velocity of an ion is equal to the drift velocity of the ion.

Observation of Eq. (27), which gives the wave velocity predicted by the modified ionic sound wave theory, shows that the velocity has the strongest dependence on σ when ν_c/ω is large. This, it turns out from the way in which ω is observed to vary with pressure, occurs usually at pressures in the range of the critical pressures, and higher. Thus, in the following derivation of an expression for σ, the high-pressure case has been considered. That is, it is assumed that the dominant velocity relevant to the ion–gas-atom collision rate is the thermal velocity. Although at pressures below the critical pressures the dominant velocity becomes the drift velocity, as was noted above the accuracy of σ is somewhat less important at the lower pressures.

Let v_D be defined as the average drift velocity which an ion acquires between collisions. Then

$$v_D = \frac{1}{2} at \,, \tag{1'}$$

where a is the acceleration of the ion due to the electric field in the column, and t is the time between collisions. Replacing a by eE/m and t by L/v_T gives

$$v_D = \frac{eEL}{2mv_T}, \tag{2'}$$

where e is the unit electronic charge, E is the electric field, L is the mean free path between ion–gas-atom collisions, m is the ionic mass, and v_T is the thermal velocity of the ions.

Replacing L in Eq. (2′) by $(N_g\sigma)^{-1}$, where N_g is the background gas density and σ is the collision cross section, and solving the resulting expression for σ gives

$$\sigma = \frac{e}{2v_T} \cdot \frac{E}{N_g} \cdot \frac{L}{v_D} \,. \tag{3'}$$

Under the assumptions made, the first factor in Eq. (3′) is constant; the second factor varies inversely with the pressure; and, from the drift velocity curves given by Brown,[29] the third factor varies approximately linearly with pressure for small fields and high pressures. Thus, for the present case, σ is approximately independent of pressure at pressures above the critical pressures. The values of σ shown in Table 4.1 were calculated by use of Eq. (3′), using a background gas pressure of 100 μ Hg. The values of σ obtained here seem reasonable when compared with charge-exchange cross-section curves appearing in the literature,[39,40] assuming that straightforward extrapolations to lower ion energies can be made for these curves.

---

[39] C. F. Barnett, W. F. Gauster, and J. A. Ray, *Atomic and Molecular Collision Cross Sections of Interest in Controlled Thermonuclear Research*, ORNL-3113 (1961), p. 48.

[40] S. N. Ghosh and W. F. Sheridan, *J. Chem. Phys.* **27**, 1436 (1957).

5. Vacuum Arc Research

5.1 DEUTERIUM ARC STUDIES

R. A. Gibbons N. H. Lazar W. F. Peed

5.1.1 Introduction

The deuterium-arc flute velocity and time-averaged cross-field plasma transport measurements have been extended to a wider range of parameters. The radial flute velocity increases very rapidly with decreasing radius near the arc core with velocities up to several times 10^6 cm/sec. The relatively weak dependence on the magnetic field strength of the time-averaged radial density gradient has been verified out to the maximum available field strength. End plate current measurements indicate the average plasma transport across the field is a monotonically increasing function of the arc current with a relatively sharp increase in transport near 170 amp.

A quadrupole Ioffe magnetic field coil was installed in the Gas Arc Facility to study stabilization of the plasma flutes. However, the high-current arc operation requires ion and electron drifts along field lines that pass through both the cathode and the anode. In the 1.2-m-long arc geometry even a rather low Ioffe field changes the field lines sufficiently to extinguish the arc. At low Ioffe fields some reduction in the ion current fluctuations was observed with a Langmuir probe, even though the time-averaged ion current was increased for all Ioffe fields over the values for normal mirror field operation.

An attempt was made to measure the plasma electron temperature by the Thomson scattering of photons from a ruby laser. However, because of difficulties with laser operation and alignment, and the pressure of other experiments, the experiment was interrupted before any electron scattering data were obtained.

5.1.2 Flute Velocity and Plasma Transport

There are at least five (magnetic field strength, arc current, deuterium flow rate, center region pressure, and radius of measurement) relatively independent parameters to be varied in measurements of the magnetically constrained high-density arc plasma. Consequently, a complete catalog of the flute velocities and cross-field plasma transport properties is difficult to obtain. However, the measurements reported previously[1] have been extended to smaller radii and higher magnetic field strength to obtain a few more guidelines to understanding the flute characteristics. At this time the mechanism of flute generation is still undetermined.

The variation in radial flute velocity with radius from the center of the arc is shown in Fig. 5.1 for the usual arc operating conditions. The cross-field velocity increases rapidly as one approaches the arc core and is equal to the ion drift velocity in the arc at approximately $2\frac{1}{4}$ cm. The velocity is reduced by about a factor of 4 (at 2 cm) by raising the center field to 9.6 kilogauss, similar to the results reported earlier at approximately 2.5 cm. It appears from the azimuthal flute velocities reported earlier that the flute is initially ejected in an almost radial direction.

The time-averaged ion currents to a movable Langmuir probe as a function of radius have been extended to higher magnetic fields since the radial velocities reported earlier indicated that there might be a strong field dependence above 7.0 kilogauss. However, the e-folding lengths remain weak functions of the field strength with less than 50% change over the range 1.1 to 9.6 kilogauss for measurements outside a 2-cm radius.

[1]R. A. Gibbons *et al.*, *Thermonuclear Div. Semiann. Progr. Rept. Oct. 31, 1963*, ORNL-3564, pp. 63–66.

Time-averaged ion currents to negatively biased "end" plates, which extended to a radius of 2.35 cm, are shown in Fig. 5.2 as a function of the arc current. The ion currents are a monotonically increasing function of the arc current with a relatively rapid change in the vicinity of 170 amp. The approximately 20% higher ion currents to the cathode end plates were found on all four quadrants of the plates and suggest an ion drift toward the cathode similar to the drift measured in the arc core.

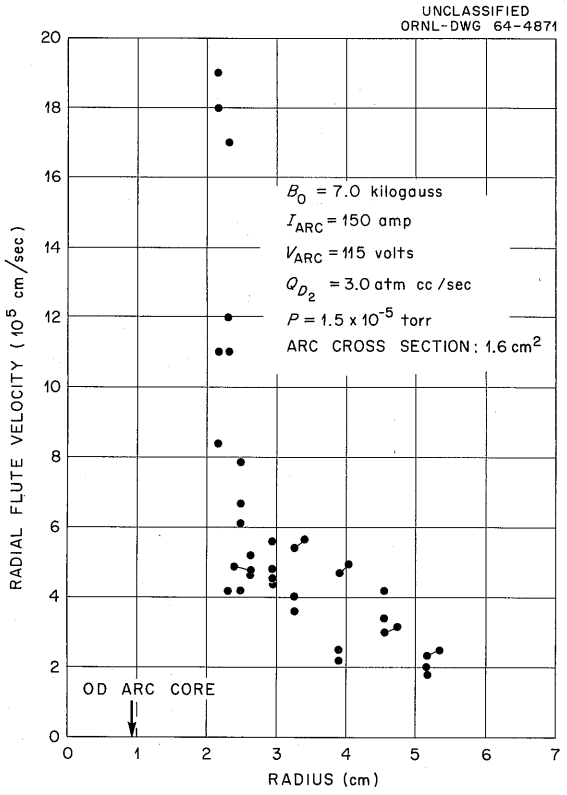

Fig. 5.1. Radial Flute Velocity as a Function of the Radial Distance from the Arc Center.

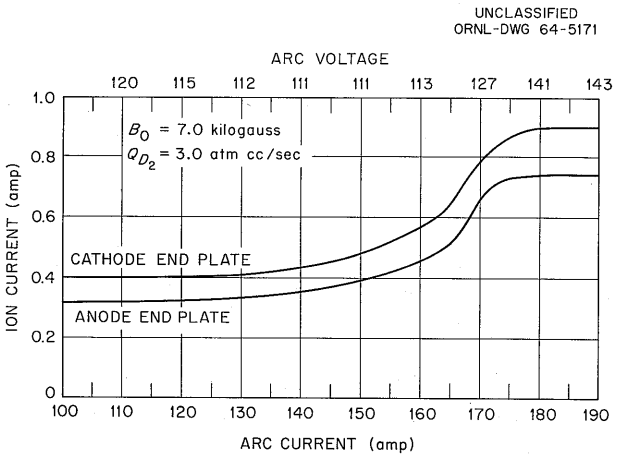

Fig. 5.2. Ion Saturation Current to the End Plates as a Function of the Arc Current.

5.1.3 Ioffe Field Experiments

A quadrupole Ioffe magnetic field coil was designed for the Gas Arc Facility by J. N. Luton, Jr., and H. L. Watts and was installed about the middle of April. Each "bar" of the coil consists of two water-cooled $\frac{1}{2}$- by $\frac{3}{4}$-in. hollow copper conductors at mean distances of $1\frac{5}{16}$ in. and $1\frac{13}{16}$ in. (to centers) along a radius and at an angle of 45° to the vertical plane. The coil produces a field of about 150 gauss at a 1-cm radius for a current of 1000 amp per conductor and was designed for a maximum current of 7000 amp.

The Ioffe field was installed to study the flute stabilization of a minimum B field. However, a Ioffe current as low as 1200 amp extinguishes the arc, and a current as low as 100 amp changes the characteristic arc current-voltage curve. Ioffe currents in the range of 400 to 700 amp reduced the fluctuations in ion current to a probe at a 3-cm radius midway between the conductors even though the time-averaged ion current increased with Ioffe current. However, the reduction in the fluctuations may have been due to the reduced arc current rather than a result of a stabilizing effect of the magnetic field.

When a weak Ioffe field is turned on, after the arc is struck, the arc impedance rises. Visually, one observes an apparent splitting of the arc cylinder into fuzzy, thin layers running from the top and bottom of the cathode. Past the cathode the plasma splits into fans which strike the top and bottom of the tank walls. Reversing the Ioffe current split the arc in the horizontal plane and plasma flowed out toward the sides of the facility. The plasma flow out between the Ioffe conductors was verified by ion-current measurements to "end" plates between the conductors. The currents to the top and bottom plates increased and the currents to the side plates decreased with increased Ioffe currents.

The ion-ion collision length in the arc is much shorter than the distance between the magnetic

mirrors, so the plasma can flow freely along field lines through the mirrors. Arc operation requires that the hot electrons leaving the cathode flow along field lines passing through the anode where the plasma ions are produced. The ions must flow back along the same field lines to heat the cathode. Since alignment of the electrodes along the same field lines is relatively critical, a relatively small distortion of the field lines can adversely affect arc operation.

The major observed effects of the Ioffe field are expected as a result of plasma flow along the mirror-field lines, distorted by the Ioffe field. The distortion has not been calculated for the Gas Arc Facility fields but a qualitative description utilizing solenoidal and Ioffe fields is sufficient to explain the results obtained. Figure 5.3 illustrates the Ioffe field cross section, showing the pure azimuthal field along a radius through the conductors and the pure radial field along a radius midway between them. Traveling in a positive field direction along the main field lines (toward the anode in the GAF and into the paper in the figure) the Ioffe field bends the field lines in at the top and bottom and out at the sides. Thus, even low Ioffe fields deflect some electrons traveling in the positive field direction out to the sides of the anode where they are unable to generate ions and the arc impedance is higher than normal. A 150-gauss field perpendicular to a 10-kilogauss field is sufficient to move a field line 1.5 cm in a 1-m length, which is more than enough to extinguish the arc.

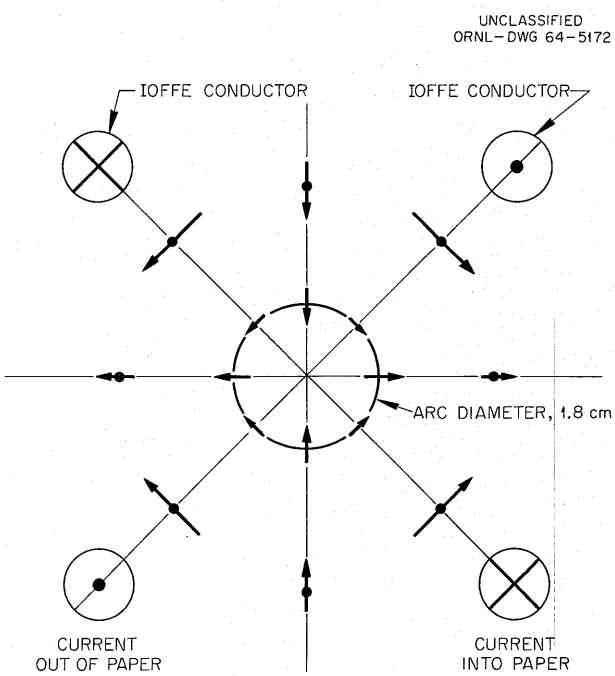

Fig. 5.3. Quadrupole Ioffe Magnetic Field Directions and Magnitudes.

The plasma as viewed in the center is reduced in height and split as described above because electrons from the top and bottom of the cathode are deflected inward and electrons from the sides are most easily deflected away from the anode by the Ioffe field. Arc operation at smaller radii would be affected less since the Ioffe field decreases with radius, but the only undistorted field line is down the center of perfect Ioffe conductors in exact alignment with the longitudinal magnetic field.

5.1.4 Laser Scattering Experiment

The high electron density, moderate electron temperature, and low luminosity of the deuterium-arc plasma make it an almost ideal plasma for the measurement of electron temperatures through Thomson scattering of photons from a pulsed ruby laser.[2] W. F. Peed has constructed the components necessary for the experiment and they were installed in the Gas Arc Facility. However, the Maser Optics 20-joule laser did not operate satisfactorily, and the laser and viewing optical systems proved difficult to align. Therefore, due to the pressure to do the Ioffe field experiments, the experiment was delayed until the necessary changes can be made.

5.2 OPERATION OF LONG SOLENOID

J. E. Francis P. R. Bell

The long solenoid has been extended from 120 to 250 in., using parts from the Chicago solenoid. A schematic of the new arrangement is shown in Fig. 5.4.

In addition to increased length, the solenoid has increased pumping speed provided by a central manifold containing two 6-in. diffusion pumps

[2]G. Fiocco and E. Thompson, *Bull. Am. Phys. Soc.* 8, 372 (1963).

UNCLASSIFIED
ORNL-DWG 64-5173

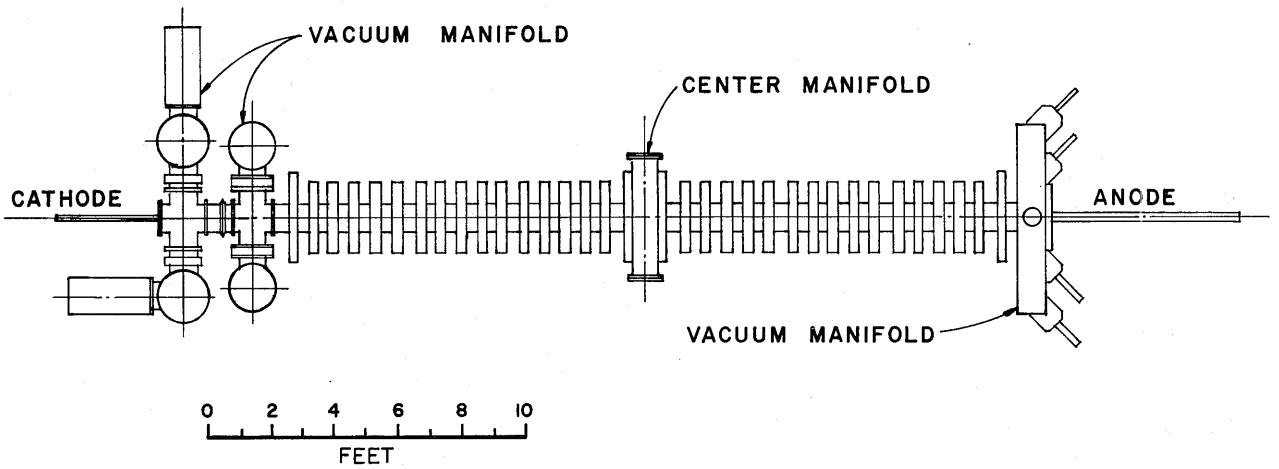

Fig. 5.4. Top View, Long Solenoid.

and four titanium evaporators. Two 10-in. diffusion pumps have been added at the cathode end making a total of six 10-in. pumps. Having two manifolds at the cathode end makes it possible to use differential pumping and gives better control of the pressure. With this new arrangement it will be possible to operate arcs as long as 240 in. and at lower pressures than previously possible.

The coils provide 3.75 gauss/amp, and with the present generators available a maximum field of 13 kilogauss can be obtained. The field is uniform except for a 15% drop at the center manifold.

The solenoid is now being used to develop suitable electrodes and baffles for a hydrogen arc to be used in DCX-2. Preliminary runs using a hydrogen arc have been made with the vacuum tank divided into three regions. Two baffles with 4-in.-ID copper tubing 17 in. long were used to separate the vacuum regions. During operation of a hydrogen arc, the lowest pressure in the central region obtained to date is 7×10^{-6} mm Hg. This was obtained using a standard hydrogen anode from the GAF. The cathode consisted of a $\frac{1}{4}$-in.-OD hollow tungsten rod surrounded by a 1-in.-ID water-cooled copper tube 15 in. long which was mounted on the cathode by means of a boron nitride insulator. Using this arrangement, the operating conditions shown in Table 5.1 were obtained.

Attempts to run the cathode without a shield have all resulted in the arc going out whenever the pressure in the cathode region falls below 2×10^{-4} mm Hg.

Experiments are now in progress directed at obtaining arc operation with much lower central pressure.

Table 5.1. Operating Conditions for Hydrogen Arc

Arc	Field	Pressure	Gas Feed
70 amp	10 kg	Anode 6×10^{-5}	1 cc/sec
220 v		Middle 7×10^{-6}	
		Cathode 5×10^{-5}	

5.3 ON A VIGOROUS ENERGY PUMPING CYCLE IN THE ENERGETIC CARBON ARCS

J. R. McNally, Jr. M. R. Skidmore

Spectroscopic studies of steady-state, high-current, magnetically confined carbon and gas-fed carbon arcs have revealed mean ion energies up to 500 ev (15 ft from the anode in a 16-ft-long carbon arc) whereas the mean electron energy appears to be of order 5 ev.[3] This unusually

[3] J. R. McNally, Jr., and M. R. Skidmore, *Appl. Opt.* 2, 699 (1963).

large energy ratio, indicative of a pronounced departure from thermodynamic equilibrium, does not occur so glaringly in magnetically confined lithium arcs ($\overline{E}_+ \sim 20$ ev with $\overline{E}_- \sim 2$ ev, with the $\overline{E}_+$ uncorrected for rotational drift or "tornado" motion of the arc column). Preliminary studies suggest that there may be present in the energetic carbon arcs a rather selective ion-heating mechanism which promotes a vigorous energy pumping cycle involving the transfer of gross amounts of kinetic energy between electrons and ions.

The attainment of high carbon-ion temperatures appears to be independent of carbon feed at both anode and cathode, or the cathode alone, although the arc is more stable when both electrodes are carbon. In general, singly ionized species have a somewhat lower "temperature" than the higher-charge states but this may be due to insufficient history in the arc. Thus, our earlier suggestion,[3] that electric field heating played a major role, seems to be incorrect, although it does provide the initial energy to trigger important collision processes involving Coulomb barriers.

Earlier,[4] we considered the role of certain atomic processes which might permit the rapid heating of ions by electrons. These processes permit the pumping of energy from the electrons into excitation or ionization states which can then undergo what may aptly be described as atomic fusion reactions. An atomic fusion reaction is defined here as any kind of electron rearrangement collision between atoms or ions in which excitation or ionization energy is converted into kinetic energy of the ions. Charge-exchange reactions between energetic ions and neutral atoms have been quite extensively investigated.[5,6] No data are available on ion-ion charge exchange or rearrangement collisions; hence, no quantitative evaluation of detailed mechanisms in the energetic carbon arc is possible at this time.

If the reaction is exothermic, the potential energy curves for the two molecular ion states are expected to cross (or at least approach each other very closely), and the reaction can occur at this critical internuclear separation with the energy defect Q of the reaction showing up as an increase in the kinetic energy of the separating ions. In order that a pumping cycle exist, for example, in the case of C^{3+} and C^+, the following typical chain of events is required:

(1) $C^{2+} + e \longrightarrow C^{3+} + 2e - 47.9$ ev (ionization)

(2) $C^{2+} + e \longrightarrow C^{+} + 24.4$ ev (recombination)

(3) $C^{3+} + C^{+} \longrightarrow C^{2+} + C^{2+}$ $+ 23.5$ ev (charge exchange)

(4) $C^{2+}{}_{hot} + e_{cold} \longrightarrow C^{2+}{}_{warm}$ $+ e_{warm}$ (collisional heating)

Step (1) in the cycle requires very energetic electrons whereas, in general, step (2) requires low-energy electrons[7] although di-electronic recombination[8] (energetic electrons captured into autoionization states followed by radiative decay) may occur with carbon ions. It is now believed that this type of pumping cycle does not play a significant role in generating hot ions in the energetic arcs because of the relatively low reaction rates expected for steps (1) and (2).

A much more direct pumping cycle and one which requires electrons of only moderate energy is that involving metastable C^{2+} ions, as follows:

(5) $C^{2+}(^1S) + e \longrightarrow C^{2+*}(^3P)$ $+ e - 6.5$ ev (excitation)

(6) $C^{2+*}(^3P) + C^{2+*}(^3P) \longrightarrow C^{2+}(^1S) + C^{2+}(^1S)$ $+ 13.0$ ev (de-excitation or charge exchange)

(7) $C^{2+}{}_{hot} + e_{cold} \longrightarrow C^{2+}{}_{warm}$ $+ e_{warm}$ (collisional heating)

If thermodynamic equilibrium were to exist at a mean electron energy of 5 ev, the population of metastables should exceed that of ground-state

[4] J. R. McNally, Jr., and M. R. Skidmore, *Thermonuclear Div. Semiann. Progr. Rept. Oct. 31, 1963*, ORNL-3564, p. 67.

[5] J. B. Hasted and R. A. Smith, *Proc. Roy. Soc. (London), Ser. A* **235**, 354 (1956), give a charge-exchange cross section of 1.2×10^{-15} cm^2 for the reaction $C^{2+} + Ar^0 \rightarrow C^+ + Ar^+ + 8.6$ ev for 200-ev C^{2+} ions.

[6] I. P. Flaks and E. S. Solov'ev, *Zh. Tekhn. Fiz.* **3**, 577 (1958).

[7] E. Hinnov and J. G. Hirschberg, *Phys. Rev.* **125**, 795 (1962), give a $T_e^{-4.5}$ dependence for three-body recombinations.

[8] H. S. W. Massey and D. R. Bates, *Rept. Progr. Phys.* **9**, 62 (1942); D. R. Bates, *Atomic and Molecular Processes*, Academic, New York, 1962.

C^{2+} ions by about 50% (inverted population). In addition, experimental data[5] demonstrate that in reversible reactions the exothermic reaction is generally favored over the endothermic reaction and especially so for large Q. Thus, reaction (6) should proceed to the right as indicated and the ions would become more energetic with residence time in the arc.

The rate at which energy can be pumped from electrons into metastable excitation of a C^{2+} ion is of order $n_e \overline{\sigma_{exc} v_e} \Delta E = 10^{14} (4 \times 10^{-9}) (6.5) \cong 2.6 \times 10^6$ ev/sec[9] (electrons are gaining energy from the arc voltage drop at a rate of about 7×10^6 ev/sec). If this is converted 50% through atomic fusion reactions to ion heating, the required charge-exchange (or de-excitation) cross section would have to be of order

$$\sigma_{cx} = \frac{1.3 \times 10^6}{3 \times 10^{13} (10^7) (13)} \sim 4 \times 10^{-16} \text{ cm}^2$$

for a density of 3×10^{13} C^{2+*} ions/cm^3 and a mean collisional velocity of 10^7 cm/sec. This cross section compares favorably with that for $C^{2+} + Ar \longrightarrow C^+ + Ar^+ + 8.6$ ev as measured by Hasted and Smith.[5] The internuclear separation corresponding to this cross section is about 1.1 A for which the Coulomb potential energy is about 50 ev – an energy readily available from the initial "tornado" motion, some randomization, and head-on collisions of ions in the arc (see Fig. 5.5).

A state of quasi-dynamical equilibrium appears to be attained at each point in the arc whereby the rate of heating ions by atomic fusion is comparable to the rate of ion cooling by Coulomb collisions with cold electrons. The rate at which each carbon ion at 400 ev would heat the cold tail of a Maxwellian distribution of electrons at 4 ev would be about 100×10^6 ev/sec (for $n_e = 10^{14}$ cm^{-3}) (see Fig. 5.6). If the distribution is a Druyvesteyn distribution the energy transfer is about 70% as large. Since the ratio of "hot" ions to very cold electrons ($v_- \lesssim v_+$ or $\overline{E}_c \sim 0.02$ ev) is about 2000, each electron in the cold tail of such a distribution would be heated out of the cold tail in about 10^{-4} of an electron-electron relaxation time of 10^{-9} sec! Since only about 10^6 ev/sec appears to be available by this mechanism for energy cycling, it would seem that the cold tail of the energy distribution of the electrons

[9] $\overline{\sigma v}$ by analogy with excitation of the $^3P_1$ level in Hg. This estimate may be low since it does not include filling of the $^3P_2$ and $^3P_0$ levels.

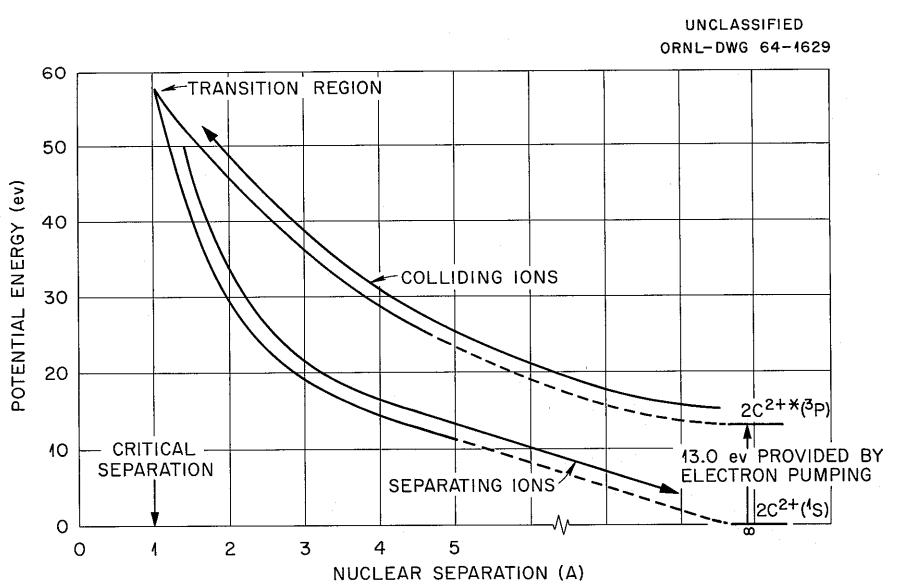

Fig. 5.5. Schema for the Energy Pumping Cycle in the Energetic Carbon Arcs. (1) Electrons pump doubly ionized carbon ions to metastable states; (2) the ions collide against the Coulomb barrier; (3) if the exothermic collision occurs, the ions separate with an increase of kinetic energy of 13.0 ev.

still must be significantly depleted with respect to a Maxwellian distribution at 5 ev mean energy in order to permit such high ion temperatures. (Energy transfer from the fast electrons to slower ions contributes also about 10^6 ev/sec.)

A similar gross perturbation of the electron energy distribution in a thermonuclear (nuclear fusioning) system may be of very considerable importance inasmuch as the so-called "ignition condition" should be determined then not by the bremsstrahlung (or electron cyclotron) radiation loss rate at least directly, but by the actual energy transfer rate to the *residual* low-energy tail. Some Fokker-Planck calculations after the method of Fowler and Rankin[10] are in process and may illuminate this point for both the carbon arc case and hypothetical thermonuclear plasmas.

The energetic carbon arc appears to be one of a large class of plasma systems which may encourage, via atomic fusion and energy pumping cycles, the development of quite high ion "temperatures." Heating in the lithium arc is apparently suppressed because of the low electron "temperature" ($\overline{E}_- \sim 2$ ev), the small population of Li^{+*} relative to all lithium ions, and the probability of "shake-off" of an electron in the competing reaction

$$Li^{+*}\ (^3P) + Li^{+*}\ (^3P) \longrightarrow Li^+ + Li^{2+} + e + 42.4 \text{ ev}.$$

Argon gas fed through the tungsten-tantalum cathode of a 16-ft-long lithium arc produced a 50% increase in the mean energy of the lithium ions near the cathode (to 32 ev). Argon ions, though present in low abundance in the arc, can introduce atomic fusion events through collisions between metastable argon ions (Ar^{+*} at 16.4 ev, Ar^{2+*} at 1.8 and 4.2 ev, etc.)

It will be especially important to correlate these ion heating effects with the relative population of C^{2+} in the arc. Preliminary evidence shows that $\overline{E}_+$ does increase markedly with increase of C^{2+} intensity (λ4647).

Further studies of energetic arcs seem desirable from the standpoints of (1) an apparently stable, hot-ion type of plasma of $\beta > 1\%$; (2) the increase in ion temperature with increase in the physical length of the arc; (3) the rotational drift or "tornado" motion of the arc column; (4) the plasma streams emanating from the cathode; (5) possible atomic fusion and energy pumping cycles; (6) the perturbation from a Maxwellian distribution of the cold tail of the energy distribution of plasma electrons in the presence of very hot ions; and (7) possible implications to nuclear fusioning systems.

[10] T. K. Fowler and M. Rankin, *J. Nucl. Energy, Part C* 4, 311 (1962).

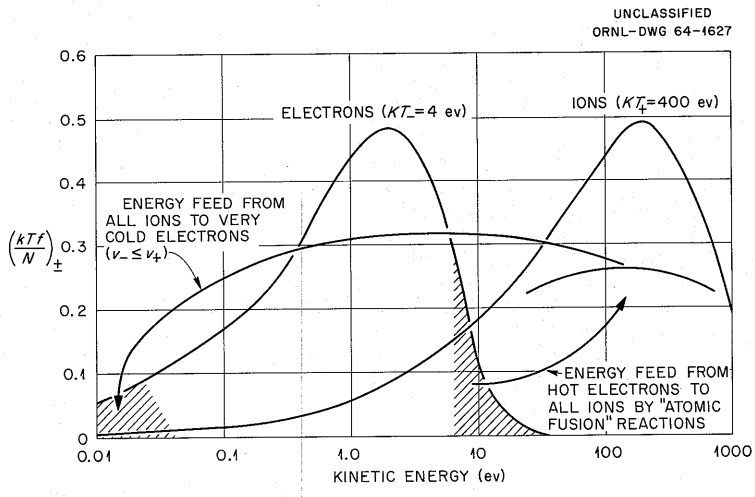

Fig. 5.6. Schema for Energy Pumping Cycle Involving Maxwellian Distributions. Ions at 400 ev feed energy to very slow electrons at a rate of 100 ev/μsec for $n_e = 10^{14}$ thus driving electrons out of the cold tail. Electrons above 6.5 ev can excite the metastable $C^{2+*}\ (^3P)$ states. Atomic fusion collisions between metastables convert internal potential energy to increased ion kinetic energy.

6. Cross-Section Measurements

C. F. Barnett J. A. Ray J. C. Thompson

6.1 CROSS-BEAM EXPERIMENTS

An inherent difficulty encountered in the measurement of atomic cross sections by the intersection of two charged beams is the large signal obtained from collisions with residual gas molecules. This so-called noise has been reduced in some experiments by modulating one or both of the charged beams and using a phase-sensitive amplifier as a detector. With such arrangements, cross sections have been measured in which the signal-to-noise ratio was 1 : 100; however, in the use of chopped beams, either electrostatic or electromagnetic beam interactions exist such that the interacting particle beams are deflected or erroneous signals are transmitted along the beams. To eliminate these unwanted interactions, an ultrahigh vacuum apparatus has been constructed and placed into operation. The vacuum system has been described in previous reports.[1] Briefly, the vacuum vessel consists of an outer chamber 2 ft in diameter and 8 ft long. Pumping is provided by NRC type 6-in. diffusion pumps with Dow-Corning 705 silicone oil and water-cooled baffles. Titanium is batch-evaporated from titanium wire wound on tantalum filaments. All valves have been eliminated and all seals are compression-type aluminum-wire gaskets. Surrounding the inner wall is a copper liner which can be heated by 400°C steam or cooled with water or liquid nitrogen. The beam interacting region is internal to an inner liner pumped only by titanium. A set of three magnetic coils have been placed external to the system to provide an axial magnetic guide field for an electron beam. Tests on the static system indicate that a pressure of 5×10^{-9} torr can be maintained with the oil diffusion pumps after prolonged bake-out at 100°C. Evaporation of titanium on the water-cooled outer liner decreased the pressure to 5×10^{-10} torr. Evaporation onto liquid-nitrogen-cooled surfaces produced no change in the pressure, nor was an improvement noted when the liquid-nitrogen-cooled surface was thermally cycled. Observations over several months of continuous pumping revealed no visible traces of oil backstreaming from the diffusion pumps.

A Veeco vacuum analyzer was placed on the system to study the individual mass peak behavior when in the pressure range 5×10^{-10} torr. After titanium evaporation on the water-cooled liner, the mass spectrum indicated a predominant mass peak of 28 with also a large water peak. Traces of hydrocarbons were present in addition to the usual peaks at mass 2, 14, 16, 32, and 44. Further evaporation of titanium with the liner at liquid-nitrogen temperatures decreased the intensity of all the peaks. The sum of the total partial pressures was decreased by a factor of 6. The mass 28 and 16 peaks decreased by a factor of 4 and 8 respectively. Since mass 28 may indicate the presence of silicon from the diffusion pumps, the heater power to the pumps was increased to 50% overload. No increase in the mass 28 peak was detected. From these tests we have drawn the following tentative conculsions:

1. the ion gages used are limited in measuring pressures below 5×10^{-10} torr;
2. the static pressure in the system is less than 10^{-10} torr;
3. back diffusion of diffusion pump oil is negligible.

The vacuum chamber has now been placed in position adjacent to the 600-kev accelerator. Various electron sources have been scanned for

[1] *Thermonuclear Div. Semiann. Progr. Rept. Apr. 30, 1963*, ORNL-3472, p. 64.

spatial electron density distributions, and a Pierce electron gun structure has been installed in preparation for measuring the dissociation of H_2^+ by electrons.

6.2 EXCITED STATES

Luce[2] has reported the axial transmission of a 750-kev H_2^+ beam through a cylindrical arc. Measurements indicated that the production of H^0 from H_2^+ was greater than 50% with 90% of the H^0 existing in excited states with the principal quantum number greater than 7. An attempt has been made to confirm these measurements and to understand the collision phenomena associated with this population inversion.

A schematic diagram of the solenoidal magnetic field and the arc is shown in Fig. 6.1. The magnetic field was generated by five coils approximately 12 in. in inside diameter with magnetic fields of 6 to 10 kilogauss. The cathode structure was a cylindrical tungsten shell, $\frac{3}{4}$ in. OD, $\frac{1}{2}$ in. ID, and 10 in. long. The shell was arc-welded to a tantalum holder which was supported by a water-cooled tube. Argon was admitted to the inner region of the cathode to aid in striking the arc and for gas feed support. The carbon anode was a cylindrical block with a $\frac{3}{16}$-in.-diam axial bore. The anode was also mounted on a copper tube with provisions made to admit gas to the arc. A 500-kev H_2^+ beam entered the solenoidal region and passed through the arc where dissociating collisions occurred. Emerging from the anode region was a beam of H_2^+, H^0, and H^+. These beams were analyzed by passing through a parallel-plate electric analyzer and then detected by a conventional nickel-foil-covered Faraday cup arranged to scan the spatial extent of the beam.

Preliminary to passing a beam through the arc, a vacuum spectrograph was mounted at the exit end of the solenoid. The slit of the spectrograph was positioned to accept spectra emitted along the central axis of the arc. Table 6.1 summarizes the spectra obtained from a 13-in. carbon-tungsten arc operating in an 8000-gauss field. The results are normalized to the C^{3+} resonant line at 1548 A and the values given are uncorrected for transition probability, grating reflectivity, and detector response. The arc current was 250 amp.

The general trend was for the arc to shift to states of higher excitation as the gas flow decreased; however, at the lowest flow permissible without melting the cathode, the existence of copious quantities of C^+ and C^{2+} in the center of the arc was evident. Decreasing the magnetic field tended to slightly enhance the state of excitation.

By admitting argon gas into the anode region we could determine the efficiency of a gas target for production of H^0 from 500-kev H_2^+. The ratio

[2] J. S. Luce and J. L. Hilton, "Massive Conversion of 750 kev Ions to Neutrals of Quantum Levels > 7," *Proc. Intern. Conf. Ionization Phenomena Gases, 6th, Paris, 1963*, pp. 83–86.

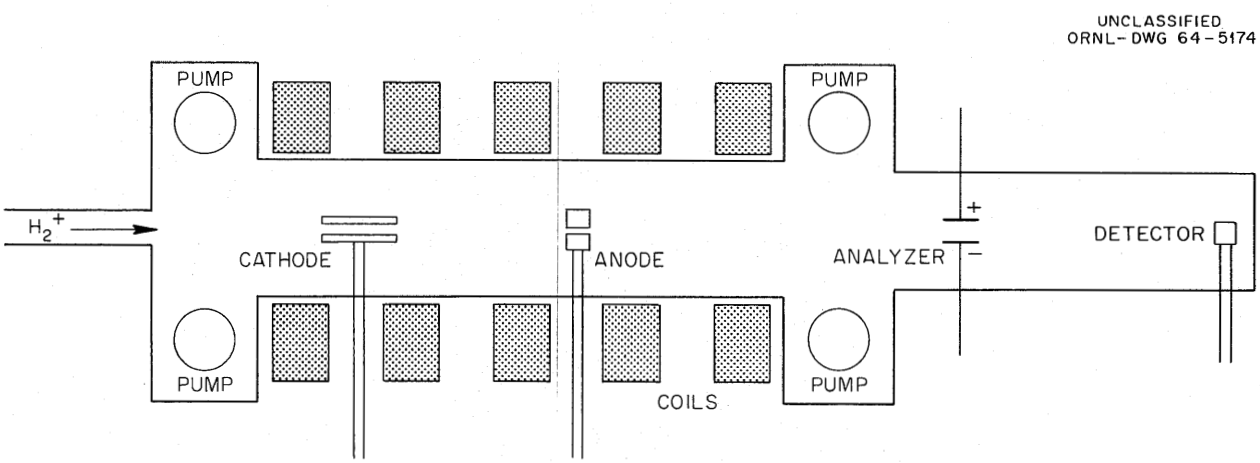

Fig. 6.1. Schematic Diagram of Solenoid Used for Arc Dissociation of H_2^+.

Table 6.1. Spectra Obtained from a 13-in. Carbon-Tungsten Arc Operating in an 8000-Gauss Field

Wavelength (A)	Relative Intensity with an Argon Gas Flow (cc/sec) of –			Line Identification
	0.5	0.2	0.075	
880	15			Ar^{2+}
835	16	11	2	O^{+}
850	16	11	4	Ar^{3+}
977	97	58	71	C^{2+}
1174	68	70	84	C^{2+}
1335	63	41	14	C^{+}
1548	100	100	100	C^{3+}
1552	84	86	103	C^{3+}
2478	3	4	0	C^{0}

of H^0 to H_2^+ was 0.12 with optimum flow of argon into the anode region. This value is within 1 to 2% of the value obtained from previous measurements. Operating the arc at 200 amp resulted in complete attenuation of the beams, whereas immediately on arc turnoff the beams would reappear at the detector. The observed attenuation could be the result of (1) high densities in the arc center, or (2) misalignment of the anode from forces resulting from the arc current.

The geometry was altered by placing an insulating hood around the cathode to provide means to admit argon to the external arc surface, and also the anode was supported in a structurally sounder manner. With the arc operating at relatively high gas flows (~0.5 cc/sec), the beams were well behaved and the ratio H^0/H_2^+ was about 0.02. However, as the gas flow was decreased the arc arrived at a stage where it became turbulent. Under these conditions the total beam transmitted through the arc decreased by a factor of 25 while the total yield of H^0 remained essentially constant. If we measured the ratio of H^0 to total beam received at the detector, we found 0.50; however, the ratio of H^0 to total beam coming into the arc was only 0.02. Investigations into the origin of the severe beam attenuation under conditions of arc turbulence have revealed two possible sources: (1) The solenoidal magnetic field was wound in such a manner as to have longitudinal current loops resulting in H_θ fields, which cause the H_2^+ beam trajectory to corkscrew through the arc. If, when the arc becomes turbulent, a large fraction of the dissociation events move to the cathode region, then the H^+ beam would be attenuated at the anode aperture. (2) Electric fields in the arc could deflect the charged beams, which would be attenuated by the anode aperture.

Present experiments are continuing in the direction of making changes in the arc electrode geometry and to sample the excited-state population of H^0.

6.3 CROSS-SECTION MEASUREMENTS

Frequently, information is needed on the total attenuation of H_2^+ or H_3^+ as the particles traverse a gaseous region. Most of the previous work has been concerned with measuring partial dissociative and electron capture cross sections whose sum is equivalent to the total attenuation cross section.

The total attenuation cross section was measured by accelerating H_2^+ or H_3^+ to the desired energy (40–220 kev) using a conventional accelerator. The ions were incident on a gas cell in which single collisions predominate. Particles undergoing any reaction were removed from the H_2^+ or H_3^+ beam by means of a parallel-plate electric analyzer. The beams were detected by means of a scanning Faraday cup. The total attenuation cross sections for H_2^+ and H_3^+ in hydrogen gas in the energy range 40–220 kev are shown in Fig. 6.2. The cross sections decrease monotonically as the energy increases. Summing the previously measured partial cross sections for H_2^+ in H_2 gas yields cross sections within 10% of the present values. Since all the partial cross sections have not been measured for H_3^+ attenuation, a comparison cannot be made with the present results. Estimates of the errors involved in the measurements are ±20%.

Dissociation of H_3^+ occurs principally by electronic excitation of the molecular ion to a repulsive state. This electronic excitation obeys the Franck-Condon principle, which states that the excitation transition takes place so quickly that the nuclei have no time to move an appreciable distance. Thus, there will be a vertical transition from the initial state of potential energy to the

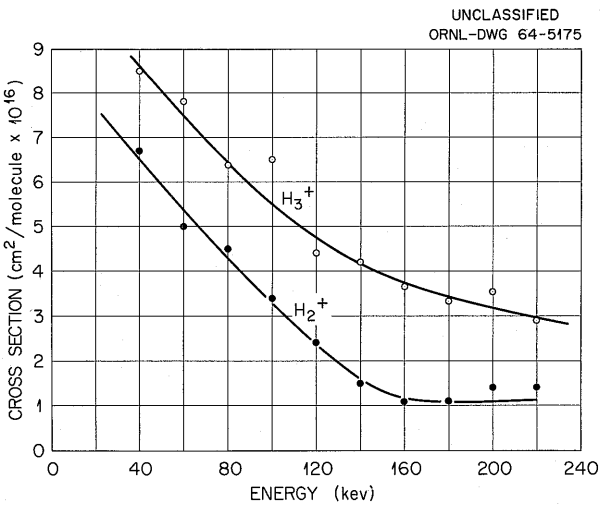

Fig. 6.2 Total Attenuation Cross Sections of H_2^+ and H_3^+ in Hydrogen Gas.

final state. If the final state is a repulsive level, the ion will dissociate into two or more fragments whose energies will be determined by the difference in the potential energy of the repulsive state and potential energy of the particles at infinite separation. This difference of energy, usually a few volts, is distributed isotropically in the center-of-mass system and can be measured in the lab system by measuring the divergence angle of the reaction products.

Measurements have been made of the angular distribution of H_2^+ and H^+ resulting from dissociation of H_3^+ in gaseous targets of H_2, H_2O, and Xe. A summary of the results is shown in Table 6.2 for H_3^+ energies of 60 and 200 kev.

Table 6.2. Angular Distribution of H_2^+ and H^+ Resulting from Dissociation of H_3^+ in H_2, H_2O, and Xe

E (kev)	Target	$\Delta\theta$ (milliradians)	
		H_2^+	H^+
60	Xe	9.2	19.1
	H_2O	9.8	24.5
	H_2	9.4	20.9
200	Xe	6.7	16.4
	H_2O	6.8	17.2
	H_2	7.5	16.3

The angle of scattering is given in milliradians and is the full angle at half maximum amplitude. These measurements of angular divergence indicate that at constant energy the reaction products originate from the same repulsive level independently of the target mass.

6.4 PROPORTIONAL COUNTER FOR PARTICLES OF LOW ENERGY

Evaluation studies have been completed of a proportional counter[3] to be used in detecting low-energy neutral particles. A schematic diagram of the counter is shown in Fig. 6.3. The beam enters the counter through a 0.001- × 1-in. aperture which is covered by a Formvar film approximately 250 A thick. The cathode assembly was constructed from a 1-in. copper tube with a 180° section cut away to form a grid structure made from twenty-five 0.002-in. molybdenum wires. The central anode wire was 0.005-in. stainless steel. A voltage of 100 v was impressed between cathode and ground with approximately 800 v applied to the anode. Methane was admitted to the counter to a pressure of 1 to 2 torrs.

Typical pulse-height spectrum curves are shown in Fig. 6.4 for a 2.5-kev and 30-kev H^+ beam. Beam energies as low as 1.7 kev were transmitted through the entrance window; however, approximately 10% of the pulses in the low-energy tail of the pulse-height distribution could not be resolved due to excessive counter noise. The resolution curve for the counter is shown in Fig. 6.5. The resolution is described in terms of $\Delta E/E$, where ΔE is the full width at half maximum of a peak occurring at pulse height E. For energies less than 5 kev, the resolution deteriorates rapidly. Variations in methane pressure and anode and cathode voltages resulted in only small changes in resolution. Another characteristic of the counter is shown in Fig. 6.6, where the linearity is plotted as a function of the particle energy. The counter departs from linearity for a particle energy of 17 kev. This deviation does not decrease the usefulness of this instrument as an absolute detector of neutral particles.

[3] G. W. McClure, *Phys. Rev.* **130**, 1852 (1963).

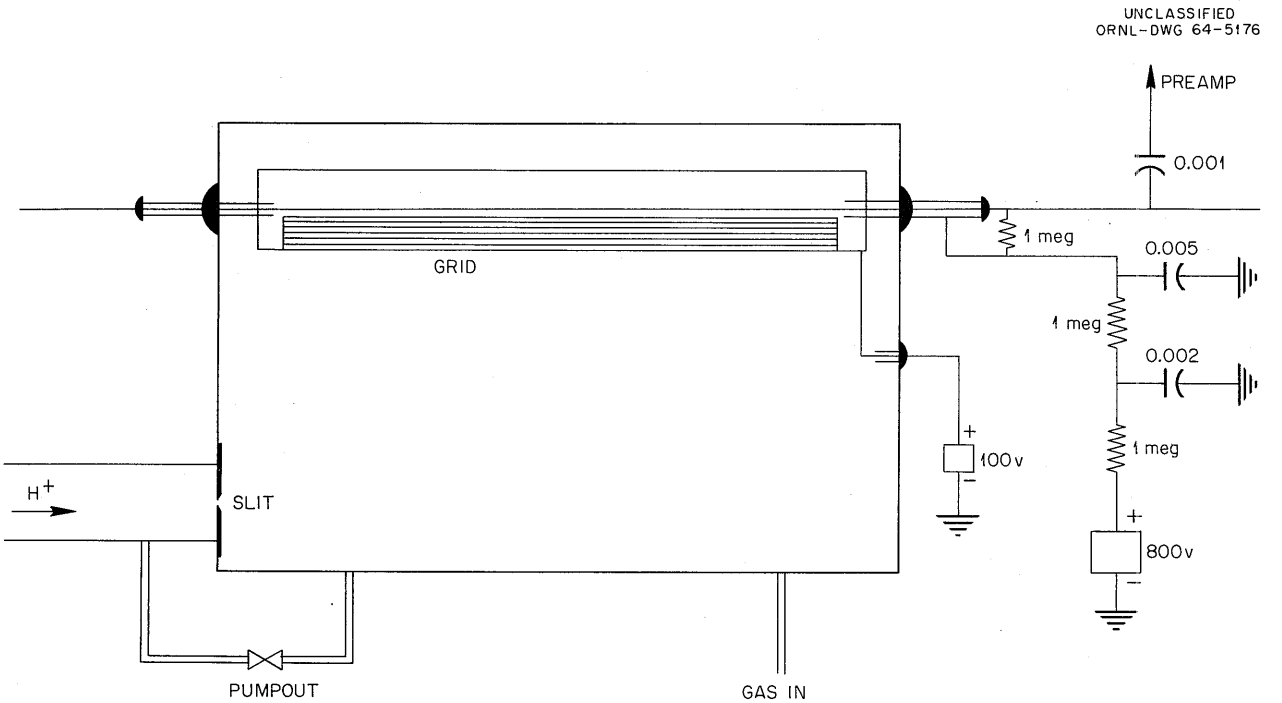

Fig. 6.3. Schematic Diagram of Proportional Counter.

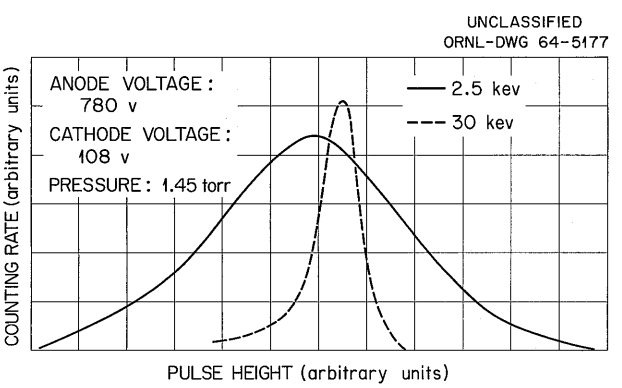

Fig. 6.4. Pulse-Height Spectrum for 2.5-kev and 30-kev H^+.

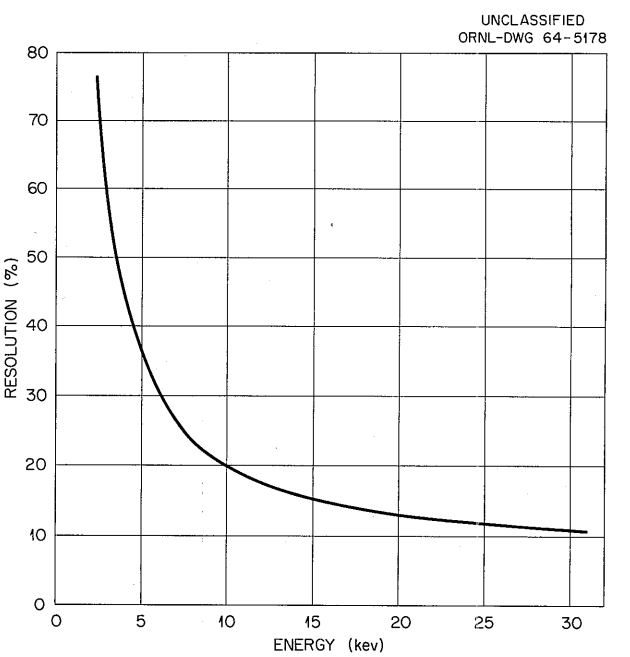

Fig. 6.5. Resolution Curve for Proportional Counter.

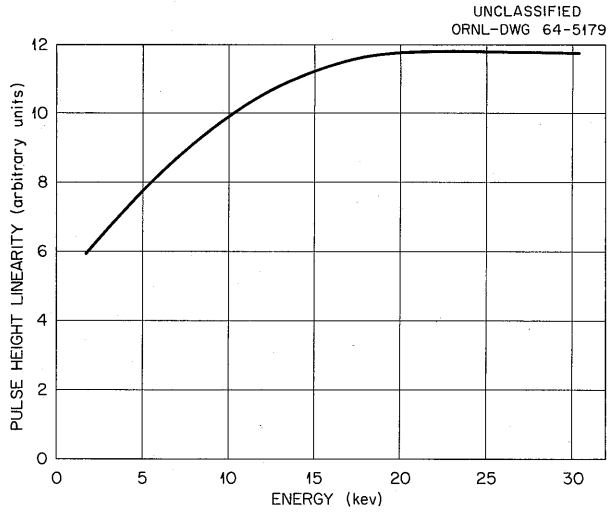

Fig. 6.6 Proportional Counter Linearity as a Function of Energy.

7. Production, Acceleration, and Injection of Ionic and Atomic Beams

7.1 HIGH-CURRENT ION-BEAM PRODUCTION AND INJECTION

R. C. Davis
R. R. Hall
G. G. Kelley
O. B. Morgan
R. F. Stratton
D. C. Weaver[1]

The operation of the DCX-2 injection system and a series of necessary repairs to the 600-kv power supply have left very little opportunity to do 600-kv beam injection studies. While this restriction has prevented a maximum effort to understand the H_2^+ beam limitations with the DCX-2 injector,[2] it has permitted studies and evaluation of ion sources and other high-current injector components with the 100-kv test stand.

The 100-kv ion-source test stand was improved and properly enclosed to make it both safer and more reliable for operating up to 120 kv, which is the upper limit of the 3.5-amp power supply. Using this facility with the modified duoplasmatron ion source,[3] total hydrogen ion beams of 500 ma at 100 kv were extracted. Several of these sources were operated continuously for 4-hr time periods with beams of 250 to 350 ma at 100 to 120 kv. As was expected from past experience, there was no deterioration of the performance of the source from this type of operating condition.

Preliminary evaluation of a modification of the extractor region of the duoplasmatron (Fig. 7.1) has proved very interesting. This source has high current capabilities with a reduced beam divergence angle. The combined initial divergence and space-charge spreading produces a beam of a size shown in Table 7.1 when a target was placed at a distance of 8 in. from the ion source. These spot sizes are approximately a factor of 2 smaller than those obtained with the previous extraction geometry.[3] Deformation of the target due to the high power density limited the total hydrogen ion beam to 400 ma at 110 kev with this source. The current capability at 50 kv was found to be ~270 ma, and since the increase is proportional to $V^{3/2}$, the source should deliver ~735 ma at 100 kv. A series of studies is planned to further evaluate this type of extraction geometry.

An attempt was made to produce a small (1 in. diameter or less), well-collimated, neutralized hydrogen ion beam in the current range of 50 ma at 50 to 100 kev. The ion source used had an anode similar to that shown in Fig. 7.1 with a set of accel-decel electrodes with apertures varying from $\frac{1}{4}$ in. up to 2 in. It was always possible to neutralize the ion beam with the ion source at plus 50 to 100 kv, the first electrode at minus 3 to 5 kv, and the second electrode at ground potential, as long as no electric field was present beneath these electrodes to drain off electrons. However, in all cases the total beam divergence angle was greater than the desired maximum of 2° except for beams of 5 ma or less.

Some preliminary evaluations have been made with multiaperture duoplasmatron ion sources. The performance of these sources was not very encouraging. The total attainable current was <50 ma at 50 kv. Some variations were made in the sources which neither increased the total current nor clarified the reason for the difficulty.

[1]On loan from Y-12.

[2]R. C. Davis *et al.*, *Thermonuclear Div. Semiann. Progr. Rept. Oct. 31, 1963*, ORNL-3564, p. 73.

[3]R. C. Davis *et al.*, *Thermonuclear Div. Semiann. Progr. Rept. Oct. 31, 1963*, ORNL-3564, p. 74.

UNCLASSIFIED
ORNL-DWG 64-5180

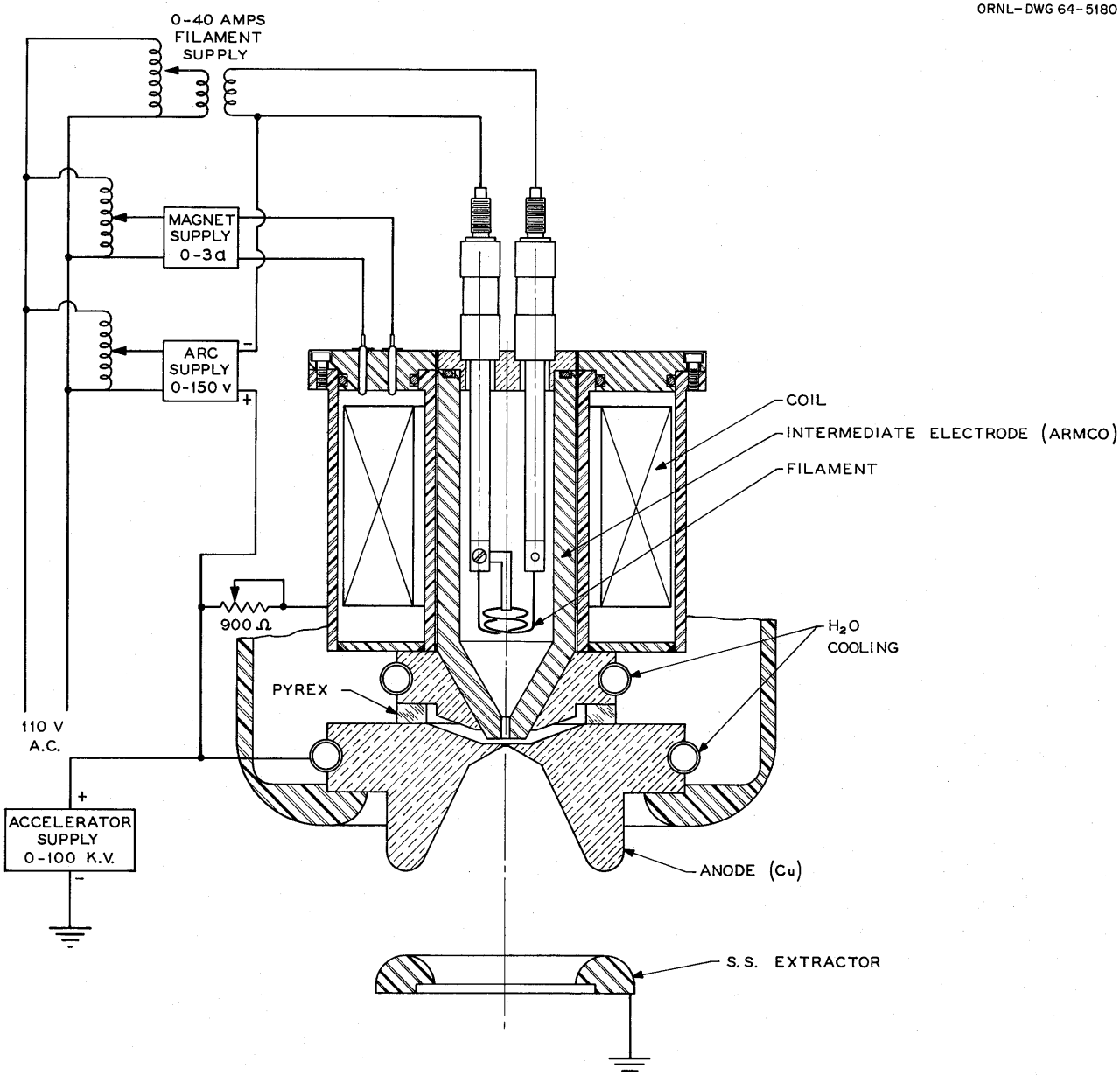

Fig. 7.1. Modified Duoplasmatron Ion Source.

This, combined with a poor gas efficiency (50% or less) and the desire to pursue more promising experiments, has temporarily restricted further studies with this type of source.

An epoxy cylinder has been evaluated on the 100-kv test stand as a potential replacement for the porcelain insulator sections of the 600-kv accelerating column. The cylinder is 15 in. ID, 17 in. OD, and 6 in. high. The section is made with 71.5% by weight of Shell resin 815 and 28.5% by weight of General Mills Versamid 140 hardener. After curing at room temperature it was attached to metal end plates with vinyl acetate. There had been no doubt about the insulating properties of the epoxy, but the feasibility of using it for a high-gradient accelerator tube with an intense ion beam was not known. The test stand vacuum system consists of two 10-in. oil diffusion pumps with a liquid-nitrogen trap and titanium evaporation during the experiments. The base pressure of the system

is $\sim 5 \times 10^{-8}$ mm Hg with either a standard porcelain insulator or the epoxy insulator. After a week of intermittent operation there was no sign of any deterioration of the operating stability of the accelerator with a voltage gradient of 200 to 300 kev/cm between stainless steel electrodes and a 50- to 200-ma ion beam at 100 kev.

In the limited time available with the power supply, the 600-kv test stand has been used to evaluate the H_2^+ current limitation with the DCX-2 injector.[2] The conical copper section previously used on the test stand, *A*, Fig. 7.2, in obtaining a 95-ma H_2^+ beam through the $1\frac{5}{8}$-in. aperture was replaced with an exact geometrical duplicate of the DCX-2 injection duct, *B*, Fig. 7.2. With this relatively small change the test stand was limited to $\sim$50 ma of H_2^+ beam through the duct at 600 kev – the same current limit as is found in DCX-2. This eliminates the possibility that the stray magnetic field[2] is the reason for the current limitation on DCX-2. It is very possible that the current limitation arises from the violent scattering mechanism found earlier.[4] The 30-in.-long, $1\frac{5}{8}$-in.-diam cylindrical section has now been removed from the duct shown in Fig. 7.2 and a $1\frac{5}{8}$-in. aperture placed at $Z = 0$. The removal of the cylindrical section will probably affect the scattering, or at least will make it possible to study the beam in this region in some detail.

[4]G. G. Kelley *et al.*, *Thermonuclear Div. Semiann. Progr. Rept. Jan. 31, 1961*, ORNL-3104, p. 19.

Table 7.1. Hydrogen Ion Beam – Target 8 in. from Ion Source

Beam energy, 100 kev

Total Current (ma)	Size (in.)
50	0.75
100	1.50
150	2.25
200	2.50

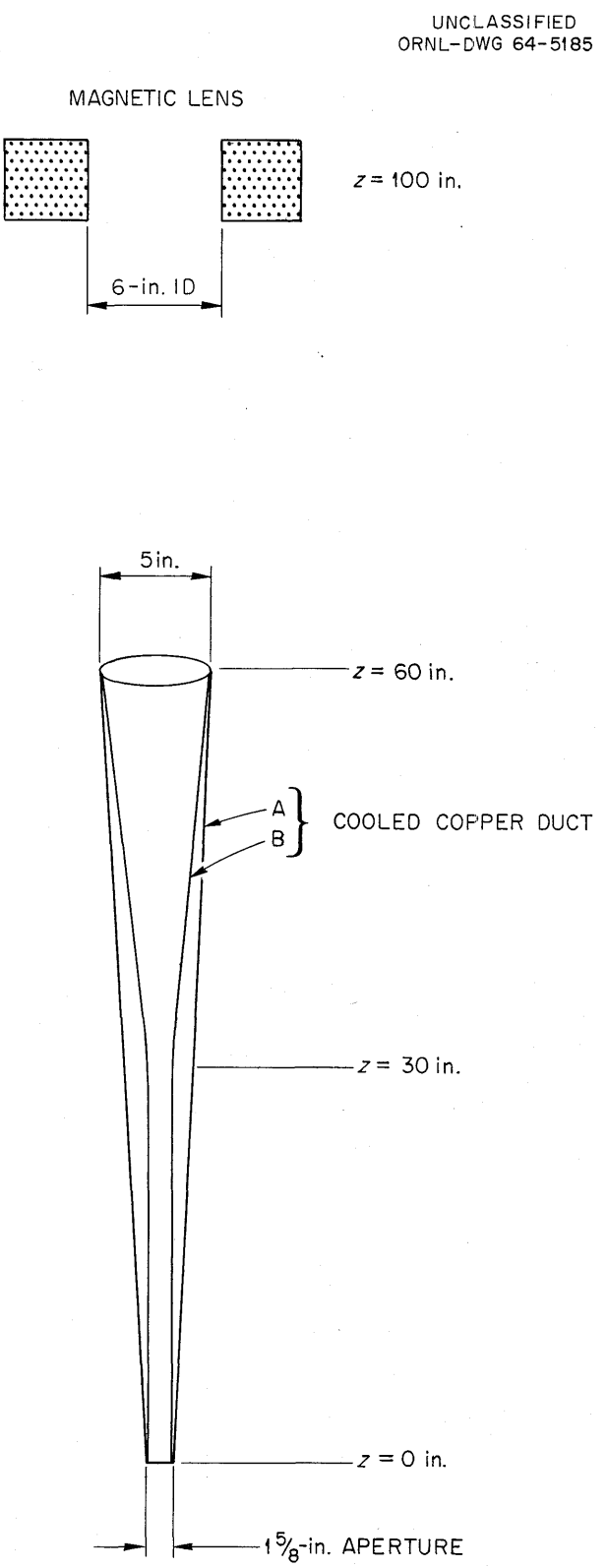

Fig. 7.2. Variation in Injection Duct Geometry Resulting in a Factor of 2 Reduction in Maximum Injected Current.

7.2 NEGATIVE ION SOURCE

O. C. Yonts A. M. Veach[5]

Operation of the negative ion source has been improved and Cl^- beams in excess of 100 ma have been obtained. It has also been possible to obtain H_2^- beams of 10 ma.

The following preliminary observations, subject to change, were made.

1. The negative ion beam was extremely stable.
2. Operation of a negative and a positive beam together improved the stability of the positive beam.
3. In the case of Cl^- there was a large loss process which resulted in beam attenuation.
4. Carbon tetrachloride, $SiCl_4$, and Cl_2 were all equally good as sources of Cl^- ions. Carbon tetrachloride is generally used because of ease of handling.
5. Production of negative ions required somewhat higher internal source pressure, but accurate determinations have not been made.

7.3 AC ION SOURCE

O. C. Yonts

Application of ac to the negative ion source results in positive ion output on one half cycle and negative ions out on the other half cycle. Peak currents of 100 ma for Cl^- and 200 ma for positive ions (C^+ and Cl^+) have been obtained. Negative carbon ions have not been detected.

Figure 7.3 shows a curve of ac output taken at a peak voltage of 25 kv.

Peak positive current – 76 ma

Peak negative current – 50 ma

Positive beam on – 6.9 msec

Negative beam on – 6.6 msec

Beam off plus to minus switch – 2.4 msec

Beam off minus to plus switch – 0.6 msec

The use of ac ion sources producing both positive and negative ions may have application in the space program.

[5]Isotopes Division.

UNCLASSIFIED
PHOTO 65514

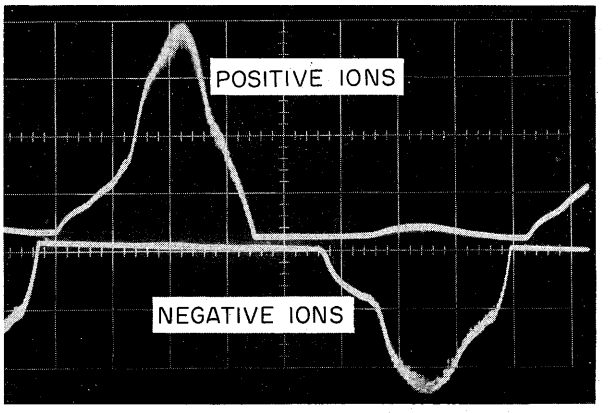

Fig. 7.3. Output of AC Ion Source. 20 ma/cm.

7.4 PIG SOURCE FOR IONS AND PLASMA

7.4.1 Ion Source Development

C. W. Blue N. H. Lazar
O. D. Matlock

The development of the PIG-type ion source reported previously[6] has been continued. No major changes in the basic design of the experimental unit have been made. However, a high degree of operational stability has been achieved. An output of 250 ma appears to be the maximum for the geometry used, that is, 3/16-in. anode diameter and 1/4-in. accelerating electrode diameter (see Fig. 7.4). The body of a 1/4-in. stainless steel Swagelok fitting has been adapted to the unit as the holder for the hollow tungsten cathode. This allows the cathode to be readily replaced without alignment difficulty.

Profile studies of the ion beam have been made calorimetrically by means of a probe that may be moved through the beam while the source is in operation. The probe may be operated in any vertical plane in the region between the source and the target (Fig. 7.4). Details for the probe are shown in Fig. 7.5. The inlet and return water paths are coaxial so that the maximum diameter is only 3/16 in. A 1/2-in. section of the probe is

[6]*Thermonuclear Div. Semiann. Progr. Rept. Oct. 31, 1963,* ORNL-3564, p. 76.

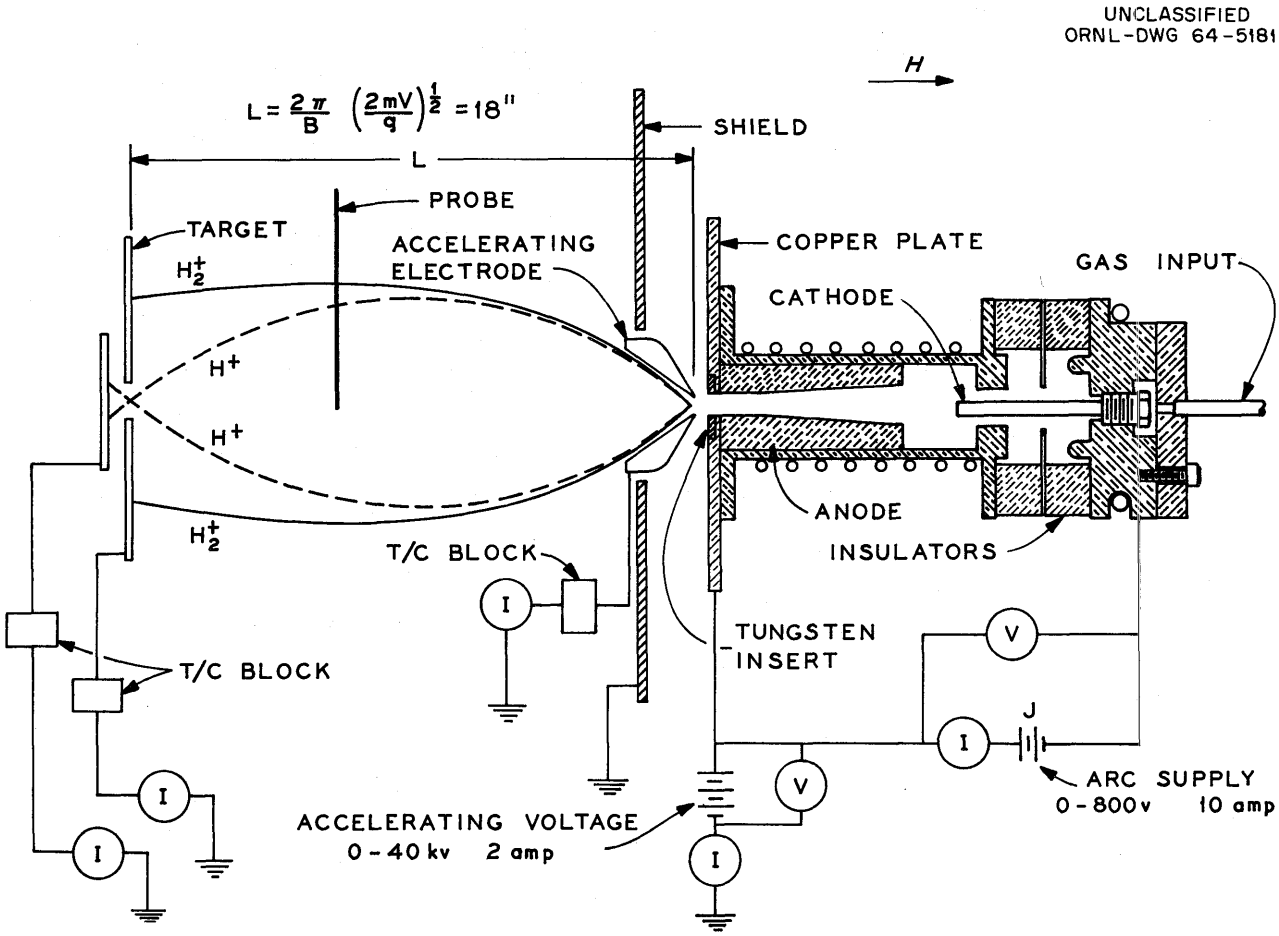

Fig. 7.4. PIG-Type Ion Source: Operated in 32-in. Gap and Uniform Magnetic Field.

exposed to the ion beam; the remainder is protected by the outer water-cooled shield. Thus the effective probe cross section is 3/32 in.^{2}. Power to the probe is measured by means of a differentially connected thermopile.[7] The results of two scans are shown in Figs. 7.6 and 7.7. The first was made with the probe 7 in. from the large target and shows very little separation of the H_1^+ and H_2^+ ions. It also shows the current density along the center line in the midregion to be quite low (about 0.1 ma/cm^2). Figure 7.7 shows data taken with the probe 2 in. from the target. At this position there is good separation of the H_1^+ and the H_2^+ ions. The total currents, from the integrals under the curves corrected for the geometry, are in agreement to approximately 5% in the two positions. These scans were made with an accelerating potential of 32.5 kv and with the magnetic field adjusted to maximize the focus of the H_1^+ ion current on the small target as indicated in Fig. 7.4. The amount of H_3^+ cannot be assessed since its distribution would overlap the H_2^+ distribution.

In a previous report[8] mention is made of a new ion source having integral magnetic coils. The principal difficulty has been in maintaining a reliable vacuum connection between the insulator and the anode and cathode. In particular, breakdowns during initial cleanup of the accelerator gap resulted in breaking of the vinyl-sealed joint. Figure 7.8 shows the latest modifications. Coils and accelerating electrode are not shown. A prototype has been in operation in tank *D* as a plasma source.

[7]Differential Temperature Transducer model No. 75-250-10; supplied by Delta-T Co.

[8]*Thermonuclear Div. Semiann. Progr. Rept. Oct. 31, 1963*, ORNL-3564, p. 78.

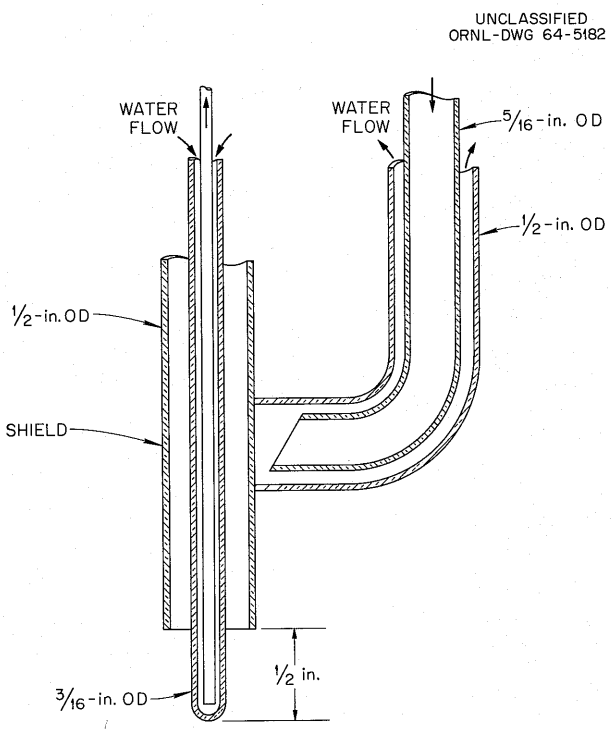

Fig. 7.5. Water-Cooled Probe Used for Differential Calorimetric Measurements of Beam Profile. Water inlets are coaxial with returns.

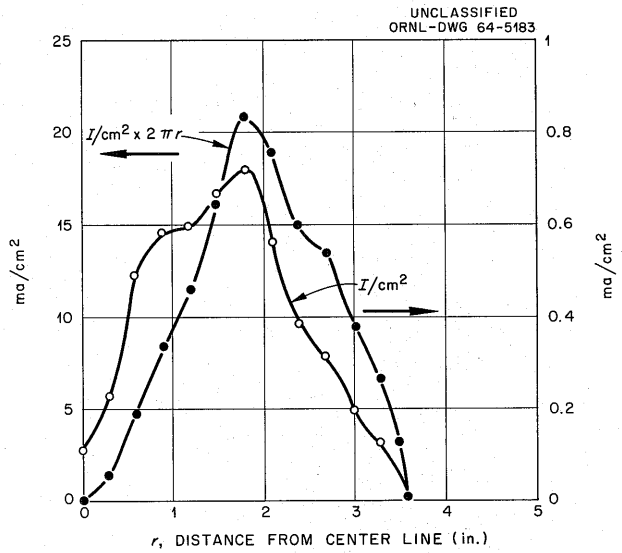

Fig. 7.6. Current Density, Midplane.

Fig. 7.7. Current Density 2 in. from Target.

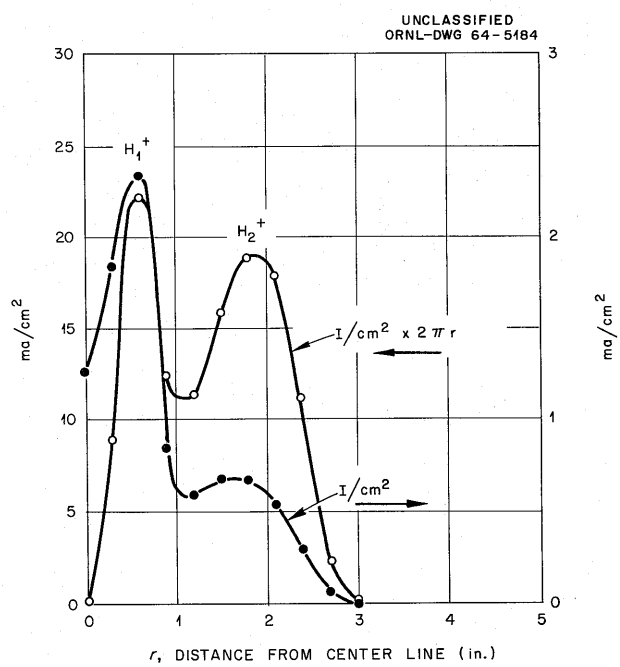

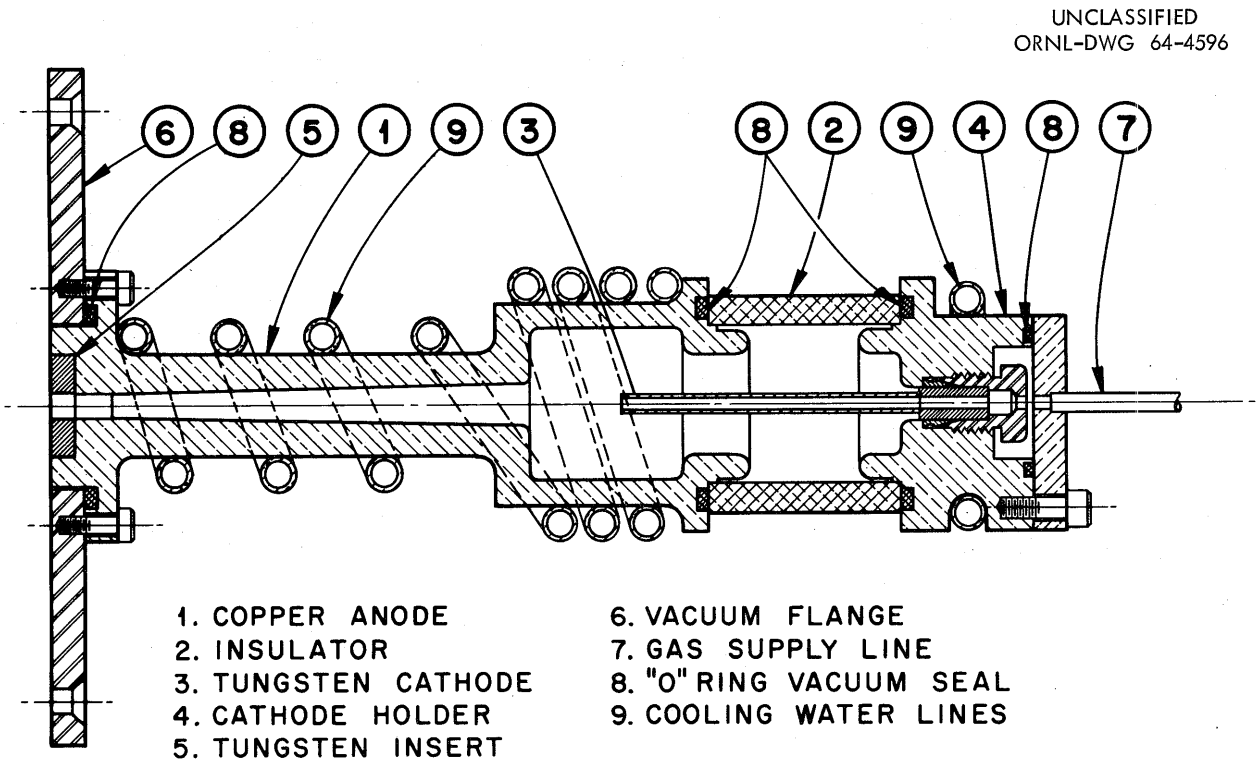

Fig. 7.8. Ion Source, New Design; Magnetic Coils and Accelerating Electrode Are Not Shown.

7.4.2 Plasma from PIG-Type Ion Source

C. W. Blue N. H. Lazar
O. D. Matlock

The plasma from the PIG-type ion source was allowed to diffuse from the anode into the nominally field-free space toward a floating target approximately 18 in. away. The source character changed only very little if the floating target was grounded. A ground plane with a 1-in. hole was placed in front of the floating target as shown in Fig. 7.4. The plasma was studied with a gridded probe, much like those used in DCX-2,[9] and with small wire probes with or without a grounded grid around it. All probes could be moved radially and, in some cases, were displaced axially in order to look for axial correlation of the time-dependent behavior.

The gridded probe is shown in Fig. 7.9. The outer grid is grounded and the second grid could be biased positive or negative to repel either ions or electrons as desired. The potential on the collector was swept at 60 cps to voltages as large as ±900 v, and the current was measured through a 100-ohm or 1-kilohm resistor.

Typical data are shown in Fig. 7.10. Referring to the ion current (Fig. 7.10a), one would expect to receive saturation ion current until the collector potential exceeds plasma potential and then the current drops as the lower-energy ions are repelled. Thus, from the slope of the curve, one obtains information of the ion energy distribution and from the breakpoint one can determine the plasma potential. It is assumed that at these densities the conductivity is sufficiently large as to rule out axial potential variations except for small sheaths near the ground planes, for example, the Debye length is approximately 2.3 mm for densities of 10^8 and an electron temperature of 10 ev. The electron current, on the other hand, must be almost equal to

[9] *Thermonuclear Div. Semiann. Progr. Rept. Apr. 30, 1963,* ORNL-3472, p. 14.

the ion current since the production of ions and electrons along field lines, whatever the mechanism, is likely to be nearly the same. The plasma potential, of course, as has been previously pointed out,[9] adjusts itself to ensure that these currents to the wall are equal. Thus the probe, acting as a wall, has very little influence on the plasma. For large positive collector potentials one expects to see saturation electron current, and this will continue until the collector potential equals the wall potential. Then the electron current drops as the slower electrons are repelled. Of course, we only see the high-energy tail of the electron distribution since the plasma potential prevents lower-energy electrons from going to the walls. However, assuming a Maxwellian distribution, one may estimate

UNCLASSIFIED
ORNL-DWG 64-4595A

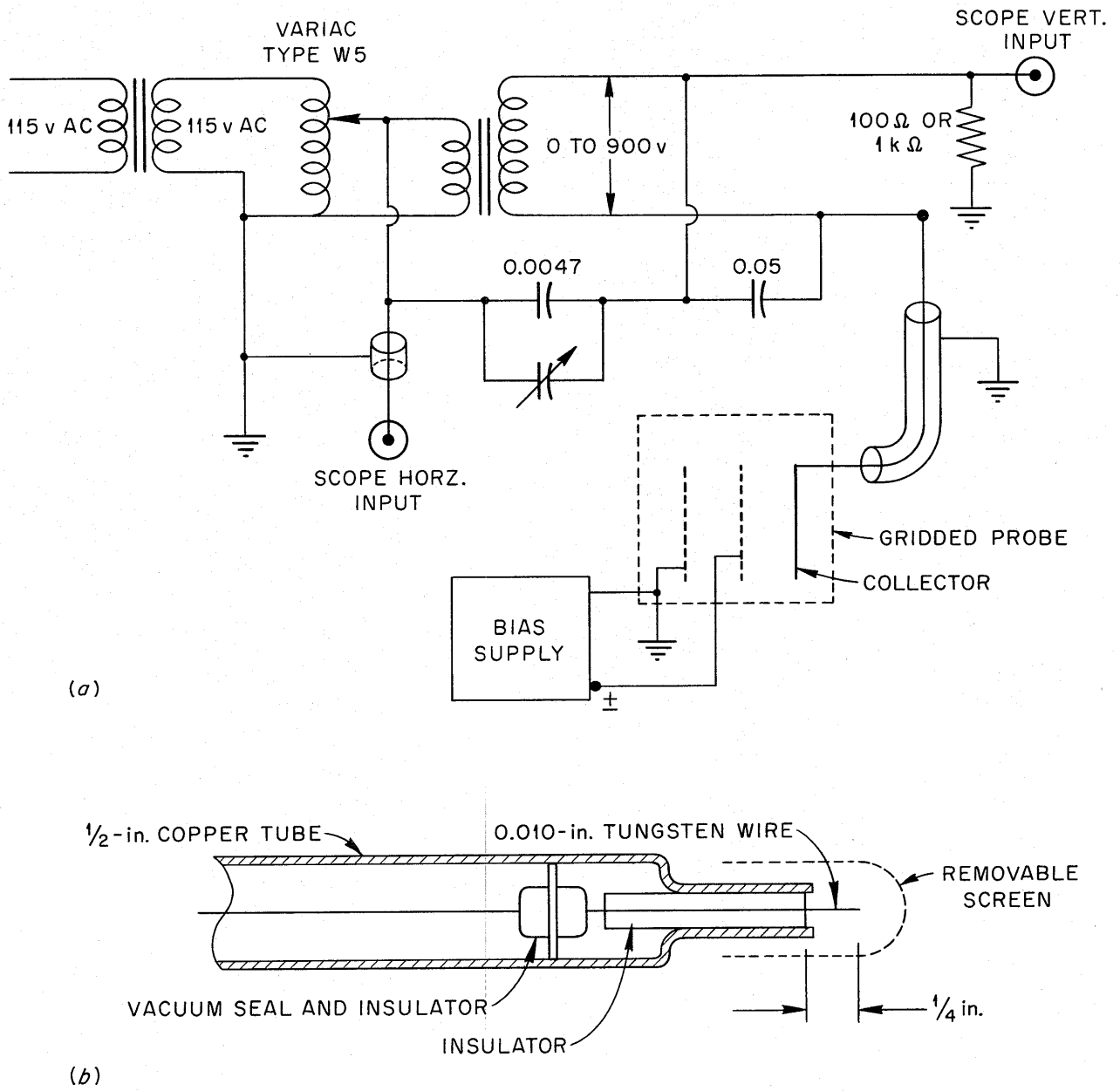

Fig. 7.9. (a) Schematic of Gridded Probe Circuitry; (b) Schematic of Small Wire Probe.

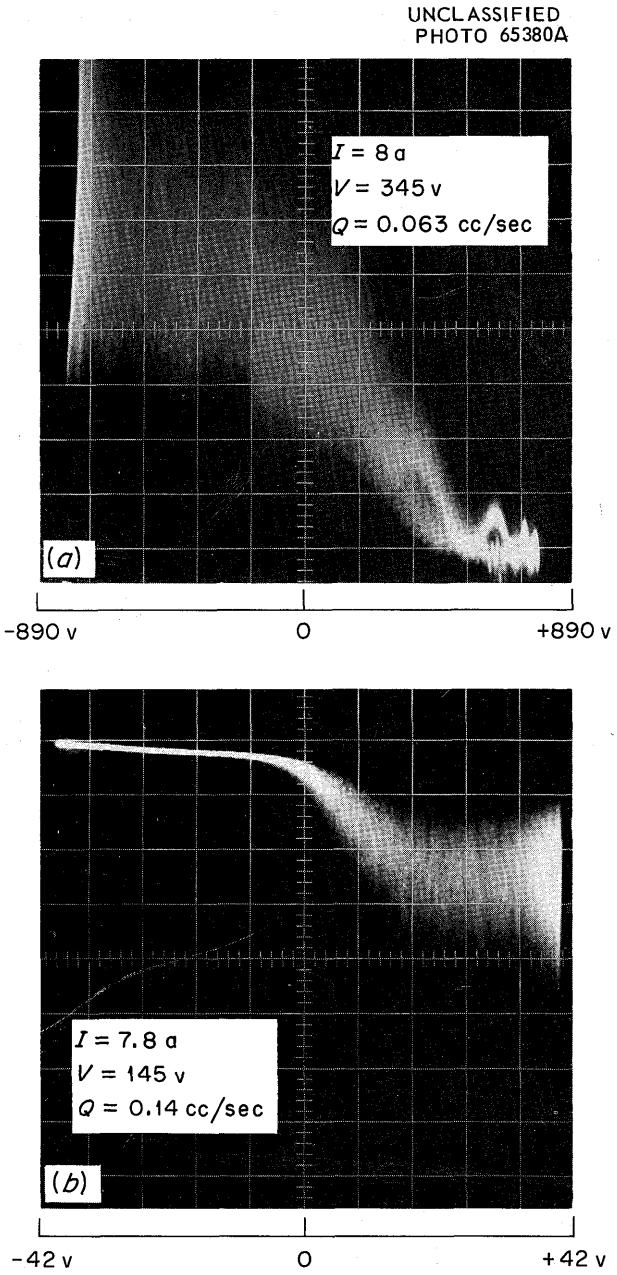

Fig. 7.10. (*a*) **Ion Current to Gridded Probe as a Function of Voltage on Collector with Electrons Suppressed by Bias on Intermediate Grid;** (*b*) **Electron Current to Gridded Probe with Ions Suppressed.**

the electron temperature. It may be noted, however, that at 10^8 electrons/cm^3 with a temperature of 10 ev, the classical self-collision time is 5 msec.

The data shown were analyzed as shown in Fig. 7.11, and the results show a plasma potential close to wall potential and a mean ion energy of approximately 360 ev. Analysis of the electron distribution gave a mean electron energy of 13 ev. Data were taken at several radial positions out to approximately 3 cm from the main column of the plasma and showed no great differences.

The most significant parameter affecting the ion energy was the gas feed rate. The data above were taken with 0.063 cc/sec. The mean energy as a function of gas feed is shown in Fig. 7.12. No sudden transitions in the character of the discharge were noted, with a variation of over a factor of 10 in feed rate. No great dependence on magnetic field was noted. The variation of ion current with source current for constant gas feed is somewhat difficult to describe, since the probe signals become significantly noisier with increasing source current. Preliminary data suggest that the temperature of the ions actually decreases and a significant, directed ion velocity appears as the

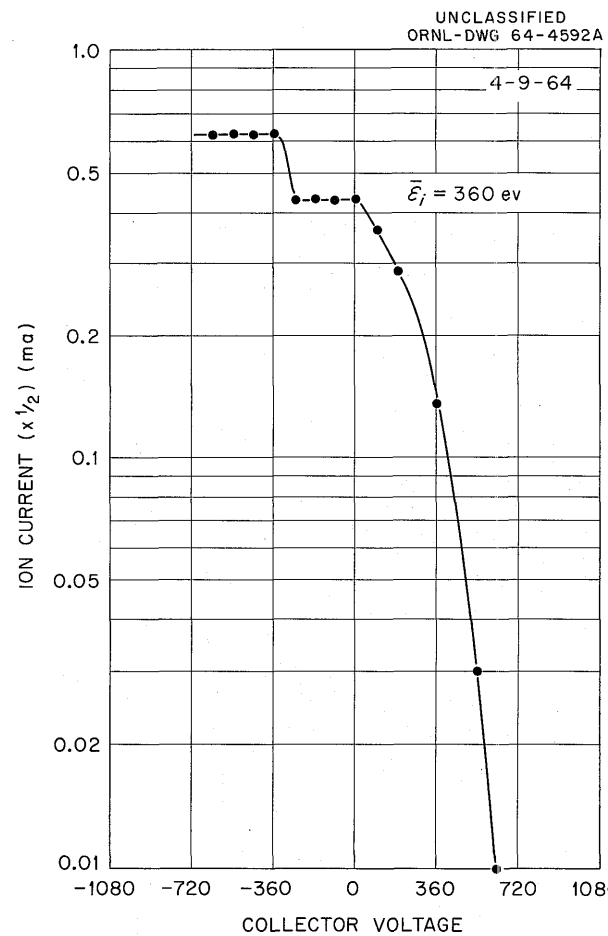

Fig. 7.11. Analysis of Fig. 7.10*a* Showing $\bar{\mathcal{E}}_i$.

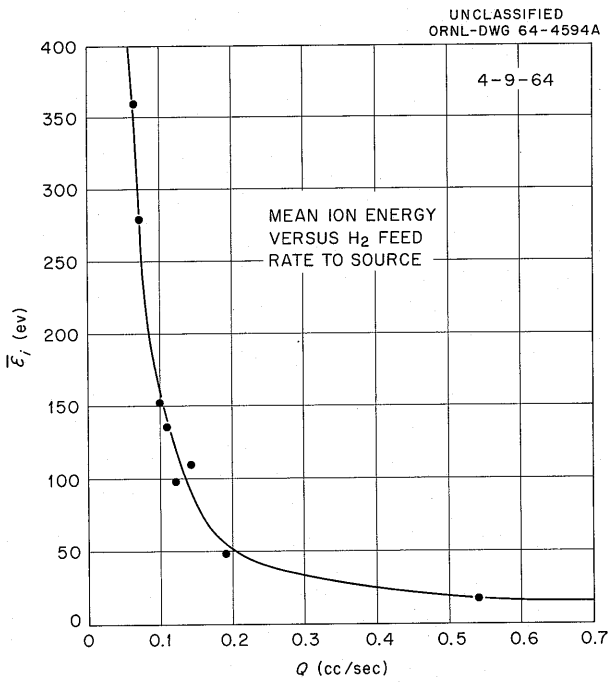

Fig. 7.12. Mean Ion Energy vs Gas Feed to Source.

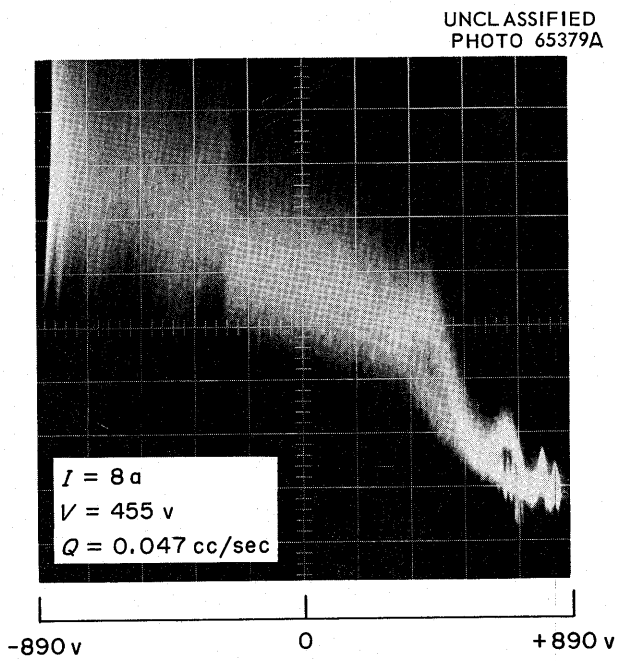

Fig. 7.13. Ion Current to Gridded Probe at Higher Source Currents Showing Directed Ions. Note the break in the ion current occurs 2 cm to the right of zero voltage (~180 v).

arc current increases. An example of these data is shown in Fig. 7.13.

The small probes were used to determine the radial, equilibrium density profile and this is shown in Fig. 7.14 for three values of magnetic field. In all cases, the density is determined from the saturation ion current and assuming $\bar{v}_z \approx 1.3 \times 10^7$ cm/sec. Data inside the radius of the anode have not yet been obtained.

The current to the probes is extremely noisy under all conditions (Fig. 7.15). Coherence of floating potentials of probes along the same field line has been established, although rather poorly, and it is not yet clear if any correlation of ion bursts to probes displaced either in z or azimuth is present.

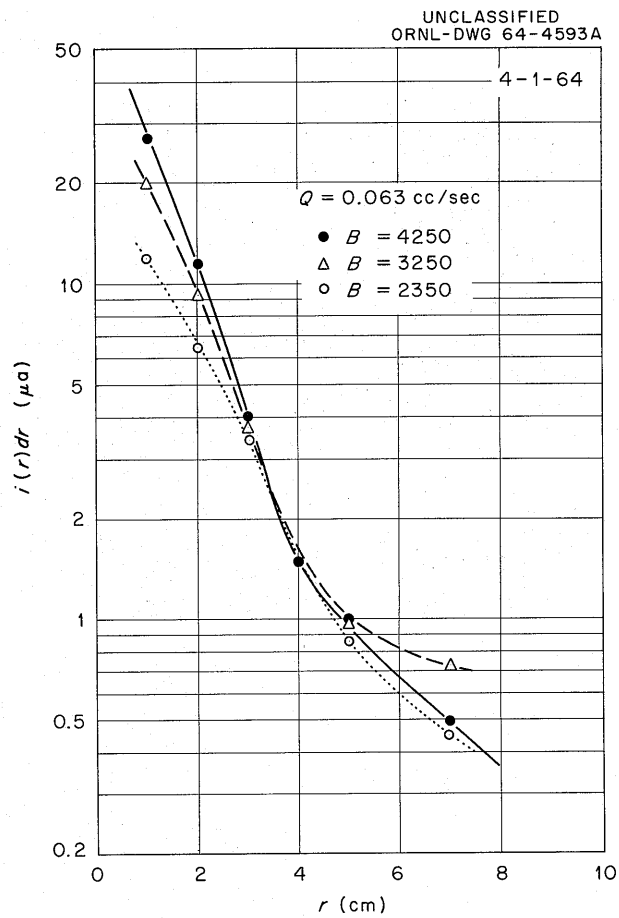

Fig. 7.14. Radial Distribution of Current to Probe Biased to Accept Only Ions. If the radial distribution of ion velocity is constant, the figure represents the density profile.

UNCLASSIFIED
PHOTO 65378A

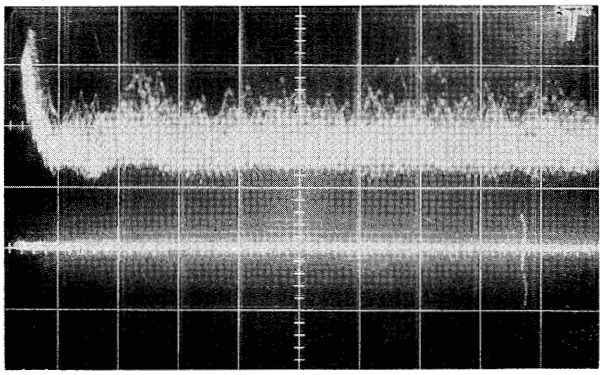

VERT. 2 μa/cm; HORIZ. 10 μsec/cm; GRID BIAS: −90 v

Fig. 7.15. Ion Current to Small Probe Biased to Receive Only Ions vs Time.

7.5 NEUTRAL BEAM SOURCE

H. C. Hoy O. D. Matlock
N. H. Lazar R. L. Knight

A duoplasmatron ion source[10] is used with a solenoidal focusing lens and charge-changing cell to produce a beam of mixed H_2^0 and H^0 atoms with an energy of 20 kev/particle for injection into the electron-cyclotron-heated plasma. The beam must travel a distance of over 17 ft and pass through a 2-in. aperture before entering the microwave cavity. Figure 7.16 shows a layout of the injection system into the EPA vacuum tank. Typically, with 40 kev

[10] G. G. Kelley, N. H. Lazar, and O. B. Morgan, *Nucl. Instr. Methods* 10, 263–71 (1961).

UNCLASSIFIED
ORNL-DWG 64-4366

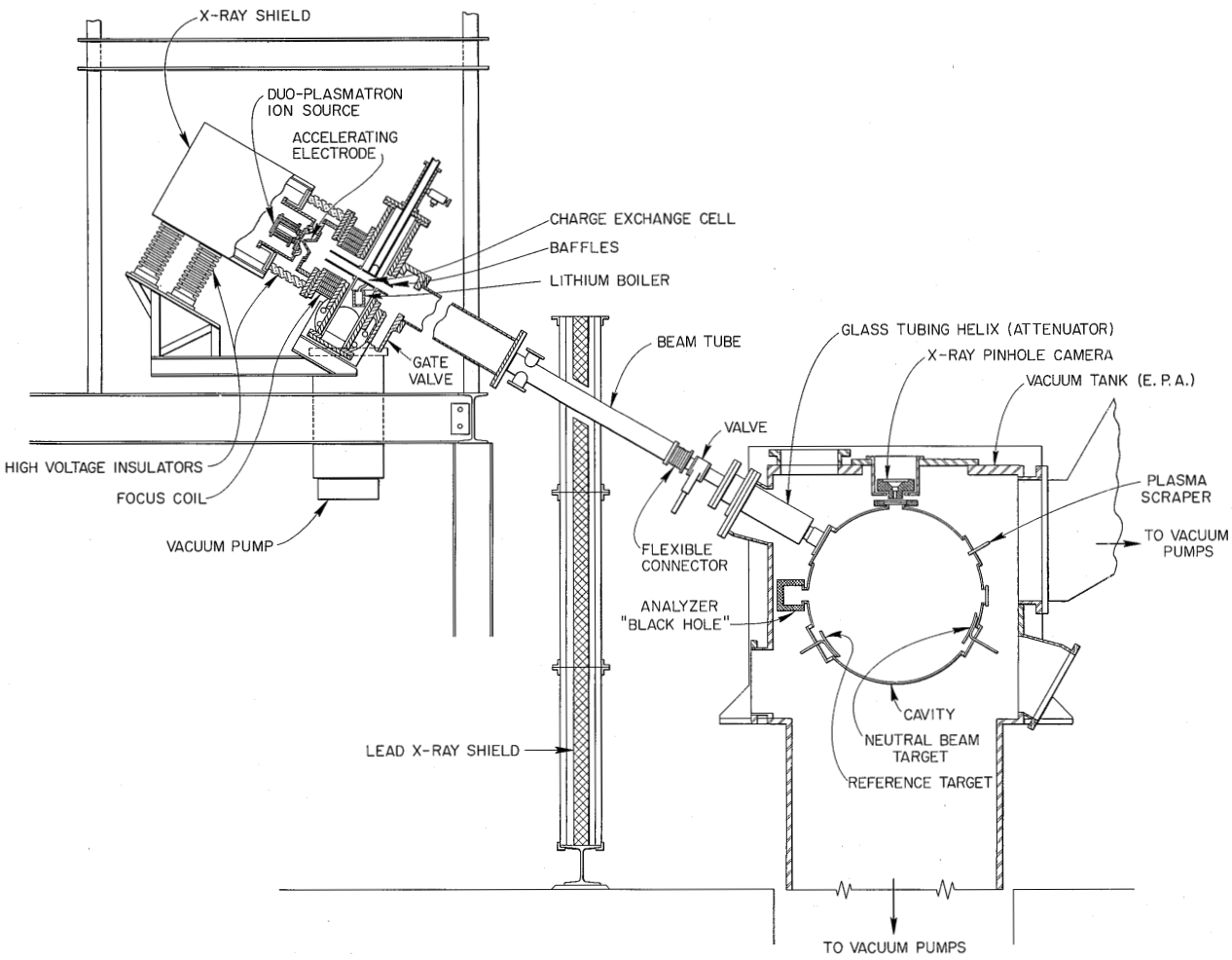

Fig. 7.16. Layout of the System for Injection of High-Energy Neutral Atoms into the Electron-Cyclotron-Heated Plasma.

accelerating potential, over 100 ma of ions may be measured in the throat of the lens (6-in. diam, ~10 in. from the accelerating gap). However, this beam is far too large in diameter to be useful. In fact, for beams in excess of ~30 ma, only ~7 ma of H_2^+ ions are seen at the target in EPA and ~15 to 20 ma are seen on the last baffle. Neutral currents of ~4 ma of the mixed species (measured calorimetrically) have been used in the initial injection experiments. Studies have been made using titanium, magnesium, and lithium charge-changing gases. All prove successful for short times, but difficulties in controlling the amount of metal vapor have required further studies before day-to-day use can be envisaged. The titanium and the magnesium vapor were sublimed from tungsten filaments while the lithium vapor was produced in a separate boiler.

8. Plasma Theory and Computation

8.1 ANOMALOUS DIFFUSION

T. K. Fowler C. O. Beasley

Previous estimates of anomalous diffusion have been extended,[1] and a paper is being submitted for publication. Theoretical upper limits on fluctuation intensity and anomalous plasma diffusion across a magnetic field are obtained from purely thermodynamic considerations. The bounds agree with anomalous diffusion observed at low temperatures, both the rapid "pumpout" in stellarators with ohmic heating currents and the slower diffusion in discharge afterglows without such currents. In both cases, thermal energy appears to feed fluctuations through a mechanism akin to expansion cooling of a gas, only possible in finite plasmas and associated with "universal" microinstabilities. An observed rapid decrease in anomalous diffusion in afterglows with radii $R > R_0 \sim 40\ \rho_i$ (ion gyroradius) can be explained if the instability radial wavelength, a parameter in the theory, is restricted to $\lesssim R_0$. Then, if $R > R_0$, the bound on the diffusion coefficient decreases like R^{-3}, about as observed. With this restriction on wavelength, plausible theoretically,[2] the bound, used as a scaling law, predicts adequately long thermonuclear confinement (0.1 sec) in a torus stabilized against interchange and other macroinstabilities (minor radius $\lesssim 100$ cm). This result is valid at least up to a β of 2 to 3%. Bounds on the velocity diffusion coefficient are obtained also.

As the predicted diffusion coefficient D_r varies with space, the corresponding diffusion decay time might be different from the usual result,

$$\tau \propto R^2 D_r^{-1} . \qquad (1)$$

However, since D_r is greatest where the density gradient is greatest, one suspects that, as with a constant coefficient, the density distribution will rapidly smooth out, D_r becoming about constant, so that (1) again holds. To test this hypothesis, an example one-dimensional case was integrated numerically. The result is the succession of curves, Fig. 8.1. As expected, starting from an initial Fermi distribution at $t = 0$, after a brief transient the density profile is gently sloping, and the decay time τ turns out to be about (1) with $R = 0.6x_0$, where x_0 is the initial radius, as indicated in the figure.

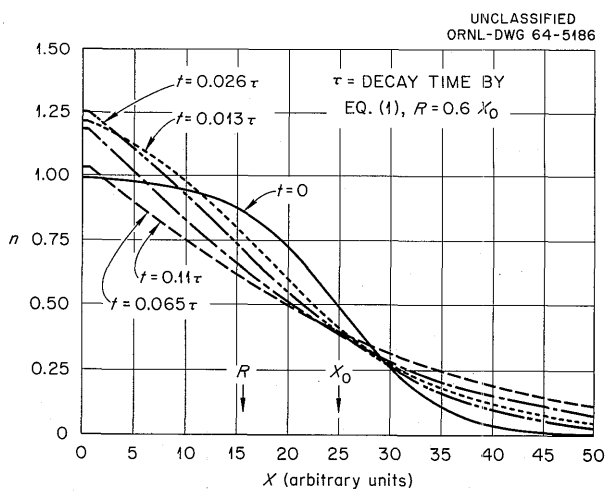

Fig. 8.1. Spatial Diffusion with a Coefficient Depending on x [Eq. (1)]. Curves are labeled by time in units of the expected decay time τ.

[1] *Thermonuclear Div. Semiann. Progr. Rept. Oct. 31, 1963*, ORNL-3564, p. 87.

[2] B. B. Kadomtsev, *J. Nucl. Energy: Pt. C* 5, 31 (1963).

8.2 EFFECT OF FINITE ION AND ELECTRON TEMPERATURES ON THE ION-CYCLOTRON RESONANCE INSTABILITY

G. K. Soper[3] E. G. Harris[4] Y. Shima

Effects of finite ion and electron temperatures on the ion-cyclotron resonance longitudinal instability in plasmas with anisotropic ion temperature, investigated previously,[5] have been surveyed further. The stability boundary in the ω_{ci}-ω_{pe} plane is determined, and growth rates are explored in various regions. Figure 8.2 shows this plot, with regions of applicability for the DCX's, OGRA, ALICE, and Phoenix injection machines. Figures 8.3–8.6 show the effects of nonzero ion-anisotropic and electron temperatures on the stability boundary. It is seen that either reducing $T_{\perp i}/T_{\parallel i}$ or increasing the electron temperature tends to stabilize these anisotropy modes. Also, even with cold electrons and $T_{\perp i} >> T_{\parallel i}$, reducing the magnetic field stabilizes a plasma of finite length, as has been observed in the Phoenix experiment.[6]

[3]Graduate Fellow, University of Tennessee.

[4]Consultant, University of Tennessee.

[5]G. K. Soper and E. G. Harris, *Bull. Am. Phys. Soc. Ser. II*, 9, 58 (1964). See also *Thermonuclear Div. Semiann. Progr. Rept. Oct. 31, 1963*, ORNL-3564, p. 84; Yu. N. Dnestrovsky, D. P. Kostomarov, and V. I. Pistunovich, *Nucl. Fusion*, 3, 30 (1963).

[6]L. G. Kuo *et al.*, Culham Laboratory Report, CLM-P32, 1963.

Stability boundaries and growth rates have also been determined when the anisotropic distribution rotates as a whole, representing diamagnetic current due to finite plasma radius. We study the extreme case, investigated by Shima,[7] of rotation at the ion-cyclotron frequency, representative of plasmas about one Larmor radius across, as in the

[7]Y. Shima, *Thermonuclear Div. Semiann. Progr. Rept. Oct. 31, 1962*, ORNL-3392, p. 61.

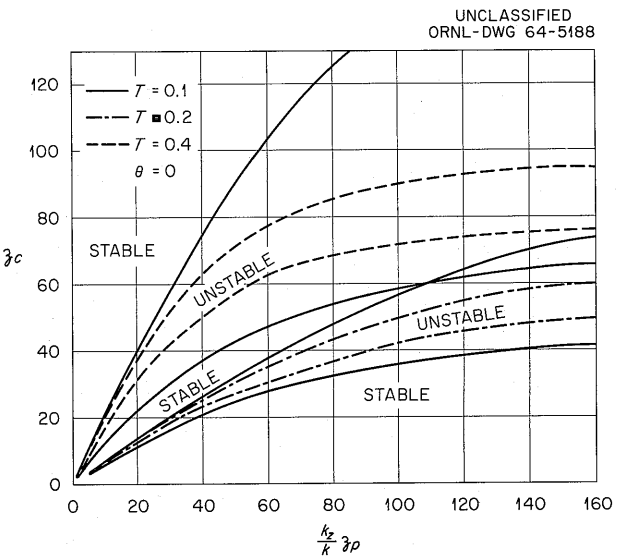

Fig. 8.3. Effect of Finite Ion Anisotropy on Cold Electron Plasma.

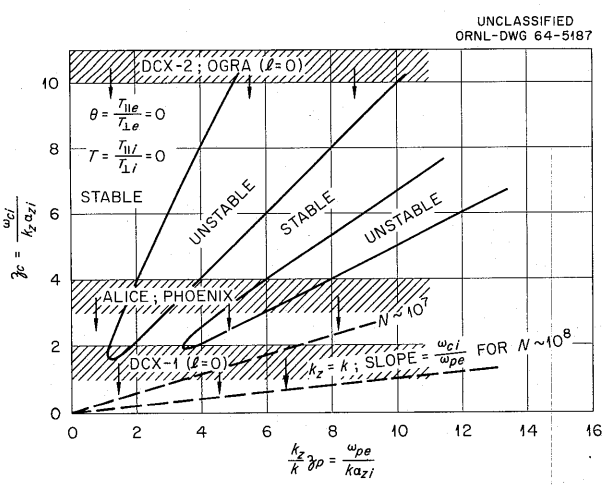

Fig. 8.2. Regions of Applicability for Different Injection Machines.

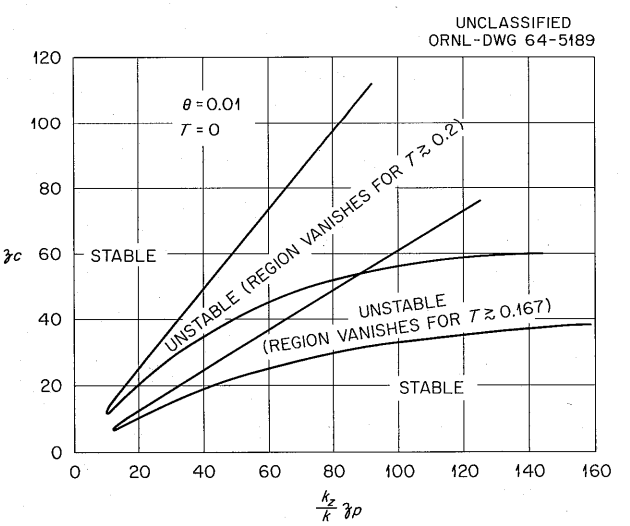

Fig. 8.4. Effect of Finite Electron Temperature on Stability Regions.

DCX's and OGRA. In this limit, most of the above anisotropic modes remain essentially unchanged. However, for each value of the azimuthal mode number $l \neq 0$, that anisotropy mode with angular velocity $(=\mathrm{Re}\,\omega/l)$ most nearly coinciding with that of the ions changes character and becomes essentially the instability found by Burt and Harris[8] in a cylinder of zero-temperature ions rotating through electrons. Figure 8.7 is a plot of these interacting modes. The ordinate of this map has been replaced by a frequency label, since for $z_c \cong 10$, $(k_z/k)\, z_p \cong \mathrm{Re}|\omega|/k_z \alpha_{zi}$. Again reducing $T_{\perp i}/T_{\parallel i}$ removes the unstable anisotropic modes but leaves the Burt-Harris mode only slightly changed.

[8]P. Burt and E. G. Harris, *Phys. Fluids* 4, 1412 (1961); E. G. Harris, Culham Laboratory Report, CLM-R32, 1963.

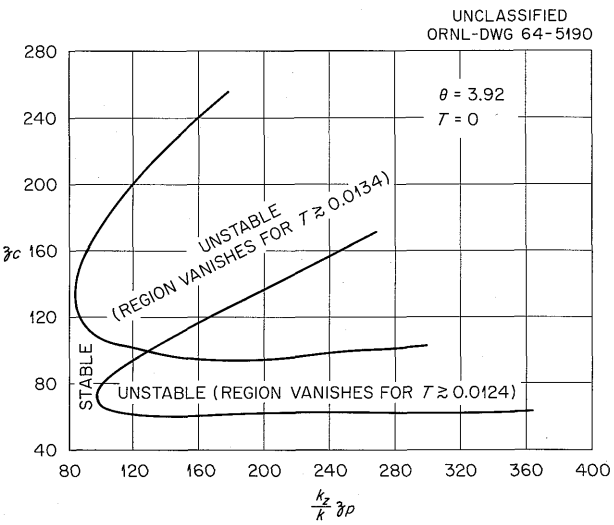

Fig. 8.5. Effect of Finite Electron Temperature on Stability Regions.

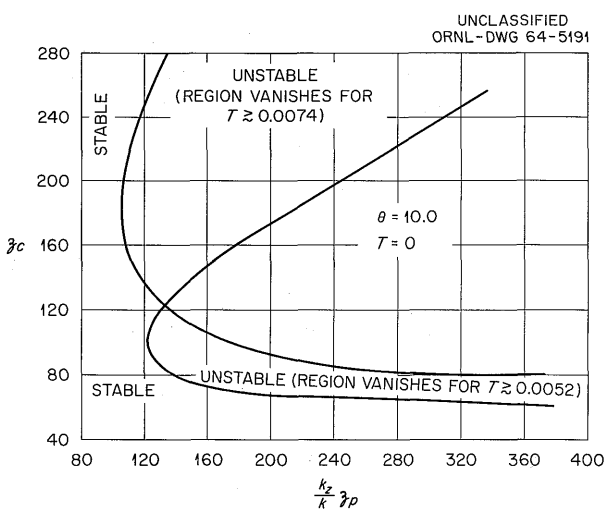

Fig. 8.6. Effect of Finite Electron Temperature on Stability Regions.

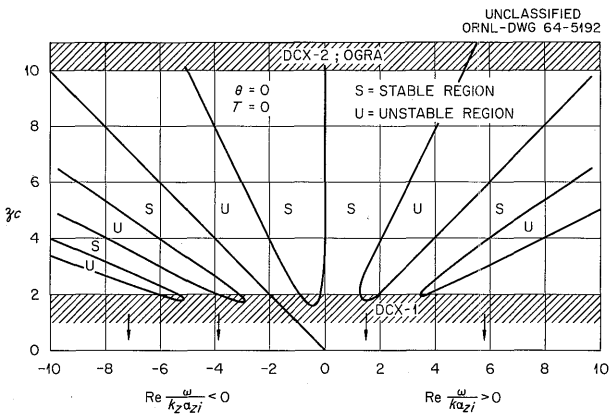

Fig. 8.7. Effect of Anisotropic Ion Distribution Rotation at ω_{ci}.

8.3 STABILITY OF FINITE PLASMAS

Y. Shima

The investigation of the stability of finite plasmas can be reduced to a consideration of an algebraic dispersion equation when the component of the perturbation wave number perpendicular to the magnetic field is small.[9] We assume the distribution function of species j to be

$$f^{(j)} = n \frac{\alpha_j c_j}{\pi^2} \frac{1}{1 + \alpha_j^2 v_z^2} e^{-a_j p \theta - c_j v_\perp^2} ,$$

$$\int f^{(j)}\, d\vec{v} = n e^{-r^2/R_0^2} ,$$

$$\frac{1}{R_0^2} = \frac{a_j \omega_j}{2} \left(1 - \frac{a_j}{2 c_j \omega_j}\right) = c_j \omega_j^2 \epsilon_j (1 - \epsilon_j) ,$$

$$\epsilon_j = \frac{a_j}{2 c_j \omega_j} .$$

[9]*Thermonuclear Div. Semiann. Progr. Rept. Apr. 30, 1963*, ORNL-3472, p. 77.

Note that $\epsilon_j(1-\epsilon_j) = r_j^2/R_0$, where r_j is the Larmor radius.

The dispersion equation for the short wave number limit has the following form:

$$C = \sum_j \frac{\omega_{pj}^2}{\omega_j^2} \int_{-\infty}^{0} dt\, e^{(p+k_z/\alpha_j)t} \Big[-il\omega_j (1 - e^{-i\omega_j t})(1-\epsilon_j+\epsilon_j e^{-i\omega_j t})^{l-1} + \frac{1}{2} k_z^2 R_0^2 \omega_j^2 t (1-\epsilon_j+\epsilon_j e^{-i\omega_j t})^l \Big], \quad (1)$$

$$\frac{1}{C} = \frac{1}{2^{l+1}\, l!} \int \frac{dy}{y + (1/2)\, k_z^2 R_0^2}\, y^l e^{-y}, \quad \epsilon_j = \frac{a_j}{2c_j\omega_j},$$

$$\omega_{pj}^2 = \frac{4\pi n e_j^2}{m_j}.$$

The perturbation is assumed to be $e^{ik_z Z + il\theta}$ with a time dependence e^{pt}.

Let us assume that the electrons are cold, and that $|p| \ll \omega_e = eH/m_e c$. Equation (1) can then be written, for $l = 1$, in the following way:

$$\frac{2C}{k_z^2 R_0^2}\frac{\omega_i^2}{\omega_{pe}^2} = \frac{1}{x^2} + \frac{m_e}{m_i}\left\{ \frac{1-\epsilon_i}{[x - i(1/z_c)]^2} + \frac{\epsilon_i}{[x-1-i(1/z_c)]^2} - \frac{2}{k_z^2 R_0^2}\left[\frac{1}{x-1-i(1/z_c)} - \frac{1}{x-1-i(1/z_c)}\right]\right\}, \quad (2)$$

where $z_c = \alpha_i\omega_i/k_z$, $p/\omega_i = ix$. The plasma is unstable when the imaginary part of x is negative.

A way to analyze the dispersion relation is to find the locus of all points where Im (x) = 0. This gives the boundaries of stability and instability. In Fig. 8.8 we do this in the plane z_c, s, where

$$s = \frac{\omega_{pe}}{\omega_i}\sqrt{\frac{20}{c\epsilon_i(1-\epsilon_i)}}.$$

The stable regions are marked *S*, and the unstable regions are marked *U*. In this example we assumed $\epsilon_i = 1/2$ and the anisotropy $T_\perp/T_{||} = 10$; $T_\perp$ is the perpendicular temperature, and $T_{||}$ is the parallel temperature $T_\perp/T_{||} = \alpha_i^2/c_i$.

It can be shown that the closed curve depends very much on $T_\perp/T_{||}$. It shrinks as $T_\perp/T_{||}$ decreases and disappears when $T_\perp/T_{||} < 2$. The other curve depends more on ϵ_i:

$$\epsilon_i(1-\epsilon_i) = \left(\frac{r_i}{R_0}\right)^2.$$

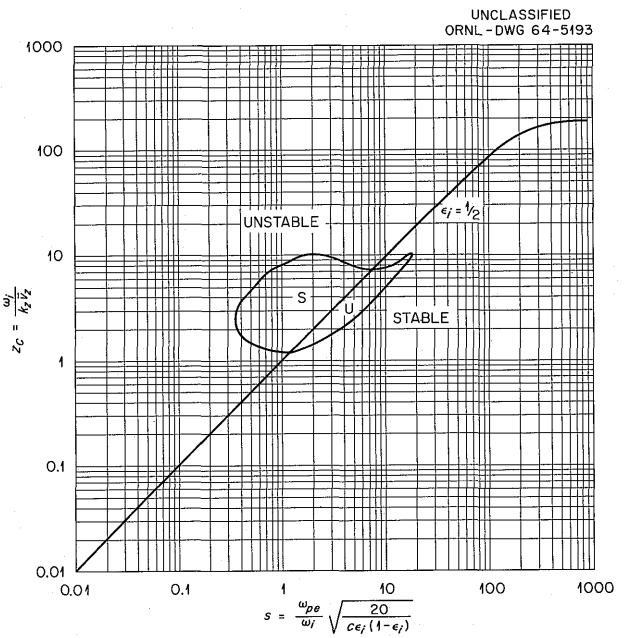

Fig. 8.8. Stable and Unstable Regions of Finite Plasma.

8.4 SOME QUALITATIVE OBSERVATIONS ON THE STABILITY OF THE CALUTRON ION BEAM

G. Guest E. D. Shipley O. Yonts

A recent model of the low-pressure calutron instability proposed by Shipley and Yonts seems to offer sufficient promise of an eventual understanding of the dominant stability features of this system that it will be outlined here in its present qualitative form in the expectation that a more complete quantitative analysis can be given in the near future.

To understand the (heuristic) foundations of the current model, one must recall that in the calutron a stream of energetic ions moves perpendicular to

the lines of magnetic induction, $\bar{B}$; whereas the electrons required for the neutralization of the ion beam oscillate along $\bar{B}$ in the electrostatic potential trough created by the beam. In the usual calutron, this potential trough varies in depth from around 10 v near the source end of the beam to 50 v or more at a point midway between the source and the collector.

We now suppose that, at least in a crude sense, electrons oscillating in the ion beam's potential trough can be classified as stabilizing or destabilizing according to their maximum kinetic energy with respect to the bottom of the potential trough. That is, electrons oscillating with large amplitudes across the potential trough are expected to lead to growing disturbances through a bunching response; while electrons with relatively little energy (and thus with small oscillatory amplitudes) would be expected to damp such disturbances by means of the "trapping" mechanism (the terms "bunching" and "trapping" are used here in the sense described, for example, by Jackson[10]).

Electrons produced by ionization in the beam of background gas atoms will, in the absence of rapid heating processes, have energies of less than around 10 v relative to the potential of the region in which they are created. These "local" electrons, then, would normally comprise the stabilizing group. However, if electrons born in a shallow region of the potential trough (e.g., near the source, where electrons are produced copiously) can be transported into the deeper regions of the trough in times short compared to energy relaxation times for ion-electron heating and electron-electron equipartition, they become members of the destabilizing group of electrons.

The detailed mechanisms by which electrons are actually transported along the beam's potential trough (and across $\bar{B}$) are not known; one can show that electric fields of only a few v/cm could, through cycloidal drift motions, provide sufficiently rapid transport to distribute the electrons from the source region along the entire length of the beam in times shorter than relaxation by the usual Coulomb interactions.

One would thus expect that as the background pressure is decreased, thereby decreasing the production rate of "local" electrons, the destabilizing effect of the electrons flowing in from the shallow regions of the trough could overcome the damping effects due to the locally produced electrons.

Present theoretical efforts center on deriving a stability criterion embodying in a rigorous fashion the classification of electrons, trapped in a potential well, according to their distribution in energy in this well.

[10] J. D. Jackson, *J. Nucl. Energy: Pt. C* 1, 171 (1960).

8.5 IMPEDANCE PROPERTIES OF A ONE-DIMENSIONAL BEAM-PLASMA SYSTEM

G. Guest

The dramatic stabilization of the calutron ion beam, brought about by its interaction with a complex external circuit network, has motivated an investigation of the effect on the impedance of a grid or aperture structure of the convective longitudinal space-charge wave in a beam-plasma system coupled to the grid structure.

The case in which a monoenergetic stream of charged particles passes through a cold background plasma and is perpendicular to the planes of the (parallel) rf grids has been analyzed to yield the impedance between the grids as a function of frequency and grid spacing.

The two groups of particles participating in the wave motion are described by suitable Vlasov equations, and the rf current density is assumed to be

$$\frac{I(t)}{A} = \epsilon_0 \frac{\partial E}{\partial t} + \int_{-\infty}^{\infty} v\, dv\, (q_1 f_{11} + q_2 f_{21}) \qquad \text{if } |x| < L/2$$

$$= 0 \text{ if } |x| > L/2 \ ,$$

where A is the area of each of the grids, and L is their separation.

The impedance Z is defined as the ratio of the Laplace transforms of the potential difference between the grids and the current flowing in the

grid circuit. Since only the spatial integral of the electric field appears in Z, detailed spatial solutions of the equations of motion for perturbations are not necessary. Instead, the problem reduces to the inversion of a well-defined Fourier transform, which is then accomplished by contour integration for the specific case under examination.

If one invokes the usual requirement that the impedance be analytic throughout the right half of the complex frequency plane, one can readily evaluate the resulting impedance in terms of the zeros of the dispersion relation appropriate to the system. In fact, if $\Gamma = \zeta + i\gamma$ signifies the complex propagation constant, the impedance is

$$Z = \frac{1}{i\omega C_0}\left\{1 + \left(\frac{\omega}{\omega_{p2}}\right)^2 \frac{\gamma L}{|\Gamma L|^4}\left[2\gamma L(|\Gamma L|^2 + i\zeta L) + (\Gamma^* L)^2 e^{-i\Gamma L} - (\Gamma L)^2 e^{-i\Gamma^* L}\right]\right\},$$

where C_0 is the vacuum capacitance of the grids, and ω_{p2} is the cold-plasma (radian) frequency. In the idealized case of no thermal motion and no loss mechanism,

$$\zeta = \frac{\omega}{V_{\text{beam}}},$$

$$\gamma = \left(\frac{\omega_{p,\text{beam}}}{V_{\text{beam}}}\right)\frac{\omega}{\sqrt{\omega_{p2}^2 - \omega^2}}.$$

However, numerical solutions of the dispersion relation for electron beams interacting with plasma electrons have been published which take into account the effects arising from thermal distributions of particle speeds;[11] and one can obtain more realistic estimates of the impedance for such electron beam systems by using these results in place of the idealized expressions for Γ.

By way of example, Fig. 8.9 shows the resistance R and the reactance X as functions of grid spacing at the frequency which maximizes the convective growth rate γ for a system containing a 500-ev electron beam of density 10^8 cm^{-3} passing through a 10-ev thermal electron population of density 10^9 cm^{-3}. For such a system, Sumi gives

$$\zeta \cong 2\text{cm}^{-1}, \qquad \gamma \cong 1.2\text{cm}^{-1}.$$

Figure 8.10 shows, for the idealized propagation constants, how the grid admittance and power factor vary with frequency in a typical case of electron beam–cold electron plasma. The physical implications of this impedance function, and particularly of the regions of negative resistance and power factor, are being further explored.

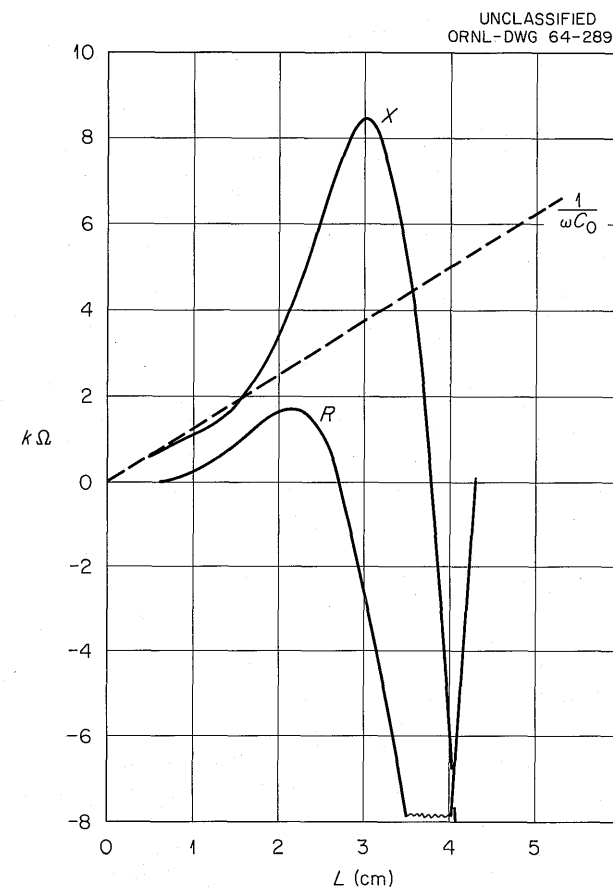

Fig. 8.9. Reactance and Resistance as Functions of Grid Separation for $\omega \cong \omega_{p2}$.

[11]See, for example, Masao Sumi, *J. Phys. Soc. Japan* 14, 653 (1959).

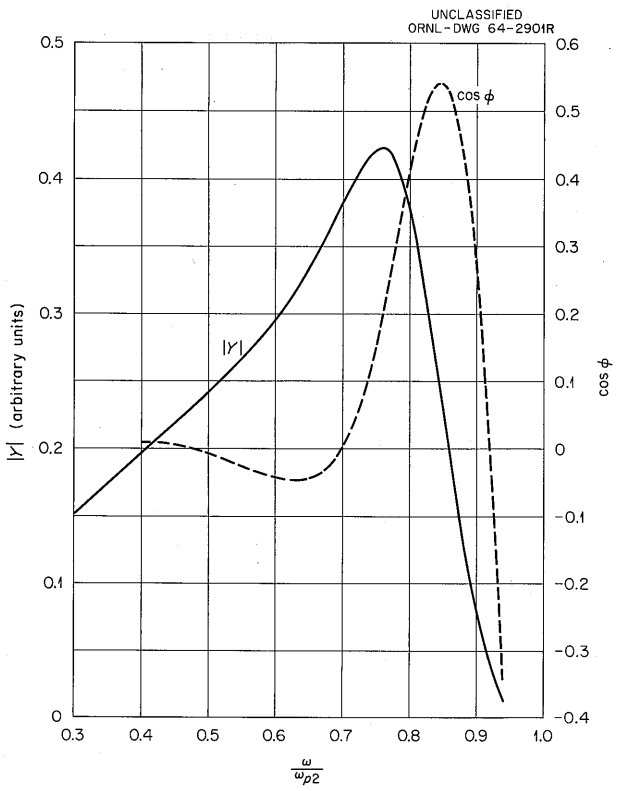

Fig. 8.10. Effective Admittance and Power Factor as a Function of the Applied Signal Frequency.

8.6 SCATTERING LOSSES IN MINIMUM-*B* EXPERIMENTS

T. K. Fowler M. Rankin

A previous investigation[12] of ambipolar scattering losses in mirror machines has been extended. The aim is to cover the new class of experiments, initiated by Ioffe,[13] which are designed to test the minimum-$|\vec{B}|$ stabilization principle. Characteristically, the mirror ratio in these experiments is small, and often T_e/T_i is $\gtrsim 1/10$, so that a sizable plasma potential develops. The plasma potential effectively weakens the mirror still more, thereby enhancing scattering losses. It is, of course, essential in these experiments to distinguish between the instabilities one seeks to cure and more ordinary plasma losses. The temperature is often not high, $\lesssim 1$ kev; hence scattering is a quite competitive loss, and even small enhancement factors may be significant.

Generally, the electrons escape more readily than ions, so that the potential is positive. If electron and ion currents I_+, I_- are equal, in principle the ambipolar potential can sufficiently weaken the effective mirror seen by ions to reduce the ion loss rate to that of the electrons, an enhancement of $\sqrt{m_i/m_e} = 43$ (H_+ ions). However, in practice the enhancement is less. The reason is that the potential ϕ reduces the scattering time but not the ion energy diffusion time. Only ions with energy very near ϕ are lost rapidly. Unless the ion distribution is a δ function at ϕ, the average loss time is the energy diffusion time in order to reach this lossy region. The potential acts to equate $I_+ = I_-$, not by ejecting ions but by trapping electrons.

The scattering time is determined by solving the ion and electron steady-state Fokker-Planck equations discussed in ref. 12. However, the simple scattering formula there has been replaced by that recommended by Bing and Roberts,[14] which is more accurate for small mirror ratios, R. Charge-exchange losses are omitted

Some results are tabulated in Table 8.1. Ion and electron heating is approximated by monoenergetic injection. The ion injection energy is $E_s^+ = 700$ ev; the scattering time τ varies as $(E_s^+)^{3/2}$; the product $n\tau$ is given. To get τ, divide by the ion density n. The plasma is charged positively, with a potential difference ϕ from interior to exterior. The potential was varied to obtain about equal ion and electron currents. The last column gives the inverse ratio of τ to that with the same ion distribution but with $\phi = 0$ in the loss term, essentially the ambipolar enhancement factor. Already in case 2 the ion distribution is approaching an unrealistic δ function. Reasonable distributions typically give an ambipolar enhancement of ~ 3 to 4.

[12] T. K. Fowler and M. Rankin, *J. Nucl. Energy: Pt. C* 4, 311 (1962).

[13] Yu. B. Gott, M. S. Ioffe, and V. G. Telkovsky, *Nucl. Fusion 1962 Suppl. Pt. III*, p. 1045.

[14] G. F. Bing and J. E. Roberts, *Phys. Fluids* 4, 1039 (1961).

Table 8.1. Scattering Lifetime

	R	E_s^-/E_s^+	ϕ/E_s^+	$n\tau$(sec cm^{-3})	Enhancement
				$\times 10^9$	
1.	1.5	0	0.2	1.2	3.3
2.	1.5	0.4	0.4	0.55	11.9
3.	3.0	0	0.3	3	2.4

8.7 MICROWAVE INDEX OF REFRACTION IN A MIRROR FIELD

T. K. Fowler

The effect of magnetic-field curvature (mirror) on the index of refraction, n, employed in microwave interferometry was investigated. The case considered is that appropriate to density determinations from phase shifts in hot-electron gases, that is, propagation with the microwave electric vector $\vec{E}$ parallel to the magnetic mirror field $\vec{B}$ (at the midplane). Previously, taking relativistic effects into account, it was shown that, for $\vec{B}$ uniform, temperature corrections to the cold-plasma index formula are not great for temperatures up to 100 kev and more.[15] Here, we find that mirror curvature also has little effect so long as $\omega \gg \omega_{ce}$, the average electron cyclotron frequency, which is the usual case for interferometry, if β is small.

The argument is only qualitative. Let $\vec{E}$ have only a component E_z (cylindrical coordinates with z along the magnetic axis). Then the index derives from the current perturbation, j_z. For two classes of hot electrons, velocity $\vec{V}$, the field curvature reduces changes in V_z (hence j_z) in response to E_z:

(1) Electrons on midplane, initially $V_z = 0$, $V_\theta \neq 0$, $B_r = 0$. Acceleration to velocity δV_z by E_z moves electrons to $\delta z = 0$, where $B_r(\delta z) \neq 0$. The force $\propto V_\theta B_r$ opposes the original V_z. However, the deceleration is negligible if $\omega \gg \omega_{ce}$, as follows.

If L is the length between magnetic mirrors, then at $\delta z \sim (\delta V_z/\omega)$, and neglecting the plasma magnetic field,

$$B_r(\delta z) = \frac{dB_r}{dz}\,\delta z \sim (-B/L)(\delta V_z/\omega) \ , \qquad (1)$$

which, crossed with V_θ, would produce a z velocity

$$\Delta V_z = \omega^{-1}\left[-\left(\frac{-e}{mc}\right)V_\theta B_r(\delta z)\right] = -\frac{eV_\theta B}{Lm\omega^2 c}\,\delta V_z \ . \qquad (2)$$

Here m, $e(>0)$ are the electronic mass and charge, and c is the speed of light. While ΔV_z in Eq. (2) opposes δV_z, it is insignificant if

$$\frac{eV_\theta B}{Lm\omega^2 c} = \frac{\rho_e}{L}\frac{\omega_{ce}^2}{\omega^2} \ll 1 \ , \qquad (3)$$

where $\rho_e = V_\theta \omega_{ce}^{-1}$ is the electron gyroradius. Usually, $\rho_e < L$, and here $\omega \gg \omega_{ce}$.

(2) Electrons not on midplane, initially $V_\theta \neq 0$, $V_z \neq 0$, $B_r \neq 0$. A perturbation $\delta V_z \propto E_z$ gives $\delta V_\theta \propto \delta V_z B_r$, and the force $\propto \delta V_\theta B_r$ decelerates δV_z. But this is effective only if $\omega \lesssim \omega_{ce}(B_r/B_z)$, as follows.

Now

$$\delta V_\theta \sim \frac{(-e)}{mc}\,\delta V_z B_r \omega^{-1} \ , \qquad (4)$$

$$\Delta V_z = \omega^{-1}\left[-\frac{(-e)}{mc}\,\delta V_\theta B_r\right] = -\left(\frac{e^2 B_r^2}{m^2 c^2 \omega^2}\right)\delta V_z \ . \qquad (5)$$

[15] H. W. Graben, *Phys. Fluids* **6**, 1659 (1963).

Again, $|\Delta V_z| \ll \delta V_z$ if

$$\frac{e^2 B_r^2}{m^2 c^2 \omega^2} = \frac{B_r^2}{B_z^2} \frac{\omega_{ce}^2}{\omega^2} \ll 1 \ . \qquad (6)$$

Generally, $B_r < B_z$, and here $\omega \gg \omega_{ce}$.

Thus, we conclude that the correct refractive index for interferometric analysis of hot electron plasmas even in mirror fields is the simple cold-plasma formula,

$$n^2 = 1 - \frac{\omega_p^2}{\omega^2} , \qquad (7)$$

where ω_p is the electron plasma frequency.

8.8 ELECTRON STREAMS AND ARCS IN FINITE PLASMAS

C. O. Beasley

Investigations are currently being performed on a model of a semi-infinite plasma; this particular model allows the applications of various hopefully realistic boundary conditions appropriate to a plasma of hot and/or cold ions through which electrons are streaming (Fig. 8.11). The inclusion of this stream as part of a physical external circuit is possible under these conditions. Explicit solutions yielding stable and unstable oscillations can be obtained in this model. These frequencies are directly dependent upon the boundary conditions imposed upon the charge density, $\rho_{k_\perp,\omega}(z)$, which is Fourier-analyzed in the x and y directions, and Laplace-transformed in time. Once these boundary conditions are imposed, $\rho_{k_\perp,\omega}(z)$ is completely determined.

Also assuming perfectly conducting walls, the Laplace-Fourier-transformed electric field $E_{\perp_{k_\perp,\omega}}(a) = E_{\perp_{k_\perp,\omega}}(b) = 0$, the electrostatic potential $\phi_{k_\perp,\omega}(z)$, and field $E_{z_{k_\perp,\omega}}(z)$ are also completely determined. Boundary conditions involving a potential drop across the plasma can exist only for $k_\perp = 0$.

One trivial boundary condition imposed is that there is no density perturbation at the left-hand boundary; this yields the result that there is no instability in the plasma other than the convective instability which cannot grow because of the finite length of the plasma. Other more interesting results arise from the application of the condition that $\vec{j}_{k_\perp,\omega}(a) = \sigma E_{k_\perp,\omega}(a)$, and $\vec{j}_{k_\perp,\omega}(b) = j_{k_\perp,\omega}(a)$, corresponding to a zero-impedance "short circuit" external circuit. These results are currently being investigated.

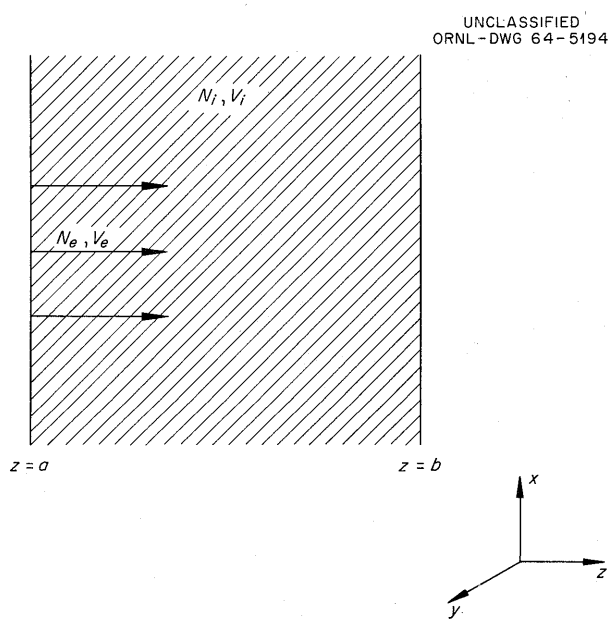

Fig. 8.11. Plasma Model.

9. Magnetics and Superconductivity

9.1 FIELD HOMOGENEITY AND POWER OPTIMIZATION OF MAGNET COIL SYSTEMS

W. F. Gauster M. W. Garrett[1]

9.1.1 Introduction

The power optimization of magnet coils has been investigated carefully by many authors.[2] Another important problem is the design of coil systems which produce very homogeneous magnetic fields. The number of publications concerned with different aspects of this latter problem is also very great.[3] Recently many special cases have been calculated for high field homogeneity but with due regard also to power requirement and volume factor.[4] Several of these solutions may approach closely the combined optimum of power and field homogeneity. However, to the knowledge of the authors, no systematic approach to the problem of a simultaneous optimization of power and field homogeneity has been made up to now. This problem can be formulated (somewhat differently) in the following manner: If the available power for producing the magnetic field is specified, what is the smallest loss of field strength in the coil center if a certain field homogeneity is required?

In the present study, the problem of simultaneous power and field homogeneity optimization is solved for any prescribed shape of the coil cross section for three different types of distribution of the current density J, namely, J is an unknown function of the coordinates z and r, J depends on z only, and rJ is an unknown function of z. The results are discussed in detail for solenoids with rectangular cross section and with specified volume factor.

9.1.2 Magnetic Field of a Symmetrical Solenoid

Figure 9.1 shows two symmetrical current loops (Q and Q'), each carrying a current I. The locations of these loops are determined by the spherical coordinates R and α. As is well known, the axial field component at any field point P (coordinates s and θ) is

$$H_z = \frac{2\pi}{5} I \frac{\sin^2 \alpha}{R} \sum_{k=0}^{\infty} P'_{2k+1}(\cos \alpha)\, P_{2k}(\cos \theta) \times \left(\frac{s}{R}\right)^{2k} . \quad (1)$$

Now consider a symmetrical solenoid with the cross section S and the current density J which is any symmetrical function of R and α:

$$J(R, \alpha) = +J(R, \pi - \alpha) . \quad (2)$$

[1]Consultant, Swarthmore College.

[2]C. Fabry, *L'Eclairage Electrique* **17**(43), 133–41 (1898) and *J. Phys.* **9**, 129–34 (1910); J. D. Cockcroft, *Proc. Roy. Soc. (London)* **227A**, 317–43 (1928); F. Bitter, *Rev. Sci. Instr.* **7**, 479–87 (1936); **8**, 318–19 (1937); **9**, 373–81 (1939); W. F. Gauster, *Trans. Am. Inst. Elec. Engr., Pt. I: Commun. and Electron.* **79**, 822–28 (1961); F. Gaume, pp. 27–38 in *Proc. Intern. Conf. High Magnetic Fields, Cambridge, Mass., Nov. 1–4, 1961*, ed. by H. Kolm *et al.*, MIT Press and Wiley, New York, 1962.

[3]M. W. Garrett, *J. Appl. Phys.* **22**(9), 1091 (September 1951). From references cited there, the following are of special interest: J. C. Maxwell, *Treatise on Electricity and Magnetism*, vol. II, sect. 715, Clarendon Press, Oxford, 1873; L. W. McKeehan, *Rev. Sci. Instr.* **7**, 150 (1936); A. E. Shaw, *Phys. Rev.* **54**, 193 (1938); M. Ference, A. E. Shaw, and R. J. Stephenson, *Rev. Sci. Instr.* **11**, 57 (1940); and A. Sauter and F. Sauter, *Zeit. Physik* **122**, 120 (1944).

[4]F. Gaume, *loc. cit.*; M. W. Garrett, *Systems of Thick Coils to Produce Strong and Uniform Fields and Gradients* (to be published). An extensive list of special cases calculated by M. W. Garrett is contained in D. B. Montgomery and J. Terrell, National Magnet Laboratory, MIT, AFOSR-1525 (1961).

UNCLASSIFIED
ORNL-DWG 64-5195

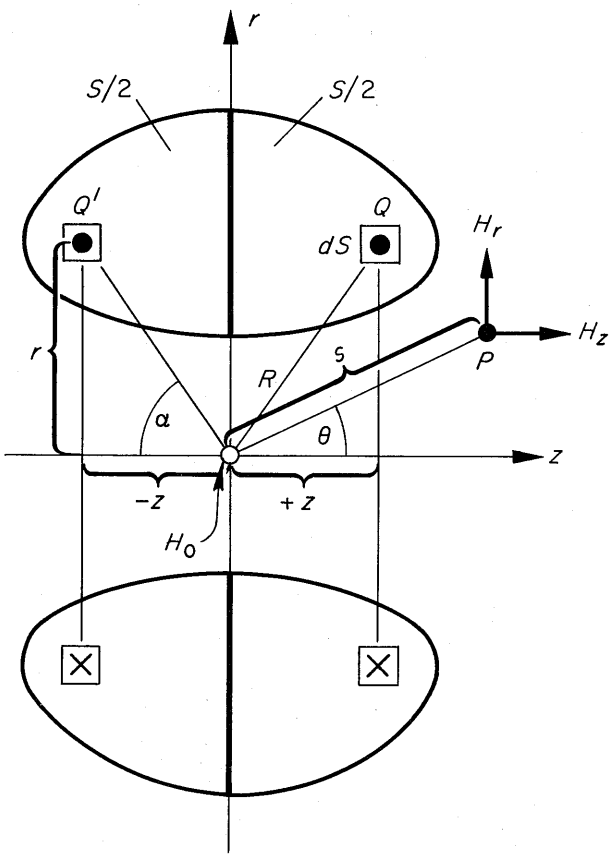

Fig. 9.1. Magnetic Field of a Symmetrical Solenoid.

The resulting axial field component at P is

$$H_z = \frac{2\pi}{5} \int_{S/2} \frac{\sin^2 \alpha}{R} \times \left[\sum_{k=0}^{\infty} P'_{2k+1}(\cos \alpha)\, P_{2k}(\cos \theta) \left(\frac{s}{R}\right)^{2k} \right] \times J(R, \alpha)\, dS \,. \quad (3)$$

With

$$A_{2k} = \frac{2\pi}{5} \int_{S/2} \frac{\sin^2 \alpha}{R^{2k+1}} P'_{2k+1}(\cos \alpha)\, J(R, \alpha)\, dS \,, \quad (4)$$

Eq. (3) becomes

$$H_z = \sum_{k=0}^{\infty} A_{2k}\, P_{2k}(\cos \theta)\, s^{2k} \,. \quad (5)$$

Obviously $A_0 = H_0$ is the field at the coil center. The field homogeneity is characterized by the higher-order values of A_k. Near the coil center the first nonzero coefficient A_k ($k > 0$) determines the field homogeneity. With the well-known Helmholtz coil pair the condition $A_2 = 0$ can be satisfied, whereas A_4 and the following coefficients are different from zero. For Maxwell's three-coil arrangement (ref. 3), $A_2 = A_4 = 0$ while A_6 and subsequent coefficients are different from zero. A magnet coil or a coaxial coil arrangement is said to be of order $2n$ if

$$\begin{aligned} A_{2k} &= 0,\ 1 \leqq k \leqq n-1, \\ A_{2k} &\neq 0,\ k = n. \end{aligned} \quad (6)$$

Therefore, a symmetrical solenoid is in general of the second, the Helmholtz coil pair of the fourth, and Maxwell's coil arrangement of the sixth order.

Equation (4) contains the spherical coordinates R and α of the coil cross section points Q and Q' over which the integration is to be carried out. The cylindrical coordinates z and r of these points are:

$$\begin{aligned} z &= R \cos \alpha, \\ r &= R \sin \alpha. \end{aligned} \quad (7)$$

Expressed in these coordinates Eq. (4) takes the form:

$$A_{2k} = \int_{S/2} f_{2k}(z, r)\, J(z, r)\, dS \,,$$
$$f_{2k} = \frac{2\pi}{5} \frac{r^2}{(z^2 + r^2)^{k+3/2}} P'_{2k+1}\left(\frac{z}{\sqrt{r^2 + z^2}}\right) . \quad (8)$$

9.1.3 Power Optimization of a Solenoid of the Second Order

If ρ is the specific resistivity and λ is the space factor (conductor cross section divided by the

total cross section area, including insulation), the power P can be written as

$$P = 4\pi\frac{\rho}{\lambda}\int_{S/2} rJ^2\, dS\,. \tag{9}$$

We consider first the power optimization for the case $n = 1$, that is, without imposing additional conditions because of field homogeneity. In this case it is somewhat simpler to use the spherical coordinates R and α of the coil cross section points Q. From Eq. (4) follows:

$$H_0 = A_0 = \frac{2\pi}{5}\int_{S/2}\frac{\sin^2\alpha}{R}J(R,\alpha)\, dS\,. \tag{10}$$

Applying Laplace's method of the undetermined multipliers we obtain

$$4\pi\frac{\rho}{\lambda}\int_{S/2} R\sin\alpha\, J^2\, dS$$

$$+\,\mu(H_0 - \frac{2\pi}{5}\int_{S/2}\frac{\sin^2\alpha}{R}J\, dS) \to \min. \tag{11}$$

Differentiation with respect to J yields

$$J = \mu\frac{\lambda}{20\rho}\frac{\sin\alpha}{R^2}\,. \tag{12}$$

Equation (12) is Maxwell's optimum current density distribution.[2] The shape of the J = constant lines does not depend on H_0 or on the coil cross section (Fig. 9.2). In order to find the numerical value of the multiplier μ, we multiply Eq. (12) by $(2\pi/5)(\sin^2\alpha)/R$ and integrate over $S/2$. By Eq. (10),

$$H_0 = \mu\frac{\pi\lambda}{50\rho}\int_{S/2}\left(\frac{\sin\alpha}{R}\right)^3 dS\,, \tag{13}$$

or

$$\mu = \frac{50\rho}{\pi\lambda}\,\frac{H_0}{\int_{S/2}(\sin\alpha/R)^3\, dS}\,. \tag{14}$$

Therefore, from Eq. (12)

$$J = \frac{5}{2\pi}H_0\frac{\sin\alpha}{R^2\int_{S/2}(\sin\alpha/R)^3\, dS}\,. \tag{15}$$

The absolute value of J depends, of course, on the shape of the coil cross section area S.

In order to find P_{min} we multiply Eq. (12) by $4\pi(\rho/\lambda)RJ\sin\alpha$ and integrate over $S/2$. Considering Eqs. (9), (10), and (14) we obtain:

$$P_{min} = \frac{\mu}{2}H_0 = \frac{25\rho}{\pi\lambda}\,\frac{H_0^{\,2}}{\int_{S/2}(\sin\alpha/R)^3\, dS}\,. \tag{16}$$

For this special case it is easy to find the Fabry factor G_{max} which is defined by

$$H_0 = G_{max}\sqrt{\frac{P_{min}\,\lambda}{\rho a_1}}\,, \tag{17}$$

where a_1 is the inner radius of the coil (see Fig. 9.3). Thus

$$G_{max} = \frac{\sqrt{\pi}}{5}\sqrt{a_1\int_{S/2}\left(\frac{\sin\alpha}{R}\right)^3 dS}\,. \tag{18}$$

Such optimized Fabry factors have been evaluated for various coil cross section shapes.[2] For instance, if we assume a spherical cavity with the radius a_1 in a coil with large outside dimensions in every direction, then G_{max} approaches 0.289 which is the highest Fabry factor value of any "sensible" coil shape.

9.1.4 Power Optimization of a Solenoid of the 2*n*th Order, $n \geqq 2$

The power optimization calculations for solenoids of the 2*n*th order ($n \geqq 2$) are similar to those shown for a solenoid of the second order. The principle of this computation will be demonstrated by the example of a solenoid of the sixth order.

From Eq. (8)

$$A_0 = \int_{S/2} f_0 J\, dS = H_0\,,$$

$$A_2 = \int_{S/2} f_2 J\, dS = 0\,, \tag{19}$$

$$A_4 = \int_{S/2} f_4 J\, dS = 0\,.$$

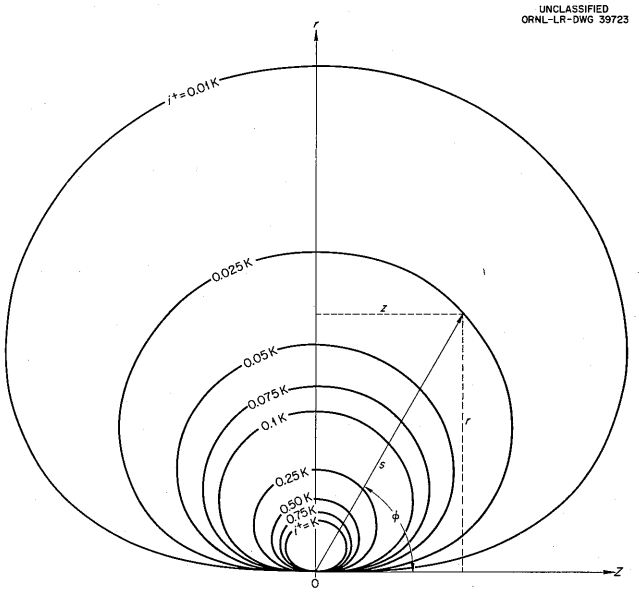

Fig. 9.2. Maxwell's Current Density Distribution.

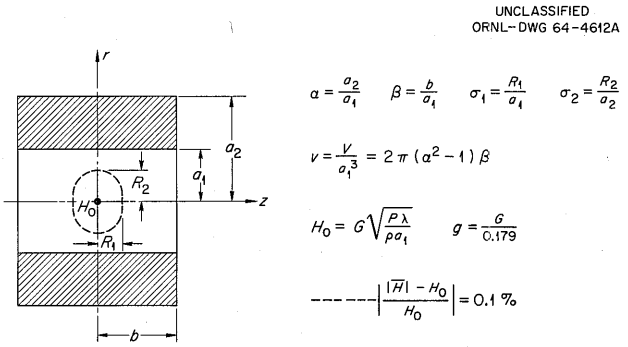

Fig. 9.3. Solenoid with Rectangular Cross Section.

Lagrange's method of undetermined multipliers yields, corresponding to Eq. (11):

$$4\pi\frac{\rho}{\lambda}\int_{S/2} rJ^2\,dS + \mu_0\left(H_0 - \int_{S/2} f_0 J\,dS\right)$$

$$-\mu_2\int_{S/2} f_2 J\,dS - \mu_4\int_{S/2} f_4 J\,dS \rightarrow \min. \quad (20)$$

After differentiation with respect to J we obtain

$$J = \frac{\lambda}{8\pi\rho r}(\mu_0 f_0 + \mu_2 f_2 + \mu_4 f_4)\,. \quad (21)$$

Successive multiplication by f_0, f_2, and f_4 and integration leads to:

$$\mu_0\int_{S/2}\frac{f_0^2}{r}\,dS + \mu_2\int_{S/2}\frac{f_0 f_2}{r}\,dS + \mu_4\int_{S/2}\frac{f_0 f_4}{r}\,dS = \frac{8\pi\rho}{\lambda}H_0\,,$$

$$\mu_0\int_{S/2}\frac{f_0 f_2}{r}\,dS + \mu_2\int_{S/2}\frac{f_2^2}{r}\,dS + \mu_4\int_{S/2}\frac{f_2 f_4}{r}\,dS = 0\,, \quad (22)$$

$$\mu_0\int_{S/2}\frac{f_0 f_4}{r}\,dS + \mu_2\int_{S/2}\frac{f_2 f_4}{r}\,dS + \mu_4\int_{S/2}\frac{f_4^2}{r}\,dS = 0\,.$$

This is a system of three linear equations in the unknowns μ_0, μ_2, and μ_4. The coefficients depend only on the shape of the coil cross section and can be evaluated by considering Eq. (8). Then Eq. (21) yields J for any coil cross section point Q.

The simplest way to find $P_{\min}$ is the following: Eq. (21) is multiplied by $4\pi\,(\rho/\lambda)\,rJ$; then integration yields, because of Eqs. (9) and (19),

$$P_{\min} = \frac{\mu_0}{2}H_0\,, \quad (23)$$

just as in Eq. (16); however, μ_0 is now the value obtained by solving Eq. (22). The procedure for any other value of $2n$ is now obvious.

9.1.5 Special Forms of $J(r, z)$

Up to now we have assumed that J is an unknown function of r and z. The optimization procedure shown above is independent of the coil cross section shape and can be applied to any "sensible" coaxial coil arrangement; S need not be a single cross section area, but may comprise several units. The integrals which represent the coefficients in the system of linear equations (22) can be evaluated in various ways. One possibility is to employ Gaussian integration. For practical purposes it is necessary to consider J as constant over finite area segments. For small surface elements ΔS the Lyle approximation[5] or even a single loop approximation can be used. If J is to

[5]See, for instance, Joseph Hak, *Eisenlose Drosselspulen*, p. 67, Edwards, Ann Arbor, Mich., 1944.

be constant over segments of large rectangular section, M. W. Garrett's forms for rectangular solid coils[6] are the most appropriate ones.

To produce a current density J which depends in a general manner on r and z is a difficult engineering problem. As will be shown later, it is hardly worth while to go to all this trouble since power optimization of solenoids of $2n$th order is also possible if J is considered as an unknown function of z alone or alternatively if rJ is equal to an unknown function $f(z)$. In these two cases the coil engineering is relatively simple, and Fabry factor and field homogeneity are almost the same as for $J = J(z, r)$. We will not treat the case where J is a function of r only; this case has no practical importance for solenoids of higher order.

Up to now we have not specified the shape of the coil cross section S, which can be rectangular, tapered, or bounded by any curve and which might even consist of several separate parts. In the following we will consider only cases of rectangular coil cross sections, and will restrict the discussion to results without describing in detail the method of calculation.[7] The designations used are shown in Fig. 9.3. In the usual way the ratios α and β will be employed. The normalized volume is represented by the volume factor v [see Eq. (24)]. The normalized Fabry factor $\acute{g}$ is referred to the optimum Fabry factor 0.1792 of a solenoid with rectangular cross section and constant current density. The dotted curve in Fig. 9.3 indicates a surface surrounding a volume in which the magnitude of the field strength differs by not more than 0.1% from the value at the coil center. The intersections of this surface with the z axis and the midplane determine R_1 and R_2 respectively. The normalized values of these lengths are σ_1 and σ_2.

[6]M. W. Garrett, ORNL-3318 (November 1962) and *J. Appl. Phys.* **34**(9), 2567 (September 1963).

[7]The mathematical procedures developed above have been programmed as subroutines of the general zonal harmonic package described in ORNL-3318.[6] The constants A_k are computed through the 16th order, while the lowest nonzero order can be set as high as 12. The solutions of orders 10 and 12 show nothing unexpected, and since they do not appear to be of much value in practice, no further mention will be made of them.

9.1.6 Optimized Solenoids of Second, Fourth, Sixth, and Eighth Order, $v = 40$, $\beta = 2.0$

As examples we consider power-optimized solenoids of second, fourth, sixth, and eighth order with rectangular cross section, with a volume factor of $v = 40$, $\beta = 2.0$, and, therefore, $\alpha = 2.04$.

Figure 9.4*a* shows the current density distributions for solenoids of the second and eighth order; Fig. 9.4*b* shows the same distributions for solenoids of the fourth and sixth order. The current density distributions are, of course, symmetric; the right half only of the current distribution is shown. In all cases the current density curves are normalized to their respective maxima. The power-optimized J values for the cases $J = J(z)$ and $rJ = f(z)$ (Gaume's distribution) differ by so little, that for each kind of solenoid only one curve of varying thickness is drawn. As indicated in Figs. 9.4*a* and 9.4*b*, the two boundaries of each curve represent the one or the other current density distribution. For solenoids of various orders, the distinctive features of the current density curves[8] are obvious:

Solenoid of order 2 — maximum in the midplane.

Solenoid of order 4 — minimum in the midplane, one maximum on each side of the midplane.

Solenoid of order 6 — maximum in the midplane, one minimum and one maximum on each side.

Solenoid of order 8 — minimum in the midplane, on each side one minimum with lower value than in the midplane, and on each side first a lower and then a higher maximum.

Similar current density distributions result for power-optimized coils with $J = J(z, r)$. As an example we consider the case of an optimized solenoid of the eighth order, $\alpha = 3.4$, $\beta = 3.0$. The entire coil cross section is represented in Fig. 9.5*a* with a part of the cross section marked by black shading. This part is shown in detail on a larger scale in Fig. 9.5*b*. The J = constant lines indicate a current density distribution similar to that previously discussed for $J = J(z)$ and $rJ = f(z)$. A current density minimum of 8.3% occurs at the midplane. Following the line z' we

[8]Actually, 20 strips were used. The curves are smoothed out.

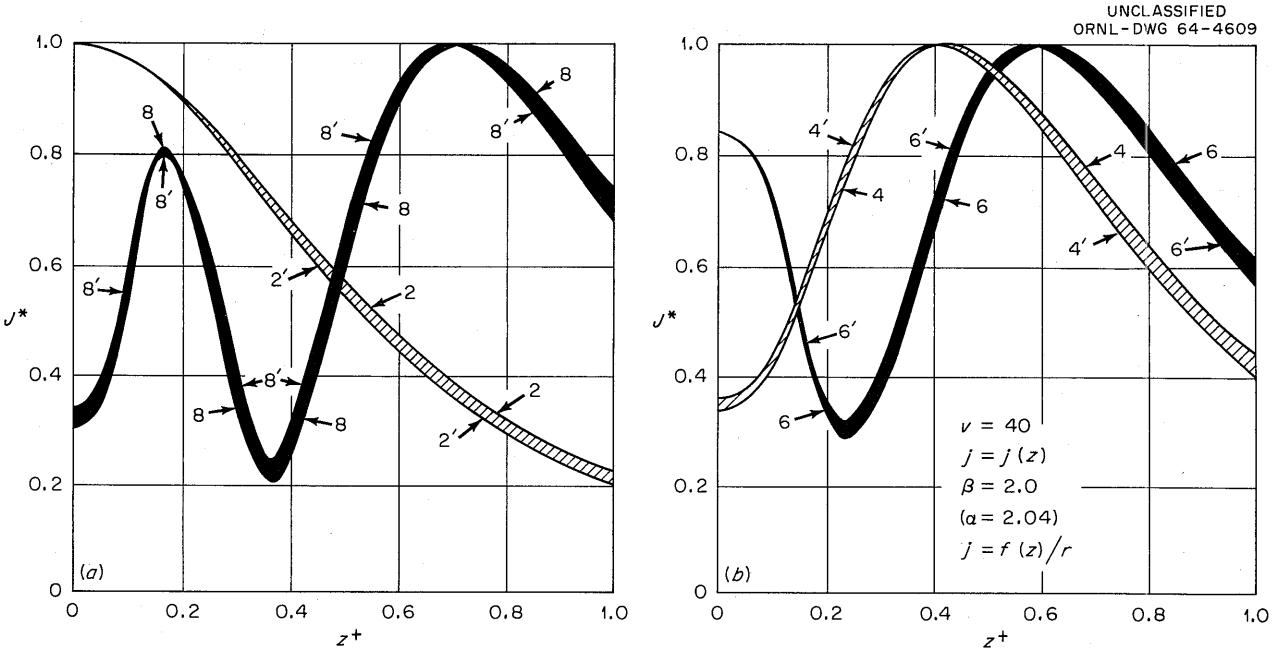

Fig. 9.4. Current Density Distribution of Power-Optimized Solenoids of 2*n*th Order.

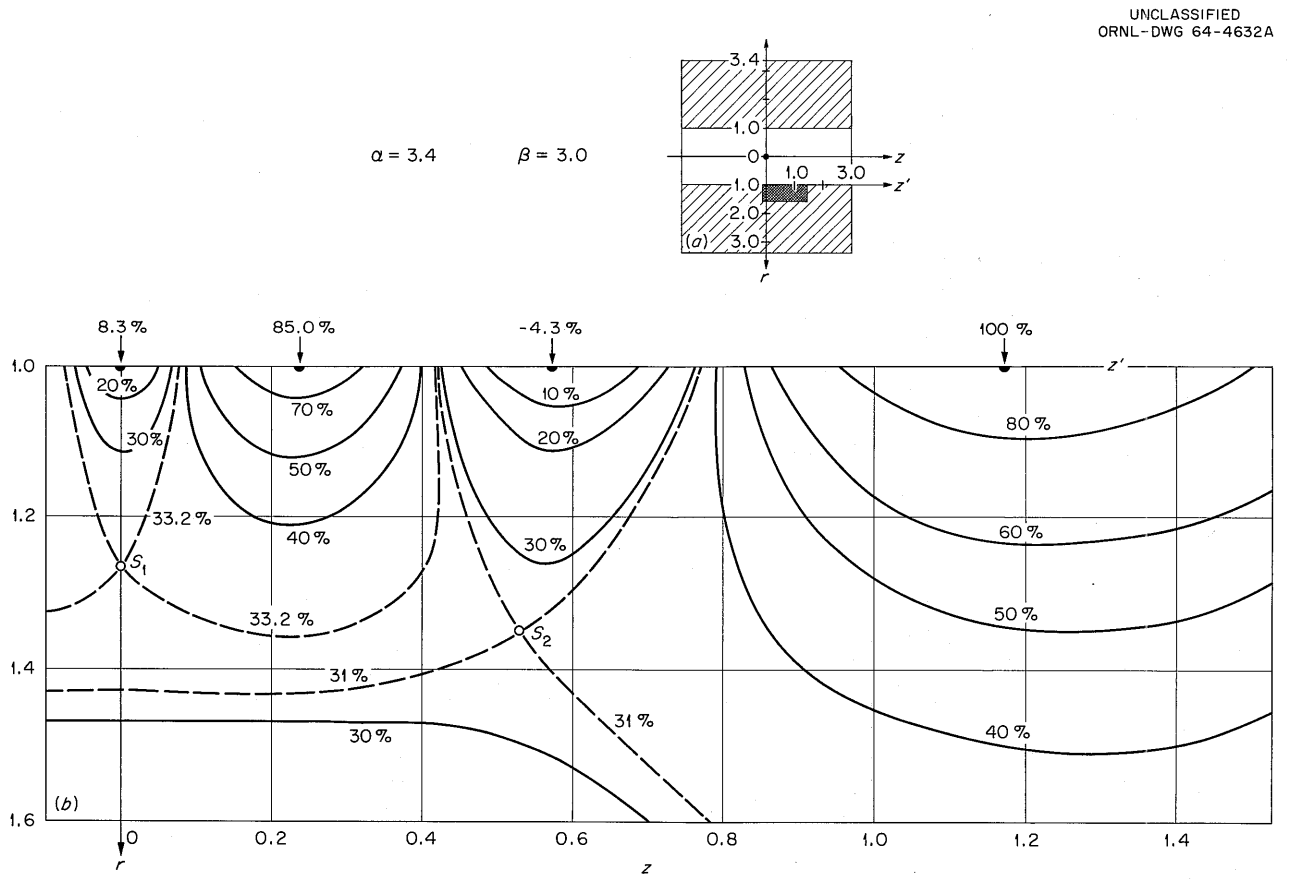

Fig. 9.5. Current Density Distribution of Power-Optimized Solenoid of Eighth Order, $J = J(z, r)$.

notice a maximum of 85%, then a minimum of −4.3%(!) and finally a maximum of 100%. The geometry of the current density distribution is rather complicated. As indicated by the J = constant lines through the singular points S_1 and S_2 respectively, the coil cross section consists topologically of nine parts. Outside the area shown in Fig. 9.5*b*, the J distribution approaches that of a power-optimized solenoid of the second order (as shown in Fig. 9.2). The high homogeneity of the solenoid of the eighth order is achieved by high J gradients in the winding volume near the coil center. Such a current density distribution is solely of theoretical interest.

9.1.7 Power-Optimized Solenoids of Second Order with Rectangular Cross Section and $v = 40$

If we consider a solenoid with rectangular cross section having certain values of α and β (see Fig. 9.3) and a current density distribution with either J = constant or rJ = constant, then the Fabry factor G (and herewith the normalized factor $g = G/0.1792$) is uniquely determined. For the current density distributions of the general forms $J = J(z)$, $rJ = f(z)$, and $J = J(z, r)$ it has been shown above how to find special J functions which make g a maximum.

Now consider the case in which the volume factor

$$v = 2\pi(\alpha^2 - 1)\beta \tag{24}$$

(see Fig. 9.3) is known. If we assume a certain value of v, say 40, and several values of β, for example β = 1.2, 1.3, . . . , 2.4, then we obtain corresponding α values which are indicated in Fig. 9.6. For the current density distribution J = constant we can calculate for each pair of values of α and β the normalized Fabry factor g, and in this way the curve g_1 is obtained. It reaches a maximum $g_{1_{max}} = 0.974$ for $\beta = 1.4$. Similarly, for rJ = constant, $g_{2_{max}} = 1.044$ for $\beta = 1.2$.

For the current density distributions $J = J(z)$, $rJ = f(z)$, and $J = J(z, r)$, again one pair of values

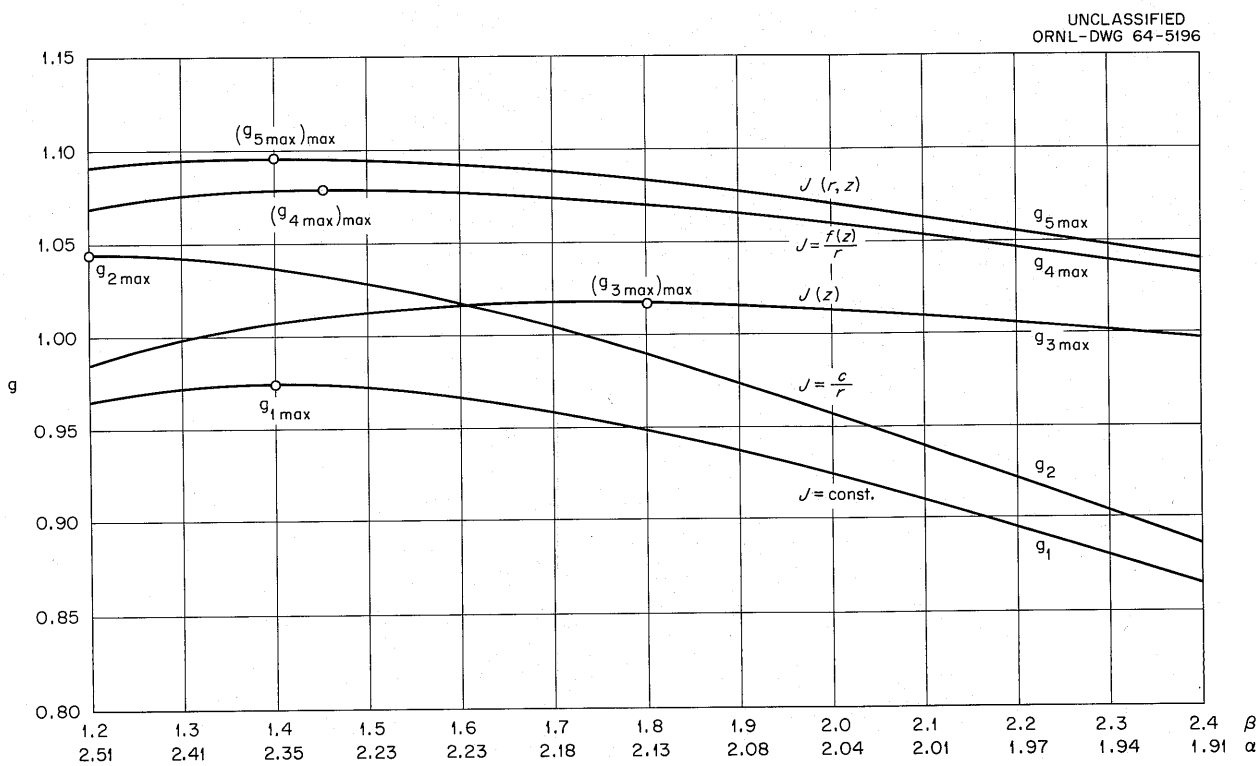

Fig. 9.6. Power Optimization of Solenoids of Second Order. Rectangular cross section, $v = 40$.

α and β determines a certain Fabry factor; however, this factor is already the result of an optimization process. The corresponding curves in Fig. 9.6 are therefore labeled g_{3max} [for $J(z)$], g_{4max} [for $rJ = f(z)$], and g_{5max} [for $J = J(z, r)$]. The maxima of these three curves are $(g_{3max})_{max} = 1.017$ (for $\beta = 1.8$), $(g_{4max})_{max} = 1.078$ (for $\beta = 1.5$), and $(g_{5max})_{max} = 1.095$ (for $\beta = 1.4$). All the curves are very flat and therefore the calculations consider only the sequence of β values indicated in Fig. 9.6; no intermediate values have been used.

9.1.8 Power-Optimized Solenoids of 2*n*th Order, $n \geq 2$, with Rectangular Cross Section and $v = 40$

Single solenoids with rectangular cross section and with the current density distributions J = constant and rJ = constant are always solenoids of the second order. However, as shown above, distribution functions of the forms $J(z)$, $rJ = f(z)$, and $J(z, r)$ can be determined in such a way that a coil of rectangular cross section becomes a power-optimized solenoid of the 2*n*th order. If instead of α and β the quantity v is given, then (e.g.) β can be arbitrarily assumed, and α and g_{max} can be calculated. That is, for the three distributions listed, g_{max} curves can be drawn for solenoids of the 2*n*th order, just as shown previously for solenoids of the second order. Likewise, $(g_{max})_{max}$ values can be determined.

Table 9.1 shows the results of such calculations. The quantities σ_1 and σ_2 (see Fig. 9.3) are listed also. For J = constant the 0.1% limit is at a normalized distance $\sigma_1 = 0.075$ on the z axis and $\sigma_2 = 0.106$ in the midplane. For rJ = constant these values are somewhat lower; g_{max}, however, is higher. This trend is even more pronounced if we consider the $J(r, z)$ current density distribution: here $g = 1.095$, $\sigma_1 = 0.056$, and $\sigma_2 = 0.079$. Thus a high normalized Fabry factor is, in general, achieved[9] at the expense of lower field homogeneity.

The trend "decreased power efficiency vs improved field homogeneity" is especially obvious if we compare the solenoids of the second order with those of the fourth. Values of σ_1 and σ_2 around 0.3 and 0.4, respectively, indicate a great improvement of the field homogeneity. This is bought by a decrease in g of 13 to 15%. The same holds if we proceed to solenoids of still higher orders. Furthermore, for a given order $2n$, we notice an increase in the Fabry factor and a simultaneous degradation of the field homogeneity in the sequence of distributions $J = J(z)$, $rJ = f(z)$, and $J = J(r, z)$.

Finally, it should be mentioned that the described optimization procedure can be extended to cross section shapes other than simple rectangles. Several of these composite shapes produce excellent field homogeneity with relatively small sacrifices of Fabry and volume factor values.[4]

[9]The J distribution rJ = constant, as used in "Bitter coils," is seen to be exceptionally favorable.

Table 9.1. Power-Optimized Solenoids of 2*n*th Order

Rectangular cross section, $v = 40$

Current Density Distribution	Second Order				Fourth Order				Sixth Order				Eighth Order			
	β	g	σ_1	σ_2	β	g	σ_1	σ_2	β	g	σ_1	σ_2	β	g	σ_1	σ_2
J = constant	1.4	0.974	0.075	0.106												
J = constant/r	1.2	1.044	0.065	0.092												
$J = J(z)$	1.8	1.017	0.064	0.090	2.2	0.888	0.32	0.41	2.4	0.831	0.54	0.65	2.4	0.796	0.68	0.80
$J = f(z)/r$	1.5	1.078	0.060	0.085	2.0	0.931	0.31	0.39	2.2	0.867	0.52	0.63	2.4	0.828	0.67	0.79
$J = J(r, z)$	1.4	1.095	0.056	0.079	1.8	0.951	0.29	0.36	2.1	0.886	0.49	0.59	2.3	0.846	0.63	0.74

9.2 FIELD STUDY ON DCX-1 WITH SUPERIMPOSED QUADRUPOLE SYSTEM

Mozelle Rankin D. A. Griffin

In a previous report[10] two plots of constant-B curves for the DCX-2 magnetic field with a superimposed Ioffe field were presented. Construction of these graphs, achieved by a person searching through printed tables of B values and plotting appropriate points, was sufficiently time consuming to preclude much production. To make such plots readily available, particularly for exploratory work with minimum-B confinement fields, a CDC-1604 code using the ORNL Calcomp Plotter has been written.

There are two versions of the code: (1) FINDRZ, which, for a fixed value of θ, gives a graph of constant-B curves in the r, z plane; and (2) FINDRT, which, for a fixed value of z, gives a graph of constant-B curves in the r, θ plane. This code uses the stored magnetic field (inboard coils only, with current adjusted to give a 3.25-in. standard orbit radius) of DCX-1 and superimposes an arbitrary Ioffe field. At present 180° symmetry in the arrangement of the Ioffe bars is assumed.

Calculation of the Ioffe field is based on equations given by W. F. Gauster.[11] By summing the contributions of many arbitrarily placed current-carrying straight conductor segments, this code calculates the fields arising from Ioffe bars of complicated shape and includes the effect of end connections.

The plotting section of the code operates on an iterative procedure in which, with one coordinate fixed, a table of B values is computed and stored. This table is searched for desired values, appropriate interpolation is made, and the points are plotted.

Figure 9.7 shows the geometry of an arrangement[12] of a quadrupole Ioffe field proposed for a first study with DCX-1. The current per bar is 600,000 amp and the current in each conductor of the end connections is 300,000 amp.

Each of the four filaments represents a conductor of circular cross section with a sufficiently large area. For practical reasons these conductor cross sections cannot be circular. The field produced by a bar of more realistic cross-section shape can better be approximated by two filaments each;[13] hence the arrangement shown in Fig. 9.8 has been used for calculations.

Figures 9.9, 9.10, and 9.11 are r, θ plots of the B-constant curves arising from a superimposition

[10] *Thermonuclear Div. Semiann. Progr. Rept. Oct. 31, 1963*, ORNL-3564, p. 101.

[11] W. F. Gauster, "A Note on the Magnetic Field of a Straight Filament Segment," this report, sect. 9.3.

[12] Informal communication with J. L. Dunlap and W. F. Gauster.

[13] Fields of quadrupoles consisting of bars with finite circumferential extent are discussed in sect. 9.4 of this report.

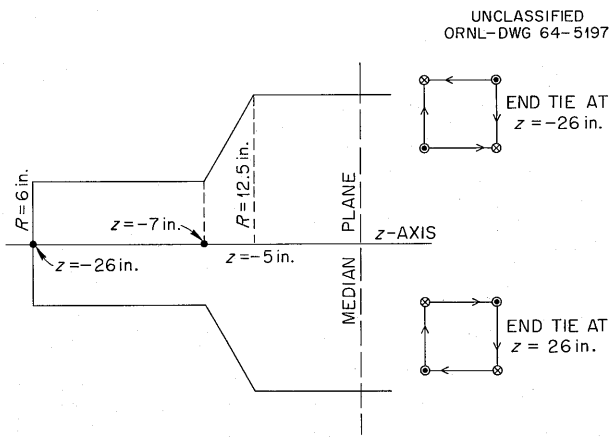

Fig. 9.7. One Proposed Ioffe Field Geometry.

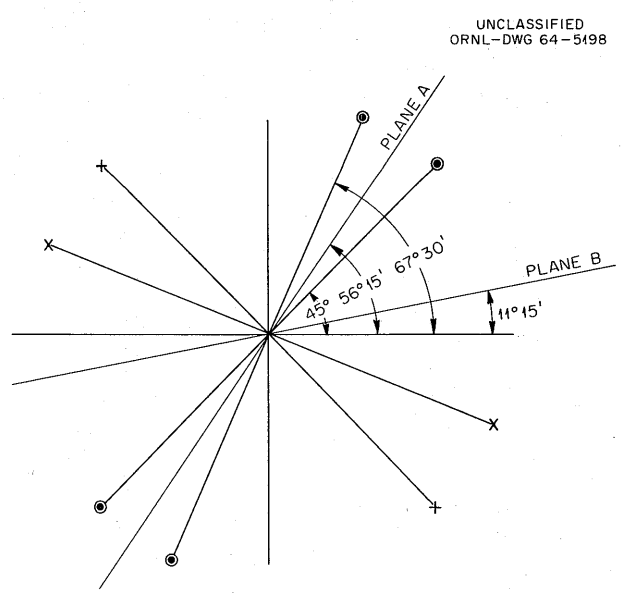

Fig. 9.8. Filament Arrangement to Simulate Quadrupole Field.

of the DCX-1 field and the field arising from the arrangement of Fig. 9.8. These are shown for the planes $z = -5$ in., $z = 0$, and $z = 5$ in. Note that the relationship between the curves in the +5 and −5 planes is a 90° rotation. At this distance along the axis, contours up to 15 kilogauss are closed. In the midplane the central value is 10.06 kilogauss and all surfaces out to about 12.5 kilogauss are closed. This provides a diamond-shaped closed region with a maximum dimension of about 7 in.

The B-constant surfaces for B greater than 16 kilogauss are strongly influenced by the fact that an eight-filament arrangement was used. For a

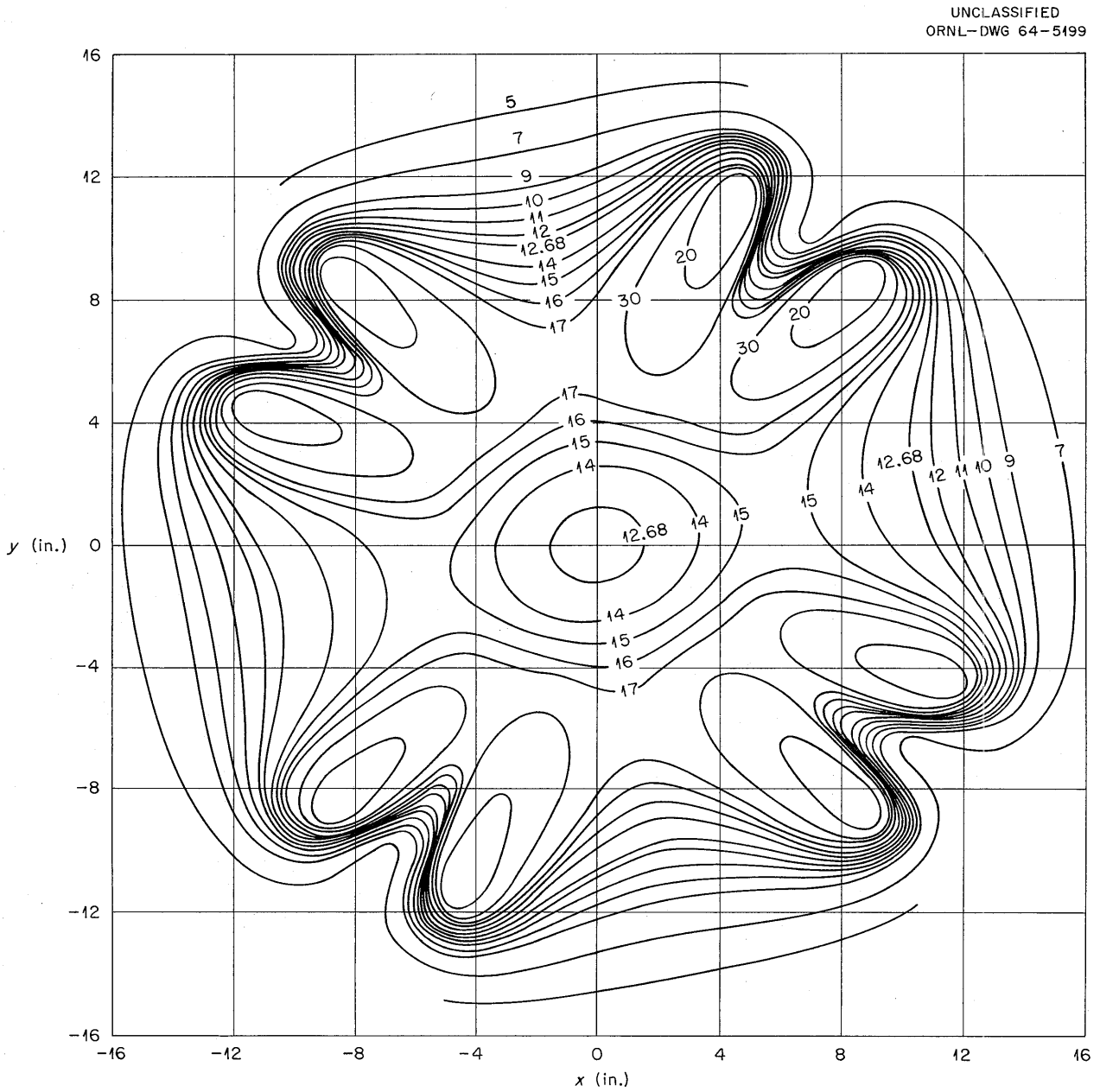

Fig. 9.9. Constant B Contours (Kilogauss). $z = -5$ plane.

practical design with realistic bar cross section these surfaces would of course be quite different. However, this detail does not appreciably influence the shape of the inner closed surfaces.

Figure 9.12 is an r, z plot of the B-constant curves for the DCX-1 field alone. Calculation of the lines inside the coil was made possible by a new code written by M. W. Garrett.[14] This code uses known properties of solenoids; calculation time has been made feasible by a rapidly converging method of calculating elliptic integrals of the third kind.

[14] M. W. Garrett, *J. Appl. Phys.* **34**, 2567–73 (1963).

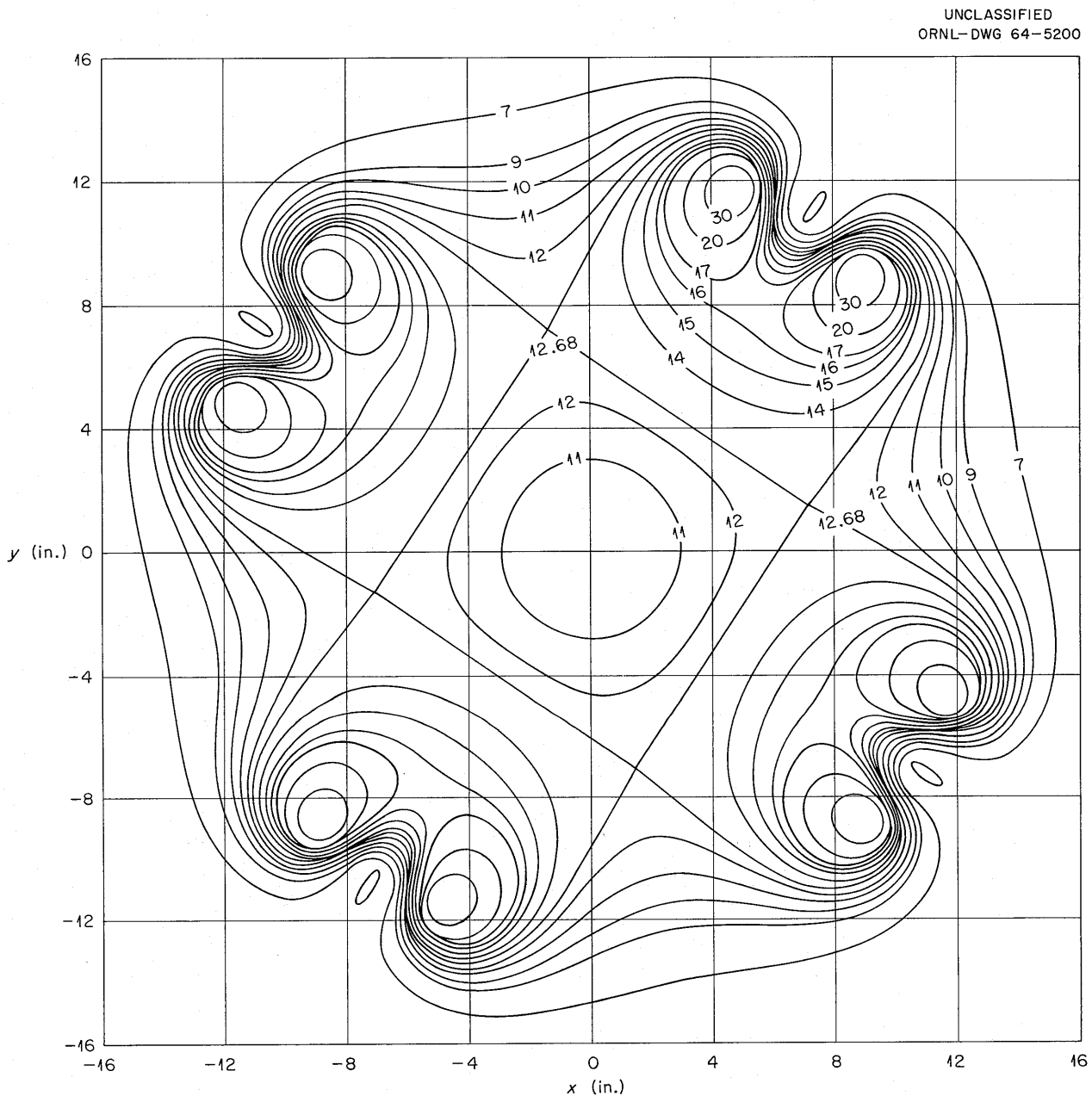

Fig. 9.10. Constant B Contours (Kilogauss). $z = 0$ plane.

A comparison of Fig. 9.12 with Figs. 9.13 and 9.14 reveals the changes in B-constant lines caused by the addition of a Ioffe field. Figure 9.13 is an r, z plot in the plane of the bars, plane A (θ = 0.98175) of Fig. 9.8; Fig. 9.14 is an r, z plot in the plane between the bars, plane B (θ = 0.19635) of Fig. 9.8. In general $|B|$ at $(r, z) \neq |B|$ at $(r, -z)$. In plane A contours out to about 16.4 kilogauss are closed; this corresponds to a radial distance of ~9.5 in. and an axial distance of ~9 in. In plane B the highest closed contour is about 12.7 kilogauss, corresponding to radial and axial dimensions of ~7.5 in. and ~5.5 in. respectively.

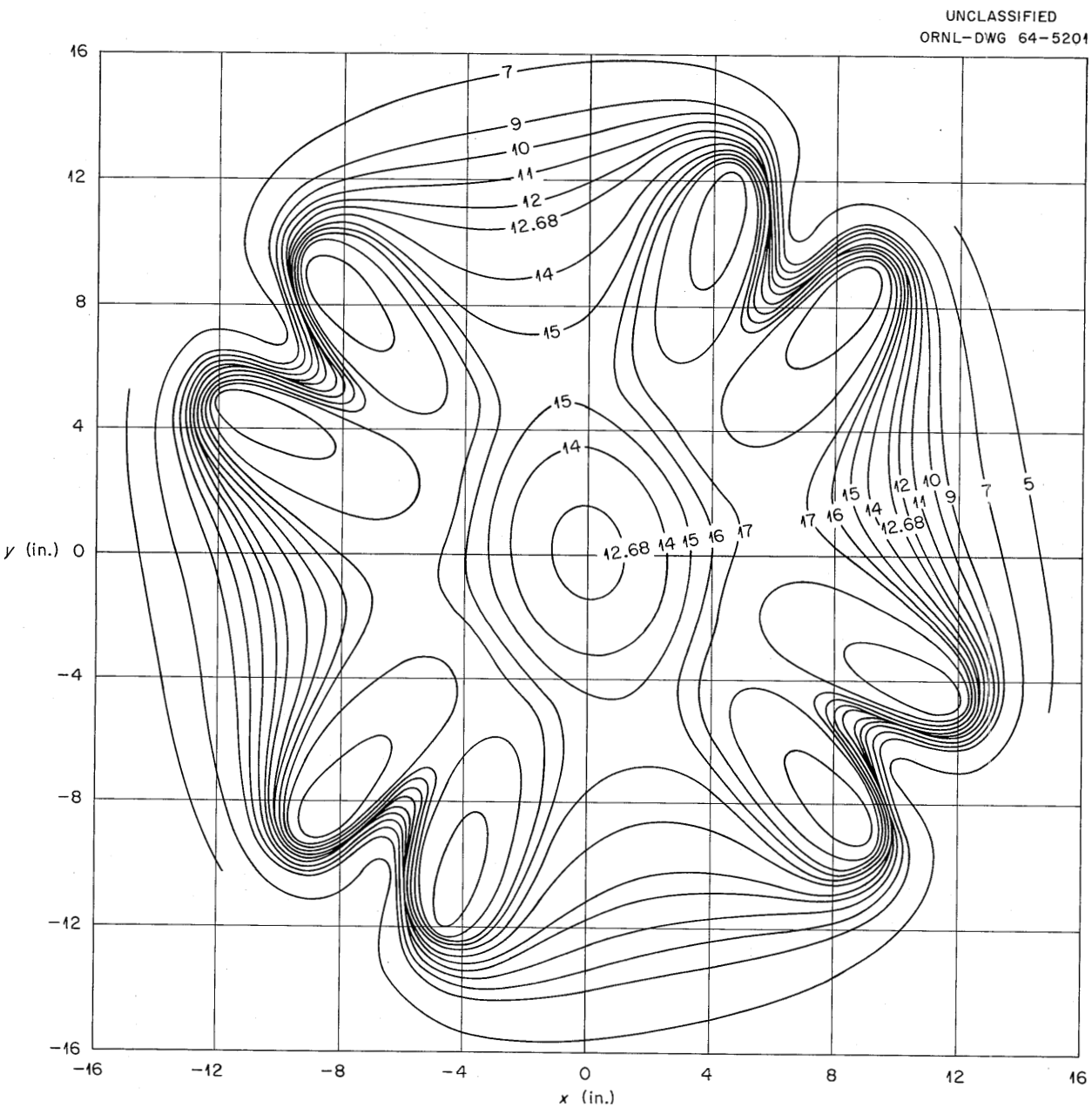

Fig. 9.11. Constant B Contours (Kilogauss). z = 5 plane.

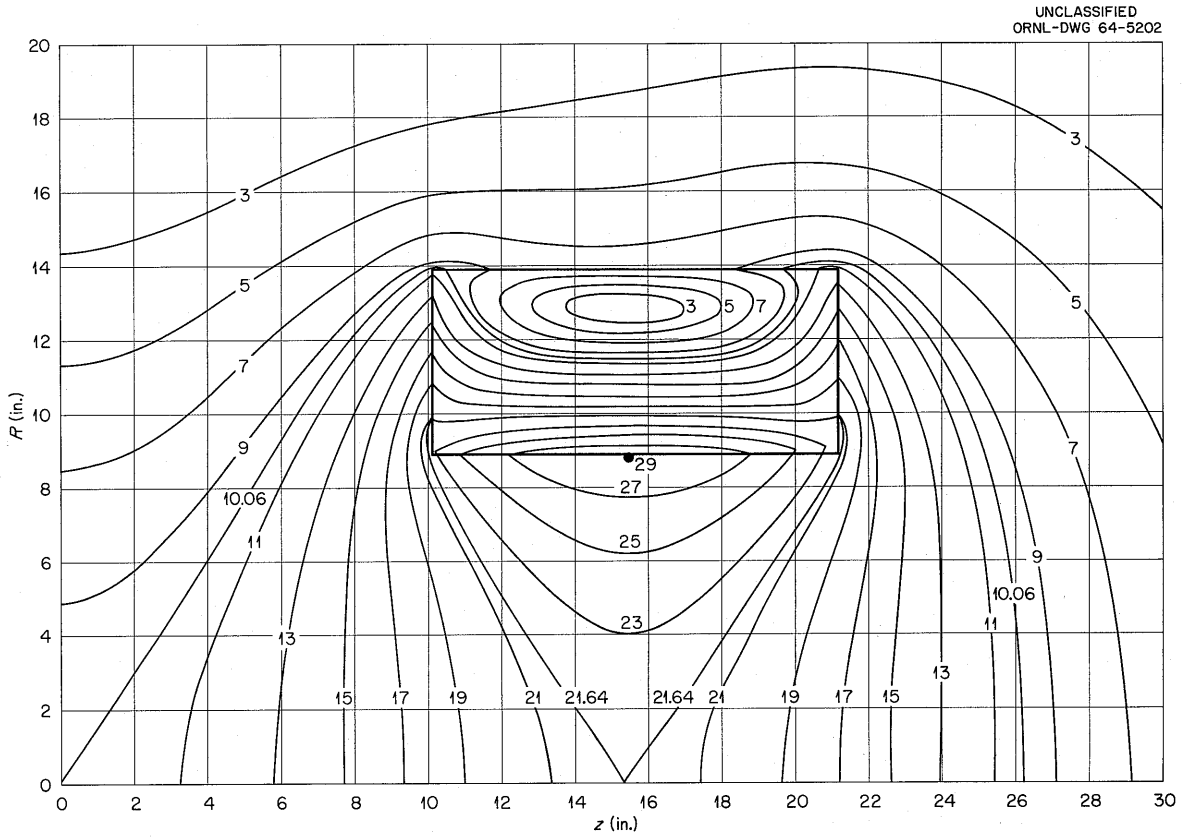

Fig. 9.12. Constant B Lines for DCX-1 (Kilogauss). Inboard coils only. Adjusted for 3.25-in. standard orbit radius.

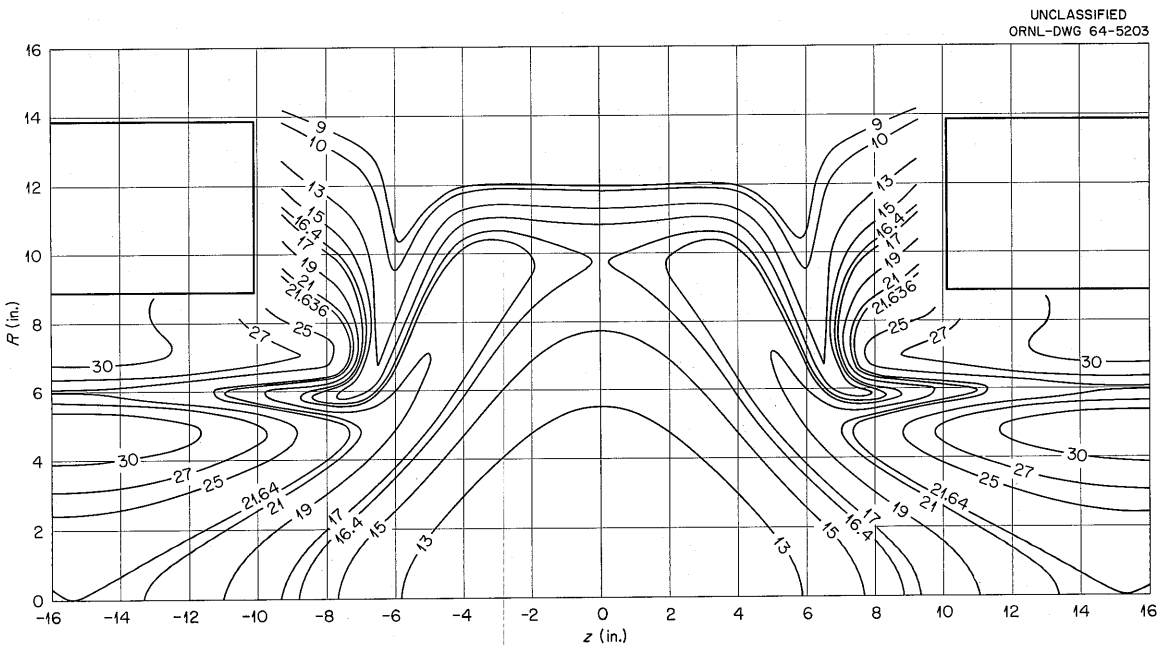

Fig. 9.13. Constant B Contours (Kilogauss). $\theta = 0.98175$.

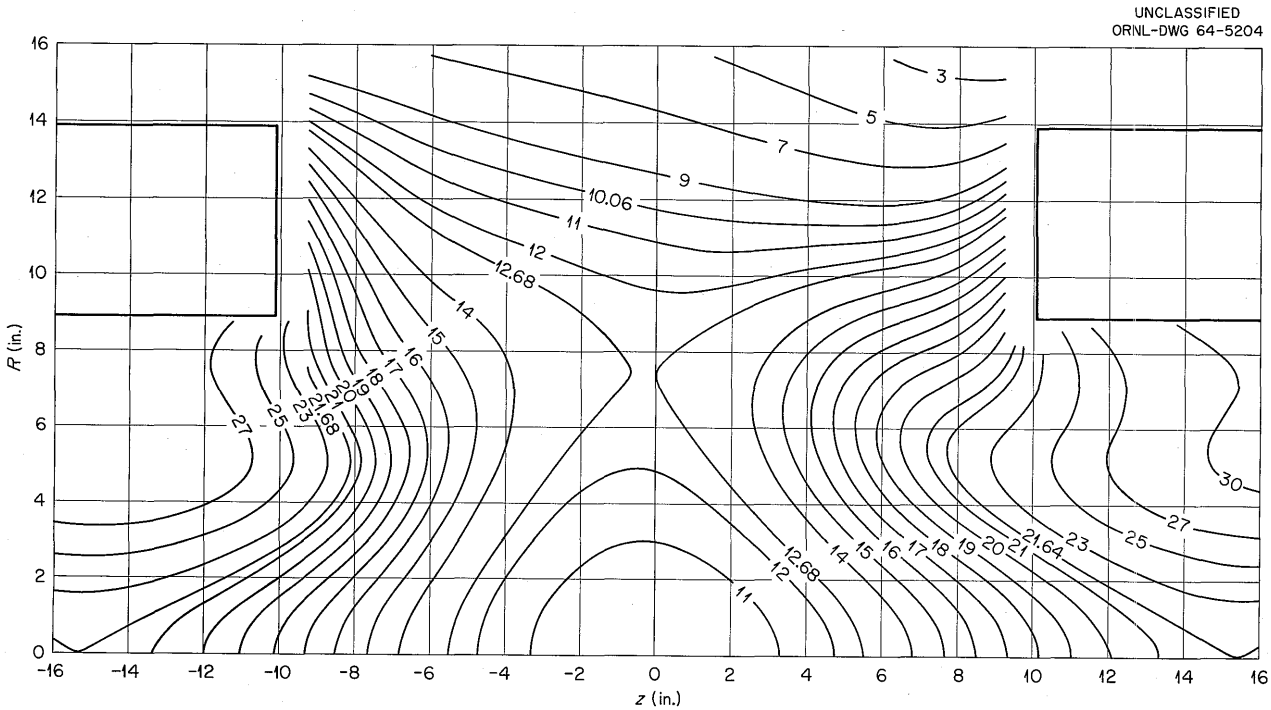

Fig. 9.14. Constant B Contours (Kilogauss). $\theta = 0.19635$.

9.3 A NOTE ON THE MAGNETIC FIELD OF A STRAIGHT FILAMENT SEGMENT

W. F. Gauster

For the study of B-min field configurations it is necessary to determine the fields produced by current filaments of various shapes. This can be achieved by replacing them by an appropriate number of straight segments. Thus the first task is to find the magnetic field generated by such a current element of finite length and of arbitrary orientation in space. It is, of course, only a matter of convenience how to handle this trivial problem. After learning recently of a code which has been written for similar purposes elsewhere[15] it might be of some interest to report briefly here about a very simple vector analytical expression[16] on which the corresponding ORNL codes are based.

Biot-Savart's law is applied to calculate the flux density $\bar{B}$ produced at the field point P by a straight current filament segment $\overline{P_1P_2}$. In Fig. 9.15 a is the distance between P and a straight line through $\overline{P_1P_2}$; $\bar{e}_1$, $\bar{e}_2$, and $\bar{e}_3$ are a system of perpendicular unit vectors, with $\bar{e}_1$ parallel to $\overline{P_1P_2}$ and $\bar{e}_2$ perpendicular to the plane determined by P and $\overline{P_1P_2}$. Using the designations shown in Fig. 9.15, the following equations can be written:

$$\bar{e}_1 = \frac{\bar{s}_2 - \bar{s}_1}{|\bar{s}_2 - \bar{s}_1|}, \tag{1}$$

$$\bar{e}_2 = \frac{\bar{s}_1 \times \bar{s}_2}{|\bar{s}_1 \times \bar{s}_2|}, \tag{2}$$

$$\bar{e}_3 = \bar{e}_1 \times \bar{e}_2, \tag{3}$$

$$a = \bar{s}_1 \cdot \bar{e}_3, \tag{4}$$

$$u = \bar{s} \cdot \bar{e}_1, \tag{5}$$

$$\bar{s} = a\bar{e}_3 + u\bar{e}_1. \tag{6}$$

[15] W. A. Perkins and J. C. Brown, *MAFCO – A Magnetic Field Code for Handling General Current Elements in Three Dimensions*, UCRL-7744 (Mar. 3, 1964).

[16] W. F. Gauster, *A Simple Method for Calculating Ioffe-Bar Fields*, Engineering Science Memo No. 13 (Dec. 13, 1963).

UNCLASSIFIED
ORNL-DWG 64-5205

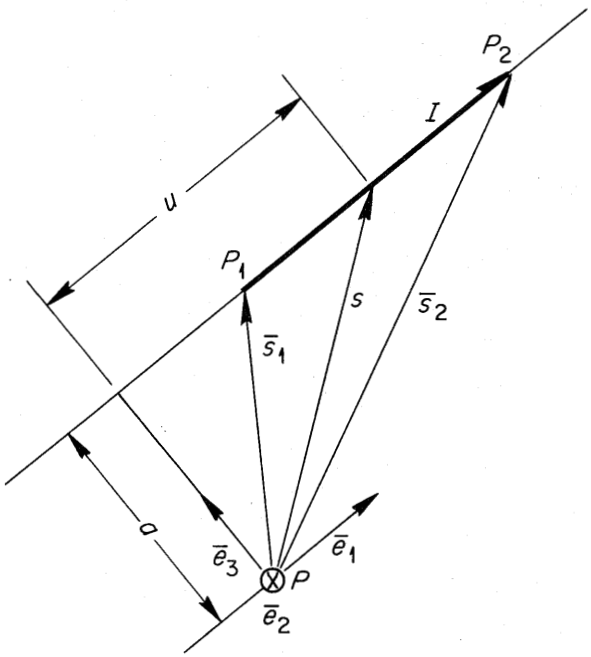

Fig. 9.15. Field of a Straight Filament Segment.

With $\bar{B}$ in gauss, I in amperes, and the length in centimeters, Biot-Savart's law yields

$$\bar{B} = \frac{I}{10}\int_1^2 \frac{\bar{s}\times d\bar{s}}{s^3}$$

$$= \frac{I}{10}\int_1^2 \frac{(a\bar{e}_3 + u\bar{e}_1)\times \bar{e}_1\, du}{(a^2+u^2)^{3/2}} \qquad (7)$$

$$= \frac{I}{10}\, a\bar{e}_2 \int_1^2 \frac{du}{(a^2+u^2)^{3/2}}$$

and, therefore,

$$\bar{B} = \frac{I}{10}\,\frac{\bar{e}_2}{a}\left(\frac{u_2}{s_2} - \frac{u_1}{s_1}\right) . \qquad (8)$$

From Eqs. 1–4 follows:

$$a = \frac{s_1{}^2 s_2{}^2 - (\bar{s}_1\cdot\bar{s}_2)^2}{|\bar{s}_2 - \bar{s}_1|\cdot|\bar{s}_1\times\bar{s}_2|} . \qquad (9)$$

Because of Eqs. (5) and (1)

$$u_1 = \frac{\bar{s}_1\cdot\bar{s}_2 - s_1{}^2}{|\bar{s}_2 - \bar{s}_1|} , \qquad (10)$$

and

$$u_2 = \frac{s_2{}^2 - \bar{s}_1\cdot\bar{s}_2}{|\bar{s}_2 - \bar{s}_1|} . \qquad (11)$$

Thus,

$$\frac{u_2}{s_2} - \frac{u_1}{s_1} = \frac{s_1 + s_2}{\bar{s}_2 - \bar{s}_1}\cdot\frac{s_1 s_2 - \bar{s}_1\cdot\bar{s}_2}{s_1 s_2} . \qquad (12)$$

Considering Eqs. (2), (9), and (12) we obtain finally from Eq. (8)

$$\bar{B} = \frac{I}{10}\,\frac{\bar{s}_1\times\bar{s}_2}{s_1 s_2}\cdot\frac{s_1+s_2}{s_1 s_2 + \bar{s}_1\cdot\bar{s}_2} . \qquad (13)$$

Another form of this equation is

$$\bar{B} = \frac{I}{10}\,\frac{\bar{s}_1\times\bar{s}_2}{(\bar{s}_1\times\bar{s}_2)^2}\,(s_1+s_2)\left(1 - \frac{\bar{s}_1\cdot\bar{s}_2}{s_1 s_2}\right), \qquad (14)$$

which has been indicated in ref. 16.

Equations (13) and (14) contain, besides I, only the vectors $\bar{s}_1$ and $\bar{s}_2$ and their magnitudes s_1 and s_2, and can be expressed easily in any coordinate system. Codes based on Eq. (14) for calculating the magnetic field produced by any current filament (which is replaced by an appropriate number of straight segments) have been written by Mozelle Rankin[17] and C. E. Parker.

9.4 A STUDY OF QUADRUPOLE CURRENT SHEET ARRANGEMENTS

W. F. Gauster C. E. Parker J. N. Luton, Jr.

The numerical evaluation of magnetic fields produced by Ioffe bar systems (considering end connections, and – if necessary – curved bars)

[17] Mozelle Rankin and D. A. Griffin, "Field Study on DCX-1 with Superimposed Quadrupole System," this report, sect. 9.2.

requires the use of appropriate computer programs.[18,19] The problem can be simplified by considering infinitely long bars, which yield a good approximation for the field except near the ends. Initially two simple cases are considered here; the first is a system of four infinite filaments, the second of six, as shown in Figs. 9.16*a* and 9.16*b*. Using b as the normalized field, and ξ as the normalized radius to the field point,

$$b = \frac{B}{I/a}, \tag{1}$$

$$\xi = \frac{R}{a}, \tag{2}$$

the following equations can be easily derived:

1. Four-bar system, plane A:

$$b_A = 0.8\,\frac{\xi}{1+\xi^4}, \tag{3}$$

$$b_{A_{max}} = 0.456 \text{ for } \xi = 0.760\,. \tag{4}$$

See Fig. 9.16c, curve A_4.

2. Four-bar system, plane B:

$$b_B = 0.8\,\frac{\xi}{1-\xi^4}\,. \tag{5}$$

See Fig. 9.16c, curve B_4.

3. Six-bar system, plane A:

$$b_A = 1.2\,\frac{\xi^2}{1+\xi^6}, \tag{6}$$

$$b_{A_{max}} = 0.635 \text{ for } \xi = 0.891\,. \tag{7}$$

See Fig. 9.16c, curve A_6.

[18]Section 9.3 of this report.

[19]Section 9.2 of this report.

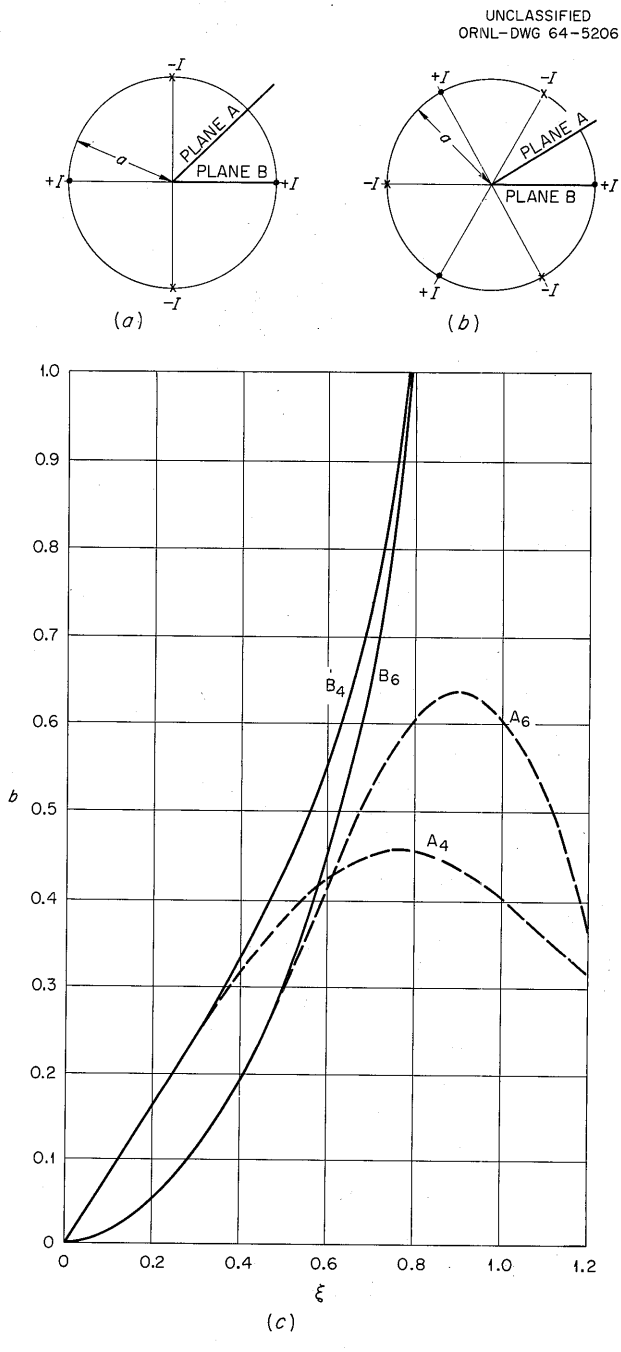

Fig. 9.16. (a) Four Filamentary Bars; (b) Six Filamentary Bars; (c) Four- and Six-Bar Filamentary Systems.

4. Six-bar system, plane B:

$$b_B = 1.2\,\frac{\xi^2}{1-\xi^6}\,. \tag{8}$$

See Fig. 9.16c, curve B_6.

H. Luc[20] has attacked the problem of applying Ioffe bars to DECA I – an existing pulse mirror machine. In his calculations he considers bars which are sectors of an annulus with negligible thickness. He derives a series expression for the multipole field, and he points out that an optimum solution is obtained when the bars occupy two-thirds of the circle on which they lie. This optimum fraction of the space occupied by bars is independent of the number of bars in the system.

Luc's calculation of the multipole field makes use of truncated series, and the errors thereby introduced are not examined in detail. We found that a different analytical treatment of multipole fields leads in a very simple way to exact forms for $\overline{B}$ at any field point. It seems worth while to describe our calculation method and to discuss the results in some detail.

In this study we restrict ourselves to a quadrupole system formed by four current sheets (Fig. 9.17).

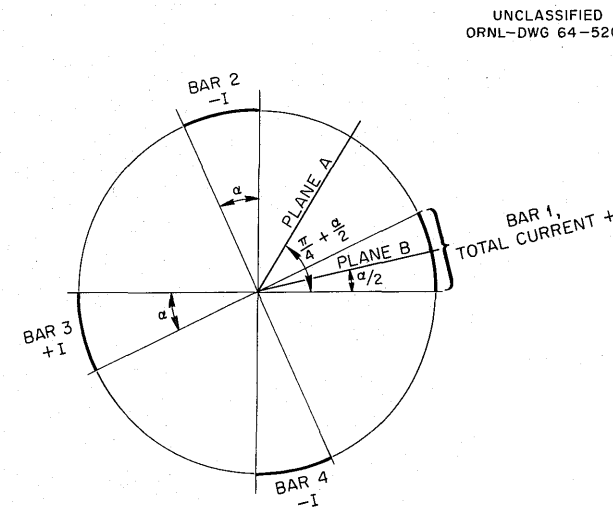

Fig. 9.17. Four Thin Bars.

Magnetic fields produced by any distribution of straight, infinitely long current filaments perpendicular to a plane are usually analyzed by determining the logarithmic potential. It is convenient to represent the potential and the stream function by the real and imaginary parts of a complex function. In our case it is simpler *not* to work with the logarithmic potential since the magnetic field vector $\overline{B}$, which will be represented by the complex number

$$B = B_x + iB_y \,, \tag{9}$$

can be determined directly in an easy way (B is not to be confused with magnitude of $\overline{B}$, which is written here as $|\overline{B}|$).

Using the nomenclature of Fig. 9.18 we have

$$z - z_0 = re^{i\phi} \,, \tag{10}$$

$$\frac{1}{z - z_0} = \frac{1}{r} e^{-i\phi} \,. \tag{11}$$

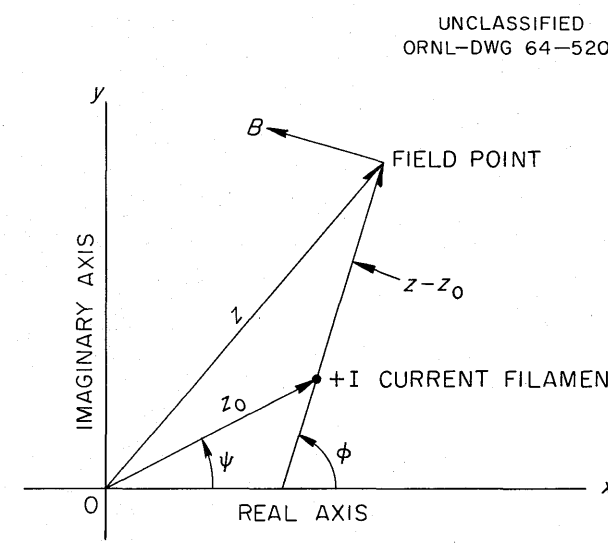

Fig. 9.18. Nomenclature.

The conjugate complex value is

$$\left(\frac{1}{z - z_0}\right)^* = \frac{1}{r} e^{i\phi} \,. \tag{12}$$

Since

$$B = \frac{I}{5r} ie^{i\phi} = \frac{I}{5} i \left(\frac{1}{z - z_0}\right)^* \,, \tag{13}$$

[20] H. Luc, *Project de "Champ Multipolaire" pour DECA*, EUR-CEA-FC-168 (June 1962). English translation by J. N. Luton, Jr., ORNL Thermonuclear Div. Eng. Sc. Memo No. 8 (June 1963).

therefore

$$B^* = -\frac{I}{5}\frac{i}{z - z_0} . \tag{14}$$

In Fig. 9.19, let the current per unit width of bar be:

$$k = \frac{I}{a\alpha} ; \tag{15}$$

then

$$dB^* = \frac{ka}{5} i \frac{d\psi}{z - ae^{i\psi}} . \tag{16}$$

For the field produced by bar 1 we obtain

$$\frac{5}{ka} iB_1{}^* = \int_{\psi=0}^{\alpha} \frac{d\psi}{z - ae^{i\psi}}$$

$$= \frac{1}{z}\left(\alpha + i \ln \frac{z - ae^{i\alpha}}{z - a}\right) . \tag{17}$$

For bars 2, 3, and 4:

$$\frac{5}{ka} iB_2{}^* = -\frac{1}{z}\left(\alpha + i \ln \frac{z - iae^{i\alpha}}{z - ia}\right), \tag{18}$$

UNCLASSIFIED
ORNL-DWG 64-5209

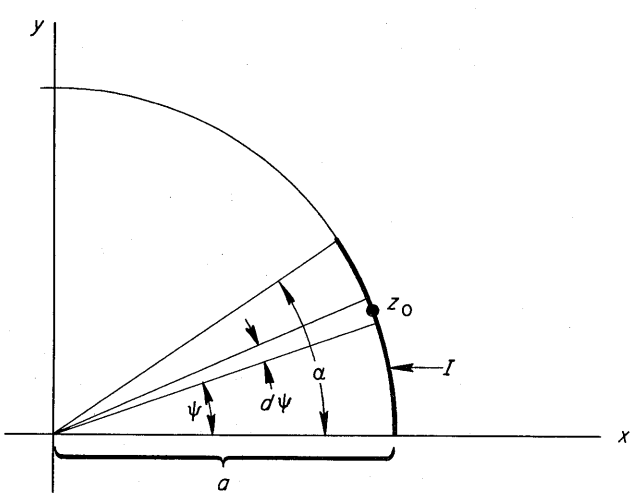

Fig. 9.19. Integration Variables.

$$\frac{5}{ka} iB_3{}^* = \frac{1}{z}\left(\alpha + i \ln \frac{z + ae^{i\alpha}}{z + a}\right), \tag{19}$$

$$\frac{5}{ka} iB_4{}^* = -\frac{1}{z}\left(\alpha + i \ln \frac{z + iae^{i\alpha}}{z + ia}\right) . \tag{20}$$

The total field B at any field point z is therefore

$$\frac{5}{ka} B^* = \frac{1}{z} \ln \frac{(z^2 + a^2)(z^2 - a^2 e^{2i\alpha})}{(z^2 - a^2)(z^2 + a^2 e^{2i\alpha})} . \tag{21}$$

Plane A (see Fig. 9.17):

$$z = Re^{i[(\pi/4) + (\alpha/2)]} . \tag{22}$$

After some calculation, Eq. (21) reduces to

$$B_A = \frac{ka}{5R} e^{i[(\pi/4) + (\alpha/2)]} \ln \frac{a^4 + R^4 - 2a^2R^2 \sin\alpha}{a^4 + R^4 + 2a^2R^2 \sin\alpha} . \tag{23}$$

With ξ defined by Eq. (2), Eq. (23) yields

$$|\bar{B}_A| = \frac{k}{5\xi} \ln \frac{1 + \xi^4 + 2\xi^2 \sin\alpha}{1 + \xi^4 - 2\xi^2 \sin\alpha}$$

$$= \frac{I}{a}\frac{1}{5\alpha\xi} \ln \frac{1 + \xi^4 + 2\xi^2 \sin\alpha}{1 + \xi^4 - 2\xi^2 \sin\alpha} . \tag{24}$$

Plane B (see Fig. 9.17):

$$z = Re^{i\alpha/2} , \tag{25}$$

$$B_B = \frac{2ka}{5R} e^{i[(\alpha/2) - (\pi/2)]} \tan^{-1} \frac{2a^2R^2 \sin\alpha}{a^4 - R^4} , \tag{26}$$

$$|\bar{B}_B| = \frac{2k}{5\xi} \tan^{-1} \frac{2\xi^2 \sin\alpha}{1 - \xi^4}$$

$$= \frac{I}{a}\frac{2}{5\alpha\xi} \tan^{-1} \frac{2\xi^2 \sin\alpha}{1 - \xi^4} . \tag{27}$$

For the special case of filamentary bars, $\alpha = 0$, Eqs. (24) and (27) reduce to Eqs. (3) and (5).

Using the IBM-7090 computer, fields for $\alpha = 0$, 5, 10, . . . , 90° were calculated from Eqs. (24) and (27), normalized by I/a, and then plotted.

Machine-drawn graphs for $\alpha = 30$, 70, and 90 for $\xi = 0$ to 1 are shown as Figs. 9.20 through

9.22. The case of $\alpha = 0$ is identical to Fig. 9.16c and therefore, is not repeated.

The normalized radius at which the field reaches a maximum is $R_{MX}/a = \xi_{MX}$, where X is A for the plane through the gap center and B for the plane through the bar center. Graphs of ξ_{MX} as functions of α are shown in Fig. 9.23. The normalized maximum field as a function of α for planes A and B is shown in Fig. 9.24.

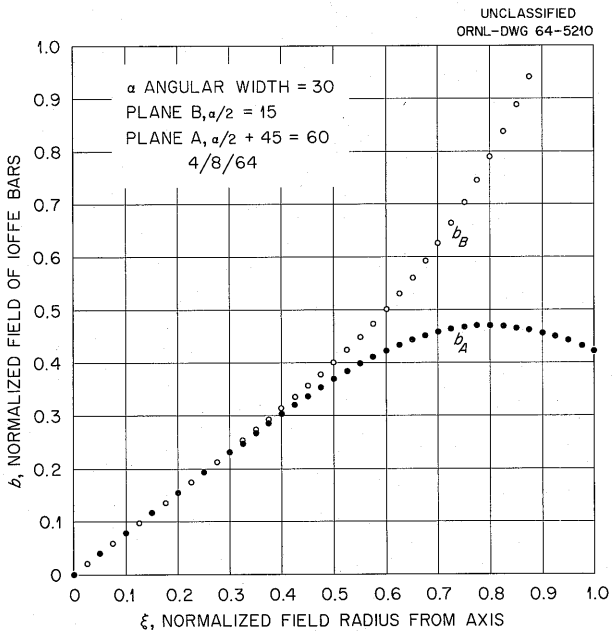

Fig. 9.20. Fields of Thin Annular Ioffe Bars, $\alpha = 30^\circ$.

We consider the following numerical example: (1) The magnitude of the field $\bar{B}$ for all azimuths is required to have a value of B_s at least 10 kilogauss at the surface of a cylinder with a radius $a_s = 10$ cm. (2) The field must rise monotonically from the center to the cylinder surface, rather than reaching a peak inside the 10-cm radius. (3) As a practical consideration, a 2-cm radial gap is left between the cylinder surface and the bars:

$$a \geq a_s + 2 \,. \tag{28}$$

(4) Bar depth = 1 cm. (5) Conductor resistivity = 2.1 microhm-cm. (6) Space factor = 0.7. The problem is to find the angle α of a quadrupole system which satisfies the above conditions and which requires the lowest possible power.

The method of solving this problem can be demonstrated as follows: We assume various angles α, for instance $\alpha = 30^\circ$. Figure 9.20 shows that for this angle ξ_{MA} has to be considered. Its value is read more accurately as $\xi_{MA} = 0.79$ from Fig. 9.23. This yields $a = 10/0.79 = 12.7$ cm. From Fig. 9.24, $b = 0.47$. Therefore, $I = 12.7 \times 10{,}000/0.47 = 271{,}000$ amp (see Fig. 9.25*b*). With $\alpha = 30^\circ$, $a = 12.7$ cm, the resistance per centimeter length of one Ioffe bar is 0.45 microhm/cm.

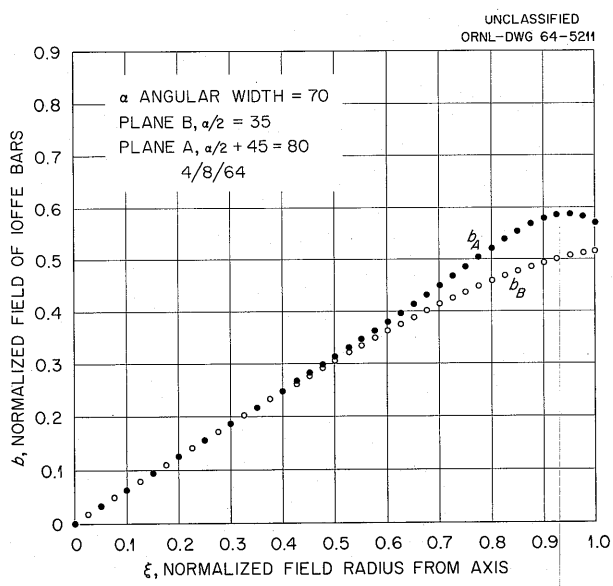

Fig. 9.21. Fields of Thin Annular Ioffe Bars, $\alpha = 70^\circ$.

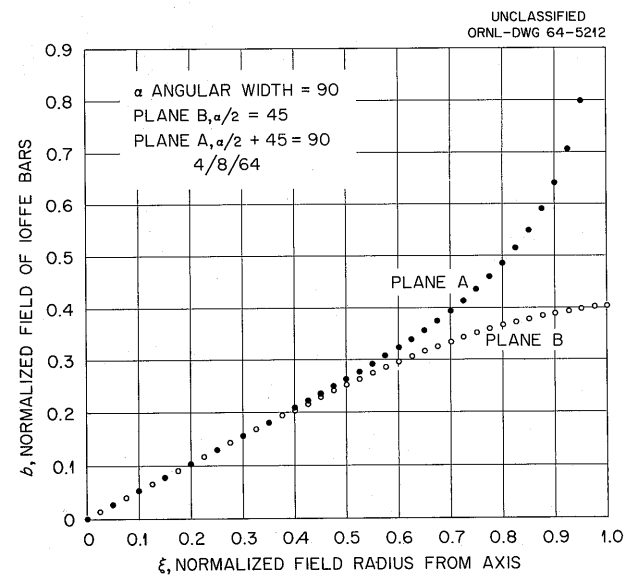

Fig. 9.22. Fields of Thin Annular Ioffe Bars, $\alpha = 90^\circ$.

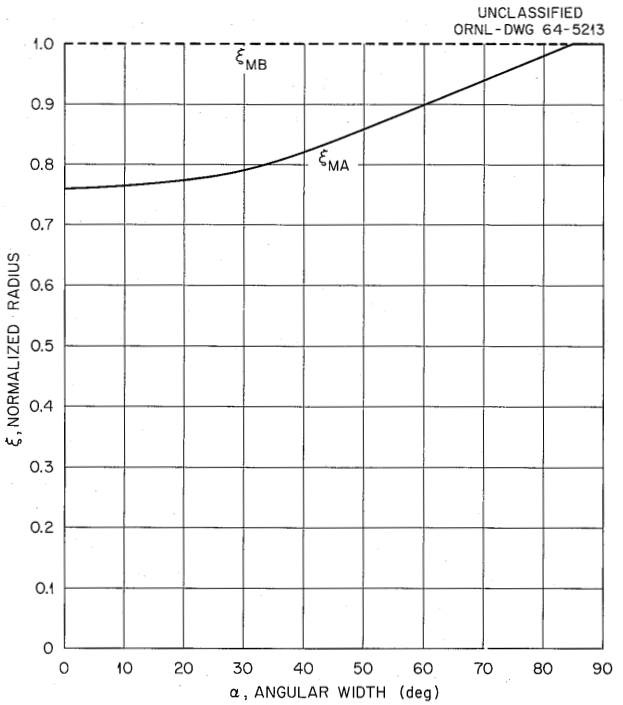

Fig. 9.23. Normalized Radius to Maximum Field vs Angular Bar Width.

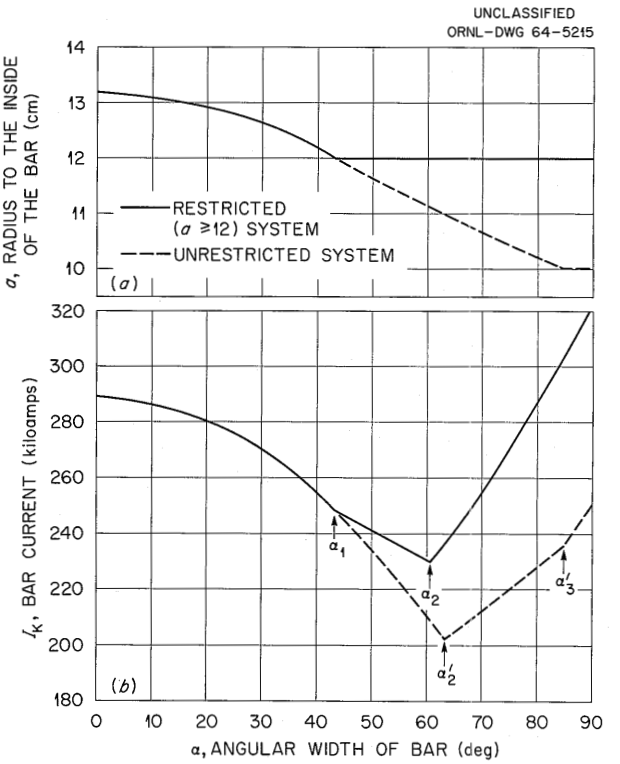

Fig. 9.25. (*a*) Bar Radius vs Angular Width; (*b*) Bar Current vs Angular Width.

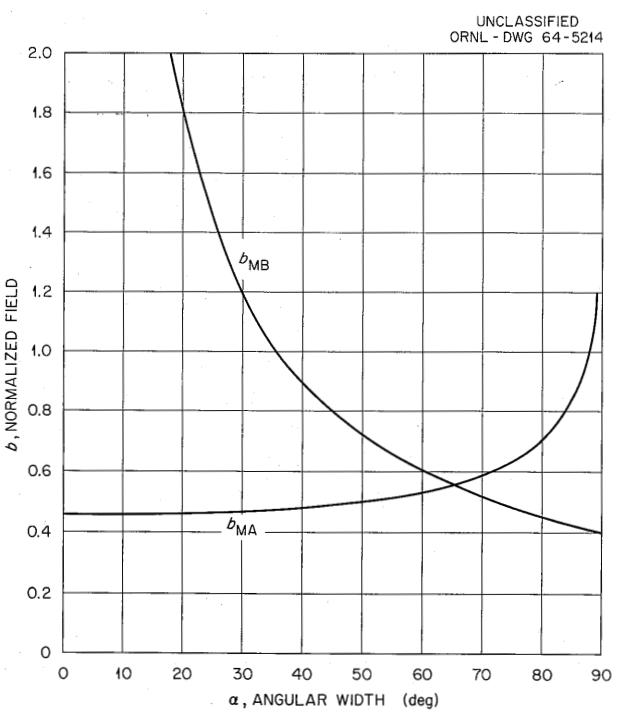

Fig. 9.24. Maximum Normalized Field as a Function of Angular Bar Width.

Therefore the power for four bars is P = 128 kw/cm.

For larger angles α the following slight complication must be considered. We assume, say, $\alpha = 70°$. Figure 9.21 shows that the b value in plane A is the higher one and that the curve reaches a maximum at $\xi_A = 0.94$ (see Fig. 9.23). Because of condition (1) the b_B value must be taken; it is $b_B = 0.503$. The bar radius following from ξ_A would be 10/0.94 = 10.63 cm. This value contradicts condition (3) and the minimum bar radius of 12 cm must be chosen. With a = 12 cm and ξ_B = 10/12 = 0.833, b_B = 0.471. Therefore, I = 120,000/0.471 = 254,000 amp (see Fig. 9.25*b*). With $\alpha = 70°$ and a = 12 cm the resistance per centimeter length of one Ioffe bar is 0.205 microhm/cm. Therefore, the power for four bars is P = 50.8 kw/cm. If we disregard condition (3), then a = 10.63 cm is acceptable, $\xi_A = 0.94$, $b_A = 0.588$, and I is only 21,500 amp, giving a total power of 39.4 kw/cm (dotted curve of Fig. 9.26).

From Fig. 9.26 it can be seen that if the bars are sufficiently wide (say 55°), then the bar power is no longer strongly dependent on bar width.

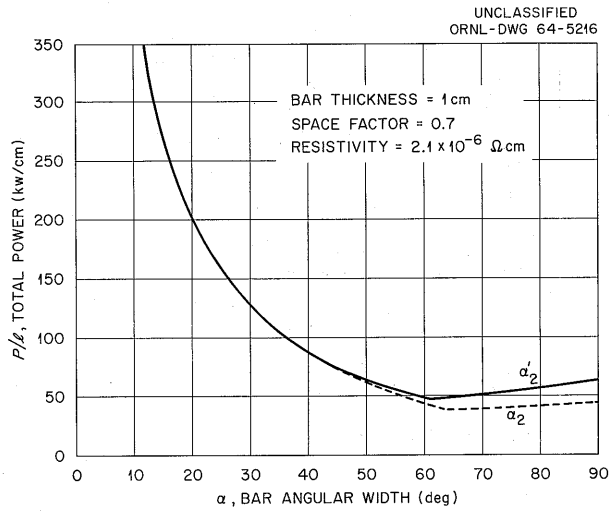

Fig. 9.26. Bar Power vs Angular Width.

Three breaks occur in Fig. 9.25*b*. The first, labeled α_1, is also a branch point for Figs. 9.25*a* and 9.26. In each case the solid branch results when *a* is restricted by Eq. (28). The dotted branch occurs when this restriction is ignored. The second break in the curves, at α_2, represents a transition point. At smaller values of α, the maximum field occurs in the plane through a bar, but at larger α's the maximum field is found in the plane between the bars. The angle α_2 is dependent on the radial gap between the cylinder surface and the bars [see condition (3)]. The value of α_2 for the dotted curve, 63°, is in close agreement with Luc's[20] optimum value of bar width (60°), and gives not only the lowest bar current but also the lowest power. The dotted curve breaks again at α_3', where a_s becomes equal to *a*.

In conclusion we can state that the optimum bar width to choose is 61°. This means 29° would be available for access for diagnostic purposes. If this is not sufficient, one can read from Fig. 9.26 the power needed for the new α.

9.5 MINIMUM-*B* CONFIGURATION WITH IRON QUADRUPOLE

P. A. Thompson

There continues to be interest in the "minimum-*B* field" configurations for plasma confinement. One of our efforts during this reporting period has been the design, construction, and investigation of a model which consists of the combination of a standard mirror field with a perpendicular quadrupole field produced by electromagnets with iron pole pieces.

Proceeding mostly on intuition, a conceptual design was evolved and existing coils were sought for the mirror field. The most suitable was the middle pair from the old "Orion" model coils – about 7 in. long, 6 in. ID, and 8 in. OD. Since there is but a single water path per coil, only about 300 amp can be tolerated without overheating (using 250-psi water); this current produces about $1\frac{1}{2}$ kilogauss at the center of the coil. Plots of axial field vs distance along the axis (B_z vs z) made for each coil revealed that they were matched closely enough for our purposes and that a separation of $4\frac{1}{2}$ in. would give the desired mirror ratio of 2.

The design of the pole pieces for the quadrupole electromagnets was again purely intuitive: four curved surfaces parallel to the mirror axis going from the face of one mirror coil to the face of the other; see Fig. 9.27. For ease of construction these curved surfaces were formed by the rounded edges of the 1-in.-thick mild steel plates. Having these plates parallel to each other provided flux return paths which were actually shorter than those from one pole tip to another so that not all the flux was concentrated at the desired locations. (A method for preventing this undesirable condition is given below in the proposal for the next version of this system.) The energizing coils, wound from hollow, $\frac{3}{16}$-in. square copper tubing with epoxy insulation, consisted of two layers, 12 turns each, on an iron form with rounded corners $1\frac{1}{2}$ in. × $3\frac{1}{2}$ in. There were no indications of saturation until a current of about 300 amp was reached; this produced a field of some 620 gauss. The maximum current obtainable from the small rectifier set in the Engineering Science Laboratory was 688 amp (865 gauss), at which current the temperature rise in the 250-psi cooling water was less than 10°C.

As indicated above, the mirror coils were arranged to give a mirror ratio of 2. However, when the iron quadrupole pieces were placed in position between the mirror coils – without their coils being excited – the mirror ratio became variable (ranging from 2.22 at 100 amp to 2.89 at 300 amp). The original criterion for this field configuration

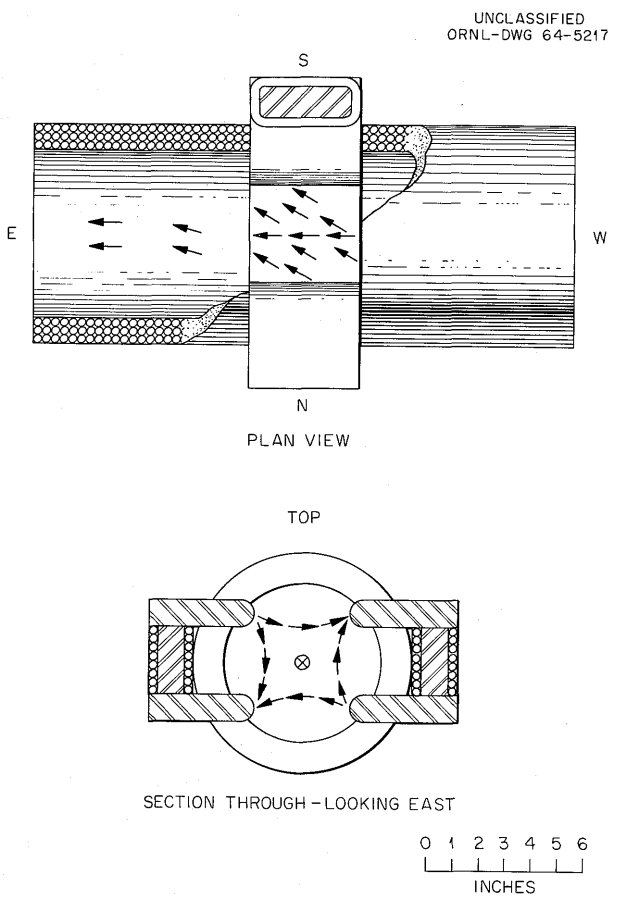

Fig. 9.27. Fe-Quad I Showing a Few B Vectors to Give General Idea of Field Shape.

was that the mirror coil field at midplane (purely axial, B_z) should have the same magnitude as the maximum quadrupole field (purely perpendicular to the axis, $B_{\perp z}$); the resulting maximum field value then would be $\sqrt{2}$ times this common value. Since the limiting parameter for the system was the temperature rise in the mirror coils (which reached its maximum acceptable value at about 300 amp), the working value of the two mutually orthogonal fields was limited to 485 gauss (which is well below saturation for the iron in the quadrupole magnets).

The first tests with both sets of magnets energized were made with a water-cooled rheostat limiting the current to the quadrupole coils, which were paralleled to the mirror coils on the small rectifier set. It was not possible to obtain the correct ratio of currents in this manner (the currents were 233 amp in the mirrors – B_0 about 380 gauss, and 200 amp in the quadrupole coils – $B_{\perp max}$ about 415 gauss), but semiquantitative readings taken with a hand-positioned Hall effect magnetometer indicated that the field magnitude varied from 375 gauss on axis at the midplane to 710 gauss some 2 in. along the axis toward the mirror coils and to 500 gauss some 2 in. perpendicular to the axis between the quadrupole magnet pole tips. The field in all other directions increased by comparable amounts, indicating that this configuration indeed produced a minimum-B field in a volume of approximately 2-in. radius.

The problem of measuring the magnetic field of this system, which is called Fe-Quad for obvious reasons, is complicated by the fact that it is no two-dimensional figure of revolution, but a truly three-dimensional one with at best elusive symmetry. A magnetometer probe head containing three mutually orthogonal Hall elements (3-D) had been constructed (see Sect. 9.6), but the electronics had not been completed. An electronically far simpler system, but one with some mechanical complications (5-DOF), is now being designed and built (see Sect. 9.6). At the time of the experiments here reported, however, the only readily usable magnetometer was the Bell 110A transistorized instrument with "transverse" and "axial" Hall elements conveniently mounted in handles. Scans of the B_z field at different points in the x-y plane were made with the axial probe and a Moseley X-Y recorder. It was qualitatively observed that even though the presence of the iron pole pieces changes the mirror ratio and field magnitude of the mirror coils, only for points in the x-y plane containing the pole pieces themselves is there much distortion of field (as compared to a normal mirror field without iron).

For the other two field directions a calibrated rotatable arm was installed on the positioning table so that the magnitude and direction of the perpendicular field component could be found with some facility. In making point readings in this manner it was noticed that the rather close mechanical tolerances at the positioner table resulted in variations in position at the Hall probe end of the arm of some $\frac{1}{2}$ in. Since the field gradients encountered were rather large, this condition led to significant ambiguities in the summation of field components. Plots of the magnitude of $B_{\perp z}$ vs z indicated that not only were there the expected

asymmetries periodic in azimuthal angle, but also there were asymmetries with no apparent ordering. This latter category cannot be explained by the uncertainties in position, but must in part be blamed on deviations in material, construction, and alignment.

By adding another power supply it was possible to adjust the fields of the mirror coils and of the quadrupole magnets to the required 485 gauss; field components were measured as above and added vectorially. Within the limits outlined it can be stated that from the center of the system (mirror midplane on axis) the magnitude of the field increases in all directions: about 27% in 1 in. along both the x and y axes (i.e., between the pole tips), about 34% in 1 in. along the diagonal between the axes (along the 45°), and about 55% in 1 in. along the stronger cube diagonal and 16% along the weaker.

It would be desirable to improve the alignment, etc., of the system and then to take more data with different ratios of mirror coil current to quadrupole coil current; however, this will have to wait until the completion of the 5-DOF probe (see above). Meanwhile, conceptual design work has begun on an improved version of this system – Fe-Quad II – which could actually be used for plasma confinement experiments. The main features, shown in Fig. 9.28, are flat pole pieces (with rounded ends) oriented along radii (so that the shortest flux paths in air will be from one pole tip to another), electromagnet energizing coils separated into eight sections and moved over the mirror coils (so that there will be a maximum of free access space for diagnostics, etc.), a clear inside diameter of 4 in., and B_0 from mirror coils and B_{1max} from quadrupole electromagnets each 1.5 kilogauss, giving a combined maximum B magnitude of $\sqrt{2} \times 1.5$ kilogauss = 2.12 kilogauss.

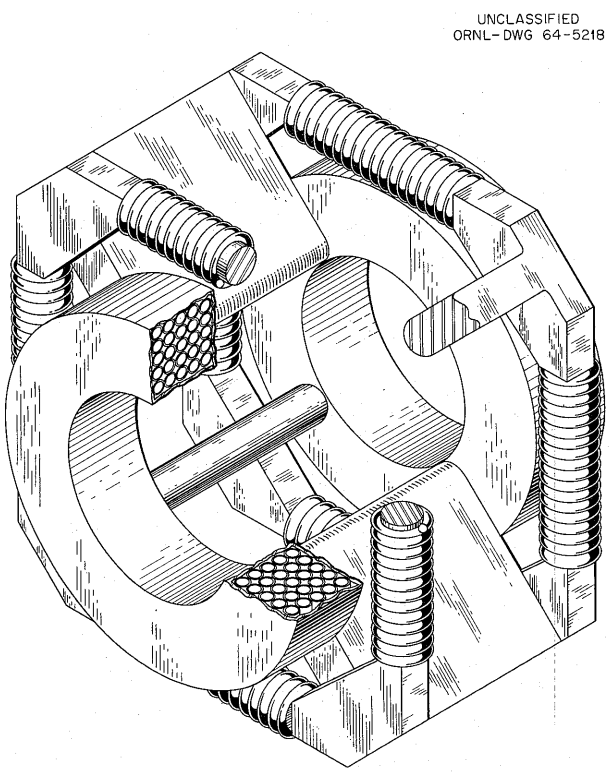

Fig. 9.28. Fe-Quad II – Conceptual Design.

9.6 SPECIAL MAGNETOMETER PROBES

P. A. Thompson

Mirror machines for thermonuclear research belong to the magnetically simple regime of rotationally symmetric fields. Using the usual cylindrical coordinate system one can say that the magnetic field at a given point is purely and predictably B_z or B_r or a combination of the two, but that there is no B_θ component. However, in investigating by actual measurement the field inside the injection duct ("snout") of DCX-2 the need was first felt for a magnetometer with a small sensitive element, which could be operated some distance from the indicating instrument and with the ability to define both magnitude and direction of the field being measured. At the time a system was fashioned from two existing Hall effect instruments provided with suitable extension cords, their sensitive elements (Siemens FC-32 Hall elements) mounted – one to read axial fields and the other to read transverse fields – on the end of a long pole. At that time it was decided to design and build a small probe head with three mutually orthogonal Hall elements.

Recently the increased interest in minimum-B fields for plasma containment (see Sect. 9.5) has renewed the necessity for measuring magnetic induction in three-dimensional fields. It is usually only the magnitude of the field strength that is desired, but this ordinarily can only be obtained by vector summation of components. Under the impetus of this renewed interest, the 3-D Hall

element probe mentioned above was built and will be described presently. Electronics for switching from one element to another and thereby reading each component in turn can easily be obtained; however, the problem of electronically taking the square root of the sum of the squares of the three components is not quite so simple. A method for accomplishing this has been suggested by the work of H. H. Wieder, U.S. Naval Ordnance Laboratory, Corona, California,[21] but a reliable circuit has not yet been developed.

In the design of the 3-D probe the two most important considerations were that it be small and that the magnetic centers of the active areas of the three Hall elements be as close together as possible. Of course, the elements must be held precisely orthogonal. Further it was desirable that enough thermal insulation and inertia be provided that ordinary temperature changes would not cause significant errors.

Figure 9.29 shows a cutaway view of the probe with its three Hall elements, the active areas of which are indicated by dotted lines; the outside diameter is $^3/_8$ in. The elements chosen were the smallest reliable ones of their type on hand; they are the Bell BH-203 axial Hall element and two Siemens EA-218 transverse Hall elements.

Another approach to the measurement of field strength and direction in three-dimensional magnetic fields avoids the electronic complications of vector summation by substituting the mechanical complication of positioning a single Hall element. The system must be capable of positioning in five degrees of freedom: three degrees of translation to put the element in the point in space at which it is desired to make the measurement, then two degrees of rotation to put the face of the element in the proper plane; the third rotational degree of freedom is about the direction of the field vector and has no significance. A mechanical arrangement to add these two degrees of rotational control to our existing three-dimensional positioning table is now under construction. Called 5-DOF, it will position a Bell BH-202 Hall element and use only standard – though reworked – gears (see Fig. 9.30). Other positioning devices using this same basic idea might be smaller (by using special gears, etc.), might have right-angle bends for making measurements in hard-to-reach places, and might be automated with suitable servo systems, feedback amplifiers, and analog computers to automatically find the magnitude and direction of the field at a given point or even to follow flux lines.

UNCLASSIFIED
ORNL-DWG 64-5219

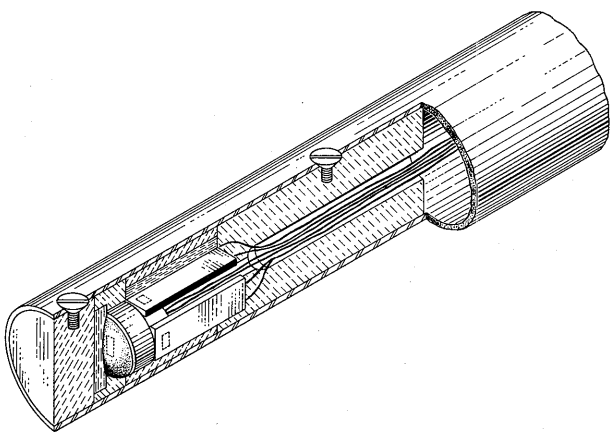

Fig. 9.29. Cutaway View of 3-D Hall Probe. The active areas of the orthogonal Hall elements are indicated by dotted lines.

UNCLASSIFIED
ORNL-DWG 64-5220

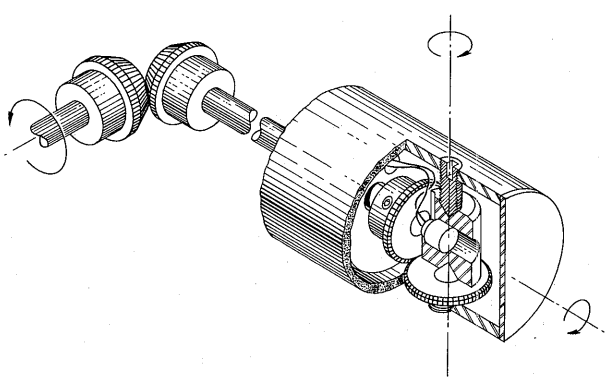

Fig. 9.30. The 5-DOF Mark I Hall Probe in Schematic Representation. The head is contained in a 5/8-in.-OD tube and the overall length from element to control gears is about 18 in.

[21] H. H. Wieder, *Rev. Sci. Instr.* **34**, 422 (1963); *Electronics* **36**(45), 46 (1963); *Electronics* **37**(4), 30 (1964).

9.7 MICROSIZE HALL PROBES FOR SUPERCONDUCTIVITY MEASUREMENTS

J. E. Simpkins

In a previous report,[22] the development of magnetometers with a thickness of only a few microns was described. These probes, based on the magnetoresistive effect, were used to measure the "proximity effect" in soft superconductors.[23] As is well known, magnetoresistance is characterized by

$$\Delta R/R(0) = \alpha H^2, \qquad (1)$$

where $\Delta R/R(0)$ is the ratio of change in resistance to resistance at zero magnetic field, α is a constant depending on the material used, and H is the magnetic field. At 4.2°K for bismuth, this relationship is correct up to fields of about 800 gauss (after which the dependency becomes almost linear). Because of this quadratic relationship, the minimum measurable field with such probes was at least several gauss.

The desire for an increase in probe sensitivity made it necessary to consider the Hall effect. In a very large range the basic Hall equation holds:

$$V_H = \frac{kI_c B}{t}, \qquad (2)$$

where V_H is the Hall voltage, I_c the control current, B the field component normal to the surface of the probe, t the probe thickness, and k a constant depending upon the material.

Recent interest in mapping small localized fields in superconductors has given new impetus to the development of small-dimensioned deposited bismuth Hall probes. These probes have the advantage of indicating the direction of the field, and with suitable electronics, can measure fields of a tenth gauss or less. These bismuth Hall effect magnetometers are also conveniently applicable to high-field measurements as well.

Both flat and cylindrical types of such microprobes have been developed. The first was a flat probe shown in Fig. 9.31. It consists of a set of voltage and current leads vapor-deposited through copper masks onto glass or other suitable substrate.[24] Both gold and silver-manganese alloy consisting of 85% silver and 15% manganese have been used.[25] The alloy preferentially evaporates, the manganese first, then the silver. This produces a film which adheres to the glass very well, provides a current path of low resistivity, and is easily soldered. Bismuth, as the active element of the probe, is then deposited through suitable masks.

A more universally adaptable probe was developed in the cylindrical model, shown in Fig. 9.32. Such probes are fabricated by casting four Formvar-covered magnet wires of suitable size (from 0.003 to 0.008 in. in diameter) in Ciba Araldite epoxy, and then metallographically polishing the end of

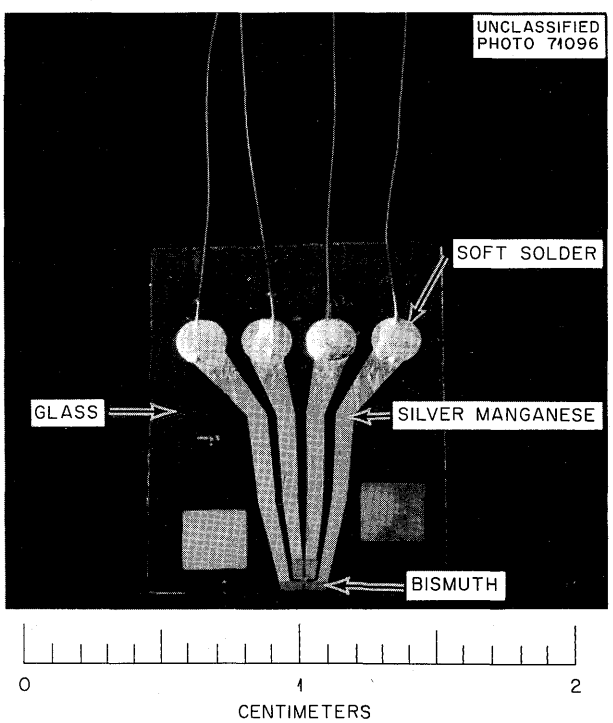

Fig. 9.31. Flat Bismuth Hall Probe, Showing the Four Conductors Converging into the Active Element.

[22] J. E. Simpkins and P. A. Thompson, *Thermonuclear Div. Semiann. Progr. Rept. Apr. 30, 1963*, ORNL-3472, p. 92.

[23] W. F. Gauster *et al.*, *Thermonuclear Div. Semiann. Progr. Rept. Apr. 30, 1963*, ORNL-3472, p. 88.

[24] J. E. Simpkins and P. A. Thompson, *op. cit.*

[25] P. Gould and J. Finnegan, *Rev. Sci. Instr.* **33**, 767 (1962).

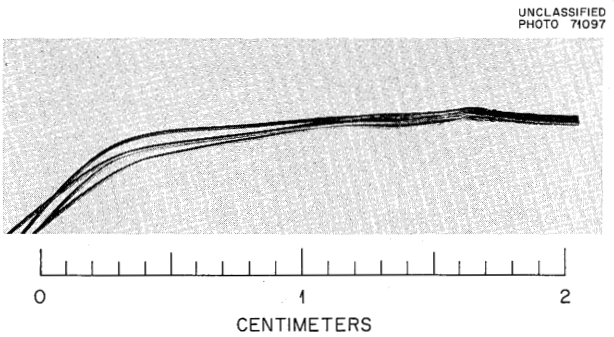

Fig. 9.32. Cylindrical Bismuth Hall Probe.

the assembly, so that a smooth surface is formed perpendicular to the axis of the wires (see Fig. 9.33). Bismuth is deposited onto this surface, and a protective covering is applied.[26] Probes of various sizes have been constructed, ranging from about 10 to 20 mils in diameter. Using 44 AWG magnet wire, a 5-mil probe would be possible.

For testing the probes, only simple instrumentation has been used. The voltages generated in fields of a gauss or so are only a few microvolts, and the usual problems involved in handling small signals are encountered, namely, thermal emf, ac noise, and ground loops. Also, since bismuth exhibits a measurable magnetoresistive effect, the probe current must be constant. A dc power supply has been used, and the Hall output amplified by a low-impedance, high-gain breaker amplifier. The output is usually fed into a Moseley *x-y* recorder.

Figure 9.34 shows the response of four probes in low magnetic fields; Fig. 9.35 represents the characteristics of two of these probes in higher fields. The curves were reproducible with a change in sensitivity of less than 10% after bringing the probes up to room temperature, and then recooling. Various values of control current have been used, with 1 to 10 ma being the usual range. One hundred milliamperes did not seem to be excessive in the flat probes, but it caused considerable local boiling of helium around the cylindrical probes. About half of them remained operative after cycling a few times from 300 to 4°K. One of the cylindrical probes has been in use in various experiments for about three months. It is used in fields up to 70 kilogauss, and has been thermally cycled many times.

[26]D. D. Roshon of IBM Laboratories suggested the possibility of fabricating a somewhat similar probe using Taylor process wires.

Since probe performance depends upon film thickness, it was desirable to monitor this parameter during evaporation. Following many helpful suggestions of K. H. Behrndt,[27] a thickness monitor was constructed using the frequency shift of an oscillating quartz crystal. An AT cut crystal (to ensure the least frequency shift due to heating) controls the frequency of a transistorized oscillator. A face of the crystal is exposed to the evaporant, and a film is deposited on it and on the substrate simultaneously. The output from the oscillator is fed into a frequency counter. As long as the thickness of the film does not amount to more than about 1% of the crystal thickness, the frequency shift is linear, proportional to the mass deposited.[28] Assuming a constant packing factor, our monitor was calibrated to read thickness. It appears that a bismuth film having a thickness of 1 μ produces optimum results. A crystal frequency of about 5 Mc is convenient since the resulting change in frequency is about 5 hertz/A.

[27]K. H. Behrndt, Bell Telephone Laboratories, Murray Hill, N. J., private communication.

[28]K. H. Behrndt and R. Love, *Vacuum* **12**, 1 (1962).

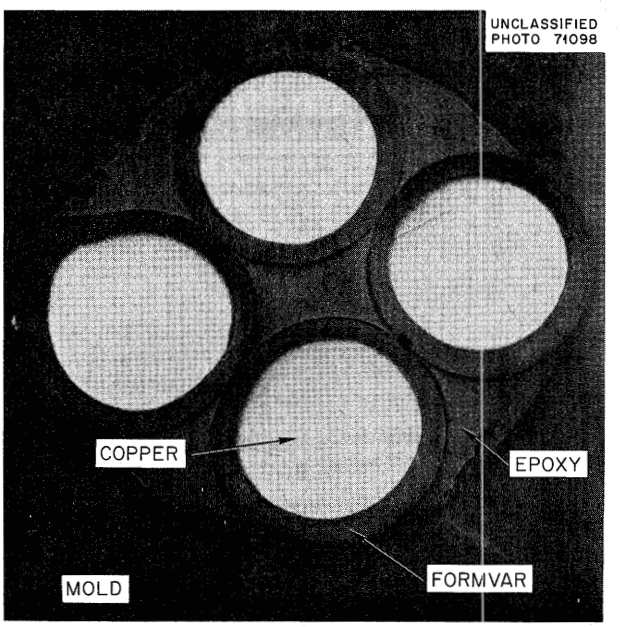

Fig. 9.33. End View of Cylindrical Probe Showing Epoxy Substrate and Copper Wire Contact Areas. Bismuth was deposited over the entire surface.

Although usable micromagnetometers of both the flat and cylindrical types have been constructed and tested, several problems remain to be solved. The failure rate due to thermal cycling is still high. In some cases, especially with the cylindrical type, the Hall voltage at zero field is relatively large due to the fact that the voltage contacts do not fall on an equipotential line. Perhaps some change in probe geometry would minimize this effect.

Recent developments in deposition technology make it possible to use compounds such as indium arsenide. Unlike bismuth, this material exhibits very little change in both electrical conductivity and Hall coefficient in the range from 100°K to less than 1°K,[29] and the sensitivity (even at room temperature) is sufficient. For our future work we are considering using this material in addition to bismuth for manufacturing micro Hall probes by deposition technique.

[29] R. Sladek, *Phys. Rev.* **105**, 460 (1957).

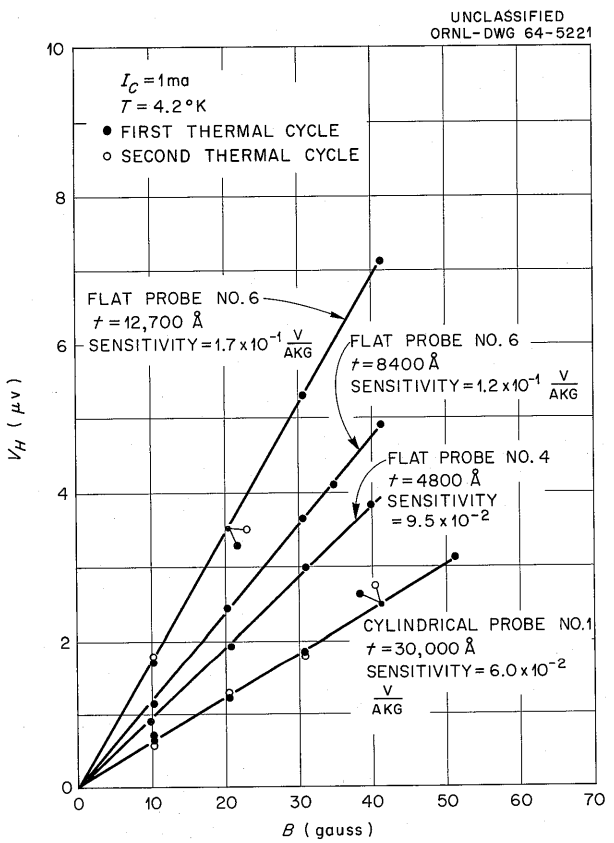

Fig. 9.34. Performance of Some of the Probes in Low Magnetic Fields.

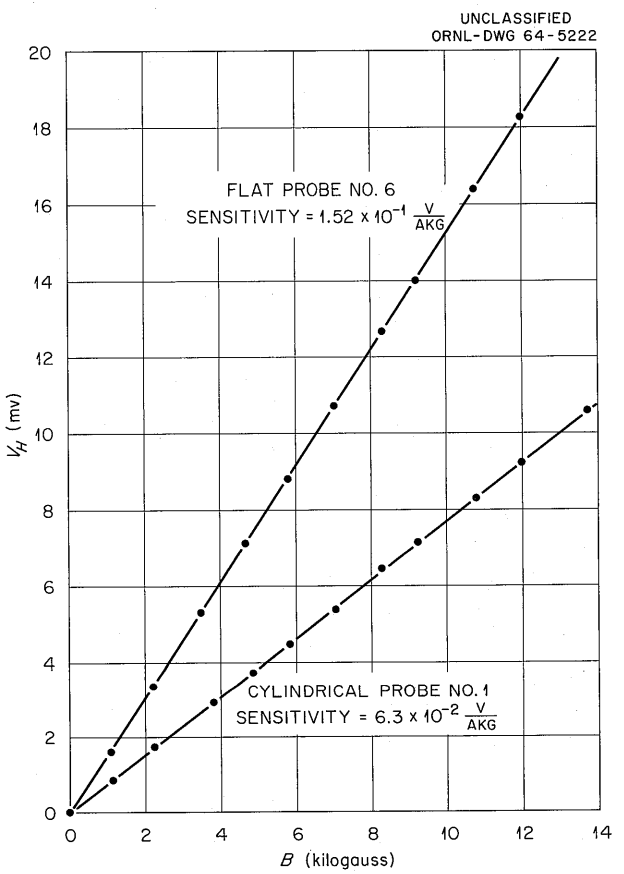

Fig. 9.35. Performance of Some of the Probes in Magnetic Fields of Medium Intensity.

10. Vacuum Systems, Techniques, and Materials Studies

10.1 ELECTRON BOMBARDMENT STUDIES

R. E. Clausing[1]

The rate of gas production by electron bombardment of surfaces has been measured in several systems under a variety of conditions. The gas evolution rates are large enough to make "electronic cleaning" appear quite useful as a vacuum technique. By the same token, electron bombardment of dirty surfaces can cause the release of large amounts of unwanted gases. The amount and kind of gas released from a surface, as the result of electron bombardment, can be used to indicate and study the nature and severity of surface contamination or conversely the degree of cleanliness. In the experiments described below, the rate of gas production varies from 10^{-4} to 10 gas molecules per incident electron depending upon the electron energy and the surface conditions. The very large yields occurred in systems containing diffusion pump oils, and apparently resulted from the decomposition of the hydrocarbons. The gases observed in these systems may have been the result of a complex combination of desorption, decomposition by electrons, and thermal decomposition of heavy ions attracted to the hot filament as discussed in Sect. 10.4. Gas yields of 10^{-2} per electron were observed in systems which were not contaminated with detectable amounts of hydrocarbons.

There are many references to electrical cleanup of gases, but most deal with ionic phenomena; there are only a few references pertaining to the use of electron bombardment for this purpose. The use of electron bombardment for cleanup in ultrahigh vacuum systems has usually been confined to applications where heating accompanies the bombardment. It has been observed, however, that electrons per se cause desorption of gases from surfaces.[2–6] Data which have recently become available give relatively large desorption ratios.[7,8] The production of brown deposits in electron microscopy has been attributed to decomposition of hydrocarbons by electrons.[9]

A simple experiment was conducted to explore the desorption of gases from surfaces by electron bombardment. The rate of gas release was measured as a function of electron current and voltage. Electrons with energies from several electron volts up to 70 kev were used.

Figure 10.1 shows a block diagram of the apparatus used for the first experiment. The chamber in which the electron bombardment took place has a volume of approximately 2.5 liters and a surface area of nearly 1000 cm^2. The wall of the chamber bombarded by the electrons was constructed of type 304 stainless steel. The chamber temperature was held constant by a combination of water and air cooling.

The entire system was assembled with metal gaskets so as to avoid hydrocarbons. The filament was a 0.015-in. tungsten wire with a heated length of 15 cm. The electron currents used were

[1]Metals and Ceramics Division.

[2]G. E. Moore, *J. Appl. Phys.* **32**, 1241 (1961).

[3]B. J. Todd, J. L. Lineweaver, and J. T. Kerr, *J. Appl. Phys.* **31**, 51 (1960).

[4]P. A. Redhead, *Vacuum* **13**, 253 (1963).

[5]J. Mark, personal communication (September 1963).

[6]D. Minzel and R. Gomer, *J. Chem. Phys.* **40**, 1164 (1964).

[7]P. A. Redhead, *Appl. Phys. Letters*, **4**, 167 (1964).

[8]L. A. Peterman, *Proc. 2nd Intern. Symp. Residual Gases in Electron Tubes*, Milan, 1963.

[9]E. A. Ennos, *Brit. J. Appl. Phys.* **4**, 101 (1953), **5**, 27 (1954).

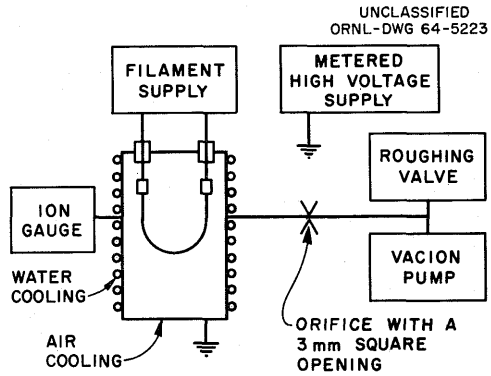

Fig. 10.1. Block Diagram of the First Electron Bombardment Experiment.

from 1 to 30 ma and the voltages applied to the filament ranged from approximately 10 v to 30 kv peak ac and 45 v to 3 kv dc negative. It was found that decreasing gas evolution occurring during long continuous operation made it difficult to reproduce initial points on a run if the system was "dirty." The electron accelerating potential was applied in 5- or 10-sec pulses to provide a consistent means of data gathering. The system required about 5 sec to reach 90% of its eventual pressure rise. The base pressure of the system with the filament operating but no electron current was initially 1.8×10^{-6} torr (the filament power was approximately 60 w). The system pressure dropped during these experiments until it reached the base pressure of the unbaked ion pump at 5×10^{-9} torr. Figure 10.2 shows the pressure increase in this system during a bombardment pulse as a function of electron energy (normalized to 1 ma of bombarding current). These data were obtained after a total bombardment of 10^{17} to 10^{18} electrons/cm^2. The scale on the right (Fig. 10.2) shows the yield of gas per electron based on the assumptions that (1) the gas is "nitrogen-like" (i.e., its mass and ionization cross section are similar to those for nitrogen), (2) it is not appreciably readsorbed in the test chamber, and (3) the pressure in the pump was $\frac{1}{3}$ the chamber pressure (this is a conservative number based on observation). The yield of gas per electron is nearly independent of total electron current. Gas yields derived from data by Redhead,[4,7] Todd,[3] and Peterman[8] are included for comparison.

A simple calculation based on the above data indicated that it might be feasible to use this technique for cleaning vacuum systems. Observations of yield and base pressure as a function of the total electron flux in this apparatus tend to support this conclusion, although they cannot be offered as proof because there was no control system for comparison.

A second experiment was tried with a different high-voltage insulator and electron source geometry but using the same pumping arrangement and methods of construction. The results were similar to those of the first system but gave yields a factor of 3 or 4 higher. This difference probably reflected differences in surface cleanliness since only several milliampere-hours (a total bombardment of 10^{15} to 10^{16} electrons/cm^2 average) of bombardment preceded the measurement.

A third experiment was conducted using the components from an x-ray tube. The same vacuum system was used. The electron gun, with a tungsten filament, was spaced approximately 1 cm from a tungsten target mounted on a massive copper block for temperature stabilization. The area bombarded by electrons was about 0.1 cm^2. The currents used ranged from 0.5 μa to 1 ma. Only small differences (a factor of about 2) in gas yield per electron were noted even with these extreme differences in current density. The total bombardment prior to taking the data was about 10^{20}/cm^2. These data are also shown on Fig. 10.2. Note that they are also similar to those from the first experiment, although they were obtained with a considerably different experiment. The vacuum system, however, was the same one used on the first experiment, and the surface contamination was probably similar.

As the result of these experiments and encouragement from earlier observations by J. Mark at RCA,[5] it was decided to try electron cleaning in DCX-1 as reported in Sect. 10.2. Related work was also undertaken in the ultrahigh vacuum facility as described in Sect. 10.4. Figure 10.3 is a composite of data for the systems presented in Figs. 10.2, 10.6, and as described in Sect. 10.4.

The data are included for the purpose of comparing the results of experiments conducted under widely varying conditions, and are not considered quantitatively accurate. They are based on ion gage readings and estimated pumping speeds, with the assumption that the gases are "nitrogen-like" as defined earlier. If the gases are predominantly hydrogen, as discussed in Sect. 10.4, the yields could be about eight times larger.

The data from the Ultrahigh Vacuum Test Facility show the yield curves for a copper system seriously contaminated with diffusion pump oil and for the same system after a mild thermal bake (20 hr at temperatures between 100 and 145°C). The yield dropped by a factor of 20 after the bake. In these two experiments the yield is not a strong function of electron energy. Additional baking dropped the yields in this system still further but because of a change in the experimental techniques no direct comparison is possible. The data from the DCX-1 end region illustrate the yields obtained after extensive electron bombardment in a complex system of stainless steel and copper. The yields at 3 kev were initially near 10 gas molecules per electron but decayed to the curve shown after electron bombardment of the exposed surface (some of the copper parts, which constitute a small fraction of the exposed surface, were baked before bombardment). The data for the DCX-1 liner were obtained after a 12-hr bake at 400°C. Although the surface had previously been coated

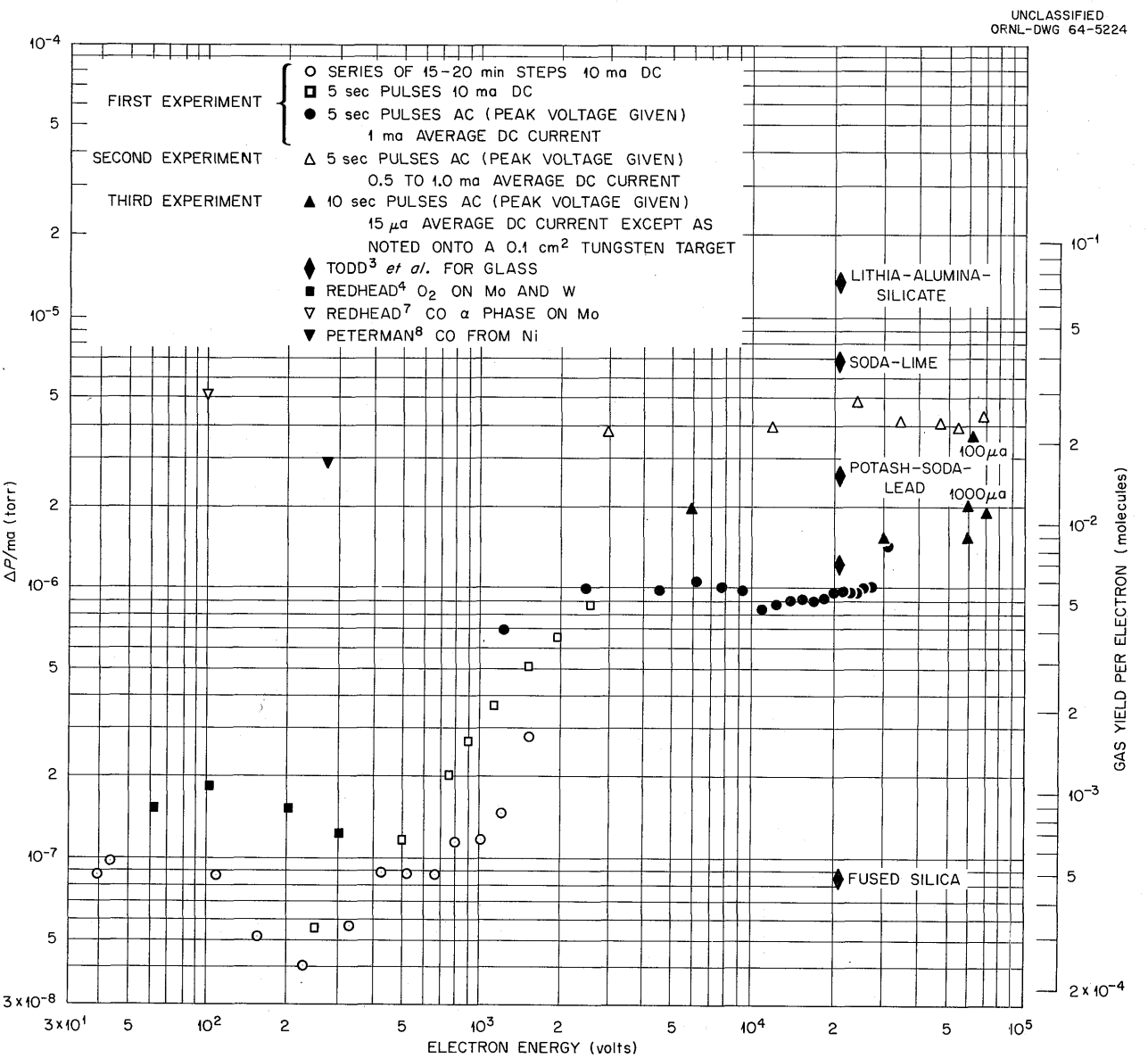

Fig. 10.2. Pressure Increase per Milliampere of Electron Current as a Function of Electron Energy.

UNCLASSIFIED
ORNL-DWG 64-5225

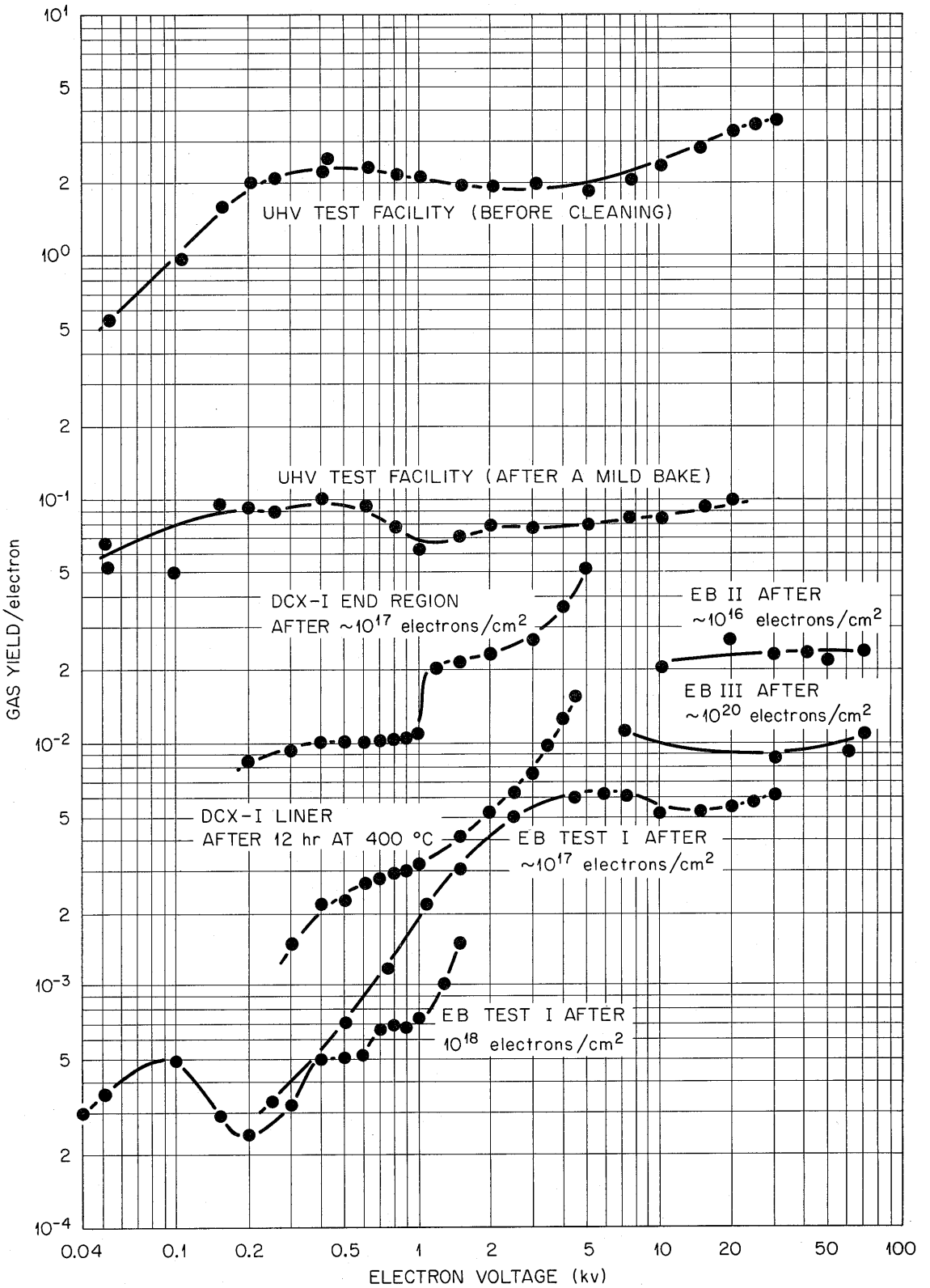

Fig. 10.3. Comparison of Data from Various Electron Bombardment Experiments.

with titanium, the getter film was no longer active, and no fresh titanium was evaporated. The surface was probably not seriously contaminated with oil. The data labeled EB-I, EB-II, and EB-III are the data reported above and were obtained in systems built so as to avoid contamination with hydrocarbons; these systems also show the effect of electronic cleaning. The curves for the cleaner surfaces all show an increase in yield in the region near 1 kev electron energy.

A mass spectrometer was added to the system described previously as the third experiment. The gases observed as the result of electron bombardment of the tungsten target from the x-ray tube were predominantly carbon monoxide and hydrogen. The height of the carbon monoxide mass 28 peak was usually five to ten times the mass 2 peak of hydrogen, but long or high-current bombardments reduced the amount of carbon monoxide more rapidly than the hydrogen. Ratios as small as 2:1 were obtained.

The mass spectrometer is now a part of the recently finished system shown in Fig. 10.4. This system is similar to the first experiment except that a liquid-helium pump has been added and provision made to valve out the VacIon pump if desired. The results of the initial system operation indicated that the system contained small amounts of hydrocarbons. The yields were about 10^{-1} gas molecule per electron but decreased to approximately 10^{-2} as the electron bombardment proceeded. The gases released were predominantly hydrogen and carbon monoxide. The ratio of mass 2 to mass 28 was initially about 6:1. This ratio increased to 20:1 as the partial pressure of hydrocarbons decreased.

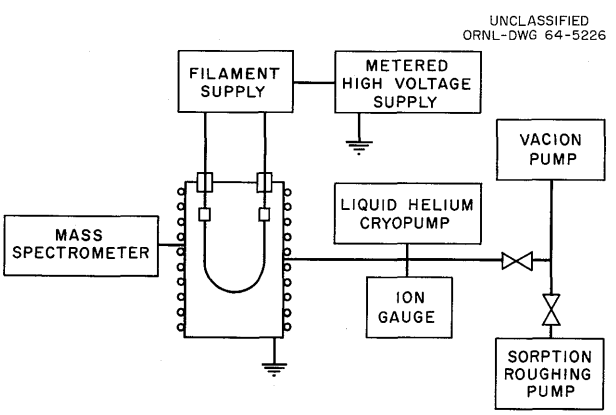

Fig. 10.4. Block Diagram of the Mark IV Electron Bombardment Apparatus.

Work now planned includes: (1) development of the practical applications in DCX-1 and other vacuum systems, (2) a more detailed investigation of the desorption of gases from stainless steel and copper to determine what results to expect in large systems, (3) electron bombardment of the titanium vapor-deposited films used for getter pumping to determine the release rate of methane and hydrogen in particular, and (4) desorption of gases from a refractory metal by both thermal and electronic methods for the purpose of making measurements with known surface conditions. In summary, the following conclusions seem to be justified:

(1) Reduction of the partial pressures of hydrocarbon vapors in vacuum systems by electronic means is both feasible and practical.
(2) Both the kind and quantity of gases evolved during electron bombardment are dependent on the type and amount of contamination on the surface, and thus provide a means of characterizing the condition of the surface.
(3) Electronic desorption is not a bulk heating effect but may be advantageously combined with thermal desorption (heat supplied by electron bombardment or other means).
(4) Electronic desorption may be capable of producing clean surfaces without heating or causing radiation damage to the substrate. If hydrocarbons are present a nonvolatile residue of carbonaceous material may be formed on the surface instead.

10.2 ELECTRONIC CLEANING IN DCX-1

E. R. Wells

The electronic cleaning technique was tried in the DCX-1 vacuum system. The first installation was in the west tank region shown in Fig. 10.5. This region is pumped by two 32-in. diffusion pumps with water-cooled baffles. Its base pressure, when all surfaces are at room temperature, is normally about 1×10^{-7} torr.

The initial yield was as high as 10 gas molecules per electron but decayed to approximately 10^{-2} per electron as the system cleaned up. Although the base pressure did not decrease greatly

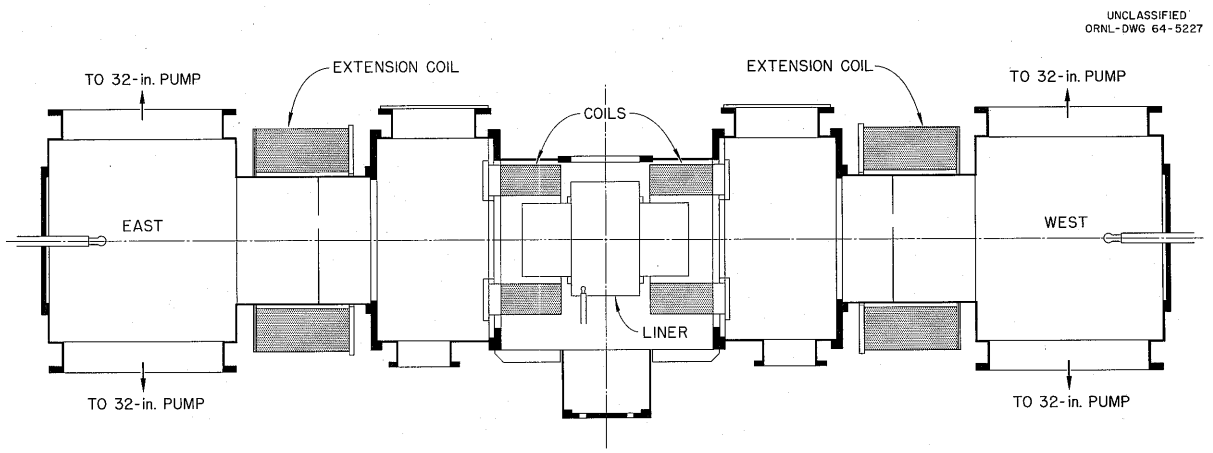

Fig. 10.5. Diagram of DCX-1 Vacuum System. The cleaning by electron bombardment was done in the end sections.

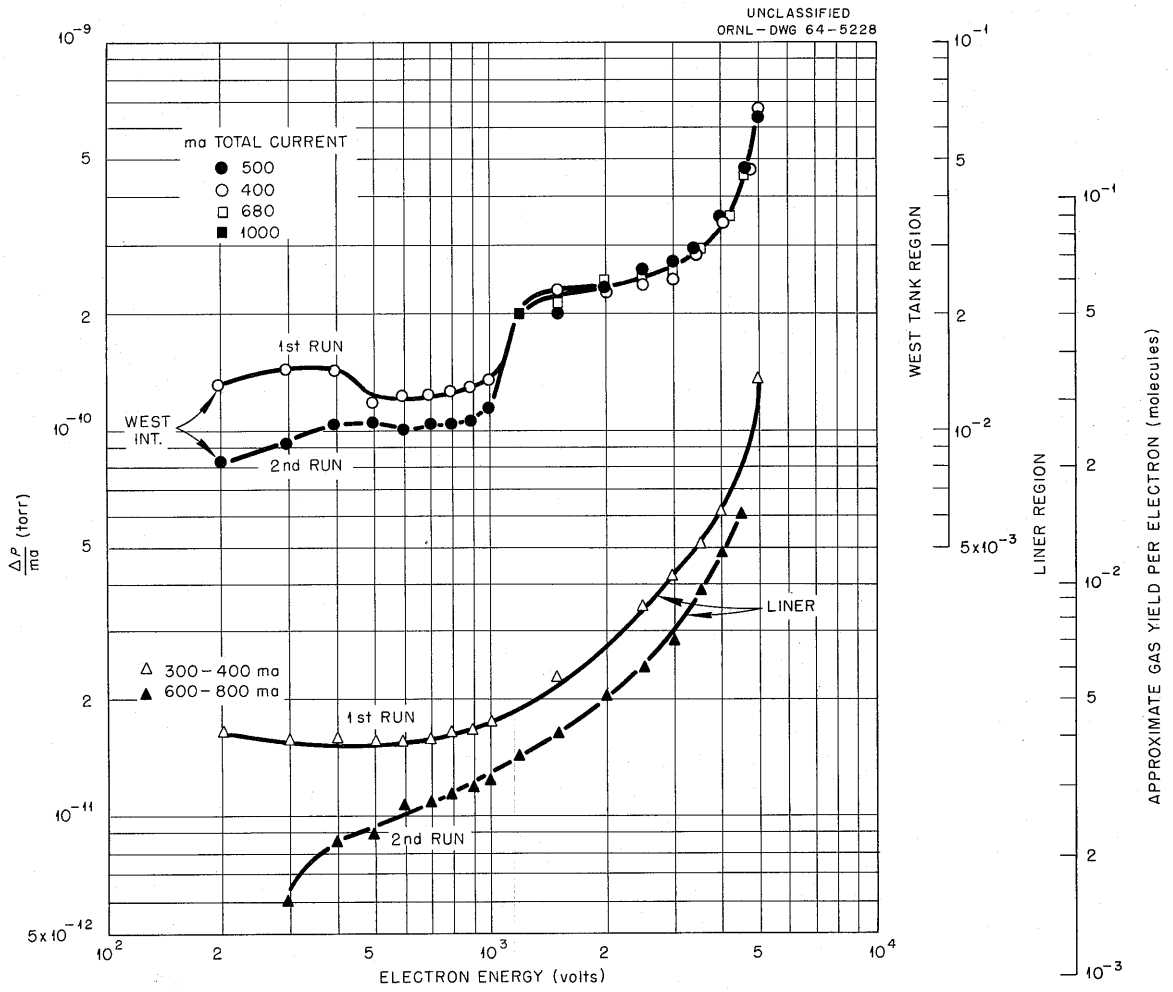

Fig. 10.6. Normalized Pressure Increase Under Electron Bombardment in DCX-1 Plotted as a Function of Electron Energy.

as the result of electron bombardment the plasma containment times inside the liner increased substantially over those normally obtained under similar conditions. Because of the complexity of DCX-1 it is not possible to attribute the improvement in containment time to the effect of electron bombardment with confidence, but it is reasonable to assume that the electron cleaning reduced the influx of hydrocarbons reaching the plasma region thereby producing improvement in containment time.

Figure 10.6 shows the yield vs voltage curve for electron bombardment in the west tank region and in the liner region. These curves were obtained with the system at room temperature after a 12-hr bake at 400°C and several hours of electron bombardment during the bake. The estimated total flux was 10^{16} to 10^{18} 3.5-kev electrons/cm^2.

Electron sources have now been added to the east tank regions and the liner. All filaments are 0.020 tungsten wire, which are heated to emission temperature by direct resistance. The first test was limited to 5 kv and 1 amp due to the high-voltage power supplies. A supply is now available which is rated at 20 kv and 10 amp. The effect of the use of the additional electron sources and higher voltages on base pressure and containment times has not yet been determined. Future plans are to continue these curves to the 20-kv range.

10.3 OFFGASSING OF SURFACES IN HIGH-VACUUM SYSTEMS

D. M. Richardson[10] R. A. Strehlow[10]

A continuing program of research is devoted to chemical factors affecting the achievement of low pressures in thermonuclear systems. The slow offgassing of high-molecular-weight organic compounds is well known to be one of the principal factors limiting the attainment of base or "equilibrium" pressures in practical vacuum systems. Cold surfaces, adsorbents of high surface area, thermal decomposition, and, most commonly, heating or baking the vacuum chamber have been used to remove nonequilibrium amounts of these substances from experimental regions of the system.

[10]Reactor Chemistry Division.

It is clear that the removal or even the detection of these materials presents many problems. The presence of organic molecules is accompanied by reactions in gages[11] yielding hydrogen, carbon oxides, methane, etc. This results in pressure measurements which are often in error by one or more orders of magnitude. The high heats of adsorption of organic molecules cause the equilibration times of connected volumes in a vacuum system to be very long[12,13] and result in an additional source of gage error.

Little detailed consideration of the surface offgassing of organic molecules has been made – attention is generally being directed to permeation and to diffusion of substances of low molecular weight. The large response times coupled with ion gage contributions and the lack of information on heats of adsorption act in concert to make offgassing studies intractable to simple interpretative techniques.

This section presents some desorption observations from 80 to 270°K, a relation between offgassing rates and heat of adsorption, and some methods which allow estimation of this heat for organic compounds.

10.3.1 Programmed Temperature Desorption

Figure 10.7 shows the results of a programmed temperature desorption from a shroud (or liner), illustrated in Fig. 10.8 and previously described.[14] The shroud (or liner) has a surface area of 6×10^4 cm^2 and a volume of 300 liters. Substances giving rise to the peaks in the pressure vs time chart were identified, on the basis of mass spectrometric scans, as including hydrocarbons up to C_4. This desorption technique is analogous to gas chromatographic desorption, which has been used[15] to identify hydrocarbons from C_5 to C_{14}; it is clear that the desorption technique can be extended, by proper design of a desorption apparatus, to

[11]Saul Dushman, *Scientific Foundations of Vacuum Techniques*, 2d ed., ed. by J. M. Lafferty, p. 328, Wiley, New York, 1962.

[12]R. A. Haefer and J. Hengevoss, *Vacuum* **13**, 123 (1963).

[13]J. Blears, *Proc. Roy. Soc. (London)* **A188**, 62 (1946).

[14]*Reactor Chem. Div. Ann. Progr. Rept. Jan. 31, 1964*, ORNL-3591, p. 241.

[15]Stephan Del Nogare and R. S. Juvet, Jr., *Gas-Liquid Chromatography*, Interscience, New York 1962.

UNCLASSIFIED
ORNL-DWG 64-5229

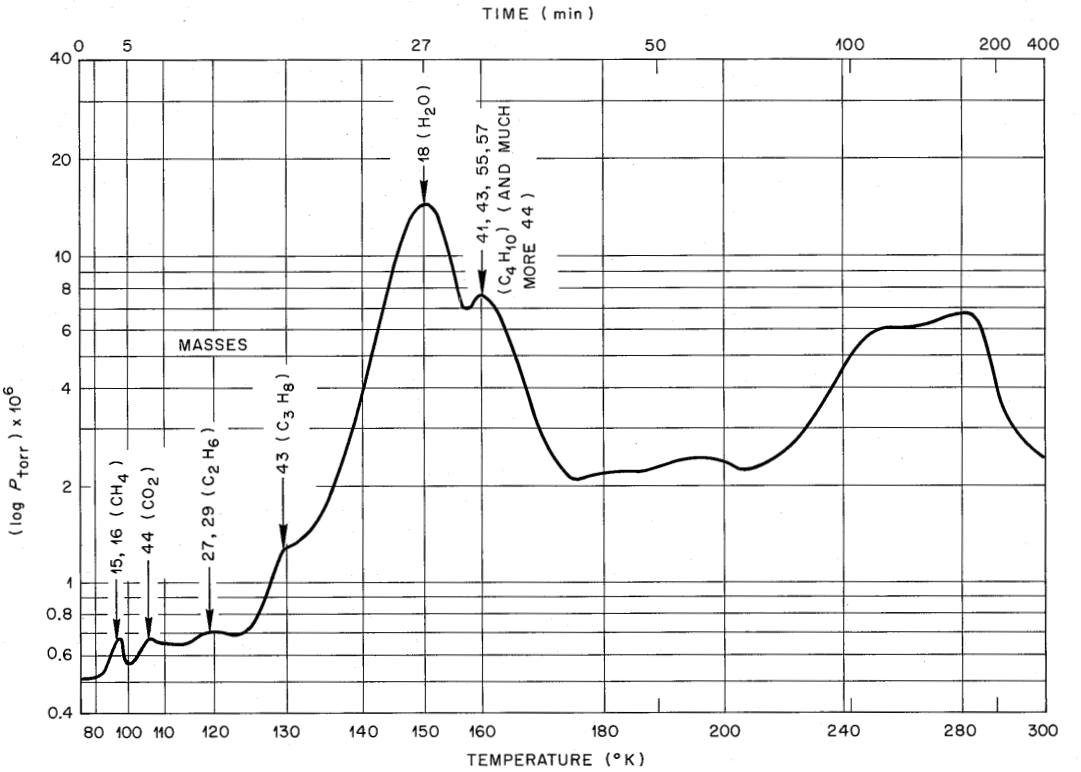

Fig. 10.7. Programmed Temperature Desorption.

UNCLASSIFIED
PHOTO 70182

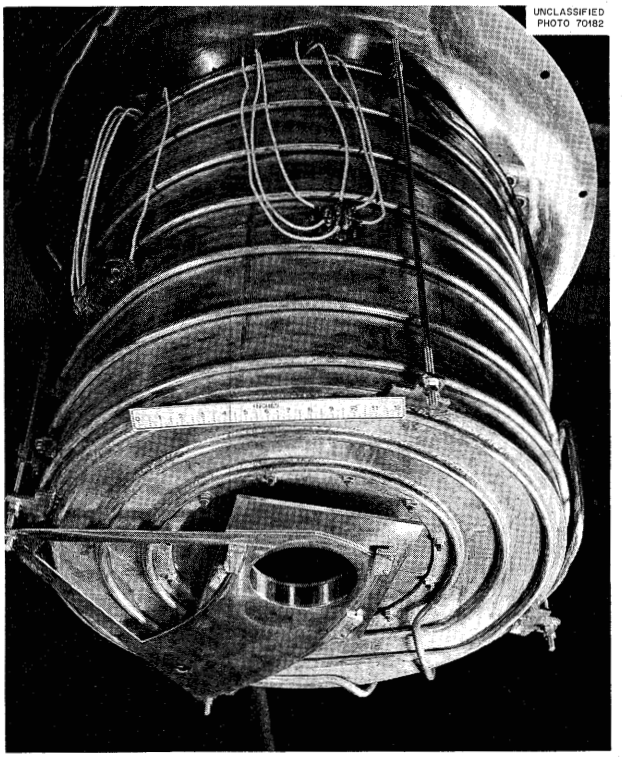

Fig. 10.8. Liner or Shroud of Vacuum System as Used for Experiments on Programmed Temperature Desorption.

the identification of the C_{18}–C_{35} hydrocarbons which are of concern in practical vacuum systems. Such identifications will be of value in the development of more effective baking procedures and in the construction of specifications for lubricants to be used in machining components for ultrahigh vacuum service.

10.3.2 A General Relation Between Molecular Flow Offgassing and Heat of Adsorption for Hydrocarbons

The rate of evaporation of high-boiling-point organic liquids is given[16] by the relation

$$G = 9.93 \times 10^2 P(MT)^{-1/2} \text{ torr-liters sec}^{-1} \text{ cm}^{-2} . \quad (1)$$

For the vaporization from a monolayer of molecules with heat of adsorption Q, the pressure in a chamber is given, via the Clapeyron-Clausius equation, by

$$\log P_{\text{torr}} = C - \frac{Q}{2.3RT} , \quad (2)$$

where a value of C was selected (based on Antoine equation constants) as 7.5 for a variety of hydrocarbons.[17]

From Eqs. (1) and (2) is obtained

$$\log G = 10.3 - \frac{1}{2} \log (MT) - \frac{Q}{4.6T} . \quad (3)$$

For the case of a hydrocarbon diffusion pump oil with $M = 450$ and $T = 300°K$ the relation simplifies to

$$\log G = 8 - \frac{Q}{4.6T} .$$

When the fraction of surface area covered, θ, is between 0.01 and unity, it may be assumed that G is proportional to θ. At lower coverage the change of Q must be taken into account.

This derived relationship, between adsorption energy and the specific offgassing rate for a single molecular species, can be used to evaluate an effective Q for offgassing data of mixtures. Further, when the system geometry and contaminants are properly characterized, it can also be used to predict the steady-state chamber outgassing rate.

10.3.3 Some Methods of Estimating the Heats of Desorption of Organic Compounds

Heat is liberated when an organic compound adsorbs on a surface (note that while Q is positive, ΔH_{ads}, the enthalpy change of the gas upon adsorption, is negative). When hydrogen bonding and permanent dipole interaction are not large, the physical properties of a compound are predominantly determined by Van der Waals forces. Consequently, Q, as well as the surface tension, refractive index, heat of vaporization, and boiling and freezing points, will be strongly related to the volume and polarizability of the molecule; therefore, these properties will be related. The steric (geometric) factors determining the entropy change for desorption will, of course, be reflected in some of the physical properties. In the absence of data on heats of adsorption, methods of estimating these heats are desired to determine conditioning requirements for vacuum systems. This section includes two estimation techniques.

Table 10.1 lists $\Delta H_{\text{vaporization}}$ and heat of adsorption, Q, for several hydrocarbons, water, and argon. The experimental heats of adsorption are shown for monolayer coverage ($\theta = 1$) and for that coverage at less than one monolayer where Q reaches a maximum (at $\theta \approx 0.6$). Values of $Q_{(\theta=1)}$ calculated from the Lennard-Jones potential function are also listed.

Table 10.2 shows the near proportionality of ΔH_v and Q at $\theta \approx 0.6$. Compared with the normal hydrocarbons containing more than four carbon atoms, the more highly branched and the less symmetric compounds (Nos. 6–8, 10) show greater deviation from proportionality. A proportionality factor of 1.51 appears to hold for the branched compounds (Nos. 6 and 7). Inasmuch as the mixed hydrocarbon diffusion pump oils appear to be highly branched, one might expect the factor 1.51 to be applicable. (In the work of Haefer and Hengevoss[12] such an oil with a ΔH_v of 23 kcal/mole appeared to have a Q of 36 kcal/mole. The factor of 1.51 yields 34.7 kcal/mole as an estimated adsorption heat for this oil.)

[16] Saul Dushman, *op. cit.*, p. 18.

[17] *Physical Properties of Chemical Compounds* ("Advances in Chemistry Series," No. 22), Am. Chem. Soc., 1955.

Table 10.1. Values for Heats of Adsorption Q of Some Hydrocarbons, Water, and Argon

	Substance	Formula	ΔH_v (338°K)[a]	Exptl $Q_{(\theta=1)}$	Calcd[b] $Q_{(\theta=1)}$	Exptl $Q_{(\theta\approx0.6)}$
1	*n*-Butane	C_4H_{10}	5.04	7.2[c]	7.0	8.8[d]
2	*n*-Pentane	C_5H_{12}	6.31	8.4[e]	8.5	10.0[e]
3	*n*-Hexane	C_6H_{14}	7.54	10.2[e]	10.0	12.1[e]
4	*n*-Heptane	C_7H_{16}	8.78	11.2[e]	11.6	14.0[e]
5	*n*-Octane	C_8H_{18}	9.92	12.8[e]	13.2	16.0[e]
6	Neohexane	2,2-Dimethyl-butane	6.61	9.6[e]	8.2	10.0[e]
7	Isooctane	2,2,4-Trimethyl-pentane	8.39	11.3[e]	11.5	12.7[e]
8	Cyclopentane	C_5H_{10}	6.82	8.4[c]	6.7	8.9[e]
9	Butene-1	C_4H_8	4.87	7.3[c]	6.2	8.4[d]
10	Benzene	C_6H_6	8.80	9.4[d,f]	8.5	10.0[e] 12.6[f]
11	Water	H_2O	10.5	10.8[e] 11.4[g]		11.4[h]
12	Argon	Ar	1.6 (87°K)	2.3[i]	2.1	2.8[j] 3.1[k]
13	Methane	CH_4	2.1 (83°K)	3.4[c]		4.3[j]
14	Carbon dioxide	CO_2		(6.0, estd)		(7.6)

[a] *Physical Properties of Chemical Compounds* ("Advances in Chemistry Series," No. 22), Am. Chem. Soc., 1959.

[b] By Kiselev (ref. e) from Lennard-Jones potential function.

[c] Estimated from column 6 (94% for cyclic hydrocarbons, 81% for straight-chain paraffins).

[d] Beebe *et al.*, *J. Am. Chem. Soc.* **69**, 2294 (1947).

[e] A. V. Kiselev, "Energy of Adsorption Forces and Heat of Adsorption of Hydrocarbons on Carbon Black," pp. 168–78 in *Proc. Intern. Congr. Surface Activity, 2d, London, 1957*, Academic, New York, 1957.

[f] S. J. Gregg and K. H. Wheatley, "The Heat and the Entropy of Adsorption of Benzene Vapour on Alumina," pp. 102–12 in *Proc. Intern. Congr. Surface Activity, 2d, London, 1957*, Academic, New York, 1957.

[g] N. N. Avgul, O. N. Dzhigit, and A. V. Kiselev, "On the Possibility of Calculating the Heat of Adsorption of Methanol on Carbon Black According to the Additive Scheme," pp. 226–27 in *Proc. Intern. Congr. Surface Activity, 2d, London, 1957*, Academic, New York, 1957.

[h] J. Coolidge, *J. Am. Chem. Soc.* **49**, 708 (1927); Stephen Brunauer, *The Adsorption of Gases and Vapors*, vol 1, p. 224, Princeton University Press, 1943.

[i] J. G. Aston and J. Greyson, "Theory of Heats of Adsorption on a Uniform Surface," pp. 39–45 in *Proc. Intern. Congr. Surface Activity, 2d, London, 1957*, Academic, New York, 1957.

[j] D. M. Richardson and R. A. Strehlow, *Trans. Natl. Vacuum Symp.*, vol. 10, Pergamon, 1964 (reported for molybdenum surface).

[k] R. A. Beebe and D. M. Young, *J. Phys. Chem.* **58**, 93 (1954).

Table 10.2. Test of Proportionality of ΔH_v and $Q_{(\theta \approx 0.6)}$

Substance[a]	$1.6\ \Delta H_v$	Exptl $Q_{(\theta \approx 0.6)}$
1	8.01	8.8
2	10.1	10.0
3	12.1	12.1
4	14.1	14.0
5	16.0	16.0
6	10.6	10.0
7	13.5	12.7
8	11.0	8.9
9	7.8	8.4
10	14.1	10.0, 12.6
11	17.1	11.4
12	2.6	3.1
13	3.4	4.3

[a]As numbered in Table 10.1.

Table 10.3 shows an even better correlation with $Q_{(\theta=1)}$ of the quantity $\Delta H_v + E_s$,[18] where

$$E_s = N\left(\frac{M}{N\rho}\right)^{2/3}\left(\gamma - T\frac{d\gamma}{dT}\right)2.4 \times 10^{-11}\ \text{kcal/mole},$$

where:

E_s = molar surface energy of a monolayer,
γ = surface tension (dynes/cm),
T = temperature (°K),
M = molecular weight (g/mole),
N = Avogadro's number, and
ρ = density (g/cm^3).

It should be noted that this quantity differs by the factor $N^{1/3}$ from the total surface energy of a molar volume, which is frequently called the total

[18]J. J. Bikerman, *Surface Chemistry, Theory and Applications*, 2d ed., p. 57, Academic Press, New York, 1958.

Table 10.3. Correlation of Surface Energy and Heats of Vaporization with Adsorption Heats[a]

Substance[b]	$\gamma_{293°K}\left(\frac{\text{dynes}}{\text{cm}}\right)$	$-\frac{d\gamma}{dT}$	$\gamma - 293\frac{d\gamma}{dT}$	$\left(\frac{M}{P}\right)_{293°K}$	$\left(\frac{M}{P}\right)^{2/3}_{293°K}$	Calcd $E_{s;\theta=1}$	$\Delta H_v + E_s$	Exptl $Q_{\theta=1}$
1	18.43	0.121	53.9	100.6	21.7	2.36	7.40	(7.2)
2	16.00	0.105	46.8	115.0	23.6	2.23	8.54	8.4
3	18.42	0.105	49.2	131.4	25.8	2.56	10.10	10.2
4	19.29	0.096	47.4	146.6	27.8	2.66	11.44	11.2
5	21.76	0.100	51.1	162.5	29.8	3.08	13.00	12.8
6	16.30	0.100	45.6	133.5	26.2	2.41	9.02	9.6
7	18.77	0.089	44.9	165.2	30.2	3.00	11.39	11.3
8	21.77	0.121	57.3	94.1	20.75	2.37	9.19	(8.4)
9	12.50	0.122	48.3	94.2	20.76	2.02	6.89	(7.3)
10	28.88	0.141	70.2	88.9	19.8	2.81	11.61	9.4
11[c]	72.75	0.152	117.25	18	6.86	1.63	12.13	10.8 11.4[d]
12			35[e]	28(78°K)	9.2	0.65	2.25	2.3
13	(20)(83°K)	(~0.22)	(38)(83°K)	36(78°K)	(11)	(0.9)	(3.0)	(3.4)

[a]Except where indicated, values for $P_{293°K}$, $\gamma_{293°K}$ are from *Physical Properties of Chemical Compounds* ("Advances in Chemistry Series," No. 22), Am. Chem. Soc., 1959.

[b]As numbered in Table 10.1.

[c]*Handbook of Chemistry and Physics*, Chemical Rubber Publishing Co., 1962.

[d]No data on adsorption in the absence of surface oxides has been found, but one should expect the heat of adsorption to be somewhat less than the value given.

[e]Baly and Donnan, *J. Chem. Soc.* **81**, 907 (1902) as given in Hirschfelder, Curtiss, and Bird, *Molecular Theory of Liquids and Gases*, p. 353, Wiley, New York, 1954.

molar surface energy.[19] [Since the minimum in the differential entropy change for adsorption occurs at θ near unity for the more symmetric molecules (1–5, 8, 9, and 10) and is not pronounced for the planar benzene and cyclopentane (8 and 10), $Q_{(\theta \approx 0.6)}$ should be expected to be larger than $Q_{(\theta=1)}$ for compounds 1–5 and 9 than for compounds 6–8 and 10, as is observed.]

In summary, two correlations have been described between heats of adsorption and physical properties of organic compounds. These considerations should allow criteria to be established for selection of lubricants used in construction of vacuum equipment and vacuum pump oils, and should aid in the specification of conditioning requirements for vacuum systems.

10.4 ELECTRON BOMBARDMENT OF OIL-COVERED VACUUM SYSTEM SURFACES IN THE ULTRAHIGH VACUUM TEST FACILITY

D. M. Richardson[10] R. A. Strehlow[10]

Recent work on molecular desorption accompanying electron bombardment has led to application of the technique to the DCX-1 apparatus.[20] An exploratory study has also been conducted in the ultrahigh vacuum test facility[21] with conditions such that the system was contaminated with the common diffusion pump oil bis-2-ethylhexyl phthalate. A mixed hydrocarbon pump oil was used in the diffusion pump, and the trap was cooled with liquid nitrogen. A mass spectrometer was connected to the vacuum system by a tubulation ($1\frac{5}{8}$ in. OD, 16 in. long) with the open end about 10 in. from the 6-in.-diam orifice to the shroud.

The initial spectrometer data from the contaminated system are listed in Table 10.4, where one unit of peak height corresponds to a pressure of about 3×10^{-9} torr. While this and other spectra listed were being taken, there were no ion gages in operation. This spectrum was identical with that of bis-2-ethylhexyl phthalate[22] (except for higher background water peaks, m/e 17 and 18, in the present work and a higher m/e 28 peak in the reference spectra, attributable to ion gage reactions, and a general lower sensitivity at high m/e for the present work).

The pattern change produced by electron bombardment of the inner surface of the shroud with 6 ma at 400 v from a 3-cm^2 thoriated-iridium filament is also shown in Table 10.4. The peak heights at m/e 72, 44, 30, and 2 were markedly increased as were most of the peaks corresponding to hydrocarbons of low molecular weight. The actual relative yield of low-molecular-weight hydrocarbons in the shroud was undoubtedly less than observed due to the bias caused by their smaller heats of adsorption. The source of the peak at m/e 72 was tentatively identified as butanal.

Operation of a 30-cm^2 tungsten filament inside the shroud at 2 kw (265 amp, 7.6 v) produced the different changes of pattern shown in Table 10.4. The predominant yield from the hot filament was carbon monoxide and hydrogen. The presence of some methane, ethylene, and ethane was also indicated.

The marked differences in the spectra produced by electron bombardment and by the hot filament are believed to show there was primarily ionization with resulting fragmentation of molecules adsorbed on the wall in the former case, and that there was primarily pyrolysis and filament reaction in the latter case. In both cases the water peaks actually decreased and indicate that the yields of carbon oxides were determined in part by the water partial pressure.

The effect of electron energy on gas yields was found to be a maximum at about 400 v. Since the observed gas-yield–electron-energy relations were similar to reported yields of secondary electrons from metals[23] it is possible that secondary wall electrons were a significant factor.

Electron bombardment of the shroud inner wall was used to follow the progress of a baking cycle. The hot filament was operated continuously for a number of hours, raising the shroud temperature to 270°C, then the shroud was cooled with compressed air. During this period the electron emission filament was intermittently operated at 6 ma and 400 v to show the course of wall cleanup. The total gas yield due to electron bombardment was about 100 times smaller after the bake than initially. The shroud contamination indicated by

[19] Samuel Glasstone, *Textbook of Physical Chemistry*, 2d ed., p. 494, Van Nostrand, Princeton, N.J., 1959.

[20] R. E. Clausing, this report, sect. 10.1; E. R. Wells, this report, sect. 10.2.

[21] *Thermonuclear Div. Semiann. Progr. Rept. Apr. 30, 1963*, ORNL-3472, p. 107.

[22] Klaus Biemann, *Mass Spectrometry, Organic Chemical Applications*, p. 170, McGraw-Hill, New York, 1962.

Table 10.4. Spectrometer Patterns from UHV Facility

(Contaminated with Bis-2-ethylhexyl Phthalate)

m/e	Peak Heights: Initial Spectrum	Increase Due to Bombardment	Increase Due to Hot Filament	m/e	Peak Heights: Initial Spectrum	Increase Due to Bombardment	Increase Due to Hot Filament
1	8	10	40	41	40	175	25
2	2	70	400	42	8	60	10
12	0	10	10	43	42	150	10
14	0	15	5	44	6	115	15
15	0	40	15	50	6	5	0
16	0	30	10	55	27	110	30
18	21	−10	−10	56	17	70	5
26	2	55	20	57	54	180	5
27	15	130	30	67	5	5	0
28	14	215	300	69	12	25	0
29	27	150	20	70	30	60	10
30	0	40	0	71	31	30	0
39	9	65	10	72	5	55	0
				149	77	0	0

m/e 72, 44, and 30 was so small as to be undetectable before the temperature had risen to 260°C.

In summary it was found that electron bombardment of surfaces covered by a contaminating oil produced fragment molecules which desorbed readily and thereby provided a diagnostic technique for assessing surface cleanliness. For the contaminant studied the products from a hot filament were readily distinguishable from those produced by electron bombardment.

10.5 USE OF ION GAGE GRID DEGASSING EFFECTS TO ASSESS SURFACE CLEANLINESS

R. A. Strehlow[10]

The work reported earlier[24,25] on tentative interpretations of the behavior of nude ion gages when the grid structure is heated has been extended to a test performed in the shroud of the ultrahigh vacuum test facility.

The method used was simply to degas the grid structure by passing a current of several amperes through it in the usual way with the exception that the filament was turned off and the electrometer sensitivity was increased. The electrometer output is a measure of positive ion flow to the gage collector and for an oil-contaminated system may be greater than 10^{-7} amp initially, but falling rapidly to a steady value of perhaps 5×10^{-9} amp.

After a baking cycle had been conducted on the shroud and the surface contamination had been reduced to a negligible value, as indicated by the electron bombardment method, application of the degassing technique gave an initial current of less than 10^{-10} amp. This appears to verify the conclusions reached earlier about the significance of these observations. Tubulated gage behavior, of course, differs markedly.

10.6 LITHIUM ION EMISSION FROM β-EUCRYPTITE

R. A. Strehlow[10] J. D. Redman[10]

The synthetic silicate $LiAlSiO_4$ (β-eucryptite) yields lithium ions when heated, which are used

[23] H. S. W. Massey and E. H. S. Burhop, *Electronic and Ionic Impact Phenomena*, p. 306, Oxford Univ. Press, London, 1952.

[24] *Reactor Chem. Div. Ann. Progr. Rept. Jan. 31, 1964*, ORNL-3591, p. 247.

[25] *Thermonuclear Div. Semiann. Progr. Rept. Oct. 31, 1963*, ORNL-3564, pp. 126–29.

as a diagnostic tool for plasma research. A brief study was made of the mass spectra of emitted ions in order to determine the most suitable filament for this application and to assess the purity of the produced ions. An adaptation was made of the high-temperature (1000°C) sample inlet system of a Bendix time-of-flight mass spectrometer to allow insertion of a filament into the volume in which electron bombardment ionization is usually accomplished. A rectified power supply was assembled to operate the filament with dc heating. Tantalum, tungsten, and platinum were studied both as bare filaments and when loaded with the silicate. The spectra obtained led to the general conclusions that:

(1) sodium and potassium ions were emitted by the three metals, with platinum yielding significantly less of these species than either tungsten or tantalum,
(2) the yield of alkali metal ions from the hot platinum filament decreased rapidly, indicating surface rather than bulk contamination,
(3) the filaments, when loaded with the silicate, yielded ions characteristic of the bare filament in substantially the same amounts in addition to masses 7 and 14; mass 14 did not appear to be related to mass 28 and was, therefore, tentatively identified as Li_2^+ rather than as N^+,
(4) platinum is recommended as the best of the three metals studied for this application,
(5) the presence of a peak at mass 30 possibly indicates the presence of Li_2O^+ or $LiNa^+$.

No analysis was made of the electron or neutral-atom emission of the silicate-loaded filaments. The mechanism for the ion emission has not been established, but nude gage degassing effects (Sect. 10.5) appear to involve a closely related process.

11. Design and Engineering: Notes

11.1 FRICTION FACTORS FOR CURVED HOLLOW COPPER CONDUCTORS

J. Lewin

An investigation was conducted of friction factors for water flowing in both straight and 360° curved copper conductors. The objectives of this work were the following:

1. to establish the relative roughness of one channel cross section used in some magnet coils by comparison of the data with the Moody curves,[1]
2. to establish the effects, if any, of a 360° looping of the conductor at various ratios of loop diameter to passage diameter,
3. to compare the results with data of Ito[2] and Beij[3] on effects of curvature of pipes.

The results indicate that the effects of 360° curvature are negligible above a D/d ratio of 100, and that hollow copper conductors with longitudinal grooves exhibit relative[1] roughness of between 0.001 and 0.003.

Description of Conductor, Samples, and Test Procedure. – The conductor chosen for these tests has a nominal $^9/_{16} \times {}^9/_{16}$ in. cross section with a nominal 0.30-in.-diam channel with four grooves, as shown in Fig. 11.1. Although under examination at 80X magnification the circular surfaces of the conductor appear to be as smooth as normal drawn copper tubing, there is some roughness in the four grooves; the question therefore arises as to the effect of the grooves on the fluid flow characteristics of the conductor.

Samples of the conductor were cut to the lengths and radii indicated in Fig. 11.2. Piezometer fittings were fabricated out of standard tees and were reamed through carefully to the same diameter as the conductor channel. Mercury manometers and bourdon gages were used for pressure measurement and in the overlapping range of pressures were used to check each other.

The water used in the tests was demineralized and at a header pressure of about 230 psi. The

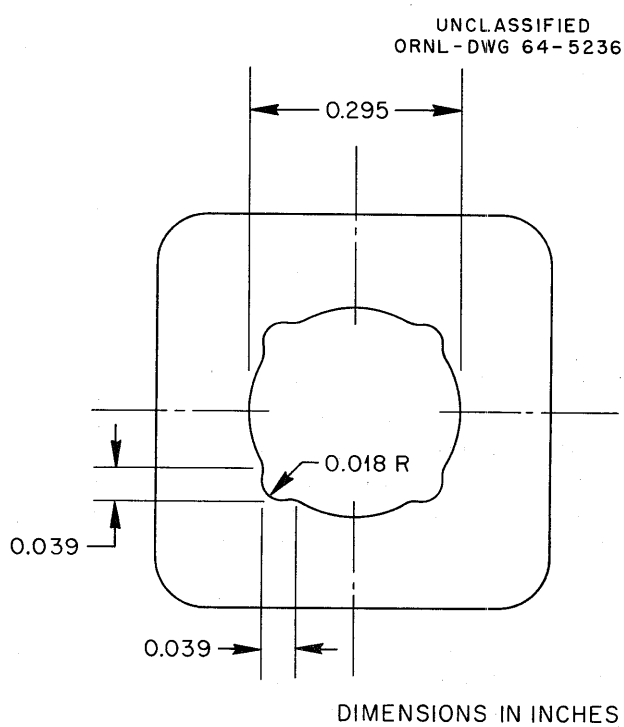

Fig. 11.1. Conductor with a Nominal $^9/_{16} \times {}^9/_{16}$ in. Cross Section with a Nominal 0.30-in.-diam Channel with Four Grooves.

[1] L. F. Moody, *Trans. ASME* **66**, 671–85 (1944).

[2] H. Ito, *Trans. ASME, Ser. D: J. Basic Eng.* **81**, 123–34 (1959).

[3] K. H. Beij, *J. Research Natl. Bur. Standards* **21**, 1 (1938).

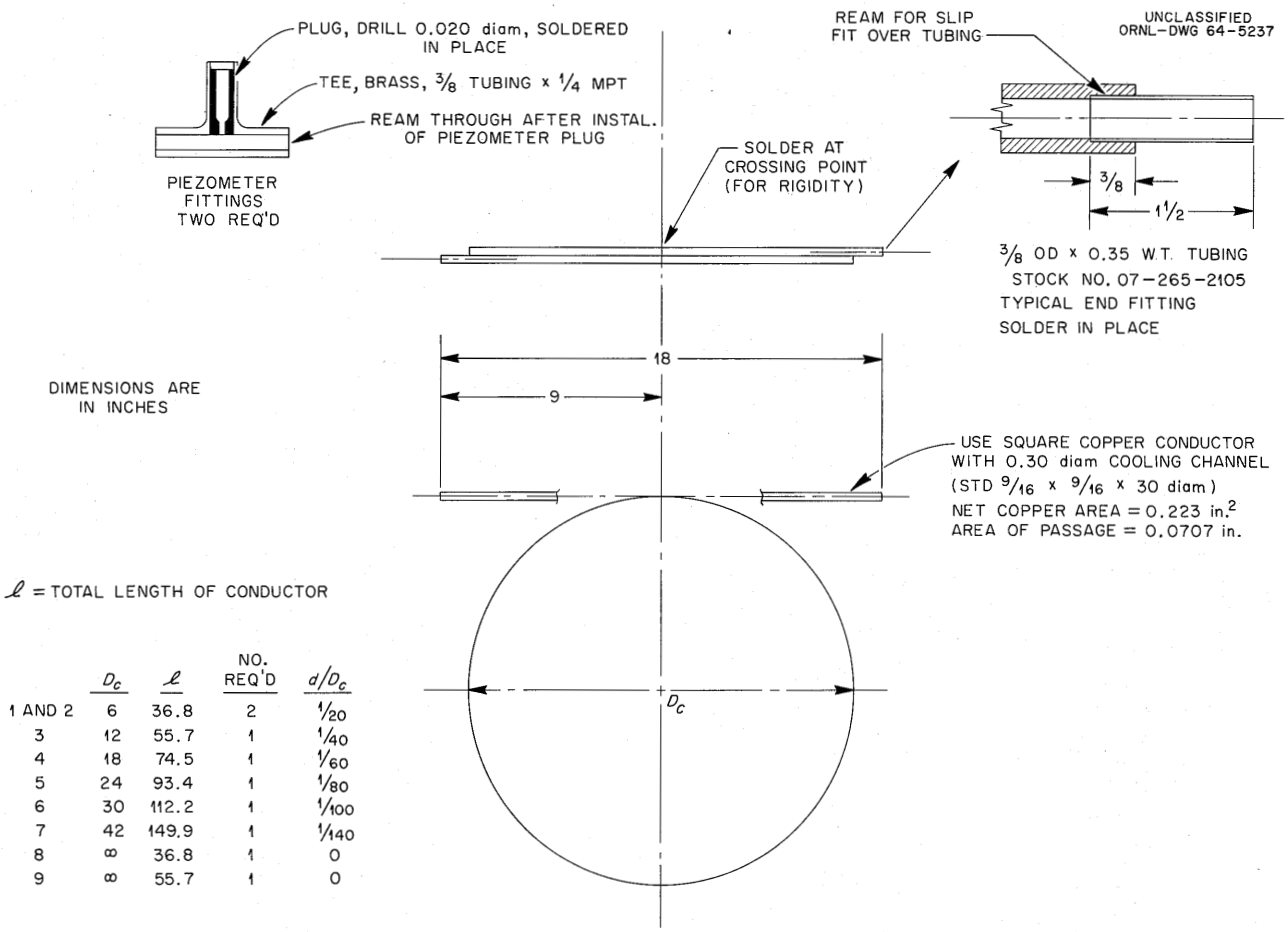

	D_c	ℓ	NO. REQ'D	d/D_c
1 AND 2	6	36.8	2	1/20
3	12	55.7	1	1/40
4	18	74.5	1	1/60
5	24	93.4	1	1/80
6	30	112.2	1	1/100
7	42	149.9	1	1/140
8	∞	36.8	1	0
9	∞	55.7	1	0

Fig. 11.2. Pressure Drop Tests.

piezometer fittings were mounted at entrance and exit of the conductor under test so that only pertinent pressure drop was measured. The entrance valving and piping was such that the flow corresponded to the "disturbed" flow condition in Ito's work.[2] This is the entrance condition for most magnets used in this Division.

From the exit piezometer fitting, the water passed through a rotameter, then to a weighing barrel, in which temperature was again read on a mercury thermometer. The readings of the rotameter were checked against the indications of the weighing barrel.

The time of flow was measured by a stopwatch that was started and stopped in synchronism with the opening and closing of the solenoid valve that opened and closed the water circuit at the header.

Discussion of Results. – The friction factor was calculated from the well-known equation for static head loss in pipe:

$$f = \Delta H \frac{D}{L} \frac{2g}{V^2} .$$

The velocity, V, was calculated as an average velocity on the basis of the nominal cross-sectional area of the channel. The results are plotted on Figs. 11.3, 11.4, and 11.5 vs Reynolds number.

Figure 11.6 shows the ratio of friction factors of curved conductors to the friction factor 0.025, exhibited by the straight conductor 8, all taken at a Reynolds number of 60,000. Beij[3] presented his results for 90° bends in the form of a bend coefficient:

$$\eta = \frac{\Delta H_{\text{total}} - \Delta H_{\text{straight}}}{V^2/2g} = (f_{\text{curved}} - f_{\text{straight}}) \frac{L}{D} .$$

He interpreted his results as indicating independence of Reynolds number for the value of η. In addition, his results and the results of others indicated an initial drop of the value of η with increasing D/d, then an increase, followed by a decrease again toward zero. The values of η obtained in this test at $R = 6 \times 10^4$ and 3×10^4 are shown in Fig. 11.7 and indicate a higher value of η for 360° bends than for the 90° bends. In addition, the point of maximum bend coefficient is displaced in the direction of higher D/d.

In Fig. 11.4 are shown the curves of friction factor vs Reynolds number for conductors 1 and 2 of diameter ratio 20 and for conductor 3, diameter ratio 40, together with data by Ito[2] for comparable curvatures. The comparatively greater tendency

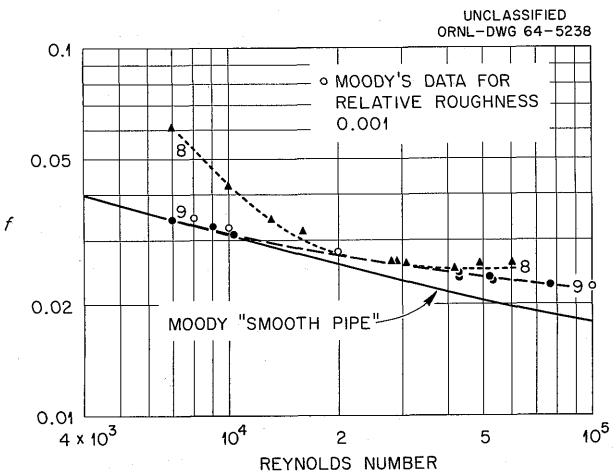

Fig. 11.3. Friction Factor vs Reynolds Number for Straight Conductors 8 and 9 Compared with Moody's Smooth Pipe Data.

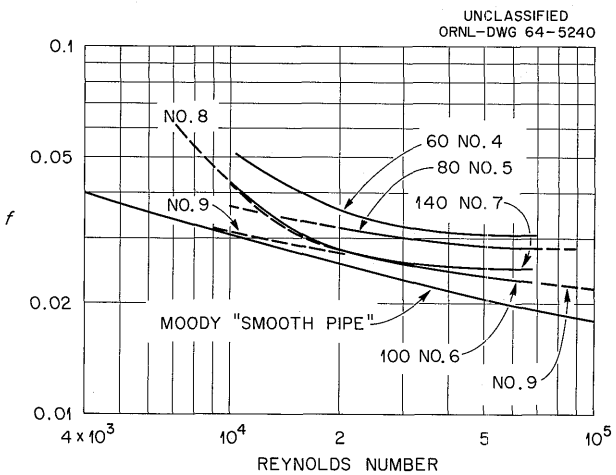

Fig. 11.5. Friction Factor vs Reynolds Number for Curved Conductors 4, 5, 6, and 7.

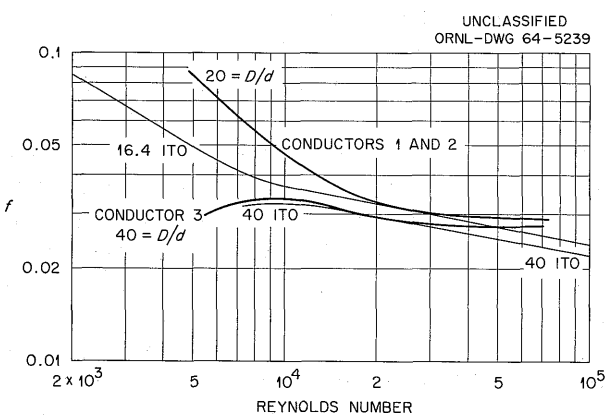

Fig. 11.4. Friction Factor vs Reynolds Number for Curved Conductors 1, 2, and 3, Compared with Data from Ito (ref. 2) for Comparable Ratios of D/d.

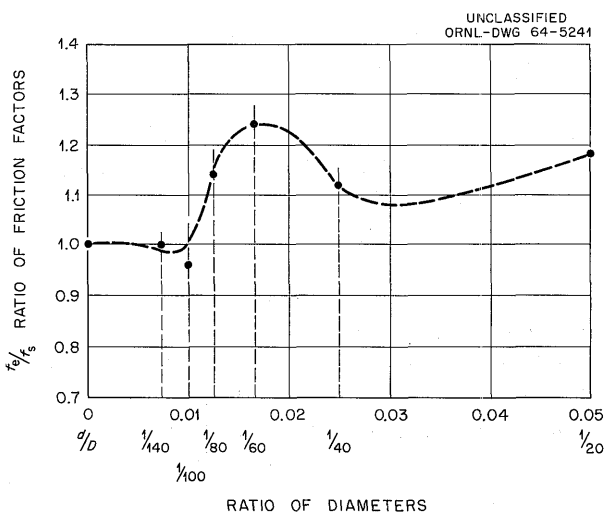

Fig. 11.6. Ratio of Friction Factors of Curved Conductors to Friction Factors of Straight Conductors vs Diameter Ratio at Reynolds Number = 6×10^4.

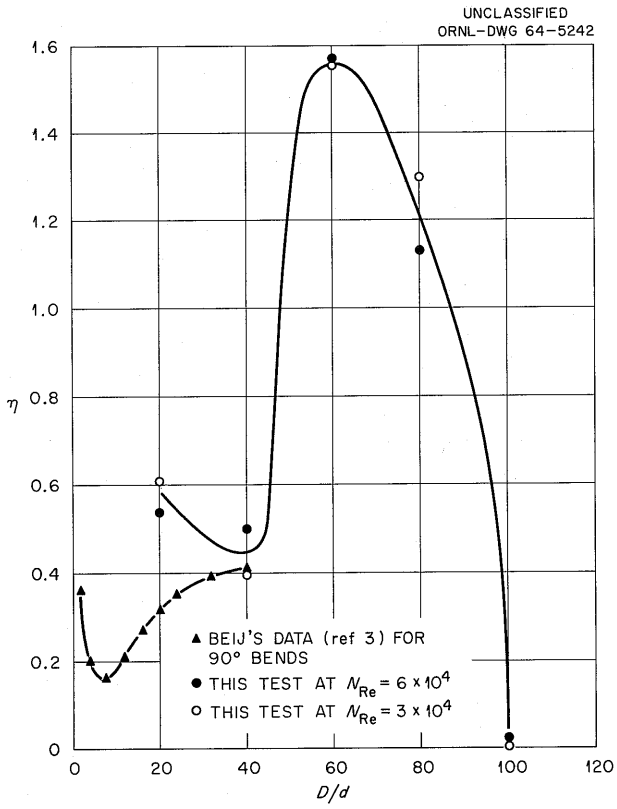

Fig. 11.7. Bend Coefficients.

of our conductors to show independence of Reynolds number with increasing flow rates again indicates an internal roughness greater than that of ordinary smooth-drawn copper tubing having a purely circular cross section.

Figure 11.5 shows the results for the other curved conductors, with the curves for straight conductors 8 and 9 also indicated. The curves for conductors 6 (D/d = 100) and 7 (D/d = 140) coincide below a Reynolds number of 30,000; above that flow rate, conductor 6 shows the same friction factors as straight conductor 9, but conductor 7 is more nearly in agreement with conductor 8.

Not all the data points are shown in the curves of Figs. 11.3, 11.4, and 11.5, and the reproducibility of the curves was checked satisfactorily in each case.

A comparison of this data with the curves of Hayes and Williams, widely used in this Division, shows essentially complete agreement for 0.30-in.-ID channels for the case of 50°F water temperature and the curvature of conductor 7 (D/d = 140), which in turn is essentially identical with the results obtained from straight conductor 8.

11.2 CONSIDERATIONS OF ENGINEERING IMPLICATIONS OF PROPOSED THERMONUCLEAR REACTORS

J. Lewin

We are continuing a survey of proposed thermonuclear reactor systems and their implications from an engineering viewpoint. The work of Impink[4] and of Homeyer[5] provides a basis for estimating heat power densities that would be available under various conditions in a blanket based on a molybdenum first wall and an LiF-BeF_2 fused salt. For a finite cylindrical source geometry with negligible self-attenuation, as would be the case for fusion neutrons, the neutron-current distribution falling on the first wall becomes strongly peaked. Blizard[6] gives the expression for incident flux distribution,

$$\phi = S_v(r^2/4D)[F(\theta,ut)] ,$$

where S is the volume source strength per cubic centimeter per second. The meaning of the other symbols is shown in Fig. 11.8, where the peaking of flux is also indicated.

A plasma cylinder of $r^2/4D = 2$ and having a source density of 10^{15} cm^{-3} sec^{-1} was postulated to determine what power densities and heat fluxes in the blanket this would imply. Using the radial energy deposition distribution derived by Homeyer[5] and assuming that power at any point in the blanket is directly proportional to neutron

[4]A. J. Impink, Jr., "Neutron Economy in Fusion Reactor Blanket Assemblies," Ph.D. Thesis, Department of Nuclear Engineering, MIT, 1963.

[5]W. G. Homeyer, "Thermal and Chemical Aspects of Thermonuclear Blanket Problems," Ph.D. Thesis, Department of Nuclear Engineering, MIT, 1962.

[6]E. P. Blizard, "Radiation Shielding," pp. 7-60–7-116 in *Nuclear Engineering Handbook*, ed. by Harold Etherington, McGraw-Hill, New York, 1958.

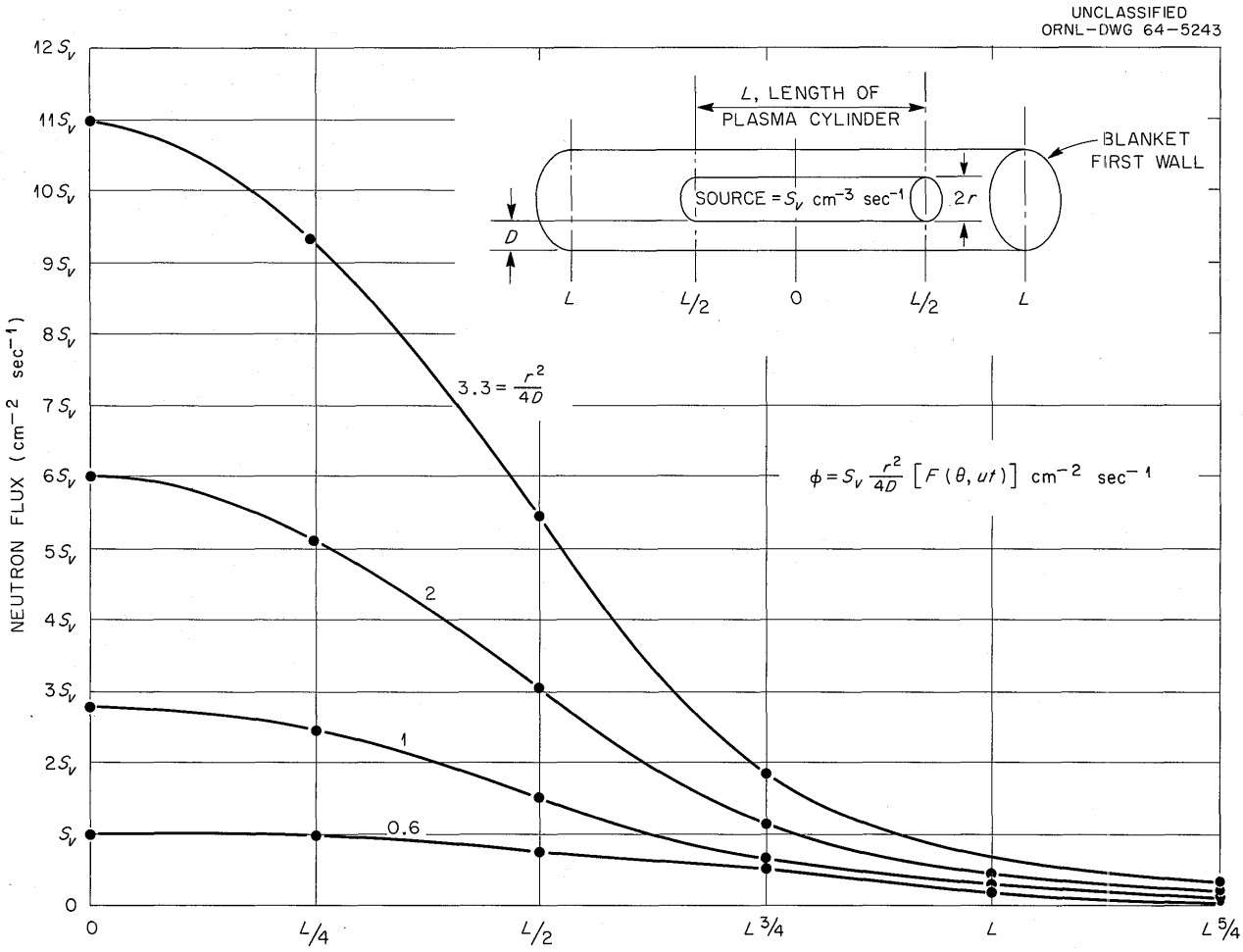

Fig. 11.8. Neutron Flux, in Terms of Source Strength, for Concentric Cylinders for Various $r^2/4D$.

current incident at the first wall, the following values were obtained:

	kw/liter
Average power density in molybdenum wall	340
Maximum power density in molybdenum wall	640
Average power density generated in first wall coolant	110
Maximum power density generated in first wall coolant	210
Average power to be removed by first wall coolant	210
Maximum power to be removed by first wall coolant	390

The maximum heat flux from the molybdenum wall to the first wall coolant then is 1.3 kw/cm^2. However, if this wall must also transfer the energy deposited by the alpha particles that are born at 3.52 Mev from the D-T reaction, plus the other charged particles born from the D-D, T-T, and ^{3}He-D reactions, it will bear an additional maximum heat flux of about 3.4 kw/cm^2, making a total of 4.7 kw/cm^2 – a rather high number, By contrast, the power densities in other parts of the blanket drop rapidly, averaging only about 16 kw/liter in the carbon and molten-salt attenuator region of the MIT blanket.

The heat flux from charged particles was arrived at simply by assuming a 10^{15} cm^{-3} sec^{-1} isotropic source of alpha particles at 3.52 Mev each.

Since the range of protons and alphas in metals is measured in thousandths of a centimeter, most of the charged-particle energy will be deposited as heat near the first wall surface. Since it appears that the charged-particle products of fusion will have to be removed from the reaction chamber, either by pulsing the magnetic field or in some other way, to prevent these fusion "ashes" from smothering the D-T fire, the effects of an intense current of charged particles on metal surfaces should be considered.

11.3 A NEW, VERSATILE VACUUM QUICK-SEAL AND VACUUM LOCK

O. D. Matlock R. L. Knight

A convenient quick-seal and vacuum lock has been developed for rapid and inexpensive installation of probes through walls in existing experimental equipment – such as the EPA and neutral-beam injection equipment. The assembly is shown schematically in Fig. 11.9.

The "quick-seal" is installed by simply drilling through the vacuum chamber wall (a $\frac{1}{2}$-in. pass hole for the $\frac{3}{8}$-in. size) and requires only an Allen wrench for assembly. Since the seal plate is floating, a certain amount of irregularity of the sealing surface can be accommodated. The vacuum valve assembly may be installed in place of the seal nut and gland as shown. Photographs of the assembly are shown in Fig. 11.10.

The valve assembly itself is shown in Fig. 11.11. It is a compact, integral valve, airlock, and pump-out system which was designed to be accommodated to the quick-seal. It has the unique feature that the gland seal at the front may be tightened after pump-out and insertion of a probe in order to isolate the volume behind, thus avoiding possible virtual leaks from this part of the assembly.

UNCLASSIFIED
ORNL-DWG 64-4049A

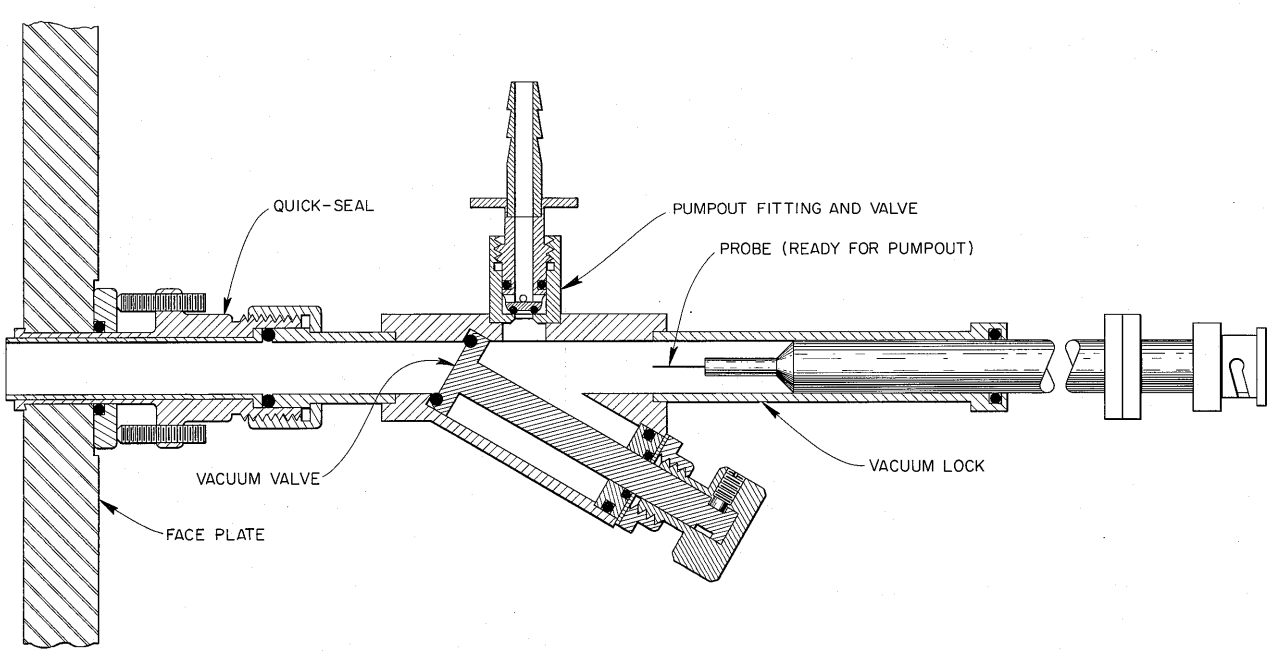

Fig. 11.9. Schematic of Quick-Seal with Vacuum Valve and Lock Assembly Attached.

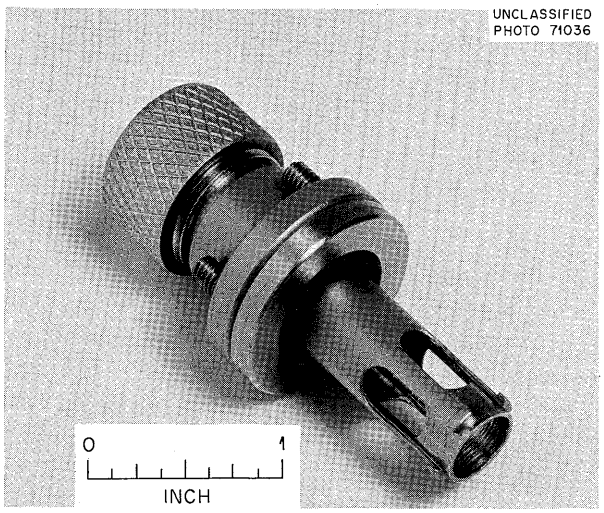

Fig. 11.10. Photograph of Quick-Seal Assembly.

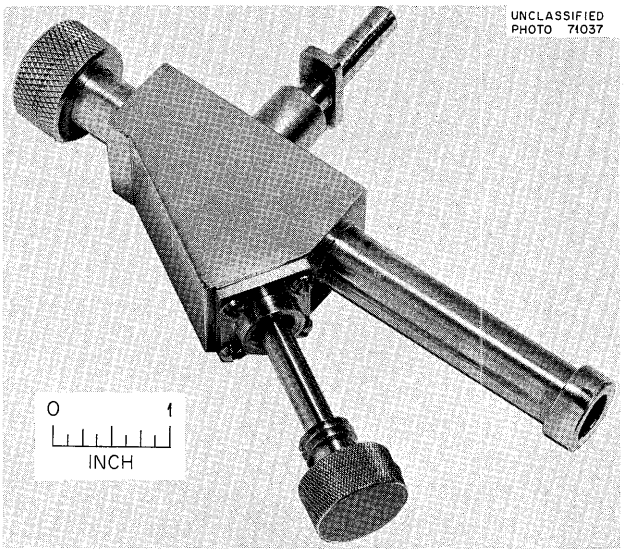

Fig. 11.11. Photograph of Vacuum Valve and Lock Assembly.

12. Design and Engineering: Service Report

J. F. Potts, Jr.

The results of the Engineering Services Group are generally reported incidentally with those of the research groups of the Thermonuclear Division. The Group executes or coordinates engineering design, shop fabrication, building operations, and maintenance for the Division.

Design activities for this reporting period are summarized as follows:

Jobs on hand 11-1-63 on which work had not started	16
New jobs received	169
Total jobs	185
Jobs completed	164
Jobs in progress	10
Backlog of jobs 4-30-64	11
Total drawings completed for period (does not include drawings for use in reports, slides, etc.)	245

Shop fabrication for this reporting period is summarized as follows:

Machine Shops

Completed jobs requiring 16 man-hours or less	179
Completed jobs requiring 17 to 1200 man-hours	169
Jobs of miscellaneous character in plating, carpenter, electrical, and millwright shops	90
Jobs by outside contractors	1
Jobs in progress	38
Average manpower (per week)	26.9

Electromagnet Fabrication

Completed jobs	3
Number of jobs in progress	1
Completed jobs by outside contractors	2
Average manpower (per week)	2

Publications, Papers, and Traveling Lecture Program

PUBLICATIONS

Author(s)	Title of Article	Journal
Igor Alexeff and W. D. Jones	Direct Measurement of Ionic Sound-Wave Velocity	*Proc. Intern. Conf. Ionization Phenomena Gases, 6th, Paris, July 8–13, 1963,* vol. III, p. 121 (1963).
W. B. Ard, A. C. England, R. A. Dandl, and R. J. Kerr[1]	Determination of Electron Density and Energy Distribution in a Very Hot Electron Plasma	*Proc. Intern. Conf. Ionization Phenomena Gases, 6th, Paris, July 8–13, 1963,* vol. IV, p. 75 (1963).
C. F. Barnett, Mozelle Rankin, and J. A. Ray	Formation of Neutral Atomic Hydrogen Beams	*Proc. Intern. Conf. Ionization Phenomena Gases, 6th, Paris, July 8–13, 1963,* vol. I, p. 63 (1963).
W. F. Gauster	Discussion on Applications of Superconducting Materials	*Proc. Inst. Elec. Engrs.* (London) **111**, 407 (1964).
W. F. Gauster	Development of Superconducting Magnets	*Electron. Power* **10**, 64 (1964).
W. F. Gauster	Magnetfelder für Experimentalle Plasmaphysik	*Physik. Bl.* **4**, 163–72 (1964).
W. F. Gauster and D. L. Coffey	Current-Carrying Capacity and Transition State of Superconducting Solenoids	*Advan. Cryog. Eng.* **9**, 316 (1964).
H. W. Graben	Relativistic Corrections to Microwave Interferometry in Plasmas	*Phys. Fluids* **6**, 1659 (1963).
C. C. Harris, P. R. Bell, J. E. Francis, Jr., M. M. Satterfield, J. C. Jordan, and J. P. Murray, Jr.	Collimators for Radioisotope Scanning	p. 25 in *Progress in Medical Radioisotope Scanning,* Proceedings of a Symposium held at Oak Ridge Institute of Nuclear Studies, Oak Ridge, Tenn., Oct. 22–26, 1962, TID-7673.

[1]Deceased.

Author(s)	Title of Article	Journal
C. C. Harris, P. R. Bell, J. E. Francis, Jr., J. C. Jordan, and M. M. Satterfield	Data Recording for Radioisotope Scanning	p. 66 in *Progress in Medical Radioisotope Scanning*, Proceedings of a Symposium held at Oak Ridge Institute of Nuclear Studies, Oak Ridge, Tenn., Oct. 22–26, 1962, TID-7673.
E. G. Harris	Ionization-Recombination Instabilities	*Proc. Intern. Conf. Ionization Phenomena Gases, 6th, Paris, July 8–13, 1963*, vol. III, p. 103 (1963).
R. J. Kerr[1]	Plasma Density Measurements with a Molecular Beam	*Nucl. Fusion* **3**, 197 (1963).
W. L. Stirling, O. D. Matlock, H. C. Hoy, and V. J. Meece	A Low-Density Plasma for Molecular Dissociation	*J. Appl. Phys.* **34**, 3466 (1963).

PAPERS PRESENTED AT SCIENTIFIC AND TECHNICAL MEETINGS

American Physical Society, Division of Plasma Physics, San Diego, Calif., Nov. 6–9, 1963

Igor Alexeff, W. D. Jones, and R. V. Neidigh, "Observations of Discharge Tube Striations Using an Image Converter."

W. B. Ard, R. A. Dandl,[1] and A. C. England, "Diamagnetic Effects of a High β Plasma."

C. F. Barnett and J. A. Ray, "Formation of Vibrationally Excited H_2^+ Ions."

C. W. Blue, N. H. Lazar, and O. D. Matlock, "High-Efficiency PIG-Type Ion Source."

R. A. Dandl,[1] H. O. Eason, A. C. England, W. B. Ard, O. D. Matlock, M. C. Becker,[1] N. H. Lazar, and H. C. Hoy, "Preliminary Results from a 50-liter Electron Cyclotron Plasma."

J. L. Dunlap, G. R. Haste, H. Postma, and L. H. Reber, "Lorentz-Force Trapping in DCX-1."

G. R. Haste, Herman Postma, and R. S. Edwards, "Electron Cyclotron Heating in DCX-1."

G. G. Kelley, P. R. Bell, J. S. Culver, S. M. DeCamp, J. C. Ezell, R. A. Gibbons, N. H. Lazar, O. B. Morgan, T. F. Rayburn, and A. J. Wyrick, "Plasma Formed by Dissociation of Molecular Ions on Arcs in DCX-2."

N. H. Lazar, P. R. Bell, J. S. Culver, S. M. DeCamp, J. C. Ezell, R. A. Gibbons, G. G. Kelley, O. B. Morgan, T. F. Rayburn, and A. J. Wyrick, "Energy Analysis of the Plasma Produced in DCX-2."

O. B. Morgan, G. G. Kelley, and R. C. Davis, "High Current 600 kv Injection."

D. Montgomery,[2] Igor Alexeff, and R. V. Neidigh, "Some Effects of a Magnetic Field on Coulomb Scattering."

R. V. Neidigh and Igor Alexeff, "Experiments with Ioffe Magnetic Fields."

---

[1]Instrument and Controls Division.

[2]Consultant, University of Maryland.

C. E. Nielsen[3] and J. L. Dunlap, "The Role of High Frequency Collective Fields in DCX-1."

J. L. Shohet[4] and R. A. Dandl,[1] "Some Microwave Cavity Electron Density Measurements in an Electron Cyclotron Resonance Heated Plasma."

W. D. Getty,[5] "High-Perveance Electron Beam–Plasma Interaction."

R. A. Gibbons and N. H. Lazar, "Deuterium Arc Flutes."

American Chemical Society, 1963 Eastern Analytical Symposium and Instrument Exhibit, New York, N.Y., Nov. 13–15, 1963

M. R. Skidmore and J. R. McNally, Jr., "A Review of Spectroscopic Studies of Energetic Ions in Steady-State Arc Plasmas."

American Association of Physicists in Medicine, Chicago, Ill., Nov. 23, 1963

C. C. Harris, D. A. Ross, M. M. Satterfield, J. C. Jordan, and P. R. Bell, "Effect of Scatter on Low Energy Gamma Ray Scanning."

Tennessee Academy of Science, Engineering Section, Nov. 29, 1963

J. F. Potts, Jr., "Engineering Aspects of the ORNL Approach in Controlled Thermonuclear Research."

Symposium on Radioactive Isotopes in Clinical Medicine and Research, Bad Gastein, Austria, Jan. 8–11, 1964

D. A. Ross, M. M. Satterfield, J. C. Jordan, C. C. Harris, and P. R. Bell, "Low-Energy Gamma Emitters in Scanning and Other Clinical Applications."

American Physical Society, New York, N.Y., Jan. 22–25, 1964

G. K. Soper[6] and E. G. Harris,[7] "The Effect of Finite Ion and Electron Temperatures on the Ion-Cyclotron Resonance Instability."

AEC Surface Physics Meeting, Germantown, Md., Jan. 30–31, 1964

J. R. McNally, Jr., "Rapid Heating of Ions by Electrons – Possible Implications to Surface Sputtering by Electrons or Photons."

R. A. Strehlow,[8] "Experimental Studies of Gaseous Desorption at Low Pressures and Liquid Nitrogen Temperatures."

A. C. England and R. A. Dandl,[1] "Insulation of a Wall by a Hot Electron Blanket."

Symposium on Scintillation Scanning in Clinical Medicine, Bowman Gray School of Medicine, Winston-Salem, N.C., Jan. 30–31, 1964

C. C. Harris, "Certain Fundamental Physical Considerations in Scanning."

1964 International Conference on Materials, American Society for Testing and Materials, Philadelphia, Pa., Feb. 3–6, 1964

J. F. Potts, Jr., "Some Materials Problems in the Construction of a Fusion Power Reactor."

---

[3]Consultant, Ohio State University.

[4]Summer participant, 1963, Johns Hopkins University.

[5]Summer participant, 1963, Massachusetts Institute of Technology.

[6]Graduate student, University of Tennessee.

[7]Consultant, University of Tennessee.

[8]Reactor Chemistry Division.

SW Chapter, Society of Nuclear Medicine, Houston, Tex., Mar. 7–8, 1964

C. C. Harris and D. A. Ross, "Window Settings for Scanning Low Energy Gamma Emitters."

Symposium on Medical Radioisotope Scanning, Athens, Greece, Apr. 20–24, 1964

C. C. Harris, P. R. Bell, M. M. Satterfield, J. C. Jordan, and D. A. Ross, "Analysis of Scan Records with a Recording Densitometer – the 'Re-Scanner'."

C. C. Harris, P. R. Bell, M. M. Satterfield, and J. C. Jordan, "The Design and Performance of a Large High Resolution Focusing Collimator."

American Physical Society, Washington, D.C., Apr. 27–30, 1964

Igor Alexeff and R. V. Neidigh, "A Possible Source of the Energetic Ions Emitted from the Pressure Gradient Arc."

P. R. Bell, G. G. Kelley, N. H. Lazar, and R. F. Stratton, "Radio-Frequency Properties of the Plasma in DCX-2."

N. H. Lazar, P. R. Bell, R. A. Gibbons, G. G. Kelley, and R. F. Stratton, "Density of Fast Protons in DCX-2."

G. G. Kelley, P. R. Bell, J. S. Culver, R. A. Gibbons, and N. H. Lazar, "Distribution of the Plasma in DCX-2."

W. D. Jones and Igor Alexeff, "The Velocity of Moving Striations in Discharge Tubes as a Function of Gas Pressure."

TRAVELING LECTURE PROGRAM

The Traveling Lecture Program is conducted in cooperation with the Oak Ridge Institute of Nuclear Studies as a part of the AEC's program of disseminating scientific and technical information to universities, particularly those in the South. Lectures delivered by ORNL personnel present unclassified information to university undergraduate and graduate students and members of the faculty. The lectures serve to stimulate interest in research in the university departments and also to assist the teaching staff in expanding the scope of instruction offered under their regular curricula. Through such personal contacts, ORNL staff members are also able to observe departmental activities at the universities. Listed below are members of the Thermonuclear Division who participated in the Traveling Lecture Program during this report period.

Igor Alexeff	Vanderbilt University, Department of Chemistry, Nov. 20, 1963, "Ionic Sound Waves in Plasmas"
W. B. Ard	Virginia Polytechnic Institute, Dec. 3, 1963, "Absorption and Emission of Microwave Radiation by Hot Magnetically Confined Plasmas"
W. B. Ard	University of Alabama, Dec. 5, 1963, "Absorption and Emission of Microwave Radiation by Hot Magnetically Confined Plasmas"
W. B. Ard	Auburn University, Dec. 6, 1963, "Absorption and Emission of Microwave Radiation by Hot Magnetically Confined Plasmas"

W. B. Ard	Louisiana State University, Mar. 3, 1964, "Absorption and Emission of Microwave Radiation by Hot Magnetically Confined Plasmas"
W. B. Ard	Texas A and M University, Mar. 5, 1964, "Production of Very Hot Electron Gases by Microwave Heating"
P. R. Bell	University of Richmond, Mar. 3, 1964; Randolph-Macon College, Mar. 3, 1964, "Thermonuclear Experiments at Oak Ridge"
J. L. Dunlap	University of Virginia, Mar. 9, 1964, "The DCX-1 Thermonuclear Experiment"
W. F. Gauster	Duke University, Apr. 21, 1964, "Magnetic Fields for Controlled Thermonuclear Research"

ORNL-3652
UC-20 – Controlled Thermonuclear Processes
TID-4500 (31st ed.)

INTERNAL DISTRIBUTION

1. I. Alexeff
2. W. B. Ard
3. C. F. Barnett
4. C. O. Beasley
5. M. C. Becker
6–11. P. R. Bell
12. D. S. Billington
13. E. P. Blizard
14. C. W. Blue
15. G. E. Boyd
16. R. L. Brown
17. R. E. Clausing
18. D. L. Coffey
19. F. L. Culler
20. J. S. Culver
21. S. Cuperman
22. R. A. Dandl
23. R. C. Davis
24. S. M. DeCamp
25. J. L. Dunlap
26. H. O. Eason, Jr.
27. R. S. Edwards
28. A. C. England
29. J. C. Ezell
30. J. L. Fowler
31. T. K. Fowler
32. J. E. Francis, Jr.
33. J. H. Frye, Jr.
34. W. F. Gauster
35. R. A. Gibbons
36. J. H. Gillette
37. P. M. Griffin
38. W. R. Grimes
39. G. E. Guest
40. E. Guth
41. G. M. Haas
42. W. Halchin
43. C. C. Harris
44. G. R. Haste
45. R. E. Hill
46. A. S. Householder
47. H. C. Hoy
48. R. P. Jernigan, Jr.
49. W. D. Jones
50. G. G. Kelley
51. M. T. Kelley
52. R. L. Knight
53. J. A. Lane
54. C. E. Larson
55. N. H. Lazar
56. G. F. Leichsenring
57. J. Lewin
58. R. S. Livingston
59. J. N. Luton, Jr.
60. J. F. Lyon
61. J. R. McNally, Jr.
62. O. D. Matlock
63. K. Z. Morgan
64. O. B. Morgan
65. R. V. Neidigh
66. M. L. Nelson
67. J. Neufeld
68. C. E. Parker
69–70. R. B. Parker
71. W. F. Peed
72. H. Postma
73. J. F. Potts
74. M. Rankin
75. J. A. Ray
76. L. H. Reber
77. R. G. Reinhardt
78. D. M. Richardson
79. D. A. Ross
80. P. W. Rueff
81. W. K. Russell
82. H. E. Seagren
83. Y. Shima
84. E. D. Shipley
85. M. R. Skidmore
86. M. J. Skinner
87–101. A. H. Snell
102. W. L. Stirling
103. R. F. Stratton, Jr.
104. R. A. Strehlow
105. J. A. Swartout
106. E. H. Taylor
107. H. L. Watts
108. A. M. Weinberg
109. E. R. Wells
110. T. A. Welton
111. G. C. Williams
112. W. L. Wright

113. A. J. Wyrick
114. O. C. Yonts
115. Gale Young
116. W. H. Bostick (consultant)
117. J. W. Flowers (consultant)
118. M. W. Garrett (consultant)
119. H. Grad (consultant)
120. E. G. Harris (consultant)
121. D. E. Harrison (consultant)
122. W. Heckrotte (consultant)
123. R. Hefferlin (consultant)
124. G. W. Hoffman (consultant)
125. V. W. Hughes (consultant)
126. E. W. McDaniel (consultant)
127. D. R. Montgomery (consultant)
128. C. E. Nielsen (consultant)
129. W. B. Pardo (consultant)
130. J. M. Reynolds (consultant)
131. H. S. Robertson (consultant)
132. H. G. Rorschach (consultant)
133. D. J. Rose (consultant)
134. L. P. Smith (consultant)
135. P. M. Stier (consultant)
136. J. D. Tillman (consultant)
137–161. Thermonuclear Division Library
162. Reactor Division Library
163. Biology Division Library
164–166. Central Research Library
167. Laboratory Shift Supervisor
168–242. Laboratory Records Department
243. Laboratory Records, ORNL RC
244–245. ORNL – Y-12 Technical Library Document Reference Section

EXTERNAL DISTRIBUTION

246. S. C. Brown, Massachusetts Institute of Technology
247. M. B. Gottlieb, Princeton University
248. J. L. Tuck, Los Alamos Scientific Laboratory
249. D. W. Kerst, University of Wisconsin
250. A. C. Kolb, Naval Research Laboratory
251. J. A. Phillips, Los Alamos Scientific Laboratory
252. R. F. Post, University of California, Lawrence Radiation Laboratory
253. A. Simon, General Atomic, San Diego, California
254. L. Spitzer, Princeton University
255. E. Teller, University of California, Lawrence Radiation Laboratory
256. C. M. Van Atta, University of California, Lawrence Radiation Laboratory
257. R. W. McNamee, Union Carbide Corporation
258–259. Research and Development Division, AEC, ORO (1 copy each to H. M. Roth and R. B. Martin)
260–261. Controlled Thermonuclear Research Branch, AEC, Washington (A. E. Ruark)
262. L. D. Smullin, Massachusetts Institute of Technology
263–274. USAEC, Division of Research, Controlled Thermonuclear Research Program (Stephen O. Dean)
275–888. Given distribution as shown in TID-4500 (31st ed.) under Controlled Thermonuclear Processes category (75 copies – OTS)